

# All-Electron GW Calculations for Perovskite Transition-Metal Oxides

Von der Fakultät für Mathematik, Informatik und  
Naturwissenschaften der RWTH Aachen University zur  
Erlangung des akademischen Grades eines Doktors der  
Naturwissenschaften genehmigte Dissertation

vorgelegt von

Dipl.-Phys. Andreas Gierlich

aus

Bonn, Deutschland

Berichter: Univ.-Prof. Dr.rer.nat. Stefan Blügel  
Univ.-Prof. Dr.rer.nat. Arno Schindlmayr

Tag der mündlichen Prüfung: 29.07.2011

Diese Dissertation ist auf den Internetseiten der  
Hochschulbibliothek online verfügbar.

*Was einmal gedacht wurde,  
kann nicht wieder zurückgenommen werden.*

DIE PHYSIKER, F. Dürrenmatt

# ABSTRACT

Ever since the middle of the 1920s, when compounds from the perovskite structure family played a key role in the groundbreaking work of Goldschmidt on material synthesis, perovskite transition-metal oxides (TMOs) have repeatedly stimulated new activities in fundamental research as well as in the development of new technical applications. Thus, many perovskite TMOs, for example the ferroelectrics  $\text{BaTiO}_3$  and  $\text{PbTiO}_3$ , have become an integral part of present-day technologies. Intriguing properties of other perovskite TMOs such as ferromagnetic  $\text{LaMnO}_{3+\delta}$  or the high- $\kappa$  dielectric  $\text{BaZrO}_3$  and their potential use in future applications are currently investigated. As a large variety of A and B cations can be combined to form the perovskite crystal structure with stoichiometric composition  $\text{ABO}_3$ , compounds with a wide range of material properties can be synthesized. This makes perovskite transition-metal oxides a unique formal laboratory to test models and theories pertaining to solid state physics.

The goal of this thesis is to shed light on the structure-composition-properties relation of this fascinating class of materials from the electronic-structure point of view. The investigations are based on density functional theory (DFT), the most successful theory for the description of ground-state electronic properties from first-principles in combination with the GW approximation (GWA) from many-body perturbation theory which has emerged as the method of choice to describe single-particle excitation spectra of solids. In this work, the full-potential linearized augmented plane-wave method (FLAPW) is used in all calculations. As an all-electron scheme it is particularly suitable to describe d and f states of transition metals and rare earths contained in the perovskite TMOs.

Trends in the electronic structure of three series of prototypical perovskite TMOs including  $\text{BaTiO}_3$ ,  $\text{BaZrO}_3$ , and  $\text{PbTiO}_3$  in the high-temperature cubic crystal phase are investigated to relate changes in the single-particle excitation spectra and band gaps to changes in the composition of the materials. In addition, the effect of symmetry-breaking relaxations from the cubic crystal phase on the electronic structure occurring at room temperature is investigated. The first-principles results emphasize the importance of including these effects in the calculations in order to quantitatively reproduce band gaps measured in experiment. Furthermore, trends in the positions of high-lying core states are analyzed. The calculated positions of the core states agree well with results from photo-emission experiments.

Secondly, GW calculations for the three band insulators  $\text{LaCrO}_3$ ,  $\text{LaMnO}_3$ , and  $\text{LaFeO}_3$  are carried out. Results from DFT calculations employing the generalized-gradient approximation with the PBE functional or results obtained from cal-

culations using the hybrid-functional HSE are used as starting point to apply many-body perturbation theory. The analysis of photo-emission spectra focuses specifically on the position of the partially filled d states of the transition metals yielding finite spin-magnetic moments at the transition-metal site of all three compounds which order antiferromagnetically. Whereas the HSE result lead to a general improvement of the PBE results for the spin-magnetic moments, band gaps and photo-emission spectra are best described by the combination of HSE+GW in the case of  $\text{LaCrO}_3$  and by PBE+GW calculations for  $\text{LaMnO}_3$  and  $\text{LaFeO}_3$ . For all three compounds, good quantitative agreement with experimental data is attained.

The last part of the thesis focuses on the question how accurately a Hubbard model can reproduce the spectrum of a subspace of the full Hilbert space, as this kind of model allows to gain insight into the electronic structure of materials even if first-principles approaches are not applicable. A simple test system is constructed to simulate partially filled valence states whose single-particle excitation spectrum can be calculated exactly. These results are compared with the description for a subspace of the full system obtained from a Hubbard model. The model is designed to yield the best possible approximation for the exact spectrum. The investigations reveal that the Hubbard model cannot reproduce the spectrum exactly as soon as the wave functions of states inside the subspace exhibit a finite overlap with wave functions of states not contained in the subspace. This limits the applicability of the Hubbard model to the description of subspaces with a small degree of hybridization between states inside and outside the subspace.

# ZUSAMMENFASSUNG

Seitdem Mitte der 1920er Jahre Materialien aus der Familie der Perowskite eine Schlüsselrolle in der bahnbrechenden Arbeit Goldschmidts zur Materialsynthese gespielt haben, tragen Übergangsmetalloxide mit Perowskitstruktur (kurz Perowskite) wiederholt und nachhaltig zu neuen Aktivitäten in der Grundlagenforschung sowie zur Entwicklung neuer Technologien bei. Da Perowskitstrukturen der stöchiometrischen Zusammensetzung  $ABO_3$  aus einer Vielzahl unterschiedlicher Kationen A und B synthetisiert werden können, existiert bereits eine Vielzahl von Verbindungen mit unterschiedlichsten Eigenschaften. Diese Vielfalt fordert und fördert die Anwendung und Weiterentwicklung von Theorien in der Festkörperphysik zum besseren Verständnis der Eigenschaften dieser faszinierenden Materialklasse.

Ziel dieser Arbeit ist es, den Zusammenhang zwischen der strukturellen und der chemischen Zusammensetzung der Perowskite auf der einen Seite und der elektronischen Eigenschaften auf der anderen Seite zu untersuchen. Dazu werden *ab-initio*-Berechnungen mit Methoden der Dichtefunktionaltheorie (DFT) in Kombination mit der GW-Näherung (GWA) durchgeführt. Während DFT sich als Theorie zur Beschreibung von Grundzustandseigenschaften von Materialien durchsetzen konnte, hat sich die GWA, eine Methode der Vielteilchenstörungstheorie, als Königsweg zur Beschreibung angeregter Zustände in Festkörpern etabliert. Für die Durchführung von Berechnungen in dieser Arbeit wird die *full-potential linearized augmented plane-wave*-Methode (FLAPW) verwendet, die besonders geeignet ist auch d- und f-Zustände in Übergangsmetallen und Seltenen Erden zu beschreiben, aus denen die Perowskite zusammengesetzt sind.

Die elektronischen Eigenschaften einer Reihe von prominenten Vertretern der Perowskite einschließlich der Verbindungen  $BaTiO_3$ ,  $PbTiO_3$  und  $BaZrO_3$  in der kubischen Kristallgitterphase werden im ersten Teil der Arbeit untersucht, um Zusammenhänge zwischen Änderungen in der chemischen Zusammensetzung und Änderungen im Spektrum angeregter Einteilchenzustände herzustellen. Des Weiteren werden Veränderungen der elektronischen Struktur aufgrund von Gitterverzerrungen bei Raumtemperatur analysiert. Der Vergleich von experimentell bestimmten optischen Bandlücken mit den Quasiteilchenbandlücken legt nahe, dass der Einfluss solcher Verzerrungen eine wichtige Rolle für eine akkurate *ab-initio*-Beschreibung dieser Materialien spielt. Außerdem werden die Energien von hoch liegenden Kernzuständen mittels der GWA berechnet, die ebenfalls gut mit Messergebnissen übereinstimmen.

Im zweiten Teil der Arbeit werden Ergebnisse von GW-Rechnungen für die Bandisolatoren  $LaCrO_3$ ,  $LaMnO_3$  und  $LaFeO_3$  präsentiert. Als Startpunkt für die

Anwendung der GWA wurden sowohl DFT- Rechnungen getestet, in denen das PBE-Funktional Verwendung fand, bei dem es sich um eine *generalized-gradient approximation* handelt, als auch solche Rechnungen, in denen das Hybridfunktional HSE verwendet wurde. Besonderes Augenmerk bei der Analyse von Zustandsdichten wird auf die Beiträge der teilweise gefüllten d-Schalen der Übergangsmetalle gelegt. Die beste Übereinstimmung von Zustandsdichten mit Photoemissionsspektren wird aber nur im Fall von  $\text{LaCrO}_3$  durch eine Kombination von HSE-Ergebnissen mit GW-Rechnungen erreicht. Für  $\text{LaMnO}_3$  und  $\text{LaFeO}_3$  liefern die auf den PBE-Ergebnissen basierenden GW-Rechnungen bessere Resultate. Eine gute Übereinstimmung mit den experimentell gemessenen Bandlücken kann so für alle drei Verbindungen erzielt werden.

Im letzten Teil wird untersucht, welche Voraussetzungen erfüllt sein müssen, damit ein Hubbard-Modell das Vielteilchenspektrum eines Unterraums des gesamten Hilbert-Raums exakt beschreiben kann, da derartige Modelle häufig Einblicke in die elektronische Struktur von Materialien erlauben, selbst wenn *ab-initio*-Berechnungen nicht realisiert werden können. Hierzu wurde ein Testsystem entwickelt, mit dem sich ein Unterraum aus teilweise besetzten elektronischen Zuständen in der Anwesenheit voll besetzter oder leerer Zustände simulieren lässt. Die exakte Beschreibung des Vielteilchenspektrums dieses Unterraums durch den Teilchenzahlformalismus wird mit der Beschreibung durch ein Hubbard-Modell verglichen, welches so konstruiert wurde, dass es die bestmögliche Näherung des exakten Vielteilchenspektrums erzielt. Die Untersuchungen zeigen, dass das exakte Spektrum nur dann reproduziert werden kann, wenn es keine Überlagerung der Wellenfunktionen der Zustände im Unterraum mit Wellenfunktionen der Zustände außerhalb des Unterraums gibt.

## ACKNOWLEDGMENT

First and foremost, I would like to express my sincere gratitude to my Ph.D. supervisor Prof. Dr. Stefan Blügel. Our first encounter in my master course about the theory of solid state physics was so inspiring that I chose to further pursue the road of solid state research. He gave me the opportunity to write my thesis in the exceptional environment of the *Institute of Solid State Research* (IFF) in the *Forschungszentrum Jülich*. He always had an open mind for new ideas and alternative approaches but he also supported me to see it through that this thesis would finally come to an end.

I am also very grateful to Prof. Dr. Arno Schindlmayr for sharing his profound knowledge of many-body perturbation theory in innumerable discussions and for helping me to find the topic of my thesis. Special thanks goes to Dr. Christoph Friedrich for teaching me how to use the SPEX code, for helping me with the nitty-gritty details of first-principles calculations with the GW method, and, most of all, for his meticulous and patient revision of my humble writing. Moreover, I thank the people at my home institute *Quantum Theory of Materials* at the IFF, in particular Dr. Gustav Bihlmayer for guidance on using the FLEUR code and Dr. Marjana Ležaić for fruitful discussions about the physics of perovskite transition-metal oxides. Last but not least, I heartily thank Mrs. Ute Winkler, who always helped me to make administration-related business run smoothly and who would always listen to my complaints about the non-physics-related problems of everyday life.

I had the chance to visit the beautiful city of Prague on several occasions during my stay at the IFF and I also had the opportunity to visit the Chiba University in Japan twice. I am indebted to RNDr. Václav Drchal, who did not only organize my stays at the Academy of Science in Prague but who became a real mentor during my time as a Ph.D. student. Furthermore, it was my great pleasure to work with Prof. Dr. Ferdi Aryasetiawan, who heartily welcomed me at the Chiba University and took me on an exciting journey to the field of model-based electronic structure calculations. And I am particularly grateful to Prof. Dr. Rei Sakuma, who made me feel at home in Japan. Without him I would have surely been lost in translation! I acknowledge financial support for my travel activities from the *Deutscher Akademischer Austausch Dienst* (DAAD), the Academy of Science of the Czech Republic and the Japan Society for the Promotion of Science (JSPS).

To my fellow master and Ph.D. students: you made the time in the IFF all the more joyful! I relished our discussions at the students seminar, the coffee breaks, the daily chit-chat at lunch, and the board-game nights. Moreover, I very much

appreciate your support in solving small and big numerical and physics-related problems. I like to thank Alex, Andreas F., Aaron, Gregor, Mathias, and Paul. In particular, I want to thank Markus B. and Martin who made a big effort to realize DFT calculations employing hybrid functionals to large systems of the size presented in this thesis and who helped me a lot to modify the corresponding parts of the FLEUR code to generate input data for subsequent GW calculations. My special thanks goes to the *old office team* Andreas, Manni, and Swantje for keeping up the good spirit during all those years!

Finally, I want to thank my friends, my father, and my brother for coping with my mood swings, if things did not go smoothly, for cheering me up, and for putting me back on track if necessary. You have all contributed a lot to make this happen! Most of all and most dearly, I thank my wife, Eva-Maria. You had to bear the most yet never stopped believing in me! I do not know how things would have been without all the concessions you made and all the loving support you gave me. I will never be able to thank you for all you have done!

Jülich, January 2011

Andreas Gierlich

# TABLE OF CONTENTS

<b>1</b>	<b>Introduction</b>	<b>1</b>
<b>2</b>	<b>Theory of electronic structure calculations from first principles</b>	<b>7</b>
2.1	The many-body problem . . . . .	8
2.2	Density-functional theory . . . . .	10
2.2.1	The Kohn-Sham (KS) formalism . . . . .	11
2.2.2	The KS-Dirac equation and spin-orbit coupling . . . . .	13
2.2.3	Local-density (LDA) and generalized-gradient (GGA) approximation . . . . .	16
2.2.4	The band-gap problem of LDA and GGA . . . . .	18
2.2.5	The generalized Kohn-Sham scheme . . . . .	19
2.3	Many-body perturbation theory . . . . .	24
2.3.1	Quasiparticles . . . . .	26
2.3.2	Equation of motion and self-energy . . . . .	27
2.3.3	The GW approximation (GWA) for the self-energy . . . . .	29
2.3.4	The GWA in electronic structure calculations . . . . .	32
<b>3</b>	<b>Implementation within the FLAPW method</b>	<b>37</b>
3.1	Basis sets . . . . .	38
3.1.1	Plane waves . . . . .	38
3.1.2	Augmented plane waves and the LAPW basis functions . . . . .	40
3.1.3	The local orbital (LO) extension . . . . .	43
3.1.4	The mixed product basis (MPB) . . . . .	44

3.2	Remarks on density-functional calculations with FLEUR . . . . .	47
3.2.1	The generalized eigenvalue problem . . . . .	47
3.2.2	Including the full potential in the LAPW method . . . . .	49
3.2.3	Scalar-relativistic approximation and SOC in second variation . . . . .	50
3.3	The SPEX code . . . . .	51
3.3.1	GW calculations with the SPEX code . . . . .	52
3.3.2	Construction of the $\mathbf{k}$ mesh . . . . .	56
3.3.3	Treatment of the $\Gamma$ point . . . . .	57
3.3.4	The density of states in GW calculations . . . . .	59
3.3.5	The dielectric function within the RPA . . . . .	61
<b>4</b>	<b>Perovskites – a short introduction</b>	<b>65</b>
4.1	Crystal structure . . . . .	66
4.2	Perovskites and crystal field theory . . . . .	70
4.3	Perovskites and molecular orbital theory . . . . .	74
4.4	Insulating properties of transition-metal oxides (TMOs) . . . . .	83
4.4.1	Band theory . . . . .	84
4.4.2	Correlation-driven insulating behavior . . . . .	87
4.4.3	Classification of the perovskite TMOs investigated in this work . . . . .	91
<b>5</b>	<b>Trends in the electronic structure of selected perovskite TMOs</b>	<b>93</b>
5.1	Numerical aspects . . . . .	94
5.1.1	Convergence of input parameters . . . . .	95
5.1.2	Convergence of the representation of the unoccupied states . . . . .	100
5.2	Trends in the electronic structure . . . . .	105
5.2.1	Valence- and conduction-band spectra . . . . .	105
5.2.2	Influence of SOC in $\text{PbBO}_3$ , $B = \text{Ti, Zr, and Hf}$ . . . . .	118
5.2.3	Semicore states . . . . .	122
5.3	GWA results versus experiment . . . . .	125
5.3.1	Room temperature crystal and electronic structures . . . . .	125
5.3.2	Transition energies and band gaps in experiment . . . . .	127
5.3.3	Band gaps, semicore states, and dielectric functions . . . . .	131
5.4	Discussion and Summary . . . . .	138

<b>6</b>	<b>First-principles calculations for <math>\text{LaCrO}_3</math>, <math>\text{LaMnO}_3</math>, and <math>\text{LaFeO}_3</math></b>	<b>143</b>
6.1	Crystal and magnetic structures . . . . .	144
6.2	KS band structures . . . . .	146
6.3	Band gaps and photo-emission spectra . . . . .	149
6.4	Magnetic moments of $B = \text{Cr, Mn, and Fe}$ in $\text{LaBO}_3$ . . . . .	156
6.5	Discussion and Summary . . . . .	157
<b>7</b>	<b>Modeling spectra of subspaces – a case study beyond the GWA</b>	<b>159</b>
7.1	Theory . . . . .	160
7.1.1	The 4-orbital model . . . . .	161
7.1.2	Hubbard Hamiltonian for a subspace . . . . .	166
7.2	Results . . . . .	172
7.2.1	Influence of fully occupied states on valence electrons . . . . .	172
7.2.2	Valence electrons and empty states . . . . .	184
7.3	Discussion and Summary . . . . .	188
<b>8</b>	<b>Conclusion</b>	<b>191</b>
<b>A</b>	<b>Many-Body Perturbation Theory</b>	<b>195</b>
A.1	Hedin Equations . . . . .	195
A.2	Vertex Correction from $v^{\text{xc}}$ in the GWA . . . . .	198
<b>B</b>	<b>Input parameters</b>	<b>201</b>
B.1	Input parameters – part 1 . . . . .	203
B.2	Input parameters – part 2 . . . . .	211
<b>C</b>	<b>A case study beyond the GWA</b>	<b>215</b>
C.1	Proof of formula (7.42) . . . . .	215
C.2	The lack of screening for $U_{\text{II}} = 0$ . . . . .	215
	<b>Bibliography</b>	<b>217</b>



The abundance of perovskite transition-metal oxides proves the perovskite structure to be one of the most versatile crystallographic hosts. Composed of formula units  $ABO_3$ , where A and B typically are cations of a simple and a transition metal, respectively, the perovskite structure is highly stable against substitution of either one of the cations thus allowing for a large number of combinations of chemical elements. In addition, it is extremely tolerant to vacancy formation. Compositions of cations at the A site with valence 1+ (Na, K), 2+ (Ca, Sr, Ba, Pb) or 3+ (Fe, La, Gd) with B-site cations of valence 3+ (Cr, Mn, Fe), 4+ (Ti, Zr, Hf) and 5+ (Nb, W) yield a huge array of phases with totally different functions comprising insulating, semiconducting, conducting and superconducting behavior as well as ferroelectricity, piezoelectricity and ferromagnetism. This diversity of material properties makes perovskite transition-metal oxides a unique formal laboratory to test models and theories pertaining to solid state chemistry and physics. Moreover, they are true multifunctional high-tech materials for present day and future technologies, which are used as catalysts, microwave dielectrics, dielectric resonators and superconductors and have become key components in capacitors, detectors, sensors and piezoelectric applications of all kinds [1, 2].

The first large scale industrial application of a perovskite transition-metal oxide,  $BaTiO_3$ , is closely tied to the history of a very different material, the phyllosilicate mineral muscovite mica. Muscovite mica had become the most widely used insulator in the production of capacitors during the first half of the 20th century. The Allies, Germany, Russia and Japan had to import mica but supply lines became increasingly tenuous with the beginning of World War II. Thus, it was a key wartime goal for all these countries to find a substitute dielectric. Within a three-years time period starting in 1942, American scientists Wainer and Salomon [3, 4], Ogawa in Japan (see comment in [5]) as well as Wul and Goldman [6] in

Russia independently identified  $\text{BaTiO}_3$  as the most promising candidate having the by far highest absorption coefficient  $\kappa$ . Shortly afterwards in 1945 and 1946, von Hippel (USA) [7] as well as Wul and Goldman [8] demonstrated ferroelectric switching in  $\text{BaTiO}_3$  ceramics thus identifying the origin of the extraordinary value of  $\kappa$ . The discovery of ferroelectricity in  $\text{BaTiO}_3$  was extremely important, as it illustrated for the first time that ferroelectricity could exist in simple oxide materials.

$\text{BaTiO}_3$  also became the first ceramic transducer material but it was soon replaced by the solid solution of two other perovskite transition-metal oxides,  $\text{PbTiO}_3$  and  $\text{PbZrO}_3$ , whose exceptional ferroelectric properties were established by Shiran *et al.* [9] as well as Jaffe and coworkers [10] during the 1950s. Since that time, new discoveries involving members from the perovskite structural family or its derivatives have repeatedly stimulated both new activities in fundamental research and the development of technical applications. One of the most outstanding examples is the discovery of high- $T_c$  superconductivity in Ba-La-Cu-O systems in 1986. These systems crystallizing in a layer-type perovskite-like phase were first synthesized and characterized by Bednorz and Müller [11]. A mere year later, they were awarded the Nobel prize *for their important break-through in the discovery of superconductivity in ceramic materials*. However, in high  $T_c$  superconductors as in many perovskite transition-metal oxides with intriguing properties the in-depth understanding of the underlying physical mechanisms is still far from complete. Further theoretical investigations are required to better understand the structure-composition-properties relations in complex quantum materials such as the perovskite transition-metal oxides, which can in turn help to optimize present-day technologies and to exploit the potential of designing new compositions for future applications. A huge step forward in gaining insight into material properties from the electronic structure point of view became possible due to the emergence of density-functional theory (DFT) [12].

Since the 1960s, first-principles calculations based on DFT have been established as the method of choice to investigate the electronic ground-state properties of large material classes including insulators, semiconductors, half-metals, simple metals, transition metals and rare-earths. The term *first-principles* or *ab initio*, respectively, indicates that no further parameters enter the calculations than those fixed by the basic assumptions and equations of quantum mechanics and DFT. Therefore, the powerful albeit numerically simple approximations within the framework of DFT such as the local-density approximation (LDA) and the generalized gradient approximation (GGA) do not only allow to characterize ground-state properties of existing compounds. These approaches can equally describe newly-formed materials requiring, in principle, only the atomic numbers of the composing atoms as input. Hence, the wide applicability and the predictive power of DFT-based schemes meet the demands of intelligent mate-

rials design. Moreover, successful extensions of the theoretical framework also allow to treat single-particle excitations by many-body perturbation theory based on Green-function techniques.

The Green function is the canonical choice to describe single-particle excitations, since it represents the probability amplitude of an excited electron or hole traveling from one place in a solid to another in a given time period. In many-body perturbation theory, the full single-particle Green function is determined with the help of the self-energy operator  $\Sigma$ . In general,  $\Sigma$  is a complex, non-local and energy-dependent operator, whose real part describes the change in energy of the excited particle due to interactions with other particles upon moving through the solid whereas the inverse of the imaginary part is proportional to the lifetime of the excitation. The self-energy also enters the quasiparticle equation, whose eigenvalues correspond to the energies of the single-particle excitations. Solving the quasiparticle equation directly allows to determine the excitation energies without the need to calculate the full Green function explicitly provided that  $\Sigma$  is known. However, the self-energy capturing all many-body effects is a complicated quantity. It is very difficult to calculate even for model systems like the electron gas. Hence, it has to be approximated in first-principles calculations for real materials.

In the GW approximation (GWA) the self-energy is expressed in terms of the Green function  $G$  describing a non-interacting particle and the screened interaction  $W$  corresponding to the Coulomb interaction which is dynamically screened due to secondary excitations of electron-hole pairs. For real materials, both  $G$  and  $W$  can be readily calculated with solutions from DFT-based schemes. Since its introduction in 1965 by Hedin [13], the GWA has been firmly established as the gold standard in calculations for the single-particle excitation energies of simple metals, semiconductors and insulators [14]. The treatment of transition metals and transition-metal compounds within the GWA is challenging due to the large numerical expense of GW calculations on the one hand and the high precision necessary to obtain an accurate description of the localized transition-metal  $d$  states on the other hand. Up to date, only few GW calculations of perovskite transition-metal oxides have been reported [15, 16, 17].

In this work, results from state-of-the-art electronic structure calculations based on DFT and the GWA for selected perovskite transition-metal oxides are presented. The DFT calculations were carried out with the FLEUR code [18], which is based on the full-potential linearized augmented plane-wave (FLAPW) method [19]. The latter is an all-electron scheme treating core and valence electrons explicitly. It is considered one of the most precise density-functional methods for multicomponent materials, open structures and surfaces. The GW implementation SPEX [20] employs the mixed basis [21, 22] for the representation of the screened interaction  $W$  and related quantities thus retaining the full accuracy of

the linearized augmented plane-wave basis of the FLAPW method.

These techniques are applied first in a systematic study of a series of prototypical perovskite transition-metal oxides including  $\text{BaTiO}_3$ ,  $\text{PbTiO}_3$  and  $\text{PbZrO}_3$  to investigate the relation between properties of the single-particle excitation spectra and the composition of these compounds. Trends in the excitation energies involving low-lying semicore states are analyzed as well. Furthermore, changes in the electronic structure are discussed, which originate from distortions in the perovskite crystal lattices. As these kind of distortions have been observed in the room-temperature crystal phases of the majority of these compounds, related changes in their electronic structure are of particular importance when comparing the calculated single-particle excitation spectra to data from optical and photo-emission spectroscopies measured at room temperature.

Secondly, the *ab initio* approach is employed to investigate the electronic structure of the three compounds  $\text{LaCrO}_3$ ,  $\text{LaMnO}_3$  and  $\text{LaFeO}_3$ . The partial filling of the d shell of the transition-metal cation in these compounds leads to the formation of a finite spin-magnetic moment at the transition-metal site. Furthermore, correlation between the d electrons is considered to have an important effect on their electronic structure. However, correlation effects are often underestimated in calculations employing the LDA or GGA. In addition, the self-interaction error inherent to these approximations becomes large for electrons occupying the more localized transition-metal 3d or La 4f states. Hybrid functionals allow to incorporate a certain degree of exact exchange into the DFT-based calculations which removes the self-interaction error at least partially. Therefore, results from calculations employing the hybrid functional HSE [23, 24] are compared with results obtained with the GGA functional PBE [25]. Furthermore, it is investigated, which scheme yields a superior starting point to apply many-body perturbation theory within the GWA. Photo-emission spectra and spin-magnetic moments obtained from different levels of approximation are compared to results from spectroscopic measurements.

For some materials, the GWA may not suffice to describe the effects of exchange and correlation especially if the latter becomes strong. For example, the strongly correlated materials  $\text{LaTiO}_3$  or  $\text{LaVO}_3$  exhibit a correlation-driven transition from a metallic to an insulating phase at low temperature. As the description of this phase transition is beyond the scope of perturbation theory one has to go beyond the GWA to analyze the electronic structure of these kind of materials. One possibility is the construction of model Hamiltonians, which only describe a certain part of the full Hilbert space explicitly including the interaction with the states in the remaining parts of the Hilbert space implicitly via the parameters defining the model Hamiltonian. One of the most celebrated models is the Hubbard model [26, 27, 28, 29, 30] which has been employed successfully in the context of dynamical mean-field theory [31] combined with LDA to treat strongly correlated

materials in recent years [32, 33, 34, 35].

For this work, a test system was designed to simulate electronic states located close to the Fermi energy in the vicinity of fully occupied or empty states similar to the partially filled 3d states in the compounds  $\text{LaCrO}_3$ ,  $\text{LaMnO}_3$  and  $\text{LaFeO}_3$ . The exact many-body solution of this system obtained with the help of the particle-number formalism is used to explore changes in the single-particle excitation spectrum upon tuning the interaction between the electrons as well as the overlap between different states. In addition, a Hubbard-type model for the system is constructed which only treats the states close to the Fermi energy explicitly. The spectra obtained from this model are compared with the exact solution to identify possible limitations of the Hubbard model. The analysis may also yield indications for the applicability of the Hubbard model in simulations of the electronic structure of real materials due to the generality of the approach.

The thesis is organized as follows. The second chapter briefly recites some fundamental aspects of DFT, the Green-function technique and many-body perturbation theory. Various approximations based on these theories, which are used throughout this work, such as the GGA and hybrid functionals as well as the GWA are introduced. The FLAPW method and its implementation in FLEUR and SPEX are discussed in chapter 3. Chapter 4 gives a short introduction to the perovskite structural family. The first part describes the crystal phases of the compounds investigated in this work. In the second part, empirical and semi-empirical approaches, i.e. crystal field and molecular orbital theory, are applied to gain qualitative insight into the electronic structure of perovskite transition-metal oxides. In chapter 5, results from GW calculations for selected perovskite transition-metal oxides are presented and in chapter 6 the electronic structure of  $\text{LaCrO}_3$ ,  $\text{LaMnO}_3$  and  $\text{LaFeO}_3$  as obtained from first-principles calculations is discussed. Model calculations beyond the GWA analyzing the range of applicability of the Hubbard model are the topic of chapter 7. The thesis is concluded in chapter 8.



## CHAPTER 2

# THEORY OF ELECTRONIC STRUCTURE CALCULATIONS FROM FIRST PRINCIPLES

This chapter provides insight into the theoretical concepts behind the methods, which are used to carry out electronic structure calculations from first principles in this work. First, the many-body Schrödinger equation is presented. This is the starting point for all further theoretical considerations. Within the Born-Oppenheimer approximation [36] the atomic and electronic degrees of freedom decouple and a Schrödinger equation of a system comprising  $N$  electrons can be obtained. Since it cannot be solved exactly the Kohn-Sham [37] and the generalized Kohn-Sham scheme [38] within density-functional theory are introduced in section two. These schemes make use of effective single-particle equations which yield the exact ground-state density of the  $N$ -electron system if they are solved self-consistently. This allows to calculate observables of the  $N$ -electron system which can be expressed as functionals of the density such as the ground-state total energy without the knowledge of the full many-body wave function. Whereas DFT-based approaches are designed to investigate the ground-state properties of materials, Green-function based techniques allow to describe single-particle excitation spectra. The concept of the Green function together with the GW approximation (GWA) [13] obtained from many-body perturbation theory is introduced in the third part of this chapter. Last but not least, it is demonstrated how the Kohn-Sham or generalized Kohn-Sham schemes combined with energy corrections obtained from the self-energy calculated within the GWA can be used to describe the excitation spectra of real materials.

## 2.1. The many-body problem

A crystal containing  $N$  electrons and  $M$  atomic nuclei is described by the many-body Schrödinger equation<sup>1</sup>

$$H\Psi(\mathbf{r}_1, \dots, \mathbf{r}_N; \mathbf{R}_1, \dots, \mathbf{R}_M) = E\Psi(\mathbf{r}_1, \dots, \mathbf{r}_N; \mathbf{R}_1, \dots, \mathbf{R}_M), \quad (2.1)$$

where the total energy  $E$  is the eigenvalue of the many-body wave function  $\Psi(\mathbf{r}_1, \dots, \mathbf{r}_N; \mathbf{R}_1, \dots, \mathbf{R}_M)$  and the vectors  $\mathbf{r}_i$  and  $\mathbf{R}_i$  denote the positions of the electrons and nuclei in space. The Hamiltonian  $H$  in eq. (2.1) consists of five terms

$$\begin{aligned} H &= T_e + T_I + V_{II} + V_{\text{ext}} + V_{ee} \\ &= -\frac{1}{2} \sum_i^N \nabla_{\mathbf{r}_i}^2 - \sum_i^M \frac{1}{2M_i} \nabla_{\mathbf{R}_i}^2 + \frac{1}{2} \sum_{\substack{i,j \\ i \neq j}}^M \frac{Z_i Z_j}{|\mathbf{R}_i - \mathbf{R}_j|} \\ &\quad + \sum_i^N v^{\text{ext}}(\mathbf{r}_i) + \frac{1}{2} \sum_{\substack{i,j \\ i \neq j}}^N v(\mathbf{r}_i, \mathbf{r}_j), \end{aligned} \quad (2.2)$$

where the first and second term,  $T_e$  and  $T_I$ , represent the kinetic energy of the electrons and the atomic nuclei with mass  $M_i$ . The third term  $V_{II}$  is the contribution resulting from the interaction between the atomic nuclei, where  $Z_i$  represents the atomic numbers. The term  $V_{\text{ext}}$  is the energy generated by the external potential  $v^{\text{ext}}(\mathbf{r}_i)$  due to the positively charged atomic nuclei acting on the electrons in the solid

$$V_{\text{ext}} = \sum_i^N v^{\text{ext}}(\mathbf{r}_i) = - \sum_i^N \sum_j^M \frac{Z_j}{|\mathbf{r}_i - \mathbf{R}_j|}. \quad (2.3)$$

The last term  $V_{ee}$  comprising the Coulomb potential  $v(\mathbf{r}_i, \mathbf{r}_j)$  originates from the electrostatic repulsion between pairs of electrons

$$V_{ee} = \frac{1}{2} \sum_{\substack{i,j \\ i \neq j}}^N v(\mathbf{r}_i, \mathbf{r}_j) = \frac{1}{2} \sum_{\substack{i,j \\ i \neq j}}^N \frac{1}{|\mathbf{r}_j - \mathbf{r}_i|}. \quad (2.4)$$

Here and throughout the whole thesis atomic units are used:  $\hbar = m = e^2 = 1$ .

Because of the two-particle terms denoted by  $V_{II}$  and  $V_{ee}$ , equation (2.1) cannot be solved analytically. Furthermore, numerical solutions are not feasible for systems containing more than a few electrons and nuclei, because the computational

<sup>1</sup>For simplicity, relativistic effects in the description of the many-body problem are omitted, because they only have a small influence on the valence electronic structure. Exceptions to this rule especially in connection with the spin-orbit interaction are discussed in section 2.2.2.

effort scales exponentially with the number of particles. For a description of a solid from first principles it is therefore inevitable to introduce approximations to solve the many-body Schrödinger equation (2.1).

One commonly applied simplification when focusing on the electronic degrees of freedom alone is the Born-Oppenheimer approximation [36]. It makes use of the fact that the nucleus' mass is higher than the electron's mass by three to four orders of magnitude. Therefore, the electrons in a solid can adapt almost instantaneously to changes in the atomic positions. Consequently, the electronic system can be described by the N-electron Schrödinger equation

$$H_e \psi(\mathbf{r}_1, \dots, \mathbf{r}_N; \{\mathbf{R}_i\}) = E(\{\mathbf{R}_i\}) \psi(\mathbf{r}_1, \dots, \mathbf{r}_N; \{\mathbf{R}_i\}) \quad (2.5)$$

with the N-electron wave function  $\psi(\mathbf{r}_1, \dots, \mathbf{r}_N; \{\mathbf{R}_i\})$  and the corresponding eigenenergies  $E(\{\mathbf{R}_i\})$ . Here, the positions  $\mathbf{R}_i$  of the nuclei only enter equation (2.5) as parameters because the Hamiltonian  $H_e$  consists of the three terms

$$H_e = T_e + V_{ee} + V_{\text{ext}}, \quad (2.6)$$

where the positions  $\mathbf{R}_i$  only appear in the last term. All calculations discussed in this thesis are ultimately based on the many-electron Schrödinger equation (2.5).

For the sake of completeness it should be mentioned here that it is equally possible to obtain an equation describing the motion of the nuclei in a solid within the Born-Oppenheimer approximation. The assumption that the degrees of freedom of the electrons and nuclei decouple allows to decompose the many-body wave function in eq. (2.1) into a product of the N-electron wave function and a wave function  $\chi(\mathbf{R}_1, \dots, \mathbf{R}_M)$  for the nuclei

$$\Psi(\mathbf{r}_1, \dots, \mathbf{r}_N; \mathbf{R}_1, \dots, \mathbf{R}_M) = \psi(\mathbf{r}_1, \dots, \mathbf{r}_N; \{\mathbf{R}_i\}) \cdot \chi(\mathbf{R}_1, \dots, \mathbf{R}_M). \quad (2.7)$$

Inserting this ansatz for the many-body wave function into eq (2.1) and integrating out the electronic degrees of freedom yields an equation of motion for the nuclei. The electronic system only provides the potential that acts on the nuclei. The assumption that this potential is quadratic with respects to the positions of the atomic nuclei leads to an equation of motion of the same form than that of the harmonic oscillator. The solutions describe the vibronic eigenstates of the crystal. Let's now return to the discussion of the many-electron Schrödinger equation (2.5).

Despite the simplifications of the Born-Oppenheimer approximation, equation (2.5) can also not be solved analytically because it still contains a two-particle term stemming from the Coulomb interaction  $v(\mathbf{r}_i, \mathbf{r}_j)$  between the electrons. Unfortunately, numerical solutions for solids typically containing  $10^{23}$  electrons are also not feasible, which can be illustrated with the following example: a single

iron atom contains  $N = 26$  electrons. For simplicity the spin-degree of freedom of the electrons is neglected here. Hence, the  $N$ -electron wave function  $\psi_I(\mathbf{r}_1, \dots, \mathbf{r}_N; \{\mathbf{R}_i\})$  depends on  $26 \times 3$  coordinates. Choosing a very crude approximation by specifying the wave function on a hyper-cubic grid with 10 points per variable would yield  $10^{78}$  numbers to store and process. Even if each hydrogen atom in our galaxy could store one bit of information, there is simply not enough storage available to save all information contained in this  $N$ -electron wave function.

This thesis aims at investigating the electronic structure and excitation spectra of solids. Fortunately, these physical observables can be calculated without the knowledge of the full many-electron eigenstates solving eq. (2.5). The Kohn-Sham formalism and the generalized Kohn-Sham scheme within density-functional theory – though originally designed to obtain the ground-state energy of a many-electron system – also provide a good estimate for excitation spectra of many materials. These formalisms and their applicability in studying electronic excitations will be discussed in the next part of this chapter.

## 2.2. Density-functional theory

The theoretical foundation of density-functional theory (DFT) was laid by Pierre C. Hohenberg and Walter Kohn in 1964 [12] and is summarized in the two Hohenberg-Kohn theorems.

**Theorem 1.** *Let  $n_0(\mathbf{r})$  be the single-particle density of a non-degenerate ground state of an interacting electron system in an external potential  $v^{\text{ext}}(\mathbf{r})$ . Then  $v^{\text{ext}}(\mathbf{r})$  is (to within an additive constant) a unique functional of  $n_0(\mathbf{r})$ .*

The external potential in turn determines the Hamiltonian in eq. (2.5). Since the  $N$ -electron eigenstates  $\psi$  of the Hamiltonian can be represented as functionals of the external potential, the eigenstates also become functionals of the ground-state density via the first Hohenberg-Kohn theorem. Consequently, any physical observable computed as expectation value of the many-electron eigenstates can be regarded as functional of the single-particle ground-state density. In particular, the ground-state total energy of the electronic system can be written as

$$E[n_0] = \langle \Psi[n_0] | T + V_{ee} + V^{\text{ext}} | \Psi[n_0] \rangle = F[n_0] + \int d^3r v^{\text{ext}}(\mathbf{r}) n_0(\mathbf{r}). \quad (2.8)$$

Here, the universal functional  $F[n]$  was introduced, which is universal in the sense that it is identical for all systems with the same number of electrons regardless of the external potential. Inserting the true single-particle ground-state density of the  $N$ -electron system into eq. (2.8) yields the ground-state total energy. This is reflected in the second Hohenberg-Kohn theorem.

**Theorem 2.** (*variational principle*) The total energy functional  $E[n]$  of the  $N$ -electron system is minimized by the ground-state electron density if the trial densities  $n(\mathbf{r})$  are restricted by the conditions  $n(\mathbf{r}) \geq 0$  and  $\int n(\mathbf{r})d^3r = N$

$$\frac{\delta}{\delta n} \left[ E[n] - \epsilon \left( \int d^3r n(\mathbf{r}) - N \right) \right] \Big|_{n=n_0} = 0, \quad (2.9)$$

where the Lagrange multiplier  $\epsilon$  ensures particle conservation.

Hence, the ground-state density is sufficient to determine the total energy of an electronic system. However, it cannot be obtained directly from the second Hohenberg-Kohn theorem as long as an explicit expression for the functional  $F[n]$  is unknown. In practice, it turns out that  $F[n]$  cannot be exactly determined for real materials. Fortunately, very efficient approximations for  $F[n]$  can be given within the Kohn-Sham and the generalized Kohn-Sham schemes. Before these schemes are introduced in more detail in the following sections, a convenient extension of the above formalism for the description of spin-polarized systems with collinear orientation of the spins should be discussed here briefly.

Spin-DFT was first introduced by von Barth and Hedin [39]. It makes use of the fact that for collinear spin orientation a separate eigenvalue problem for each spin direction can be formulated. The full single-particle density is then obtained as a sum of the densities of the electrons with spin up and spin down orientation. Furthermore, magnetic moments can be calculated as differences of spin up and spin down densities. The calculations for magnetic systems, presented in chapters later on, are based on the spin DFT. However, further discussions in this chapter are only based on DFT omitting the spin degree of freedom, because all theoretical aspects of DFT playing an important role in this work can readily be derived without explicitly taking the electrons' spin into account.

### 2.2.1. The Kohn-Sham (KS) formalism

The question of how an explicit expression for the universal functional  $F[n]$  in eq. (2.8) can be derived was addressed by Kohn and Sham in 1965 [37]. They suggested to replace the system of  $N$  interacting electrons by  $N$  non-interacting electrons in an artificial, external potential. This potential is to be constructed in such a way that the single-particle density of the non-interacting system equals the density of the interacting system. The  $N$ -electron eigenstates of a non-interacting electron system can be represented by single Slater determinants  $\Phi$  of suitable single-particle wave functions  $\varphi_i(\mathbf{r})$ . These Slater determinants are used to evaluate the expectation value of the universal functional under the constraint that

the determinants yield the single-particle density of the interacting system

$$\min_{\Phi \rightarrow n} \langle \Phi | T + V_{ee} | \Phi \rangle = T^{\text{KS}}[n] + \min_{\Phi \rightarrow n} \langle \Phi | V_{ee} | \Phi \rangle. \quad (2.10)$$

The expectation value  $T^{\text{KS}}[n]$  of the kinetic energy can be calculated readily from the single-particle functions  $\varphi_i(\mathbf{r})$ . Therefore, Kohn and Sham suggested the following form for the universal functional

$$F[n] \equiv T^{\text{KS}}[n] + U_{\text{H}}[n] + E_{\text{xc}}[n], \quad (2.11)$$

where the second term on the right hand side is the Hartree energy

$$U_{\text{H}}[n] = \frac{1}{2} \iint d^3r d^3r' \frac{n(\mathbf{r})n(\mathbf{r}')}{|\mathbf{r} - \mathbf{r}'|}. \quad (2.12)$$

The third term is called exchange-correlation energy. It accounts for all exchange and correlation effects on the one hand and for the approximation made by replacing the kinetic energy of the interacting system by that of the non-interacting one on the other. Inserting expression (2.11) for the universal functional  $F[n]$  into eq. (2.8) for the total energy yields

$$E[n] = T^{\text{KS}}[n] + U_{\text{H}}[n] + E_{\text{xc}}[n] + \int d^3r v^{\text{ext}}(\mathbf{r})n(\mathbf{r}). \quad (2.13)$$

Applying the variational principle from the second Hohenberg-Kohn theorem to that equation in turn leads to

$$\frac{\delta T^{\text{KS}}[n]}{\delta n(\mathbf{r})} + \int d^3r' \frac{n(\mathbf{r}')}{|\mathbf{r} - \mathbf{r}'|} + \frac{\delta E_{\text{xc}}}{\delta n(\mathbf{r})} + v^{\text{ext}}(\mathbf{r}) - \epsilon = 0. \quad (2.14)$$

This equation is formally equivalent to that obtained for a system of non-interacting electrons, the Kohn-Sham (KS) system, with the effective potential given by

$$V^{\text{KS}}(\mathbf{r}) = v^{\text{ext}}(\mathbf{r}) + \int d^3r' \frac{n(\mathbf{r}')}{|\mathbf{r} - \mathbf{r}'|} + v^{\text{xc}}(\mathbf{r}) \quad (2.15)$$

where the last term, the exchange-correlation potential  $v^{\text{xc}}(\mathbf{r})$ , is obtained as the functional derivative of the exchange-correlation energy

$$v^{\text{xc}}(\mathbf{r}) = \frac{\delta E_{\text{xc}}}{\delta n(\mathbf{r})}. \quad (2.16)$$

Consequently, the ground-state density  $n_0(\mathbf{r})$  of the interacting system is found by solving the single-particle KS equations

$$\left[ -\frac{1}{2} \nabla_{\mathbf{r}}^2 + V^{\text{KS}}(\mathbf{r}) \right] \varphi_i(\mathbf{r}) = \epsilon_i \varphi_i(\mathbf{r}). \quad (2.17)$$

The density of the KS electrons is given by

$$n(\mathbf{r}) = \sum_i^{\text{occ}} |\varphi_i(\mathbf{r})|^2. \quad (2.18)$$

Since the density enters in the construction of the potential  $V^{\text{KS}}(\mathbf{r})$ , the eqs. (2.17) and (2.18) have to be solved self-consistently. The resulting density equals the ground-state density of the interacting system by construction and consequently yields the true ground-state total energy of the interacting N-electron system when inserted into eq. (2.13).

### 2.2.2. The KS-Dirac equation and spin-orbit coupling

Up to now, relativistic effects were not taken into account in the description of the N-electron system of a solid. This is justified as long as the velocity of the electrons is much smaller than the speed of light such that relativistic effects have a negligible effect on the observables to be calculated. However, both core and valence electrons have finite probability amplitudes near the nucleus, where the kinetic energy is large. This kinetic energy enhancement becomes more significant for heavier elements and compounds. Additionally, only relativistic effects, in particular the spin-orbit coupling (SOC), introduce a link between spatial and spin coordinates. Thus, information about the orientation of spins relative to the lattice can only be gained if relativity is taken into account. In this work, the effect of SOC on the energy spectrum of the electronic system of a solid will be investigated in the context of density-functional (DF) calculations. Therefore, the origin of SOC and its further treatment within DF calculations is outlined in this section.

To treat relativistic effects within DFT in the context of the KS formalism, the KS equation (2.17) is replaced by the single-particle KS-Dirac equation [40]

$$[c\underline{\alpha} \cdot \mathbf{p} + (\underline{\beta} - \underline{1}_4) mc^2 + \underline{1}_4 V^{\text{KS}}(\mathbf{r})] \Psi(\mathbf{r}) = \epsilon \Psi(\mathbf{r}), \quad (2.19)$$

where  $\mathbf{p} = -i\nabla$ ,  $m$  is the mass of the electron and  $c$  the speed of light. The matrices  $\underline{\alpha}$  and  $\underline{\beta}$  are defined as

$$\underline{\alpha} = \left( \left( \begin{pmatrix} \underline{0}_2 & \underline{\sigma}_x \\ \underline{\sigma}_x & \underline{0}_2 \end{pmatrix}, \begin{pmatrix} \underline{0}_2 & \underline{\sigma}_y \\ \underline{\sigma}_y & \underline{0}_2 \end{pmatrix}, \begin{pmatrix} \underline{0}_2 & \underline{\sigma}_z \\ \underline{\sigma}_z & \underline{0}_2 \end{pmatrix} \right) \right)^T \quad (2.20)$$

and

$$\underline{\beta} = \begin{pmatrix} \underline{1}_2 & \underline{0}_2 \\ \underline{0}_2 & -\underline{1}_2 \end{pmatrix}, \quad (2.21)$$

where  $\underline{\sigma}_x, \underline{\sigma}_y, \underline{\sigma}_z$  are the Pauli matrices,  $\underline{1}_2$  denotes a  $(2 \times 2)$  unit matrix and  $\underline{0}_2$  is a  $(2 \times 2)$  matrix containing only zeros. The potential  $V^{\text{KS}}(\mathbf{r})$  is the effective potential of the non-relativistic KS equation defined in (2.15). The eigenfunctions  $\Psi(\mathbf{r})$  of (2.19) are four-component vectors usually written as

$$\Psi(\mathbf{r}) = \begin{pmatrix} \Phi(\mathbf{r}) \\ \chi(\mathbf{r}) \end{pmatrix}, \quad (2.22)$$

and the two-component vectors  $\Phi(\mathbf{r})$  and  $\chi(\mathbf{r})$  are called large and small component of the wave function. Inserted into eq. (2.19), two differential equations coupling the large and small component are obtained

$$c\underline{\sigma} \cdot \mathbf{p} \chi(\mathbf{r}) = \underline{1}_2(\epsilon - V^{\text{KS}}(\mathbf{r})) \Phi(\mathbf{r}) \quad (2.23)$$

$$c\underline{\sigma} \cdot \mathbf{p} \Phi(\mathbf{r}) = \underline{1}_2(\epsilon - V^{\text{KS}}(\mathbf{r}) + 2mc^2) \chi(\mathbf{r}) \quad (2.24)$$

with  $\underline{\sigma} = (\underline{\sigma}_x, \underline{\sigma}_y, \underline{\sigma}_z)^\top$ . Here, the two equations will be used to further investigate the influence of relativistic effects on the valence electrons of a solid.

Since the probability amplitude of a valence electron near the nucleus is small, relativistic effects caused by the kinetic energy enhancement are small, too. In particular, its rest energy  $mc^2$  is much larger than its kinetic and potential energies. Consequently, the small component of the four-component wave function  $\Psi(\mathbf{r})$  of a valence electron is indeed smaller than its large component, since  $mc^2$  only appears in (2.24) and not in (2.23). Hence, eqs. (2.24) and (2.23) can be solved approximately by eliminating the small component. Applying a Foldy-Wouthuysen transformation [41] to eqs. (2.24) and (2.23) results in a new form, in which the off-diagonal elements of the Hamiltonian are so small that the leading order estimate of the small component is sufficient to get an effective Hamiltonian for the large component up to order  $\frac{\mathbf{p}^4}{m^3c^2}$ . The derivation is lengthy but well documented in the literature (see, e.g., reference [42]). Here, only the resulting differential equation for the large component is presented

$$H \Phi(\mathbf{r}) = \epsilon \Phi(\mathbf{r}). \quad (2.25)$$

The Hamiltonian  $H$  can be divided into three parts

$$H = H^{\text{KS}} + H_{\text{SC}} + H_{\text{SOC}}. \quad (2.26)$$

The first term  $H^{\text{KS}}$  corresponds the Hamiltonian of the non-relativistic KS equation (2.17). The second term is given by

$$H_{\text{SC}} = -\frac{\mathbf{p}^4}{8m^3c^2} + \frac{\nabla^2 V^{\text{KS}}(\mathbf{r})}{8m^2c^2}, \quad (2.27)$$

where the index SC indicates that this term enters in the scalar-relativistic approximation [43] to eq. (2.25) discussed in some more detail in section 3.2. The first

term in  $H_{\text{SC}}$  called mass-velocity term describes the variation of the mass with velocity. The second term is the Darwin term. It takes into account the non-locality of the Coulomb interaction between the electron and the nuclei, which originates from quantum fluctuations in the position of the electron (Zitterbewegung).

The term  $H_{\text{SOC}}$  in (2.26) describes the spin-orbit coupling given by

$$H_{\text{SOC}} = \frac{1}{4m^2c^2} \underline{\sigma} \cdot [\nabla V^{\text{KS}}(\mathbf{r}) \times \mathbf{p}]. \quad (2.28)$$

The most important contribution to the spin-orbit coupling term comes from the strong nuclear field in the vicinity of the nucleus, where non-spherical parts of the potential  $V^{\text{KS}}(\mathbf{r})$  are small compared to the spherical contribution. Neglecting the non-spherical parts in (2.28) leads to a spin-orbit coupling term of the following form

$$\tilde{H}_{\text{SOC}} = \frac{1}{2m^2c^2} \frac{1}{r} \frac{dV^{\text{KS}}(r)}{dr} \mathbf{L} \cdot \mathbf{S}, \quad (2.29)$$

with the angular momentum  $\mathbf{L} = (\mathbf{r} \times \mathbf{p})$  and  $\mathbf{S} = \underline{\sigma}/2$ . Approximating  $H_{\text{SOC}}$  by (2.29) illustrates that SOC couples the spin and the orbital degrees of freedom of the electron. Furthermore, SOC will have no influence on electrons occupying  $s$  orbitals, since their orbital momentum is zero. The SOC is expected to be strongest for  $p$  orbitals followed by  $d$  and finally  $f$  orbitals, because  $p$  wave functions start as  $\varphi(r) \sim r$  while  $d$  and  $f$  behave like  $r^2$  and  $r^3$ , respectively. To illustrate why SOC is more significant for heavier elements, the spherical part of the potential close to the nucleus is approximated by the core potential. This yields  $(1/r)dV/dr \sim -Z/r^3$ , where  $Z$  is the atomic number. Hence, the SOC is stronger in materials containing elements with large atomic numbers.

In this work, calculations including SOC are carried out in two steps. First, eq. (2.25) is solved approximately using the scalar-relativistic approximation [43]. Then, SOC in the form of (2.29) is introduced as a perturbation to the system described by  $H^{\text{KS}} + H_{\text{SC}}$  and the resulting new eigenvalue problem is solved within second variation [43, 44]. Some details about the implementation of the procedure used in this work can be found in section 3.2.

Any calculations based on the KS formalism with or without relativistic corrections require an explicit expression for the total-energy functional, eq. (2.13). Unfortunately, the exchange-correlation energy  $E_{\text{xc}}$  cannot be determined exactly for real materials and has to be approximated. Some of the most common approximations will be introduced in the next section. For simplicity, the non-relativistic form of the KS equation, eq. (2.17), will be used in the further discussion in this chapter.

### 2.2.3. Local-density (LDA) and generalized-gradient (GGA) approximation

In order to solve the KS equations (2.17) the effective potential  $V^{\text{KS}}(\mathbf{r})$  has to be determined. Unfortunately, the exact exchange-correlation energy  $E_{\text{xc}}$  and exact exchange-correlation potential, eq. (2.16), for real solids are unknown. Therefore, one has to find approximate expressions for  $v^{\text{xc}}(\mathbf{r})$  in  $V^{\text{KS}}(\mathbf{r})$ . Nevertheless, the KS formalism has become the standard workhorse of modern materials science. One reason is that all terms in (2.13) except  $E_{\text{xc}}$  can be calculated explicitly, and they already yield the by far largest contributions to the total energy for a huge variety of electronic systems in solids. On the other hand, even seemingly simple approximate expressions for the exchange-correlation energy yield both accurate and reliable results.

One of the oldest and still widely used expressions for  $E_{\text{xc}}$  is given by the local-density approximation (LDA), which was already introduced in the work by Kohn and Sham [37]. In the LDA it is assumed that each electron locally has the same exchange and correlation energy  $\epsilon_{\text{xc}}(n)$  as an electron in a uniform electron gas of the same density  $n$ . Whereas the exchange energy of the electron gas can be calculated exactly within the Hartree-Fock method [45], the remaining correlation contribution is parametrized by a fit to quantum Monte-Carlo calculations [46]. Finally, the exchange-correlation energy in LDA has the form

$$E_{\text{xc}}^{\text{LDA}}[n] = \int d^3r n(\mathbf{r}) \epsilon_{\text{xc}}(n(\mathbf{r})). \quad (2.30)$$

Since  $E_{\text{xc}}^{\text{LDA}}[n]$  is exact for an electron gas of density  $n$ , it yields a good approximation for the exchange-correlation energy of many systems with slowly varying density.

For systems exhibiting larger inhomogeneities in the density distribution, it appears natural to introduce functions  $f$  of the density and its derivative. This approach was realized in the generalized gradient approximation (GGA) by Perdew and Wang [47]. It yields exchange-correlation energies of the general form

$$E_{\text{xc}}^{\text{GGA}}[n] = \int d^3r f(n(\mathbf{r}), \nabla n(\mathbf{r})). \quad (2.31)$$

Whereas  $\epsilon_{\text{xc}}$  in the LDA is derived directly from the electron gas, the choice of the function  $f$  in the GGA is not unique. Over the last decades, a large number of GGA exchange-correlation functionals have been suggested. The functional used throughout this work is called PBE named after the authors Perdew, Burke, and Ernzerhof, who first proposed it [25]. This functional was chosen for two reasons: (1) among the most frequently used GGA functionals, the PBE functional yields the most accurate and reliable results in most benchmark calculations [48, 49]

and (2) to stay consistent with the treatment of  $E_{xc}$  in the application of the hybrid functional HSE [23, 24] used for calculations based on the generalized Kohn-Sham scheme.

After the LDA and GGA have been introduced as practical approaches to actually calculate the ground-state total energy, the question remains, how LDA and GGA can be of any use to determine excitation spectra of solids. In practice, the eigenvalues  $\epsilon_i$  solving the KS equations (2.17) are interpreted as excitation energies of the electrons in the interacting  $N$ -electron system. However, there is neither a mathematical nor a physical justification for this interpretation of the KS eigenvalues. Only the eigenvalue corresponding to the highest occupied KS state is identical to a physical observable, namely the ionization energy [50]. However, the qualitative agreement of the KS eigenspectrum with photoemission spectra mostly for  $sp$ -electron systems of real materials has led to a general acceptance of this interpretation.

Despite the qualitative agreement of the predicted excitation spectra with experiment, discrepancies can already be observed for some  $sp$  systems. These become larger in  $d$  and  $f$  system. In addition, there are systematic deviations between LDA and GGA results and experimental observations:

- already in simple semiconductors and insulators, such as Si, GaAs, C, and MgO, the band gaps are systematically underestimated often by as much as 50 % [51],
- in many  $f$ -electron systems, the positions of the  $f$ -states is in strong disagreement with experiment, e.g., for Ce [52] and GdN [53], and
- in strongly correlated materials the band gaps are much too small, e.g., in antiferromagnetic NiO and MnO [54], and systems in the Mott-insulating phase are erroneously predicted to be metallic, for example paramagnetic NiO and MnO [54].

The second and third discrepancy originates from the underestimation of exchange and correlation effects in  $E_{xc}^{LDA}$  and  $E_{xc}^{GGA}$  on the one hand and the self-interaction error inherent to these approximation on the other hand. The self-interaction error arises from a spurious interaction of an electron with itself. It was first defined for the case of a one-electron systems [55] and later generalized to the case of  $N$  electrons [56]. From the further discussion, it will be seen, how the use of hybrid functionals within the generalized Kohn-Sham (gKS) formalism can partly correct the self-interaction error. Before the gKS is introduced, the underestimation of semiconductor band gaps in LDA and GGA is further investigated here.

### 2.2.4. The band-gap problem of LDA and GGA

The fundamental band gaps  $E_{\text{gap}}$  of semiconductors can be obtained from energy differences of the total ground-state energies of an  $N$ -electron and  $N \pm 1$ -electron system

$$E_{\text{gap}} = (E(N-1) - E(N)) - (E(N) - E(N+1)), \quad (2.32)$$

where the first term in brackets corresponds to the ionization energy and the second to the electron affinity of the system under consideration. Since DFT is a theory to calculate ground-state total energies for a given number of electrons the fundamental band gaps are, in principle, accessible by DFT. Therefore, the discrepancies between experimentally observed and LDA or GGA band gaps must be attributed to the approximate treatment of the exchange-correlation energy in LDA and GGA. To gain a more detailed understanding of the origin of these discrepancies, it is convenient to rewrite the above expression in the following manner

$$E_{\text{gap}} = \underbrace{-\frac{E(N-1) - E(N)}{N-1-N}}_{\rightarrow -\mu(N-0)} + \underbrace{\frac{E(N+1) - E(N)}{N+1-N}}_{\rightarrow \mu(N+0)}, \quad (2.33)$$

For systems with  $N \gg 1$  electrons the two fractions can be replaced by the chemical potential defined by  $\mu(N) = \frac{\delta E(N)}{\delta N}$ , where  $\pm 0$  in  $\mu(N \pm 0)$  denotes the derivative from the right and left, respectively. The chemical potential can be identified with the Lagrange multiplier  $\epsilon$  introduced in the second Hohenberg-Kohn theorem

$$\mu(N) = \frac{\delta E(N)}{\delta N} = \int d^3r \underbrace{\frac{\delta E[n]}{\delta n(\mathbf{r})}}_{\epsilon(N)} \bigg|_{n=n_0, N} \frac{\delta n(\mathbf{r})}{\delta N} = \epsilon(N). \quad (2.34)$$

Hence, the band gap results from the discontinuity of the functional derivatives of the total energy with respect to the density

$$E_{\text{gap}} = \frac{\delta E[n]}{\delta n(\mathbf{r})} \bigg|_{n=n_0, N+0} - \frac{\delta E[n]}{\delta n(\mathbf{r})} \bigg|_{n=n_0, N-0}. \quad (2.35)$$

For a system containing  $N \gg 1$  electrons, the change in the single-particle density itself upon adding or subtracting another electron will be infinitesimally small. Thus, it can be seen from the expression for the total energy

$$E[n] = T^{\text{KS}}[n] + \frac{1}{2} \iint d^3r d^3r' \frac{n(\mathbf{r})n(\mathbf{r}')}{|\mathbf{r} - \mathbf{r}'|} + \int d^3r v^{\text{ext}}(\mathbf{r})n(\mathbf{r}) + E_{\text{xc}}[n] \quad (2.36)$$

that the energy difference of the derivatives of  $E$  in eq. (2.35) must arise from a discontinuity in the kinetic energy  $T^{\text{KS}}[n]$  and the exchange-correlation energy  $E_{\text{xc}}[n]$

Applying the above argumentation to the KS system, it can be seen that the KS band gap amounts to

$$E_{\text{gap}}^{\text{KS}} = \left. \frac{\delta T^{\text{KS}}[n]}{\delta n(\mathbf{r})} \right|_{n=n_0, N+0} - \left. \frac{\delta T^{\text{KS}}[n]}{\delta n(\mathbf{r})} \right|_{n=n_0, N-0} = \epsilon_{N+1}^{\text{KS}} - \epsilon_N^{\text{KS}} \quad (2.37)$$

due to the specific form of the total energy functional of the KS system

$$E^{\text{KS}}[n] = T^{\text{KS}}[n] + \int d^3r V^{\text{KS}}(\mathbf{r})n(\mathbf{r}). \quad (2.38)$$

Combining eqs. (2.35) to (2.38), the true band gap of the N-electron system can be expressed by

$$E_{\text{gap}} = \epsilon_{N+1}^{\text{KS}} - \epsilon_N^{\text{KS}} + \Delta_{\text{xc}}, \quad (2.39)$$

where the exchange-correlation discontinuity  $\Delta_{\text{xc}}$  was introduced. It represents the discontinuity of the derivative of the exchange-correlation energy with respect to the density  $n$ . Equation (2.39) yields the exact band gap of the interacting N-electron system obtained from KS-DFT.

In practice, equation (2.37) is used to calculate the band gap of the N-electron system. This will only yield a good approximation for the true band gap if  $\Delta_{\text{xc}}$  is small, which is not to be expected for arbitrary electronic systems. However, in DFT calculations employing the LDA or GGA, the attempt to improve the resulting KS band gap by applying equation (2.39) will only reproduce the KS band gap as

$$\Delta_{\text{xc}}^{\text{LDA}} = \Delta_{\text{xc}}^{\text{GGA}} = 0. \quad (2.40)$$

This is a direct consequence of the construction of the LDA and GGA exchange-correlation energy as smooth, local functionals of the density. Hence, due to the approximations made in the construction of the exchange-correlation energy functional in LDA and GGA,  $E_{\text{gap}}^{\text{KS}}$  will always differ from the true band gaps for systems, where the exact  $\Delta_{\text{xc}}$  is appreciable.

### 2.2.5. The generalized Kohn-Sham scheme

One of the advantages of the generalized Kohn-Sham (gKS) formalism over the conventional KS scheme is explained best by looking at yet another theory of first principle electronic-structure calculations. In Hartree-Fock (HF) theory, the many-electron wave functions in (2.5) are approximated by single Slater determinants  $\Phi$  of one-particle wave functions  $\varphi_i(\mathbf{r})$  obtained from the self-consistent solution of the HF equations<sup>2</sup>. The total energy of the N-electron system in HF theory is

<sup>2</sup>For convenience, the same symbols for the Slater determinant and the wave functions as in the discussion of the KS formalism are used although the single-particle eigenstates of the HF and KS equation are, in general, not the same.

approximated by the expectation value of the Hamiltonian (2.6) with respect to  $\Phi$ . Hence, the expectation value of the electron-electron interaction  $V_{ee}$ , eq. (2.4), decomposes into two terms: the Hartree energy introduced in eq. (2.12) and the exact exchange energy  $E_x$

$$\langle \Phi | V_{ee} | \Phi \rangle = U_H + E_x. \quad (2.41)$$

In terms of the single-particle wave functions  $\varphi_i(\mathbf{r})$ , the exact exchange energy is given by

$$E_x \equiv -\frac{1}{2} \sum_{i,j}^{\text{occ}} \iint d^3r d^3r' \frac{\varphi_i^*(\mathbf{r}) \varphi_j(\mathbf{r}) \varphi_j^*(\mathbf{r}') \varphi_i(\mathbf{r}')}{|\mathbf{r} - \mathbf{r}'|}. \quad (2.42)$$

The crucial point is that the terms diagonal in the wave-function indices  $i, j$  in  $U_H$  and  $E_x$  exactly cancel each other in eq. (2.41). Therefore, the HF total energy is self-interaction free in contrast to the total energy obtained from the LDA or GGA within the KS scheme. On the other hand, the Hartree energy  $U_H$  is fully included in the KS-derived expression for the total energy, eq. (2.13). Hence, the approximate treatment of the exchange energy in the KS formalism leads to the self-interaction error in the LDA and GGA.

One major draw back of the HF theory is the large overestimation of band gaps compared to experiment because of the neglect of correlation effects. In particular, the bare Coulomb interaction enters in (2.42) whereas in solids the Coulomb interaction is screened by the charges of the other electrons and nuclei. For metals the lack of metallic screening in HF theory even leads to an unphysical, logarithmic singularity in the derivative of the single-particle spectrum with respect to the wave vector  $\mathbf{k}$  at the Fermi level. In the KS scheme, the exchange-correlation potential accounts for correlation effects but the band gaps obtained from the most commonly used approximations LDA and GGA are typically too small for the reasons discussed in the previous section. The true band gaps thus lie inbetween the HF and the LDA or GGA results. Therefore, Seidl *et al.* [38] introduced the generalized Kohn-Sham (gKS) scheme which allows to take fractions of the exact exchange energy  $E_x$  explicitly into account in calculations of the total ground-state energy of a N-electron system within DFT. Thus, one can expect to obtain better estimates for band gaps. Furthermore, the self-interaction error inherent to the LDA and GGA can be removed at least partially in the gKS formalism.

To construct the gKS scheme the interacting N-electron system is again replaced by a non-interacting one with its wave functions represented by single Slater determinants of single-particle wave functions  $\varphi_i(\mathbf{r})$  that are chosen under the constraint to reproduce the single-particle density of the interacting system. In the same manner as in the KS scheme, the expectation value of the kinetic energy operator defined in (2.2) can be evaluated with respect to these Slater

determinants  $\Phi$ . The resulting expression is denoted from now on as

$$T^{\text{gKS}} \equiv \min_{\Phi \rightarrow n} \langle \Phi | T | \Phi \rangle. \quad (2.43)$$

In contrast to the KS scheme, the remaining part of the universal functional  $F[n]$  is separated in the following way

$$\begin{aligned} F[n] &= \underbrace{T^{\text{gKS}}[n] + \alpha \min_{\Phi \rightarrow n} E_x\{\varphi_i[n]\}}_{\equiv S[n]} + \alpha U_{\text{H}}[n] + (1 - \alpha) U_{\text{H}}[n] + E_{\text{xc}}^{\text{gKS}}[n] \\ &= T^{\text{gKS}}[n] + U_{\text{H}}[n] + \alpha \min_{\Phi \rightarrow n} E_x\{\varphi_i[n]\} + E_{\text{xc}}^{\text{gKS}}[n], \end{aligned} \quad (2.44)$$

where the dimensionless parameter  $\alpha \in [0, \dots, 1]$  can be used to admix contributions from the exact exchange energy. For  $\alpha = 0$  the separation of the universal functional of the KS formalism is recovered. For  $\alpha = 1$  the resulting expression for  $F[n]$  yields a Hartree-Fock-type total energy when inserted into equation (2.13). The exchange-correlation energy  $E_{\text{xc}}^{\text{gKS}}$  plays the same role as  $E_{\text{xc}}^{\text{KS}}$  in the KS scheme. The functional  $S$  was introduced to simplify the notation in the following.

Following the same procedure as in the derivation of the KS equations (2.17), equation (2.44) is inserted into the expression for the total ground-state energy, eq. (2.13), and the variational principle is applied

$$\frac{\delta S}{\delta n(\mathbf{r})} + (1 - \alpha) \int d^3 r' \frac{n(\mathbf{r}')}{|\mathbf{r} - \mathbf{r}'|} + \frac{\delta E_{\text{xc}}^{\text{gKS}}}{\delta n(\mathbf{r})} + v^{\text{ext}}(\mathbf{r}) - \epsilon = 0. \quad (2.45)$$

Introducing the gKS potential as

$$V^{\text{gKS}}(\mathbf{r}) = v^{\text{ext}}(\mathbf{r}) + \int d^3 r' \frac{n(\mathbf{r}')}{|\mathbf{r} - \mathbf{r}'|} + V_{\text{xc}}^{\text{gKS}}(\mathbf{r}) \quad (2.46)$$

with

$$V_{\text{xc}}^{\text{gKS}}(\mathbf{r}) = \frac{\delta E_{\text{xc}}^{\text{gKS}}}{\delta n(\mathbf{r})} \quad (2.47)$$

leads to the single-particle equations of the generalized Kohn-Sham scheme

$$\left[ -\frac{1}{2} \nabla^2 + V^{\text{gKS}}(\mathbf{r}) \right] \varphi_i(\mathbf{r}) - \alpha \sum_j \int d^3 r' \frac{\varphi_j^*(\mathbf{r}') \varphi_i(\mathbf{r}')}{|\mathbf{r} - \mathbf{r}'|} \varphi_j(\mathbf{r}) = \epsilon_i \varphi_i(\mathbf{r}). \quad (2.48)$$

Equation (2.48) has to be solved self-consistently in the single-particle density  $n(\mathbf{r})$  obtained from eq. (2.18).

For practical applications in electronic structure calculations it is necessary to find an explicit expression for  $E_{\text{xc}}^{\text{gKS}}$ . Furthermore, the free parameter  $\alpha$  has to be

chosen appropriately. Both aspects are addressed in the construction of hybrid functionals  $E_{\text{hyb}}$  that can be formally introduced as the sum of the last two terms in eq. (2.44)

$$E_{\text{hyb}}[\{\varphi_i\}] = \alpha \min_{\Phi \rightarrow n} E_x[\{\varphi_i\}] + E_{\text{xc}}^{\text{gKS}}[n]. \quad (2.49)$$

Since the choice of  $\alpha$  as well as the approximation to  $E_{\text{xc}}^{\text{gKS}}$  are not unique, there are numerous ways to construct an explicit expression for  $E_{\text{hyb}}$ . In this work, the HSE functional [23, 24] was used in all calculations employing the gKS formalism. This hybrid functional is based on the PBE0 functional, which was first motivated by a heuristic approximation to equation (2.49) by Becke [57]

$$E_{\text{hyb}} \approx E_{\text{xc}}^{\text{DFT}} + \alpha (E_x - E_x^{\text{DFT}}). \quad (2.50)$$

Becke suggested this specific form for  $E_{\text{hyb}}$  based on the analysis of the adiabatic connection formula [58, 59, 60] and the observed over-binding tendencies of local density functionals in the description of molecular bonds. In equation (2.50),  $E_x^{\text{DFT}}$  and  $E_{\text{xc}}^{\text{DFT}}$  are the exchange and exchange-correlation energy as defined within the conventional KS scheme, respectively. Perdew, Ernzerhof, and Burke [61] rederived eq. (2.50) from a simple model expression for the adiabatic connection formula and furthermore estimated  $\alpha$  to be 1/4 by examining the convergence of the Møller-Plesset perturbation expansion [62] in 4th order for the total energy of an N-electron system. Adamo and Barone [63] suggested to set  $E_x^{\text{KS}} = E_x^{\text{PBE}}$  and  $E_{\text{xc}}^{\text{KS}} = E_{\text{xc}}^{\text{PBE}}$  in eq. (2.50) due to the numerous successful applications of PBE within the conventional KS scheme. They named the resulting hybrid functional PBE0, where "0" indicates that  $E_{\text{hyb}}^{\text{PBE0}}$  contains no further parameters than those necessary to determine  $E_x^{\text{PBE}}$  and  $E_{\text{xc}}^{\text{PBE}}$ .

In a case study of 20 materials comprising ionic, semiconducting and metallic systems, Paier *et al.* [51] demonstrated that equilibrium lattice constants, bulk moduli and atomization energies of insulators and semiconductors obtained from PBE0 calculations agree better with experimental data than the corresponding LDA and GGA predictions. On the other hand, these quantities are better described within LDA or GGA in metallic systems. Heyd, Scuseria, and Ernzerhof [23] attributed this deficiency of PBE0 and similar hybrid functionals to the neglect of the metallic screening of the Coulomb potential. Therefore, they introduced a screening mechanism by partitioning the Coulomb potential into a short-range (SR) and a long-range (LR) component

$$\frac{1}{r} = \underbrace{\frac{1 - \text{erf}(sr)}{r}}_{\text{SR}} + \underbrace{\frac{\text{erf}(sr)}{r}}_{\text{LR}}, \quad (2.51)$$

where the screening parameter  $s$  defines the screening range and the error function is given by

$$\text{erf}(sr) = \frac{2}{\sqrt{\pi}} \int_0^{sr} e^{-x^2} dx. \quad (2.52)$$

By applying the partitioning of the Coulomb potential only to the long-range part of the exact exchange, Heyd, Scuseria and Ernzerhof obtained a hybrid functional of the form

$$E_{\text{hyb}}^{\text{HSE}}(s) = \frac{1}{4} E_x^{\text{SR}}(s) + \frac{3}{4} E_x^{\text{PBE,SR}}(s) + E_x^{\text{PBE,LR}}(s) + E_c^{\text{PBE}}, \quad (2.53)$$

where  $E_x^{\text{SR}}$  is the short-range component of the exact exchange energy defined in eq. (2.42),  $E_x^{\text{PBE,SR}}$  and  $E_x^{\text{PBE,LR}}$  are the short-range and long-range components of the PBE exchange functional obtained by integration of the model PBE-exchange hole and  $E_c^{\text{PBE}}$  is the PBE correlation energy. The formula definitions of the terms in eq. (2.53) are lengthy. Therefore, the interested reader is referred to the literature for further details [23]. Reexamining their work in 2006 [24], Scuseria and co-workers suggested to chose  $s = 0.11 \text{ bohr}^{-1}$ . For convenience, the functional with this particular choice of  $s$  is called HSE functional throughout this work.

Kresse and co-workers [51] found the results obtained from a similar implementation of the HSE functional with  $s = 0.15 \text{ bohr}^{-1}$  to resemble the PBE0 results with some improvements for example of values obtained for the heat of formation. They also emphasized the better convergence of this functional compared to PBE0 with respect to the number of  $\mathbf{k}$  points used to sample the Brillouin zone. However, the most important question in the context of this work is if the gKS scheme and the hybrid functionals can be useful for the description of electronic spectra and electronic excitations. As in the conventional KS formalism, the interpretation of gKS eigenenergies as the electronic spectra of an N-electron system cannot be theoretically justified. The estimates for fundamental band gaps of insulators and semiconductors are, in general, larger than LDA and GGA results [24, 51]. In large-gap systems both PBE0 and HSE still underestimate the band gap. Increasing the amount of exact exchange in the construction of  $E_{\text{hyb}}$  would systematically increase the value for the band gap. However, in HF calculations, where the exact exchange is fully included, band gaps, in general, come out way too large compared to the experimental results indicating that exact exchange alone cannot be the final answer to this problem.

The reason for the discrepancies between experiments, the HF theory and the KS and gKS formalisms is the insufficient treatment of correlation in all three approaches. In HF theory, two electrons of opposite spin are allowed to occupy the same single-particle state at the cost of a large Coulomb energy. However, the Coulomb repulsion keeps electrons away from each other creating a screening hole around each electron, which reduces the interaction with the other electrons and thereby the Coulomb energy. The energy cost for transferring an electron from one site to a neighboring site is substantially reduced by screening. Thus, correlation or screening reduces the gap from its HF value. The KS and gKS band gaps for solids, in general, agree much better with experimental results than the HF band gaps because they incorporate a certain amount of correlation in  $E_{\text{xc}}^{\text{KS}}$

or  $E_{xc}^{\text{gKS}}$ , respectively. However, both schemes only allow for a static treatment of correlation. The dynamics of the screening mechanism is completely neglected in both formalisms. Therefore, the GW approximation within many-body perturbation theory is introduced in the next part of this chapter, which allows to take into account dynamical screening effects in the description of electronic spectra.

### 2.3. Many-body perturbation theory

The key quantity in many-body perturbation theory is the one-particle Green function. It can be introduced using the field operators  $\hat{\psi}(\mathbf{r}, t)$ ,  $\hat{\psi}^\dagger(\mathbf{r}, t)$  in the Heisenberg representation given by

$$\hat{\psi}^{(\dagger)}(\mathbf{r}, t) = \exp(iHt) \hat{\psi}^{(\dagger)}(\mathbf{r}) \exp(-iHt), \quad (2.54)$$

where  $H$  is the Hamiltonian  $H_e$  defined in (2.6). The operators  $\hat{\psi}(\mathbf{r}, t)$ ,  $\hat{\psi}^\dagger(\mathbf{r}, t)$  can annihilate or create an electron at position  $\mathbf{r}$ . The latter process is described by

$$\hat{\psi}^\dagger(\mathbf{r}_j)|\mathbf{r}_i; i = 1, \dots, N\rangle = \begin{cases} \sqrt{N+1}|\mathbf{r}_i; i = 1, \dots, N+1\rangle, & \text{if } \mathbf{r}_j \neq \mathbf{r}_i \\ 0, & \text{if } \mathbf{r}_j \in \{\mathbf{r}_i\} \end{cases}, \quad (2.55)$$

where the Fock state  $|\mathbf{r}_i; i = 1, \dots, N\rangle$  represents the  $N$ -electron wave function defined in eq. (2.5). Applying  $\hat{\psi}^\dagger(\mathbf{r})$  to  $|\mathbf{r}_i; i = 1, \dots, N\rangle$  increases the number of electrons in Fock space by 1. Thus, the state  $|\mathbf{r}_i; i = 1, \dots, N+1\rangle$  corresponds to a wave function containing  $(N+1)$  electrons. Applying  $\hat{\psi}(\mathbf{r}_j)$  to  $|\mathbf{r}_i; i = 1, \dots, N\rangle$  lowers the number of electrons by one creating an  $(N-1)$ -electron state. In the further discussion, the shorthand notation  $|N, i\rangle$  is used, where  $i = 0$  denotes the ground state and  $i \neq 0$  labels the excited states of the  $N$ -electron system. More details on field operators in condensed matter physics can be found in standard textbooks [64, 65, 66].

The one-particle Green function  $G$  is defined as

$$\begin{aligned} G(\mathbf{r}_1, t_1; \mathbf{r}_2, t_2) &= -i \langle N, 0 | \hat{T}[\hat{\psi}(\mathbf{r}_1, t_1) \hat{\psi}^\dagger(\mathbf{r}_2, t_2)] | N, 0 \rangle \\ &= -i \langle N, 0 | \hat{\psi}(\mathbf{r}_1, t_1) \hat{\psi}^\dagger(\mathbf{r}_2, t_2) | N, 0 \rangle \theta(t_1 - t_2) \\ &\quad + i \langle N, 0 | \hat{\psi}^\dagger(\mathbf{r}_2, t_2) \hat{\psi}(\mathbf{r}_1, t_1) | N, 0 \rangle \theta(t_2 - t_1), \end{aligned} \quad (2.56)$$

where  $\hat{T}$  is the time-ordering operator. From the definition of the field operators the Green function can now be interpreted as the probability amplitude of the creation of an electron at  $\mathbf{r}_2$  for  $t_1 > t_2$  that propagates to  $\mathbf{r}_1$  or the probability amplitude of the annihilation of an electron for  $t_2 > t_1$ . The annihilation of an electron in turn is interpreted as the creation of a hole at  $\mathbf{r}_1$  that propagates to  $\mathbf{r}_2$ .

In photo-emission experiments, the occupied density of states of a solid is determined by measuring the excitation spectrum of the solid after shining light on it. An incident photon ejects an electron from a valence state thus creating a hole. Knowing the energy of the photon and measuring the kinetic energy of the ejected electron provides information about the energy distribution of the electrons in the crystal. The complementary process is used in inverse photo emission to probe the unoccupied density of states by measuring the excitation spectrum after injection of an additional electron into a conduction state of the crystal. From the above definition of  $G$  it follows that the Green function describes exactly these processes.

The excitation spectrum of a solid can be obtained directly from  $G$  upon Fourier transformation of the time-coordinate to the corresponding frequency. First, the closure relation  $\sum_i |N \pm 1, i\rangle \langle N \pm 1, i| = 1$  is inserted between the field operators in eq. (2.56), where  $\{|N \pm 1, i\rangle\}$  is the complete set of eigenstates of the  $(N \pm 1)$ -electron system. Using the identity in eq. (2.54) and defining new single-particle wave functions called quasiparticle states

$$\psi_i^{N-1}(\mathbf{r}) = \langle N-1, i | \hat{\psi}(\mathbf{r}) | N, 0 \rangle \quad \text{and} \quad \psi_i^{N+1}(\mathbf{r}) = \langle N, 0 | \hat{\psi}(\mathbf{r}) | N+1, i \rangle \quad (2.57)$$

along with the excitation energies

$$\epsilon_i^{N-1} = E_0^N - E_i^{N-1} \quad \text{and} \quad \epsilon_i^{N+1} = E_i^{N+1} - E_0^N \quad (2.58)$$

leads to

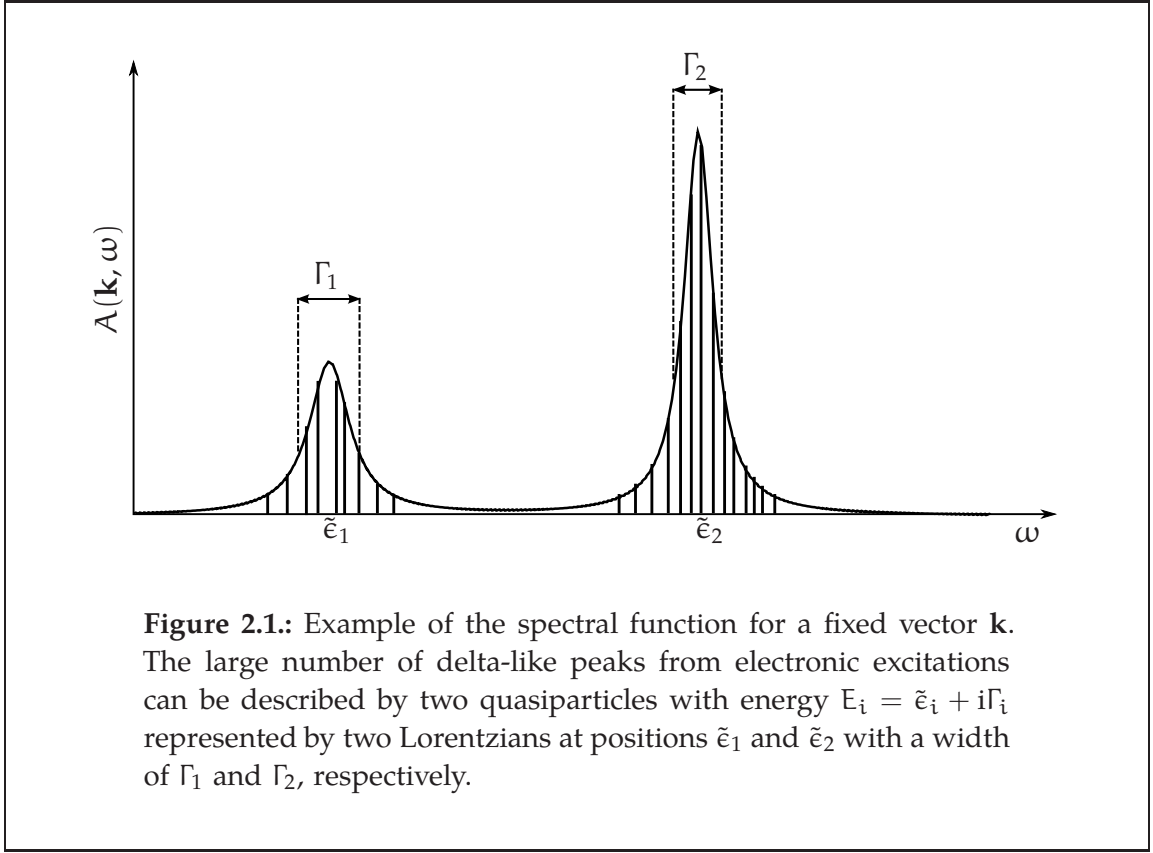
$$\begin{aligned} G(\mathbf{r}_1, t_1; \mathbf{r}_2, t_2) = & -i \sum_i \psi_i^{N+1}(\mathbf{r}_1) \psi_i^{N+1*}(\mathbf{r}_2) \exp\{-i\epsilon_i^{N+1}(t_1 - t_2)\} \theta(t_1 - t_2) \\ & + i \sum_i \psi_i^{N-1}(\mathbf{r}_1) \psi_i^{N-1*}(\mathbf{r}_2) \exp\{-i\epsilon_i^{N-1}(t_1 - t_2)\} \theta(t_2 - t_1). \end{aligned} \quad (2.59)$$

The Fourier transformation of the above expression yields Lehmann representation of the Green function

$$G(\mathbf{r}_1, \mathbf{r}_2; \omega) = \sum_i \frac{\psi_i^{N+1}(\mathbf{r}_1) \psi_i^{N+1*}(\mathbf{r}_2)}{\omega - \epsilon_i^{N+1} + i\eta} + \sum_i \frac{\psi_i^{N-1}(\mathbf{r}_1) \psi_i^{N-1*}(\mathbf{r}_2)}{\omega - \epsilon_i^{N-1} - i\eta}, \quad (2.60)$$

where  $\eta$  is an infinitesimally small, positive number that enters due to the Fourier transformation of the  $\theta$  function. Hence, the poles of  $G$  are the electronic excitation energies eq. (2.58) of the  $N$ -electron system measured in (inverse) photo-emission experiments.

Since the further discussion is closely related to the concept of quasi-particles and the quasiparticle states formally introduced in eq. (2.57), it will be explained in more detail in the next section.



### 2.3.1. Quasiparticles

With the help of the spectral function  $A$ , equation (2.60) can be rewritten as an integral over frequencies

$$G(\mathbf{r}_1, \mathbf{r}_2; \omega) = \int_{-\infty}^{\infty} \frac{A(\mathbf{r}_1, \mathbf{r}_2; \omega')}{\omega - \omega' + \text{sgn}(\omega' - \mu)i\eta} d\omega', \quad (2.61)$$

with  $\max(\epsilon_i^{N-1}) \leq \mu \leq \min(\epsilon_i^{N+1})$ . According to the definition of the excitation energies, eq. (2.58), and the discussion in section 2.2.4,  $\mu$  is equal to the chemical potential in systems with  $N \gg 1$ .

In finite systems the excited states are well separated. Consequently, the spectral function is given by a sum over discrete delta peaks

$$A(\mathbf{r}_1, \mathbf{r}_2; \omega) = \sum_i \psi_i(\mathbf{r}_1) \psi_i^*(\mathbf{r}_2) \delta(\omega - \epsilon_i), \quad (2.62)$$

and each peak is weighted by the product of those quasiparticle states  $\psi_i(\mathbf{r})$ , eq. (2.57) that contribute to the excitation. In order to simplify the notation, the index  $(N \pm 1)$  of the quasiparticle states and energies will be dropped from now on. The above form of  $A$  follows directly from eq. (2.59). As the number of

electrons gets larger, the number of peaks in the spectrum increases. Furthermore, the peaks move closer in energy. If the resulting spectral features are of Lorentzian shape, the spectral function becomes

$$A(\mathbf{r}_1, \mathbf{r}_2; \omega) = \sum_i \psi_i(\mathbf{r}_1) \psi_i^*(\mathbf{r}_2) \frac{\Gamma_i}{(\omega - \tilde{\epsilon}_i)^2 + \Gamma_i^2}, \quad (2.63)$$

where the  $\tilde{\epsilon}_i$  are the peak positions and  $|\Gamma_i|$  the corresponding peak widths of Lorentzians as shown in figure 2.1. With the above representation of  $A$  inserted into eq. (2.61) the frequency integral can still be carried out analytically yielding a discrete sum over  $i$  as in the Lehmann representation, eq. (2.60), provided that the real energies  $\epsilon_i$  are replaced by the complex numbers  $E_i = \tilde{\epsilon}_i + i\Gamma_i$ . However, a Fourier transformation of  $G$  now leads to additional terms  $\exp\{-|\Gamma_i|(t_1 - t_2)\}$  in eq. (2.59), which correspond to damping factors. Thus, the particle propagating from  $\mathbf{r}_1$  to  $\mathbf{r}_2$  now has a finite lifetime given by  $|\Gamma_i|^{-1}$ . Therefore, to be precise it does not represent an excited electron moving through the solid, but it is the excitation itself pictured as a particle called quasiparticle with energy  $E_i$  and wave function  $\psi_i(\mathbf{r})$ . The quasiparticle naturally decays over time as the excitation energy dissipates into the infinite crystal. This corresponds to the physical process of de-excitation of excited electrons that lose energy via Auger transitions. From now on, the Green function eq. (2.60) is referred to as a quasiparticle propagator, and it is the spectrum of the quasiparticles that is to be determined.

The quasiparticle spectrum corresponding to a certain quasiparticle state may have more than one peak. These additional spectral features are called satellites and can be related to collective excitations of the electrons such as plasmons or magnons. Hence, the exact quasiparticle spectrum indeed represents all interaction processes of an  $N$ -electron system.

### 2.3.2. Equation of motion and self-energy

In second quantization the Hamiltonian  $H_e$  defined in (2.6) is written as

$$\hat{H} = \int \hat{\psi}^\dagger(\mathbf{r}_1) h(\mathbf{r}_1) \hat{\psi}(\mathbf{r}_1) d^3 r_1 + \frac{1}{2} \iint \hat{\psi}^\dagger(\mathbf{r}_1) \hat{\psi}^\dagger(\mathbf{r}_2) v(\mathbf{r}_1, \mathbf{r}_2) \hat{\psi}(\mathbf{r}_2) \hat{\psi}(\mathbf{r}_1) d^3 r_1 d^3 r_2, \quad (2.64)$$

where the kinetic energy of an electron and the external potential introduced in (2.2) and (2.3) are contained in the first term  $h(\mathbf{r}_1) = -\frac{1}{2}\nabla_1^2 + v^{\text{ext}}(\mathbf{r}_1)$  and the second term describes the electron-electron interaction with the Coulomb potential  $v(\mathbf{r}_1, \mathbf{r}_2)$  given in (2.4). From the Heisenberg equation of motion for the field operator

$$i \frac{\partial}{\partial t_1} \hat{\psi}(\mathbf{r}_1, t_1) = \hat{\psi}(\mathbf{r}_1, t_1) \hat{H} - \hat{H} \hat{\psi}(\mathbf{r}_1, t_1) \quad (2.65)$$

the equation of motion of the Green function can be obtained

$$i \frac{\partial}{\partial t_1} G(\mathbf{r}_1, t_1; \mathbf{r}_2, t_2) = \delta(\mathbf{r}_1 - \mathbf{r}_2) \delta(t_1 - t_2) + h(\mathbf{r}_1) G(\mathbf{r}_1, t_1; \mathbf{r}_2, t_2) - i \int v(\mathbf{r}_1, \mathbf{r}_3) \langle N, 0 | \hat{T} [\hat{\psi}^\dagger(\mathbf{r}_3, t_1 + \eta) \hat{\psi}(\mathbf{r}_3, t_1) \hat{\psi}(\mathbf{r}_1, t_1) \hat{\psi}^\dagger(\mathbf{r}_2, t_2)] | N, 0 \rangle d^3 r_3 . \quad (2.66)$$

The expectation value of four field operators in the second line is a special case of the two-particle Green function

$$G_2(\mathbf{r}_1, t_1; \mathbf{r}_2, t_2; \mathbf{r}_3, t_3; \mathbf{r}_4, t_4) = (i)^2 \langle N, 0 | \hat{T} [\hat{\psi}(\mathbf{r}_1, t_1) \hat{\psi}(\mathbf{r}_2, t_2) \hat{\psi}^\dagger(\mathbf{r}_4, t_4) \hat{\psi}^\dagger(\mathbf{r}_3, t_3)] | N, 0 \rangle . \quad (2.67)$$

Hence, equation (2.66) can be rewritten as

$$i \frac{\partial}{\partial t_1} G(\mathbf{r}_1, t_1; \mathbf{r}_2, t_2) = \delta(\mathbf{r}_1 - \mathbf{r}_2) \delta(t_1 - t_2) + h(\mathbf{r}_1) G(\mathbf{r}_1, t_1; \mathbf{r}_2, t_2) - i \int v(\mathbf{r}_1, \mathbf{r}_3) G_2(\mathbf{r}_1, t_1; \mathbf{r}_3, t_1; \mathbf{r}_2, t_2; \mathbf{r}_3, t_1 + \eta) d^3 r_3 . \quad (2.68)$$

The next step to solve for  $G$  would be to determine  $G_2$ . Setting up an equation of motion for  $G_2$  would yield an expression coupling  $G_2$  to the three-particle Green function. Hence, this procedure would lead to an infinite series of coupled integro-differential equations, and the need arises to either truncate or sum up this series. The latter is done here using a mathematical trick: the self-energy operator  $\Sigma$  is introduced as the operator that formally solves eq. (2.66). The integral containing  $G_2$  is then split into two terms

$$- i \int v(\mathbf{r}_1, \mathbf{r}_3) G_2(\mathbf{r}_1, t_1; \mathbf{r}_3, t_1; \mathbf{r}_2, t_2; \mathbf{r}_3, t_1 + \eta) d^3 r_3 = V^H(\mathbf{r}_1) \delta(t_1 - t_2) G(\mathbf{r}_1, t_1; \mathbf{r}_2, t_2) + \int \Sigma(\mathbf{r}_1, t_1; \mathbf{r}_3, t_3) G(\mathbf{r}_3, t_3; \mathbf{r}_2, t_2) d^3 r_3 dt_3 , \quad (2.69)$$

where  $V^H$  is the Hartree potential

$$V^H(\mathbf{r}_1) = \int \frac{n(\mathbf{r}_2)}{|\mathbf{r}_1 - \mathbf{r}_2|} d^3 r_2 , \quad (2.70)$$

and the second term contains the self-energy operator  $\Sigma$ . (Expression (2.69) is discussed in more detail in appendix A.1.) With the help of the Hartree Hamiltonian

$$H^H(\mathbf{r}_1) = h(\mathbf{r}_1) + V^H(\mathbf{r}_1) \quad (2.71)$$

eq. (2.66) can now be written as

$$\left[ i \frac{\partial}{\partial t_1} - H^H(\mathbf{r}_1) \delta(t_1 - t_2) \right] G(\mathbf{r}_1, t_1; \mathbf{r}_2, t_2) = \delta(\mathbf{r}_1 - \mathbf{r}_2) \delta(t_1 - t_2) + \int \Sigma(\mathbf{r}_1, t_1; \mathbf{r}_3, t_3) G(\mathbf{r}_3, t_3; \mathbf{r}_2, t_2) d^3 r_3 dt_3 . \quad (2.72)$$

The electronic system described by the Hartree Hamiltonian  $H^H$  will be taken as a reference system of non-interacting electrons in the sense that an electron can move freely in the potential resulting from the sum of the potential caused by the atomic nuclei  $v^{\text{ext}}$  and the Hartree potential  $V^H$ . The equation of motion for the Hartree Green function  $G_H$  describing such a free electron is given by

$$\left[ i \frac{\partial}{\partial t_1} - H^H(\mathbf{r}_1) \delta(t_1 - t_2) \right] G_H(\mathbf{r}_1, t_1; \mathbf{r}_2, t_2) = \delta(\mathbf{r}_1 - \mathbf{r}_2) \delta(t_1 - t_2). \quad (2.73)$$

It can be derived in the same way as the equation of motion (2.66) of the quasiparticle Green function. Multiplying equation (2.72) from the left with  $G_H$  and integrating over the additional degrees of freedom then leads to the Dyson equation for the quasiparticle Green function

$$G(\mathbf{r}_1, t_1; \mathbf{r}_2, t_2) = G_H(\mathbf{r}_1, t_1; \mathbf{r}_2, t_2) + \iint G_H(\mathbf{r}_1, t_1; \mathbf{r}_3, t_3) \Sigma(\mathbf{r}_3, t_3; \mathbf{r}_4, t_4) G(\mathbf{r}_4, t_4; \mathbf{r}_2, t_2) d^3r_3 d^3r_4 dt_3 dt_4. \quad (2.74)$$

A physical interpretation of the Dyson equation can be given by writing it in the form of a geometric series by subsequently replacing  $G$  on the right-hand side by  $G_H + G_H \Sigma G$ , which leads to, symbolically written,

$$G = G_H + G_H \Sigma G_H + G_H \Sigma G_H \Sigma G_H + G_H \Sigma G_H \Sigma G_H \Sigma G_H + \dots \quad (2.75)$$

The quasiparticle  $G$  propagating through the system is represented by the free Hartree-electron  $G_H$  that is scattered upon moving through the solid due to all possible exchange-correlation effects encoded in the self-energy  $\Sigma$ . Since  $G_H$  of an  $N$ -electron system can be easily calculated, the calculation of  $G$  now reduces to the calculation of the self-energy.

### 2.3.3. The GW approximation (GWA) for the self-energy

The self-energy  $\Sigma$  may be obtained in several ways for example using Wick's theorem [67, 64] or by the Schwinger functional derivative method [68, 69]. Following the latter, a set of self-consistent integro-differential equations for the self-energy called Hedin equations were introduced by Hedin [13] in 1965. In principle, these equations yield the exact description of the interacting  $N$ -electron system (see appendix A.1 for a derivation of the Hedin equations). Unfortunately, this set of equations cannot be solved numerically, because it contains a functional derivative of  $\Sigma$  with respect to  $G$ . However, the equations may be iterated analytically in order to derive feasible approximations for  $\Sigma$ . If only one iteration is performed, the following expression for the self-energy is obtained

$$\Sigma^{\text{GW}}(\mathbf{r}_1, t_1; \mathbf{r}_2, t_2) = i G_H(\mathbf{r}_1, t_1; \mathbf{r}_2, t_2) W(\mathbf{r}_1, t_1 + \eta; \mathbf{r}_2, t_2), \quad (2.76)$$

which is coined GW approximation (GWA) for the self-energy due to the form of the mathematical expression. While  $G_H$  is again the Hartree Green function,  $W$  is the screened interaction obtained from the random-phase approximation (RPA)

$$W(\mathbf{r}_1, t_1; \mathbf{r}_2, t_2) = v(\mathbf{r}_1, \mathbf{r}_2)\delta(t_1 - t_2) + \iiint v(\mathbf{r}_1, \mathbf{r}_3)P(\mathbf{r}_3, t_1; \mathbf{r}_4, t_4)W(\mathbf{r}_4, t_4; \mathbf{r}_2, t_2) d^3r_3 d^3r_4 dt_3 dt_4, \quad (2.77)$$

where the polarization function  $P$  is given as a product of two non-interacting Green functions

$$P(\mathbf{r}_1, t_1; \mathbf{r}_2, t_2) = -iG_H(\mathbf{r}_1, t_1; \mathbf{r}_2, t_2)G_H(\mathbf{r}_2, t_2; \mathbf{r}_1, t_1). \quad (2.78)$$

Furthermore, the relation between the polarization function and the dielectric function

$$\epsilon(\mathbf{r}_1, t_1; \mathbf{r}_2, t_2) = \delta(\mathbf{r}_1 - \mathbf{r}_2) - \int v(\mathbf{r}_1, \mathbf{r}_3)P(\mathbf{r}_3, t_1; \mathbf{r}_2, t_2) d^3r_3 \quad (2.79)$$

is used to calculate the screened interaction as

$$W(\mathbf{r}_1, t_1; \mathbf{r}_2, t_2) = \int \epsilon^{-1}(\mathbf{r}_1, t_1; \mathbf{r}_3, t_2)v(\mathbf{r}_3, \mathbf{r}_2) d^3r_3. \quad (2.80)$$

Just like the Dyson equation for the Green function, equation (2.77) for the screened interaction  $W$  can be written as a geometrical series

$$W = v + vPv + vPvPv + vPvPvPv + \dots, \quad (2.81)$$

where  $P$  is given by eq. (2.78). This expansion is written in terms of Feynman diagrams in figure 2.2, where the straight lines represent the Hartree Green function  $G_H$  and the dashed lines the bare Coulomb potential  $v(\mathbf{r}_1, \mathbf{r}_2)$ , respectively. It shows the RPA screening mechanism that consists of the subsequent creation and

$$W(\mathbf{r}_1, t_1; \mathbf{r}_2, t_2) = \text{-----} + \text{---} \begin{array}{c} \circlearrowleft \\ \circlearrowright \end{array} \text{---} + \text{---} \begin{array}{c} \circlearrowleft \\ \circlearrowright \end{array} \text{---} \begin{array}{c} \circlearrowleft \\ \circlearrowright \end{array} \text{---} + \dots$$

**Figure 2.2.:** The first terms of expression (2.77) for the screened interaction  $W$  illustrated by Feynman diagrams. The dashed line represents the bare Coulomb potential whereas straight lines symbolize Green functions.

annihilation of electron-hole pairs drawn as bubbles out of two Green functions that can be pictured as small dipoles, which screen the bare Coulomb potential. The interaction of a quasiparticle with a test charge via the resulting screened Coulomb potential  $W$  is encoded in the expression for self-energy, eq. (2.76), of the GWA.

In this work, results of single-shot GW calculations are reported, where the eqs. (2.76) to (2.78) are only evaluated once with a suitable initial Green function  $G_0$  as input. In single-shot calculations, it is expected that the choice of  $G_0$  will determine the quality of the resulting self-energy to a large extent. In this sense, the Green functions constructed from the solution of the (generalized) Kohn-Sham equations (2.17) and (2.48) yield a much better choice for  $G_0$  than the Hartree Green function, since they yield a much better approximation for the electronic structure of most solids than  $G_H$ . For a non-interacting system like the (g)KS system, the Lehmann representation (2.60) reduces to

$$G_0(\mathbf{r}_1, \mathbf{r}_2; \omega) = \sum_i^{\text{unocc}} \frac{\varphi_i(\mathbf{r}_1)\varphi_i^*(\mathbf{r}_2)}{\omega - \epsilon_i + i\eta} + \sum_i^{\text{occ}} \frac{\varphi_i(\mathbf{r}_1)\varphi_i^*(\mathbf{r}_2)}{\omega - \epsilon_i - i\eta}, \quad (2.82)$$

where the wave function  $\varphi_i$  are the solutions of the (g)KS equations and  $\epsilon_i$  the corresponding eigenvalues. The first sum only runs over the unoccupied states whereas the second sum runs over the occupied states. From this expression the polarization function  $P$  can be calculated in frequency space as

$$P(\mathbf{r}_1, \mathbf{r}_2; \omega) = \sum_i^{\text{occ}} \sum_j^{\text{unocc}} \varphi_i^*(\mathbf{r}_1)\varphi_j(\mathbf{r}_1)\varphi_i(\mathbf{r}_2)\varphi_j^*(\mathbf{r}_2) \times \left( \frac{1}{\omega + \epsilon_i - \epsilon_j + i\eta} - \frac{1}{\omega - \epsilon_i + \epsilon_j - i\eta} \right). \quad (2.83)$$

With the polarization function, equation (2.79) for the dielectric function  $\epsilon$  can be evaluated, and from the inverse of  $\epsilon$  the screened interaction  $W$  is obtained from eq. (2.80). To calculate the GW self-energy,  $W$  is separated into the bare interaction and a remainder

$$W(\mathbf{r}_1, \mathbf{r}_2; \omega) = v(\mathbf{r}_1, \mathbf{r}_2) + W^c(\mathbf{r}_1, \mathbf{r}_2; \omega), \quad (2.84)$$

which leads to a decomposition of  $\Sigma^{\text{GW}}$  into two terms

$$\Sigma^{\text{GW}}(\mathbf{r}_1, \mathbf{r}_2; \omega) = \Sigma_x^{\text{GW}}(\mathbf{r}_1, \mathbf{r}_2) + \Sigma_c^{\text{GW}}(\mathbf{r}_1, \mathbf{r}_2; \omega). \quad (2.85)$$

The first term is given by the integral

$$\Sigma_x^{\text{GW}}(\mathbf{r}_1, \mathbf{r}_2) = \frac{i}{2\pi} \int G_0(\mathbf{r}_1, \mathbf{r}_2; \omega + \omega')v(\mathbf{r}_1, \mathbf{r}_2)e^{i\eta\omega'} d\omega', \quad (2.86)$$

which can be evaluated analytically leading to the Hartree-Fock exchange term

$$\langle \varphi_i(\mathbf{r}_1) | \Sigma_x^{\text{GW}}(\mathbf{r}_1, \mathbf{r}_2) | \varphi_i(\mathbf{r}_2) \rangle = - \sum_j^{\text{occ}} \iint \frac{\varphi_i^*(\mathbf{r}_1) \varphi_j(\mathbf{r}_1) \varphi_j^*(\mathbf{r}_2) \varphi_i(\mathbf{r}_2)}{|\mathbf{r}_1 - \mathbf{r}_2|} d^3r_1 d^3r_2. \quad (2.87)$$

The second term in eq. (2.85) is given by

$$\Sigma_c^{\text{GW}}(\mathbf{r}_1, \mathbf{r}_2; \omega) = \frac{i}{2\pi} \int G_0(\mathbf{r}_1, \mathbf{r}_2; \omega + \omega') W^c(\mathbf{r}_1, \mathbf{r}_2; \omega') d\omega'. \quad (2.88)$$

It describes correlation effects due to the dynamical screening of the Coulomb potential and must be, in general, evaluated analytically.

Finally, it should be mentioned that the choice of  $G_0$  instead of  $G_H$  is not completely consistent with the GW approximation as given by the Hedin equations. This inconsistency can be removed introducing a vertex correction into eq. (2.76) for the self-energy and (2.78) for the polarization function. This correction originates from the exchange-correlation potential  $v^{\text{xc}}$  in the Hamiltonian of the KS equation (2.17). (See appendix A.2 for a detailed discussion.) In practice, the inclusion of such a vertex correction in  $\Sigma^{\text{GW}}$  and  $P$  leads to similar or worse results than simply neglecting it (see i.e [70] and discussions therein). Therefore, these vertex corrections are not taken into account in this work.

### 2.3.4. The GWA in electronic structure calculations

The approximate GW self-energy, eq. (2.76), could be used to solve the Dyson equation (2.74) to obtain an estimate for the quasiparticle Green function,  $G$ . However, there is a more direct way to obtain the quasiparticle spectrum, which is the main focus of this work. First, equation (2.72) is Fourier transformed to yield

$$[\omega - H^H(\mathbf{r}_1)] G(\mathbf{r}_1, \mathbf{r}_2; \omega) - \int \Sigma(\mathbf{r}_1, \mathbf{r}_3; \omega) G(\mathbf{r}_3, \mathbf{r}_2; \omega) d^3r_3 = \delta(\mathbf{r}_1 - \mathbf{r}_2). \quad (2.89)$$

Then, the Lehmann representation for  $G$ , eq. (2.60), is inserted

$$\sum_i \frac{\psi_i^*(\mathbf{r}_2)}{\omega - E_i \mp i\eta} \left\{ [\omega - H^H(\mathbf{r}_1)] \psi_i(\mathbf{r}_1) - \int \Sigma(\mathbf{r}_1, \mathbf{r}_3; \omega) \psi_i(\mathbf{r}_3) d^3r_3 \right\} = \delta(\mathbf{r}_1 - \mathbf{r}_2). \quad (2.90)$$

Now, the above expression is multiplied with  $(\omega - E_j)$  and the limit  $\omega \rightarrow E_j$  is taken on both sides. Assuming that the system is non-degenerate, i.e., all  $E_i$  are

different, the left-hand side becomes

$$\begin{aligned} \lim_{\omega \rightarrow E_j} (\omega - E_j) \sum_i \frac{\psi_i^*(\mathbf{r}_2)}{\omega - E_i \mp i\eta} \left\{ [\omega - H^H(\mathbf{r}_1)] \psi_i(\mathbf{r}_1) - \int \Sigma(\mathbf{r}_1, \mathbf{r}_3; \omega) \psi_i(\mathbf{r}_3) d^3 r_3 \right\} \\ = \psi_j^*(\mathbf{r}_2) \left\{ [E_j - H^H(\mathbf{r}_1)] \psi_j(\mathbf{r}_1) - \int \Sigma(\mathbf{r}_1, \mathbf{r}_3; E_j) \psi_j(\mathbf{r}_3) d^3 r_3 \right\}, \end{aligned} \quad (2.91)$$

and the right-hand side becomes

$$\lim_{\omega \rightarrow E_j} (\omega - E_j) \delta(\mathbf{r}_1 - \mathbf{r}_2) = 0. \quad (2.92)$$

Since  $\psi_j^*(\mathbf{r}_2)$  does not vanish for all  $\mathbf{r}_2$ , the expression in the curly brackets must be zero. This leads directly to the quasiparticle equation

$$H^H(\mathbf{r}_1) \psi_i(\mathbf{r}_1) + \int \Sigma(\mathbf{r}_1, \mathbf{r}_2; E_i) \psi_i(\mathbf{r}_2) d^3 r_2 = E_i \psi_i(\mathbf{r}_1). \quad (2.93)$$

(In the degenerate case an arbitrary, external potential  $\hat{\phi}$  is introduced that lifts the degeneracy such that the same derivation holds and  $\hat{\phi}$  is set to 0 afterwards.)

The quasiparticle equation (2.93) is nonlinear in the energies  $E_i$ . Furthermore,  $\Sigma$ , in general, is not Hermitian such that the quasiparticle energies  $E_i$  usually are complex and the quasiparticle wave functions  $\psi_i(\mathbf{r})$  are not orthogonal. Nevertheless, equation (2.93) has a similar form like the single-particle DFT-KS equation (2.17) restated here for comparison

$$H^H(\mathbf{r}_1) \varphi_i(\mathbf{r}_1) + v^{xc}(\mathbf{r}_1) \varphi_i(\mathbf{r}_1) = \epsilon_i^{\text{KS}} \varphi_i(\mathbf{r}_1). \quad (2.94)$$

If the quasiparticle equation is rewritten as

$$[H^H(\mathbf{r}_1) + v^{xc}(\mathbf{r}_1)] \psi_i(\mathbf{r}_1) + \int [\Sigma(\mathbf{r}_1, \mathbf{r}_2; E_i) - v^{xc}(\mathbf{r}_1) \delta(\mathbf{r}_1 - \mathbf{r}_2)] \psi_i(\mathbf{r}_2) d^3 r_2 = E_i \psi_i(\mathbf{r}_1) \quad (2.95)$$

and it is assumed that the KS eigenfunctions  $\varphi_i(\mathbf{r})$  and eigenvalues  $\epsilon_i^{\text{KS}}$  yield a good approximation for the quasiparticle states and energies, the latter can be approximated by applying perturbation theory in first order as

$$E_i \approx \epsilon_i^{\text{KS}} + \iint \varphi_i(\mathbf{r}_1) [\Sigma(\mathbf{r}_1, \mathbf{r}_2; E_i) - v^{xc}(\mathbf{r}_1) \delta(\mathbf{r}_1 - \mathbf{r}_2)] \varphi_i(\mathbf{r}_2) d^3 r_1 d^3 r_2. \quad (2.96)$$

This expression evaluated with  $\Sigma^{\text{GW}}$ , as obtained in the previous section, yields a direct estimate for the quasiparticle spectrum. Since the quasiparticle energy appears on both sides, equation (2.96) has to be solved self-consistently.

Calculations of quasiparticle spectra based on equation (2.96) in combination with the GWA for the self-energy have been established as the method of choice

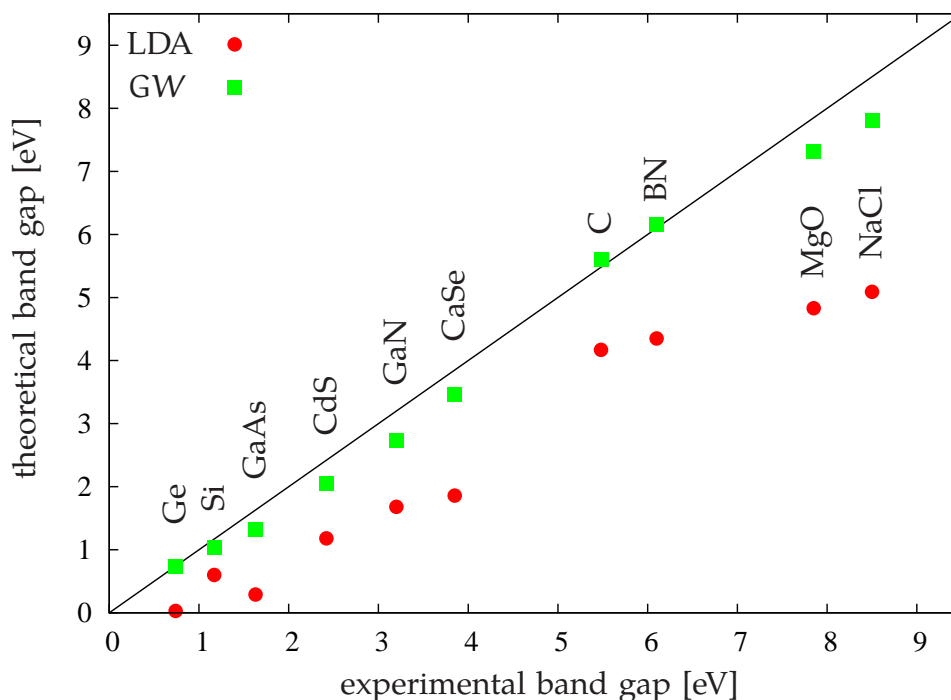


**Figure 2.3.:** Fundamental GW and LDA band gaps calculated with the codes FLEUR and SPEX are compared with the gaps seen in experiment. The GW calculations clearly improve on the LDA results.

to compute excited electronic states from first principles. The reasons are the excellent agreement of these spectra with experimental measurements for insulators, semiconductors as well as simple metals such as sodium or aluminum [14]. Furthermore, GW calculations of the band gaps of many insulators and semiconductors improve on the corresponding LDA and GGA estimates and yield values for the band gaps that agree with the observed gaps within a few tenths of an eV or better. This is demonstrated in figure 2.3 for a selection of prototype semiconducting and insulating materials calculated with the GW implementation SPEX [20]. However, in practice the solution of equation (2.96) is hampered by two things: (1) the calculation of  $\Sigma^{\text{GW}}$  is numerically very expensive and (2) it must be assumed that the ansatz is only applicable in a regime where the KS eigenvalues and states yield a good approximation for the quasiparticle self-energy such that perturbation theory is applicable.

Due to the numerical effort necessary to calculate  $\Sigma^{\text{GW}}$ , additional approximations like the plasmon-pole approximation for the inverse dielectric function [71, 72] are used in particular in many early implementations of the GWA. Furthermore, many implementations are based on pseudo-potentials using a plane-wave basis. These implementations are mostly limited to materials with extended sp

states, since plane waves are not well suited to describe the more localized d and f electron states in transition metals or rare-earth elements. The last aspect will be discussed in more detail in the next chapter.

Concerning the choice of DFT calculations as a starting point to apply perturbation theory, it was already discussed in section 2.2.1 that the conventionally employed LDA and GGA within the KS scheme can lead to large deviations between the theoretically predicted and experimentally observed spectra. For some materials LDA and GGA even fail to yield a qualitatively correct description as discussed in section 2.2.3. To overcome this obstacle various strategies have been suggested: different schemes to calculate either G or W or both quantities self-consistently to determine  $\Sigma^{\text{GW}}$  have been applied in calculations for the electron gas [73] and real materials [74, 75]. These approaches are numerically even more expensive than the single-shot GW calculation. A different ansatz is to introduce a vertex correction in the calculation of the polarization function P and  $\Sigma$ . These corrections usually stem from higher-order terms in the diagrammatic expansion of P and the screened interaction W. Although some improvement of the description of spectral satellites has been reported, the resulting quasiparticle spectra are more or less unchanged compared to calculations without vertex corrections [76, 77]. It was already noted by DuBois in 1959 [78] that this is due to a mutual cancellation of the changes in P and  $\Sigma$  upon the inclusion of vertex corrections. An approach yet very different in spirit employs the LDA+U method [79] as an alternative starting point for the calculation of  $\Sigma^{\text{GW}}$  and the quasiparticle energies. However, the value of U cannot be uniquely determined and values obtained from different approaches, e.g., constrained LDA [80, 81, 82, 83] or constrained RPA [84] can differ by up to 100%. In practice, U is therefore often treated as a parameter, which is obtained by fitting to experimental data.

In this work, solutions of the gKS equation using the HSE hybrid functionals will be used to calculate  $\Sigma^{\text{GW}}$  and the quasiparticle energies, whenever GGA calculations yield an insufficient starting point to apply perturbation theory. In this way, all calculations are carried out in an *ab initio* manner. Furthermore, a full-potential all-electron implementation [85] was used for the solution of the KS and the gKS equations as well as in the evaluation of  $\Sigma^{\text{GW}}$  within the GWA [20]. For these implementations the linearized augmented plane wave basis was used that will be described in more detail in the next chapter. Last but not least, the full inverse dielectric function is calculated without additional approximations, e.g., the plasmon-pole approximation, to determine the screened interaction W and  $\Sigma^{\text{GW}}$ . Equipped with these tools, it will be shown that the GWA yields an accurate, quantitative descriptions of electronic excitations of perovskite transition-metal oxides calculated from first principles.



## CHAPTER 3

# IMPLEMENTATION WITHIN THE FLAPW METHOD

In the first chapter, the theoretical ground was laid for the characterization of the electronic structure of real materials within density-functional theory and the GW approximation. To solve the corresponding equations numerically the full-potential linearized-augmented-plane-wave (FLAPW) method is used throughout this work. In this all-electron approach, a basis set of augmented plane waves is used to transform the differential Kohn-Sham (KS) equations (2.17) [or the generalized KS equations (2.48)] into a generalized eigenvalue problem. In turn, products of the KS wave functions are expanded in the mixed product basis in order to transform the equations yielding the GW self-energy (2.76) into matrix equations. Details of the construction of the augmented plane waves as well as the mixed product basis will be discussed in the first part of this chapter.

The second and third parts of the chapter deal with selected aspects of the implementation of the KS scheme and the GW approximation in the computer codes FLEUR and SPEX [18], respectively. Besides delivering insight into the general structure of the implementations, only those features are discussed in detail which were particularly used in the calculations for transition metal oxides in this work. A more detailed discussion of algorithms used in FLEUR can be found, e.g., in the PhD thesis of Kurz [86] and references therein. An in-depth description of the implementation of the SPEX code is presented in references [20] and [22].

## 3.1. Basis sets

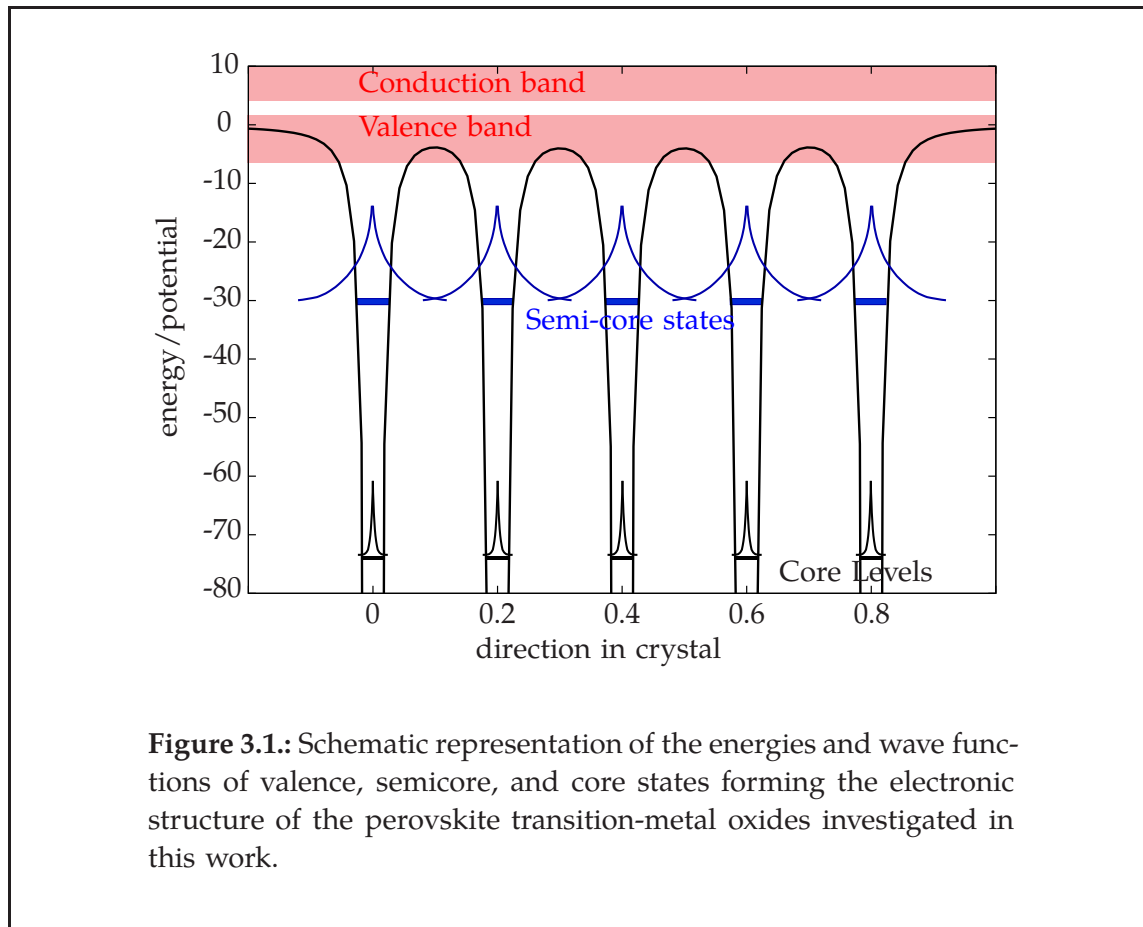
The basis best suited to describe a given problem should yield the most accurate description with the least numerical effort. The strife to find the optimal balance between efficiency and accuracy demands a detailed analysis of the specifics of the problem to be solved.

Figure 3.1 is a simple qualitative picture of the energetic positions and wave functions of the electronic states of perovskite transition-metal oxides (TMOs) investigated in this work. Figure 3.1 allows to distinguish between three different types of states. The atomic-like core levels are completely localized at the atomic sites. In particular, the overlap of their wave functions with those from neighboring atoms is negligible. On the contrary, the wave functions of the valence and conduction states have a large overlap with those from neighboring sites. This overlap causes the states from different sites to hybridize, which leads to the formation of energy bands (see section 4.4 for a more detailed discussion on band formation). In-between the core levels and valence states there exists a third group of energy levels of semi-core states. They are mostly localized at the atomic sites but they also have a small but finite overlap with wave functions of semi-core states at neighboring sites. To study perovskite TMOs a basis set is needed that can simultaneously describe the three different types of states. As first step in the quest for such a basis, an efficient representation of only the valence states is considered.

### 3.1.1. Plane waves

Since the electrons in the core levels and semi-core states screen the Coulomb potential of the nuclei, the potential is comparably weak in those regions, where the probability amplitude of the valence electrons is large. In these regions where the potential is smooth and varies slowly plane waves constitute an efficient basis to represent the wave function of the valence states, since a plane wave  $e^{i\mathbf{k}\cdot\mathbf{r}}$  with the crystal momentum  $\mathbf{k}$  is an eigenstate of the kinetic energy operator (together with a constant potential that may be chosen to be zero). Furthermore, plane waves diagonalize the Poisson equation with the Laplace operator, which has to be solved to calculate the Hartree potential. In addition, the Fast Fourier transformation provides an efficient algorithm to switch between reciprocal-space and a real-space representations. The latter is needed to calculate the exchange-correlation potential  $V_{xc}(\mathbf{r})$ .

The major drawback arises from the fact that the representation of the wave function in terms of plane waves does not converge at the presence of a  $1/r$ -potential. Consequently, an accurate representation of any state in a region close



to the atomic nuclei would require a prohibitively large number of basis functions. Hence, a plane-wave basis set can only be used efficiently in the context of the pseudo-potential approximation where the  $1/r$  potential is replaced by an artificial, non-divergent potential. The corresponding ground-state wave functions mimic the all-electron wave function outside a selected core radius. Density-functional and GW calculations relying on the pseudo-potential approximation have been employed successfully in numerous electronic structure calculation for simple metals as well as for semiconductors and insulators, where mostly  $s$  and  $p$  orbitals contribute to the valence- and conduction-band states (see reference [14] and references therein).

In materials containing transition metals or rare-earth elements, the more localized  $d$ - or  $f$ -electron orbitals appear around the Fermi energy. Therefore, pseudo-potential-based approaches become inefficient, because a very large number of basis functions is needed to accurately describe these states, which are typically much more localized in the region close to the atomic nuclei than  $s$  and  $p$  orbitals. An additional complication arises if semi-core states are present since they are even more localized. Treating them as pseudized core states may be

a too drastic approximation especially in the context of the GW approximation, where all occupied states are needed, e.g., to calculate the polarization function, eq. (2.78), which is in turn used to obtain the RPA dielectric function. As an example, a detailed analysis of the electron-energy loss spectrum of Ni, ref. [22], already exhibits non-negligible contribution to the RPA dielectric function due to the presence of high-lying semi-core states.

In the light of the above discussion an all-electron approach treating the  $1/r$  potential exactly is much more suited for the investigation of transition metal oxides. For example, the linear muffin-tin orbital (LMTO) [19] method employs a basis set comprising atomic-like orbitals to treat the  $1/r$  divergence. The Korringa-Kohn-Rostocker (KKR) [87, 88] method is formulated in terms of Green functions. Another strategy is pursued in the full-potential linearized-augmented plane-wave (FLAPW) method [19]: the plane waves as basis functions are retained but augmented in the region close to the nuclei to allow for an exact treatment of the  $1/r$  potential. Details of the construction of the resulting augmented plane-wave (LAPW) basis functions are discussed in the following.

### 3.1.2. Augmented plane waves and the LAPW basis functions

In the FLAPW method space is partitioned into atom-centered spheres, the muffin-tin (MT) spheres, and into the remaining interstitial region. The partitioning is illustrated schematically in figure 3.2. The radius  $s_a$  of the MT sphere of atom  $a$  is chosen to be as large as possible under the constraint that MT spheres from neighboring atoms should not overlap. Consequently, the potential from the nuclei in the interstitial region is smooth and plane waves constitute an efficient basis in this part of space.

According to the Rayleigh decomposition a plane wave can be decomposed into a sum over products of spherical Bessel functions and spherical harmonics  $Y_{lm}(\mathbf{e}_r)$ , where the notation  $\mathbf{e}_r = \mathbf{r}/r$  with  $r = |\mathbf{r}|$  indicates the unit vector in the direction of  $\mathbf{r}$ . Furthermore, the index  $\sigma$  will be used to denote the electron's spin. Slater suggested in 1937 [89] to replace the Bessel functions by radial functions  $u_{al}^\sigma(\epsilon, r)$  matching the Bessel functions in value at the sphere radius  $s_a$ . It is this procedure, what is understood by the term *augmentation*. The radial functions are the numerical solutions of the radial KS equation

$$\left\{ -\frac{\partial^2}{\partial r^2} + \frac{l(l+1)}{r^2} + \bar{V}_{\text{eff},a}^\sigma(r) - \epsilon_{al}^\sigma \right\} r u_{al}^\sigma(\epsilon, r) = 0, \quad (3.1)$$

where  $\bar{V}_{\text{eff},a}^\sigma(r)$  is the spherical average of the effective potential. Linear combinations of these radial functions  $u_{al}^\sigma(\epsilon, r)$  together with plane waves in the interstitial region constitute a basis of augmented plane waves (APWs) that allow for an exact treatment of the  $1/r$  potential.

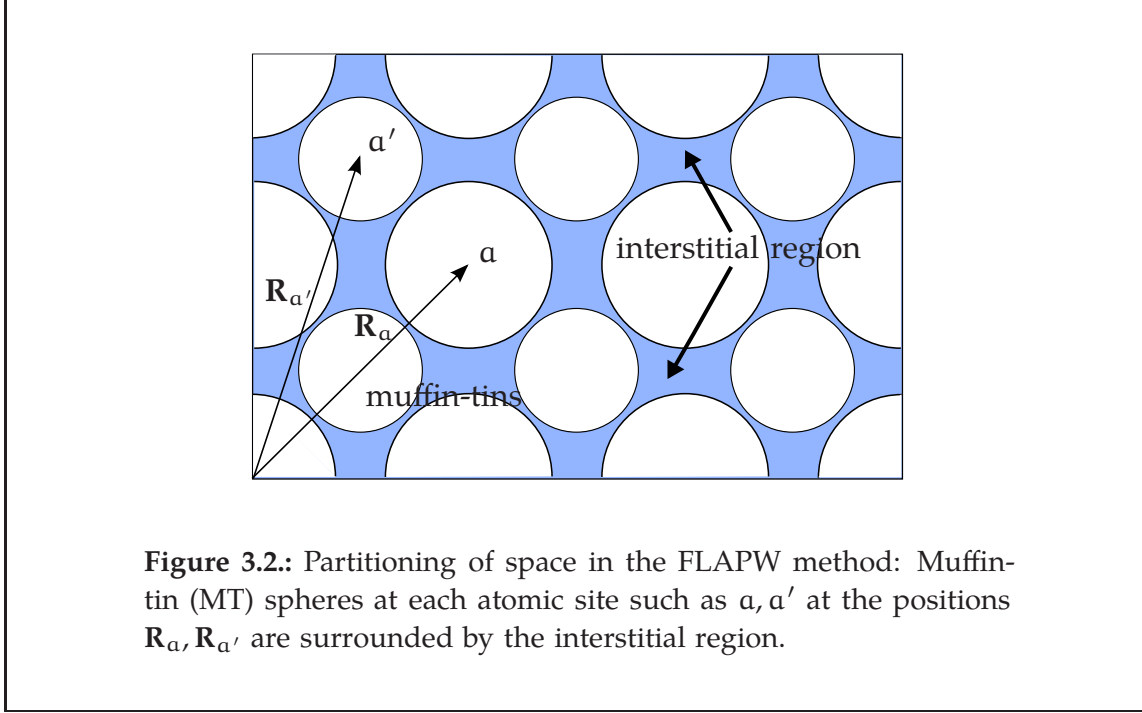


**Figure 3.2.:** Partitioning of space in the FLAPW method: Muffin-tin (MT) spheres at each atomic site such as  $a, a'$  at the positions  $\mathbf{R}_a, \mathbf{R}_{a'}$  are surrounded by the interstitial region.

In practice, eq. (3.1) has to be solved self-consistently in the energies, since the radial solutions  $u_{a_l}^\sigma(\epsilon, r)$  are energy-dependent. Hence, the solution of eq. (3.1) is much more computationally demanding than the solution of a standard eigenvalue problem, where the energies  $\epsilon_{a_l}^\sigma$  are simply treated as fixed parameters. Furthermore, the resulting radial functions lack variational freedom to allow for changes in the wave function as the band energy deviates from the reference energy  $\epsilon_{a_l}^\sigma$ , e.g., in open shell systems, where the spherical average of the effective potential in eq. (3.1) is a rather crude approximation to the real potential. A detailed discussions of the limitations of the APW method is beyond the scope of this work. Further information can be found in the book by Loucks [90], where reprints of the original publications of Slater can be found as well.

To avoid the problems originating from the energy dependence of the APW basis functions, Marcus [91] suggested to replace the radial functions by their Taylor expansion terminated after the linear term

$$u_{a_l}^\sigma(\epsilon, r) = u_{a_{l0}}^\sigma(r) + u_{a_{l1}}^\sigma(r)(\epsilon - \epsilon_{a_l}^\sigma) + \mathcal{O}[(\epsilon - \epsilon_{a_l}^\sigma)^2], \quad (3.2)$$

where  $\mathcal{O}[(\epsilon - \epsilon_{a_l}^\sigma)^2]$  denotes errors that are quadratic in this energy difference. The function  $u_{a_{l0}}^\sigma(r) = u_{a_l}^\sigma(\epsilon_{a_l}^\sigma, r)$  is the radial solution of eq. (3.1) and  $u_{a_{l1}}^\sigma(r) \equiv \partial u_{a_l}^\sigma(\epsilon, r) / \partial \epsilon|_{\epsilon = \epsilon_{a_l}^\sigma}$  its energy derivative. However,  $u_{a_{l0}}^\sigma(r)$  and  $u_{a_{l1}}^\sigma(r)$  are evaluated at the fixed energy  $\epsilon_{a_l}^\sigma$  chosen to minimize the linearization errors, i.e., in the center of gravity of the  $l$ -like band. Marcus' work was extended by Andersen [19] as well as Koelling and Arbman [92] who proposed a method in which the

radial functions  $u_{a10}^\sigma(\mathbf{r})$  and  $u_{a11}^\sigma(\mathbf{r})$  are matched continuously to the plane waves in the interstitial region at the MT sphere boundaries. With the shorthand notation  $u_{a1mp}^\sigma(\mathbf{r}) \equiv u_{a1p}^\sigma(\mathbf{r})Y_{lm}(\mathbf{e}_r)$ , where  $p = 0, 1$  labels the two radial functions in the Taylor expansion (3.2), the resulting APWs can be written as

$$\chi_{\mathbf{k}\mathbf{G}}^\sigma(\mathbf{r}) = \begin{cases} \frac{1}{\sqrt{N}} \sum_{l=0}^{l_{\max}} \sum_{m=-l}^l \sum_{p=0}^1 A_{lmp}^{\alpha\sigma}(\mathbf{k}, \mathbf{G}) u_{a1mp}^\sigma(\mathbf{r} - \mathbf{R}_a) & \text{if } \mathbf{r} \in \text{MT}(a) \\ \frac{1}{\sqrt{V}} e^{i(\mathbf{k}+\mathbf{G}) \cdot \mathbf{r}} & \text{if } \mathbf{r} \in \text{interstitial} \end{cases}, \quad (3.3)$$

where  $\mathbf{R}_a$  is the position of atom  $a$ ,  $N$  is the number of unit cells and  $V$  denotes the volume of the crystal. These APWs become the new LAPW basis functions of the FLAPW method.

The error in the wave function originating from the energy linearization is of quadratic order. This leads to an error of order  $\mathcal{O}[(\epsilon - \epsilon_{a1}^\sigma)^4]$  in the band energies according to reference [93]. Furthermore, using two radial functions for each index  $l$  instead of one makes the APWs (3.3) more flexible than the energy-dependent solutions of (3.1). Altogether, the increase in flexibility as well as the smallness of the linearization error typically allows to treat all valence states with a single set of energies  $\{\epsilon_{a1}^\sigma\}$  making the LAPWs a very efficient yet accurate set of basis functions. In numerical applications an appropriate choice for the cutoff  $l_{\max}$  for the  $l$  quantum number has yet to be found. This aspect will be discussed in more detail in section 3.2 about the implementation of the FLAPW method in the FLEUR code.

For the sake of completeness an explicit form of the coefficients  $A_{lmp}^{\alpha\sigma}(\mathbf{k}, \mathbf{G})$  shall be given here as well. The coefficients are determined subject to the requirement that the LAPW basis functions and their spatial derivatives are continuous at the MT boundary. This leads to the following expressions for the coefficients

$$\begin{aligned} A_{l_{m0}}^{\alpha\sigma}(\mathbf{k}, \mathbf{G}) &= e^{i\mathbf{K} \cdot \mathbf{R}_a} 4\pi \frac{1}{w_{a1}^\sigma} i^l Y_{lm}^*(\hat{\mathbf{K}}) \\ &\quad [u_{a11}^\sigma(s_a) \text{Kj}'_l(s_a \text{K}) - u'_{a11}^\sigma(s_a) j_l(s_a \text{K})] \\ A_{l_{m1}}^{\alpha\sigma}(\mathbf{k}, \mathbf{G}) &= e^{i\mathbf{K} \cdot \mathbf{R}_a} 4\pi \frac{1}{w_{a1}^\sigma} i^l Y_{lm}^*(\hat{\mathbf{K}}) \\ &\quad [u_{a10}^\sigma(s_a) \text{Kj}'_l(s_a \text{K}) - u'_{a10}^\sigma(s_a) j_l(s_a \text{K})] \end{aligned} \quad (3.4)$$

with  $\mathbf{K} = \mathbf{k} + \mathbf{G}$  and the abbreviation  $\partial u / \partial r = u'$  for the spatial derivative. The prefactor  $e^{i\mathbf{K} \cdot \mathbf{R}_a}$  shifts the origin of the coordinate system into the center of the MT sphere of atom  $a$ . The Wronskian  $w$  is defined as

$$w_{a1}^\sigma = [u_{a11}^\sigma(s_a) u'_{a10}^\sigma(s_a) - u_{a10}^\sigma(s_a) u'_{a11}^\sigma(s_a)]. \quad (3.5)$$

### 3.1.3. The local orbital (LO) extension

Core states are completely contained within the MT spheres, i.e., the corresponding wave functions are practically zero at the MT sphere boundaries. It can be shown (cf. ref. [94]) that these states and the LAPW basis functions are orthogonal. Since the wave functions describing semi-core states are not zero at the MT boundary they are not orthogonal to the LAPW basis functions. Due to a finite overlap between a semi-core state and a APW basis function with corresponding  $l$  quantum number the latter can now reproduce the former. However, the semi-core state will now appear in the valence- or conduction-band region since the energetic position of the LAPW basis function is fixed at the linearization parameter  $\epsilon_{\alpha l}^{\sigma}$  typically placed in the region around the Fermi energy. The resulting spurious bands are called ghost bands. If the semi-core states are treated as valence-band states right from the start, they can be described properly by the LAPW basis functions if the energy parameter of the corresponding radial function is set at the position of the semi-core states. However, this would in turn diminish the flexibility of the LAPW basis to represent states in the valence-band region with the same  $l$  quantum number.

This dilemma can be resolved with the help of the local-orbital extension, Refs. [95, 96]. A local orbital (LO) is constructed from an additional radial function  $u_{\alpha}^{\sigma, lo}(r)$ , which is obtained from the solution of eq. (3.1) just like the radial functions  $u_{\alpha l 0}^{\sigma}(r)$  but for a different energy parameter  $\epsilon_{\alpha}^{\sigma, lo}$ . If used to improve the basis to better describe a semi-core state, the energy  $\epsilon_{\alpha}^{\sigma, lo}$  of the LO is typically chosen to match the position of this state. The local orbital is then constructed as a linear combination of the products of spherical harmonics with the three radial functions  $u_{\alpha}^{\sigma, lo}(r)$ , and  $u_{\alpha l 0}^{\sigma}(r)$  and  $u_{\alpha l 1}^{\sigma}(r)$  with the same  $l$  quantum number under the constraint that the resulting new basis function and radial derivative become zero at the MT sphere boundary. Hence, no additional plane waves in the interstitial region have to be added to continuously match the newly introduced function across the sphere boundary. In this sense, the local-orbital extension is a very efficient procedure to increase the flexibility of the LAPW basis set. For example, a particular semi-core state can usually be described by adding just one additional radial function  $u_{\alpha}^{\sigma, lo}(r)$  to the basis set. Since the local orbitals still have to satisfy Bloch boundary conditions, when used in calculations for periodic solids, they are matched to "fictitious" plane waves in the same way as the LAPW basis functions. This leads to

$$\chi_{\mathbf{k}\mathbf{G}_{lo}}^{\sigma\alpha}(\mathbf{r}) = \sum_m (a_{lo}^{\alpha\sigma}(\mathbf{k}, \mathbf{G}_{lo})u_{\alpha l 0}^{\sigma}(r) + b_{lo}^{\alpha\sigma}(\mathbf{k}, \mathbf{G}_{lo})u_{\alpha l 1}^{\sigma}(r)) Y_{lm}(\mathbf{e}_{\mathbf{r}}) \\ (c_{lo}^{\alpha\sigma}(\mathbf{k}, \mathbf{G}_{lo})u_{\alpha}^{\sigma, lo}(r)) Y_{lm}(\mathbf{e}_{\mathbf{r}}) \quad (3.6)$$

with

$$a_{lo}^{\alpha\sigma}(\mathbf{k}, \mathbf{G}_{lo}) = e^{i\mathbf{K}_{lo} \cdot \mathbf{R}_{\alpha}} \tilde{a}_{lo}^{\alpha\sigma} 4\pi \frac{1}{\mathcal{W}} i^l Y_{lm}^*(\hat{\mathbf{K}}_{lo}) \quad (3.7)$$

and similar expressions for the b and c coefficient with  $\mathbf{K}_{l_0} = \mathbf{k} + \mathbf{G}_{l_0}$ .

The energy parameters for the construction of the LAPW basis functions are typically chosen in the energy range close to the Fermi level to minimize the linearization error for the representation of the valence states. The resulting basis set is optimized for the description of occupied states which are the only states necessary to calculate the charge density, eq. (2.18), and hence the only states needed to solve the KS equation self-consistently. High-lying unoccupied states are usually described poorly by this basis since the deviation due to the linearization error grows if  $|\epsilon - \epsilon_{al}^\sigma|$  becomes large. However, the RPA polarization function in eq. (2.83) and the KS Green function in eq. (2.82) comprise a summation over all unoccupied states. Therefore, further local orbitals for selected l channels are added to the LAPW basis in this work to converge the representation of the unoccupied states.

To determine the energy parameter of these LOs the matching conditions between the solutions of the radial KS eq. (3.1) and the interstitial plane waves are considered. If the latter are replaced by the Rayleigh expansion, the following conditions have to be fulfilled at the MT sphere boundary  $s_a$

$$j_l(ks_a) = u_{al}^\sigma(\epsilon, s_a) \quad \text{and} \quad j_l'(ks_a) = u_{al}'^\sigma(\epsilon, s_a). \quad (3.8)$$

Dividing the equation on the right by  $u_{al}^\sigma(\epsilon, s_a)$  leads to

$$\frac{j_l'(ks_a)}{j_l(ks_a)} = \frac{u_{al}'^\sigma(\epsilon, s_a)}{u_{al}^\sigma(\epsilon, s_a)}. \quad (3.9)$$

The right hand side of eq. (3.9) is identical to the logarithmic derivative  $D(\epsilon)$  of the radial function evaluated at the MT sphere boundaries  $s_a$

$$D(\epsilon) \equiv \left. \frac{u_{al}'^\sigma(\epsilon, r)}{u_{al}^\sigma(\epsilon, r)} \right|_{r=s_a}, \quad (3.10)$$

The logarithmic derivative is an ever-decreasing cotangent-like function with vertical asymptotes separating different branches. Each branch of  $D(\epsilon)$  corresponds to a particular number of radial nodes of the radial function  $u_{al}^\sigma(\epsilon, r)$  in the interval  $0 < r < s_a$ . Requiring the logarithmic derivative to satisfy the condition (cf. ref. [19])

$$D(\epsilon) = -(l+1) \quad (3.11)$$

yields a criterion to determine the energy parameter of the corresponding LO and ensures that the radial functions in different branches are orthogonal.

### 3.1.4. The mixed product basis (MPB)

Previously, the LAPW basis and its local-orbital extension were introduced to properly represent the single-particle spectrum of the KS eigenstates. To obtain

matrix elements of the exchange contribution to the self-energy eq. (2.87) and to calculate the polarization function eq. (2.83) of the GW approximation products of KS wave functions have to be calculated. Therefore, in the last part of this section the mixed product basis (MPB), refs. [21, 22], for the representation of wave-function products is introduced. Unlike the LAPW basis functions that are defined everywhere in space, the MPB consists of two disjunct subsets of functions only defined within the MT spheres and the interstitial region, respectively. This allows to optimize each subset of basis functions separately leading to a small and efficient basis set. First, the MPB functions for the MT region are introduced,

Inside each MT sphere basis functions are constructed from the radial functions of the LAPW basis. With  $p, p' = 1, 2$  labeling the LAPW radial functions and their energy derivative and  $p, p' > 2$  counting local orbitals for a given angular quantum number  $l$ , these products of two radial functions are expanded in spherical harmonics

$$\begin{aligned} u_{\text{almp}}^{\sigma*}(\mathbf{r})u_{\text{al'm'p'}}^{\sigma}(\mathbf{r}) &= u_{\text{alp}}^{\sigma}(r)Y_{lm}^*(\mathbf{e}_r)u_{\text{al'p'}}^{\sigma}(r)Y_{l'm'}(\mathbf{e}_r) \\ &= \sum_{L=|l-l'|}^{l+l'} \sum_{M=-L}^L C_{lm'l'm'LM} U_{\text{aLP}}^{\sigma}(r)Y_{LM}(\mathbf{e}_r), \end{aligned} \quad (3.12)$$

with the Gaunt coefficients given by

$$C_{lm'l'm'LM} = \int Y_{lm}^*(\mathbf{e}_r)Y_{l'm'}(\mathbf{e}_r)Y_{LM}^*(\mathbf{e}_r)d\Omega. \quad (3.13)$$

Here,  $U$  is defined as  $U_{\text{aLP}}^{\sigma}(r) = u_{\text{alp}}^{\sigma}(r)u_{\text{al'p'}}^{\sigma}(r)$ , where  $P$  counts the functions for a given angular quantum number  $L$ .

In practice, it is often sufficient to completely neglect the energy derivatives of the LAPW radial functions as well as most of the local orbitals in the construction of the MPB. Furthermore, only radial functions with a certain  $l$  quantum number can be selected. These measures allow to keep the total number of radial functions  $U_{\text{aLP}}^{\sigma}(r)$  small. Still, the resulting set of functions usually has a high degree of (near) linear dependence. In other words, the set still contains a certain number of functions that do not contribute significantly to the representation of the wave-function products. Furthermore, the radial functions  $U_{\text{aLP}}^{\sigma}(r)$  are neither normalized nor orthogonal.

To optimize the set of radial functions, the overlap matrix is diagonalized and only those eigenfunctions  $M_{\text{aLP}}(r)$  with eigenvalues exceeding a certain threshold value (typically  $10^{-4}$ ) are kept, ref. [20]. This removes the (near) linear dependency. Furthermore, the resulting product functions  $M_{\text{aLMP}}(\mathbf{r}) = M_{\text{aLP}}(r)Y_{LM}(\mathbf{e}_r)$  are orthonormal and become spin-independent, because the

spin-up and spin-down products, eq. (3.12), are optimized together. The number of basis functions can be further reduced by introducing a cutoff value  $L_{\max}$ . On the other hand, a constant MT function has to be included in the set for each atom in the unit cell, which is later needed to represent the eigenfunction that corresponds to the divergent eigenvalue of the Coulomb matrix in the limit  $\mathbf{k} \rightarrow \mathbf{0}$ . Finally, Bloch functions are constructed

$$M_{\alpha\text{LMP}}^{\mathbf{k}}(\mathbf{r}) = \frac{1}{\sqrt{N}} \sum_{\mathbf{T}} e^{i\mathbf{k} \cdot (\mathbf{T} + \mathbf{R}_\alpha)} M_{\alpha\text{LP}}(|\mathbf{r} - \mathbf{T} - \mathbf{R}_\alpha|) Y_{\text{LM}}(\mathbf{e}_{\mathbf{r} - \mathbf{T} - \mathbf{R}_\alpha}), \quad (3.14)$$

where the sum runs over all lattice translation vectors  $\mathbf{T}$ . The radial functions  $M_{\alpha\text{LP}}(r)$  are zero by definition if  $r$  is larger than the MT radius  $s_\alpha$ .

In the interstitial region, wave-function products are represented by the products of two plane waves, which is given by yet another plane wave. Thus, the MPB functions in the interstitial region are given by

$$M_{\mathbf{G}}^{\mathbf{k}}(\mathbf{r}) = \frac{1}{\sqrt{V}} e^{i(\mathbf{k} + \mathbf{G}) \cdot \mathbf{r}} \Theta(\mathbf{r}) \quad (3.15)$$

with the step function

$$\Theta(\mathbf{r}) = \begin{cases} 0 & \text{if } \mathbf{r} \in \text{MT} \\ 1 & \text{if } \mathbf{r} \in \text{interstitial} \end{cases} \quad (3.16)$$

that has to be introduced to guarantee that  $M_{\mathbf{G}}^{\mathbf{k}}(\mathbf{r}) = 0$  if  $\mathbf{r} \in \text{MT}(\alpha)$ . The representation of wave-function products in the interstitial space becomes exact with the cutoff  $G'_{\max} = 2G_{\max}$ , but a much smaller value for  $G'_{\max}$  often suffices as will be demonstrated in section 5.1 of chapter 5. Together with the MT functions the full MPB is given by  $\{M_{\mathbf{I}}^{\mathbf{k}}(\mathbf{r})\} = \{M_{\alpha\text{LMP}}^{\mathbf{k}}(\mathbf{r}), M_{\mathbf{G}}^{\mathbf{k}}(\mathbf{r})\}$ , where the index  $\mathbf{I}$  is introduced to label the MPB functions.

The functions  $M_{\mathbf{G}}^{\mathbf{k}}(\mathbf{r})$  are not orthogonal since they are restricted to the interstitial region. The overlap matrix of these functions is given by

$$\langle M_{\mathbf{G}}^{\mathbf{k}} | M_{\mathbf{G}'}^{\mathbf{k}'} \rangle = \delta_{\mathbf{k}\mathbf{k}'} O_{\mathbf{G}\mathbf{G}'}(\mathbf{k}) = \delta_{\mathbf{k}\mathbf{k}'} \Theta_{\mathbf{G}-\mathbf{G}'}, \quad (3.17)$$

where  $\Theta_{\mathbf{G}}$  are the Fourier coefficients of the step function defined above. The overlap matrix is  $\mathbf{k}$  dependent because the size of the MPB varies for different  $\mathbf{k}$  vectors. Since the MT functions of the MPB are orthonormalized the overlap matrix of the functions  $M_{\mathbf{G}}^{\mathbf{k}}(\mathbf{r})$  yields the only non-trivial contribution to the overlap matrix of the full MPB  $O_{\mathbf{I}\mathbf{J}}(\mathbf{k}) = \langle M_{\mathbf{I}}^{\mathbf{k}} | M_{\mathbf{J}}^{\mathbf{k}} \rangle$ , which is used to introduce the biorthogonal basis set with basis functions

$$\tilde{M}_{\mathbf{I}}^{\mathbf{k}}(\mathbf{r}) = \sum_{\mathbf{J}} O_{\mathbf{J}\mathbf{I}}^{-1}(\mathbf{k}) M_{\mathbf{J}}^{\mathbf{k}}(\mathbf{r}). \quad (3.18)$$

It fulfills the identities

$$\langle \tilde{M}_I^k | M_J^k \rangle = \langle M_I^k | \tilde{M}_J^k \rangle = \delta_{IJ} \quad \text{and} \quad \sum_I |M_I^k\rangle \langle \tilde{M}_I^k| = \sum_I |\tilde{M}_I^k\rangle \langle M_I^k| = 1, \quad (3.19)$$

where the completeness relation is only valid in the subspace spanned by the MPB, though.

## 3.2. Remarks on density-functional calculations with FLEUR

In the FLEUR code [18] the FLAPW method is employed to solve the KS equation (2.17) or the gKS equation (2.48) self-consistently. Some general aspects of the implementation together with information about the input data necessary to run this code are given in the first part of this section. Some remarks on the treatment of the potential are given afterwards. The last part of this section describes how relativistic effects within the scalar-relativistic approximation [43] are taken into account in calculations with FLEUR and how the spin-orbit coupling in second variation can be included.

### 3.2.1. The generalized eigenvalue problem

It is convenient to treat the core levels and the valence-band states (including semi-core states) separately, i.e., to decompose the charge density according to

$$n(\mathbf{r}) = n_{\text{val}}(\mathbf{r}) + n_{\text{core}}(\mathbf{r}). \quad (3.20)$$

Since the core levels are well separated in energy and localized at the atomic sites (cf. figure 3.1) the corresponding eigenvalue problem always fulfills the boundary conditions of isolated atoms. Consequently, the potential felt by the core electrons is nearly spherically symmetric. On the other hand, the core electrons have a high kinetic energy since the potential close to the core is large. Hence, relativistic effects such as spin-orbit coupling due to the large potential gradient become important for a proper description of the core electrons. Thus, the core levels in FLEUR are obtained by a solution of the fully relativistic Dirac equation (2.19) with the spherical part ( $l = 0$ ) of the potential.

To further treat valence-band and semi-core states the corresponding KS or gKS wave functions are expanded in terms of the APWs<sup>1</sup>  $\chi_{\mathbf{k}G}^\sigma(\mathbf{r})$ , eq. (3.3), including

<sup>1</sup>Inside the MT spheres, the scalar-relativistic approximation described in section 3.2.3 is used. Therefore, the MT parts of the LAPW basis functions, eq. (3.3), are replaced by solutions of eq. (3.27).

local orbitals to better describe semi-core and high-lying conduction-band states

$$\varphi_{n\mathbf{k}}^\sigma(\mathbf{r}) = \sum_{|\mathbf{k}+\mathbf{G}|\leq G_{\max}} z_G^\sigma(n, \mathbf{k}) \chi_{\mathbf{k}\mathbf{G}}^\sigma(\mathbf{r}). \quad (3.21)$$

To simplify the notation, the spin index will be neglected from now on. Inserting this expansion in (2.48) transforms the gKS equation into a generalized eigenvalue problem (GEP)

$$\sum_{\mathbf{G}} [H_{\mathbf{G}'\mathbf{G}}(\mathbf{k}) + \alpha V_{x,\mathbf{G}'\mathbf{G}}(\mathbf{k})] z_{\mathbf{G}}(n, \mathbf{k}) = \epsilon_{n\mathbf{k}} \sum_{\mathbf{G}} S_{\mathbf{G}'\mathbf{G}}(\mathbf{k}) z_{\mathbf{G}}(n, \mathbf{k}) \quad (3.22)$$

for the eigenvectors  $z_{\mathbf{G}}^\sigma(n, \mathbf{k})$  with

$$H_{\mathbf{G}'\mathbf{G}}(\mathbf{k}) = \int d^3r \chi_{\mathbf{k}\mathbf{G}'}^*(\mathbf{r}) \left[ -\frac{1}{2} \nabla_{\mathbf{r}}^2 + V^{\text{gKS}}(\mathbf{r}) \right] \chi_{\mathbf{k}\mathbf{G}}(\mathbf{r}), \quad (3.23)$$

$$S_{\mathbf{G}'\mathbf{G}}(\mathbf{k}) = \int d^3r \chi_{\mathbf{k}\mathbf{G}'}^*(\mathbf{r}) \chi_{\mathbf{k}\mathbf{G}}(\mathbf{r}) \quad \text{and} \quad (3.24)$$

$$V_{x,\mathbf{G}'\mathbf{G}}(\mathbf{k}) = - \sum_{n',\mathbf{q}}^{\text{occ}} \iint \frac{\chi_{\mathbf{k}\mathbf{G}'}^*(\mathbf{r}) \varphi_{n',\mathbf{q}}(\mathbf{r}) \varphi_{n',\mathbf{q}}^*(\mathbf{r}') \chi_{\mathbf{k}\mathbf{G}}(\mathbf{r}')}{|\mathbf{r} - \mathbf{r}'|}. \quad (3.25)$$

A GEP for (2.17) is obtained in the same manner. It has the same mathematical form as (3.22) with  $\alpha = 0$  and  $V^{\text{gKS}}(\mathbf{r})$  replaced by  $V^{\text{KS}}(\mathbf{r})$  in eq. (3.23). The generalized eigenvalue problems are reduced to a standard ones employing the Cholesky decomposition.

At the beginning of a density-functional calculation a starting guess for the charge density is needed. Typically, atomic-like orbitals for each atom in the unit cell of the solid are calculated thus neglecting all kinds of interactions between them. The resulting orbitals are used to obtain the starting density according to eq. (2.18), which is used to construct the Hartree potential as well as the exchange-correlation potential yielding the Hamiltonian of eq. (2.48). The corresponding GEP, eq. (3.22), is then solved. Afterwards, the charge density is recalculated, a new GEP is obtained and the two steps are iterated until the densities computed in the last and last but one step are sufficiently close. As an explicit measure of convergence the root mean square of the difference between the input and output densities in  $\text{me}/\text{bohr}^3$  is considered, where  $e$  is the elementary charge. If this difference falls below  $10^{-5} \text{ me}/\text{bohr}^3$ , the calculation is considered to be converged. In practice, calculations within the gKS scheme are always started from a converged solution of the KS equation (2.17). Hence, the initial wave functions  $\varphi_{n\mathbf{q}}(\mathbf{r})$  entering into the term  $V_{x,\mathbf{G}'\mathbf{G}}(\mathbf{k})$  of the GEP for the gKS equation (2.48) are the KS wave functions from a prior solution of the KS equation.

In practice, an appropriate choice for the plane-wave cutoff  $G_{\max}$  as well as for the  $l$  cutoff  $l_{\max}$  in the construction of the LAPW basis functions inside the

MT spheres (3.3) has to be made. Due to the requirement that the LAPW basis functions are continuous across the MT boundary both convergence parameters cannot be treated independently. The real or imaginary part of a plane wave with wave vector  $G_{\max}$  has  $G_{\max}/\pi$  nodes per atomic unit. A spherical harmonic  $l = l_{\max}$  has  $2l_{\max}$  nodes along a great circle on the MT sphere, i.e there are  $l_{\max}/\pi s_{\alpha}$  nodes per atomic unit. Therefore, a reasonable choice of the  $l$  cutoff is  $l_{\max} = s_{\alpha} G_{\max}$ , where  $s_{\alpha}$  again denotes the MT radius of atom  $\alpha$ . The choice of  $G_{\max}$  must be converged for example with respect to the total energy. Furthermore, for calculations withing the generalized KS scheme, the number of conduction bands also enters as parameter and has to be converged. For a detailed discussion about the implementation of hybrid functionals in the FLEUR code the reader is referred to the publication by Betzinger *et al.* [85].

Finally, it should be mentioned that results do depend on the choice of MT radii. On the one hand, this is not surprising, because the MT radii enter in many different parts of the algorithms. On the other hand, the partitioning of space into the MT spheres and the interstitial region is just a mathematical trick to better describe the behavior of the wave functions in different regions of space and the results should be independent of the choice of the MT radii. Indeed, the dependence on the MT radii becomes negligible if all input parameters are converged properly. Apart from a reasonable choice of the convergence parameters the only other information necessary to run FLEUR are the number of atoms in the unit cell, which kind of atoms are contained and how they are distributed in space.

### 3.2.2. Including the full potential in the LAPW method

For open-shell systems such as the TMOs investigated in this work an accurate representation of the potential felt by the electrons occupying the semi-core and valence-band states is indispensable. The flexibility of the LAPW basis is therefore exploited in FLEUR to include the full potential without any shape-approximations in the interstitial region (IR) or inside the MT spheres. Whereas in the APW approach the potential in the IR is usually described by a constant  $V_{\text{IR}}^0$  and the potential inside the MT spheres is spherically averaged (see eq. (3.1)), FLEUR routinely takes into account non-spherical terms inside the MT spheres as well as a warped interstitial. The full potential is thus given by

$$V(\mathbf{r}) = \begin{cases} \sum_{lm} V_{\text{MT}}^{lm}(\mathbf{r}) Y_{lm}(\mathbf{e}_{\mathbf{r}}) & \text{if } \mathbf{r} \in \text{MT}(\alpha) \\ \sum_{\mathbf{G}} V_{\text{IR}}^{\mathbf{G}} e^{i\mathbf{G} \cdot \mathbf{r}} & \text{if } \mathbf{r} \in \text{IR} \end{cases} . \quad (3.26)$$

The charge density takes a form analogous to the above equation for the potential. In practice, the functions  $Y_{lm}(\mathbf{e}_r)$  are replaced by lattice harmonics and the plane waves by symmetrized plane waves called stars. Further details can be found in reference [86].

### 3.2.3. Scalar-relativistic approximation and SOC in second variation

As discussed in section 2.2.2, for electrons occupying valence states relativistic effects are small. It is therefore reasonable to treat the interstitial region non-relativistically. In the construction of the APWs inside the MT spheres relativistic effects are approximately taken into account within the scalar-relativistic (SC) approximation [43]. The SC approximation captures relativistic effects described by the term  $H_{SC}$ , eq. (2.27). The radial KS equation (3.1) is replaced by

$$\mathcal{H}_{SC} \begin{pmatrix} g_l(\mathbf{r}) \\ \phi_l(\mathbf{r}) \end{pmatrix} = \epsilon \begin{pmatrix} g_l(\mathbf{r}) \\ \phi_l(\mathbf{r}) \end{pmatrix} \quad (3.27)$$

with

$$\mathcal{H}_{SC} = \begin{pmatrix} \frac{1}{2M(\epsilon, r)} \frac{l(l+1)}{r^2} + V^{KS}(r) & -\frac{2c}{r} - c \frac{\partial}{\partial r} \\ c \frac{\partial}{\partial r} & -2mc^2 + V^{KS}(r) \end{pmatrix}. \quad (3.28)$$

Here,  $g_l(\mathbf{r})$  and  $\phi_l(\mathbf{r})$  are the wave functions of the large and small component, respectively,  $M(\epsilon, r) = m + (1/2c^2)(\epsilon - V^{KS}(r))$  and  $V^{KS}(r)$  is the spherical part of the KS effective potential, eq. (2.15). This leads to a modified basis set of APWs, where  $u_{a1}^\sigma(r)$  and  $\dot{u}_{a1}^\sigma(r)$  are replaced by  $(g_l(\mathbf{r}), \phi_l(\mathbf{r}))^T$  and  $(\dot{g}_l(\mathbf{r}), \dot{\phi}_l(\mathbf{r}))^T$ . Only the large component is then matched to plane waves at the boundary between the MTs and the interstitial region, because the small component is already negligible at this distance from the nucleus. The advantage of this procedure is twofold:  $l$  and  $\sigma$  are still good quantum number, since SOC linking the spin and orbital degrees of freedom is not taken into account. Secondly, the increase in the numerical effort is moderate, i.e., comparable to that needed in spin-polarized non-relativistic calculations, since the size of the basis and the Hamiltonian remains the same as in non-relativistic calculation. However, the problem has to be solved twice, once for each direction of spin, as in non-relativistic calculations employing spin-DFT to describe magnetic systems with collinear orientation of the spins.

The effect of SOC on the valence- and conduction-band states can be included self-consistently inside the MT spheres using the procedure outlined in reference [44]. It consists of three steps:

1. The KS equation including the SC approximation is solved self-consistently yielding the SC eigenfunctions denoted by  $\varphi_{\mathbf{n}\mathbf{k}}^{\sigma}(\mathbf{r})$  and the corresponding eigenvalues  $\epsilon_{\mathbf{n}\mathbf{k}}^{\sigma}$  for each spin direction up and down.
2. A second variational secular equation is set up using as basis functions the lowest  $N$  SC eigenfunctions for both spins calculated in the previous step. This yields a  $(2N \times 2N)$  matrix equation with Hamiltonian

$$H_{\mathbf{n}\mathbf{n}'}^{\sigma\sigma'}(\mathbf{k}) = \epsilon_{\mathbf{n}\mathbf{k}}^{\sigma}\delta_{\mathbf{n}\mathbf{n}'}\delta_{\sigma\sigma'} + \langle \varphi_{\mathbf{n}\mathbf{k}}^{\sigma} | \tilde{H}_{\text{SOC}} | \varphi_{\mathbf{n}'\mathbf{k}}^{\sigma'} \rangle, \quad (3.29)$$

where the second term on the right denotes matrix elements of  $\tilde{H}_{\text{SOC}}$  introduced in eq. (2.29) with the SC eigenfunctions. The solution of the corresponding eigenvalue problem yields a new set of eigenvalues and eigenstates.

3. From the new eigenstates a new single-particle density is constructed, which is used to determine the effective potential, eq. (2.15), of a new KS equation.

In reference [93], a detailed description of the implementation of this procedure within the FLAPW method can be found.

A spin quantization axis has to be defined to evaluate the vector product  $\mathbf{L} \cdot \mathbf{S}$  contained in the term  $\tilde{H}_{\text{SOC}}$ . The solution of the KS equation including relativistic corrections from the SC approximation does not favor a certain spin direction energetically, since it does not link the spin and orbital degrees of freedom. Therefore, the spin quantization axis must be chosen manually in the procedure described above. On the contrary, the solutions of the new eigenvalue problem with Hamiltonian eq. (3.29) can yield different total energies for different choices of the spin quantization axis if the electronic system exhibits ferromagnetic or anti-ferromagnetic spin order. For example, the magnetic anisotropy  $\Delta E$  of such a system can be obtained from the differences of the total energies

$$\Delta E = E(\Sigma_1) - E(\Sigma_2), \quad (3.30)$$

where  $\Sigma_1$  and  $\Sigma_2$  denote different spin orientations. For non-magnetic systems the total energy is independent of the choice of the spin orientation even if SOC is included in the calculation. In this case, the initial spin quantization axis can be chosen arbitrarily.

### 3.3. The SPEX code

In the first part of the last section of chapter 3, the different steps of a GW calculation as implemented in the computer code SPEX [18] will be outlined and the input parameters necessary to conduct calculations are described. Then, some technical aspects of the utilization of spatial symmetry in SPEX and the

analytic treatment of matrix elements evaluated at the  $\Gamma$  point of the  $\mathbf{k}$  point mesh are addressed. The chapter closes with some remarks on calculations of the quasi-particle band structure, the density of states and the dielectric function. The main purpose of this last section is to deliver insight into how to calculate physical observables with SPEX rather than discussing technical aspects of its implementation. For more details on the algorithms used in the code the reader is referred to the article by Friedrich *et al.* [20].

### 3.3.1. GW calculations with the SPEX code

Figure 3.3 summarizes the different steps of a calculation with SPEX yielding the quasi-particle spectrum of a given material. First, some information from a previous density-functional calculation are read in such as the number of atoms in the unit cell, information about the types of atoms and about the symmetry of the unit cell. Furthermore, matrix elements of the exchange-correlation potential have to be provided, since they are subtracted later-on from the matrix elements of the GW self-energy (cf. eq. (2.96)). Last but not least, the radial functions and the plane-wave cutoff of the LAPW basis have to be given. They are used to construct the MPB as described in section 3.1.4. Finally, information about the  $\mathbf{k}$  point mesh namely the number of points along the  $x$ ,  $y$  and  $z$  direction have to be specified. The density-functional input must have been calculated on the same mesh of  $\mathbf{k}$  points.

In the first step, the Coulomb matrix in MPB representation

$$v_{IJ}(\mathbf{k}) = \langle M_I^k | v | M_J^k \rangle = \iint \frac{M_I^{k*}(\mathbf{r}) M_J^k(\mathbf{r}')}{|\mathbf{r} - \mathbf{r}'|} d^3r d^3r' \quad (3.31)$$

is calculated. Details on the algorithm can be found in ref. [22]. For the next step, the GW self-energy  $\Sigma^{GW}$  is divided into an exchange-only and a correlation part according to eq. (2.85). Expectation values of the distinct contributions  $\Sigma_x^{GW}$  and  $\Sigma_c^{GW}(\omega)$  with respect to the KS wave functions  $\varphi_{n\mathbf{k}}^\sigma(\mathbf{r})$  are then calculated in different parts of the program.

It was already mentioned in section 2.3.3 that the expectation value of  $\Sigma_x^{GW}$  is the well-known Hartree-Fock exchange term, which can be calculated for the  $n$ -th band at the Bloch vector  $\mathbf{q}$  according to

$$\langle \varphi_{n\mathbf{q}}^\sigma | \Sigma_x^\sigma | \varphi_{n\mathbf{q}}^\sigma \rangle = - \sum_{\mathbf{k}} \sum_{n'} \sum_{IJ} v_{IJ}(\mathbf{k}) \langle \varphi_{n'+\mathbf{q}+\mathbf{k}}^\sigma | \varphi_{n\mathbf{q}}^\sigma \tilde{M}_I^k \rangle \langle \tilde{M}_J^k \varphi_{n\mathbf{q}}^\sigma | \varphi_{n'+\mathbf{q}+\mathbf{k}}^\sigma \rangle \quad (3.32)$$

with the projections

$$\langle \tilde{M}_J^k \varphi_{n\mathbf{q}}^\sigma | \varphi_{n'+\mathbf{q}+\mathbf{k}}^\sigma \rangle = \int \tilde{M}_I^{k*}(\mathbf{r}) \varphi_{n\mathbf{q}}^{\sigma*}(\mathbf{r}) \varphi_{n'+\mathbf{q}+\mathbf{k}}^\sigma(\mathbf{r}) d^3r. \quad (3.33)$$

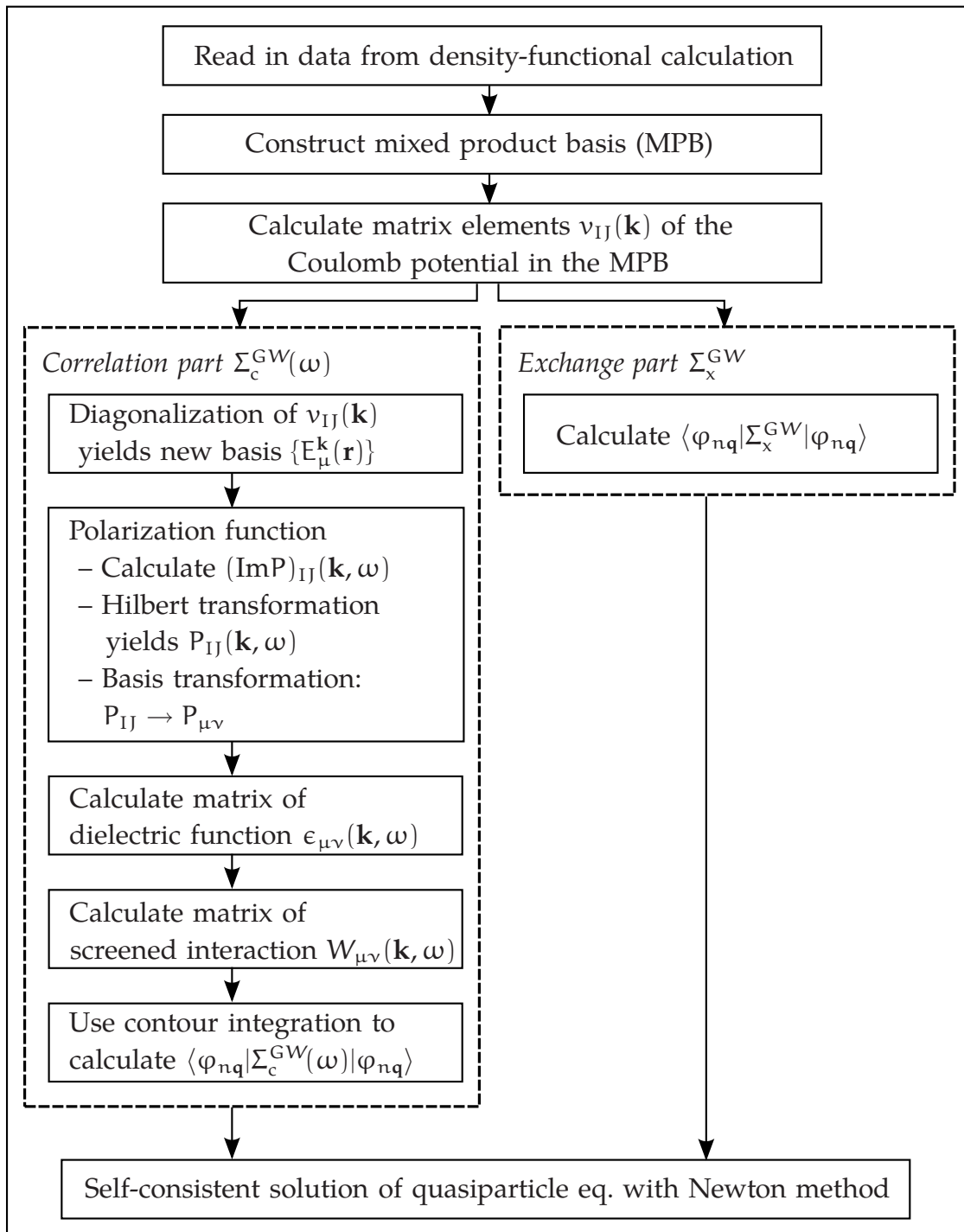


**Figure 3.3.:** Flow chart of a GW calculation carried out with the computer code SPEX.

The first sum on the left-hand side of eq. (3.32) runs over all  $\mathbf{k}$  points in the whole Brillouin zone (BZ), whereas the second sum over the occupied states comprises the states in the valence-band region as well as the core states, which can be treated as dispersionless bands. Using a formalism derived by Dagens and Perrot [97], the summation over the core states can thus be simplified considerably. A scheme for the efficient calculation of the non-local Fock exchange potential can be found in the article by Betzinger *et al.* [85].

The first step to obtain the correlation part of the GW self-energy is to calculate the polarization function which is given in MPB representation by

$$P_{IJ}(\mathbf{k}, \omega) = \sum_{\sigma} \sum_{\mathbf{q}} \sum_{\substack{\text{occ} \\ n}} \sum_{\substack{\text{unocc} \\ n'}} \langle \tilde{M}_I^{\mathbf{k}} \varphi_{n\mathbf{q}}^{\sigma} | \varphi_{n'\mathbf{q}+\mathbf{k}}^{\sigma} \rangle \langle \varphi_{n'\mathbf{q}+\mathbf{k}}^{\sigma} | \varphi_{n\mathbf{q}}^{\sigma} \tilde{M}_J^{\mathbf{k}} \rangle \times \left( \frac{1}{\omega + \epsilon_{n\mathbf{q}}^{\sigma} - \epsilon_{n'\mathbf{q}+\mathbf{k}}^{\sigma} + i\eta} - \frac{1}{\omega - \epsilon_{n\mathbf{q}}^{\sigma} + \epsilon_{n'\mathbf{q}+\mathbf{k}}^{\sigma} - i\eta} \right). \quad (3.34)$$

Here, the projections eq. (3.33) were used again and the energies  $\epsilon_{n\mathbf{q}}^{\sigma}$  and  $\epsilon_{n'\mathbf{q}+\mathbf{k}}^{\sigma}$  are the KS eigenvalues from a prior density-functional calculation. The sum over the BZ in the above expression is difficult to evaluate due to the rational expression in the brackets. It is more convenient to first calculate the spectral function  $S_{IJ}(\mathbf{k}, \omega)$  given by

$$S_{IJ}(\mathbf{k}, \omega) = \sum_{\sigma} \sum_{\mathbf{q}} \sum_{\substack{\text{occ} \\ n}} \sum_{\substack{\text{unocc} \\ n'}} \langle \tilde{M}_I^{\mathbf{k}} \varphi_{n\mathbf{q}}^{\sigma} | \varphi_{n'\mathbf{q}+\mathbf{k}}^{\sigma} \rangle \langle \varphi_{n'\mathbf{q}+\mathbf{k}}^{\sigma} | \varphi_{n\mathbf{q}}^{\sigma} \tilde{M}_J^{\mathbf{k}} \rangle \times [\delta(\omega + \epsilon_{n\mathbf{q}}^{\sigma} - \epsilon_{n'\mathbf{q}+\mathbf{k}}^{\sigma}) - \delta(\omega - \epsilon_{n\mathbf{q}}^{\sigma} + \epsilon_{n'\mathbf{q}+\mathbf{k}}^{\sigma})] = -\frac{1}{\pi} (\text{Im}P)_{IJ}(\mathbf{k}, \omega) \text{sgn}(\omega), \quad (3.35)$$

which can be related to the imaginary part of the polarization function denoted  $(\text{Im}P)_{IJ}(\mathbf{k}, \omega)$  if expression (3.34) for the polarization function is decomposed into the Cauchy principal value  $\mathcal{P}$  and a delta function according to

$$\frac{1}{x \pm i\eta} = \mathcal{P} \left( \frac{1}{x} \right) \mp i\pi\delta(x). \quad (3.36)$$

The full polarization function for all frequencies  $\omega \in \mathbb{C}$  is then accessible via a Hilbert transformation

$$P_{IJ}(\mathbf{k}, \omega) = \mathcal{P} \int_{-\infty}^{\infty} \frac{S_{IJ}(\mathbf{k}, \omega')}{\omega - \omega' + \text{sgn}(\omega)i\eta} d\omega'. \quad (3.37)$$

In practice, the calculation of the spectral function has to be converged with respect to the number of unoccupied states. Likewise, the number of frequencies  $\omega'$  and  $\omega$  used in the Hilbert transformation and for the representation of

the polarization function, respectively, enter as convergence parameters in each GW calculation. Both frequency meshes are dense for frequencies close to zero, since the frequency-dependent quantities exhibit more structure in this region. Furthermore, the frequencies  $\omega$  are chosen along the imaginary axis, whenever this is possible, since the frequency-dependent quantities show a smooth behavior there and can therefore be sampled with typically 10 or even less than 10 frequency mesh points.

In the next two steps, the polarization function is used to calculate the dielectric function eq. (2.79) which is then inverted to obtain the screened interaction according to eq. (2.80). Equations (2.79) and (2.80) become matrix equations in the MPB representation. However, they can be easily calculated, if a representation in terms of the eigenstates  $\{E_\mu^k(\mathbf{r})\}$  of the Coulomb matrix is used. The basis transformation  $\{M_I^k(\mathbf{r})\} \rightarrow \{E_\mu^k(\mathbf{r})\}$  involves no additional approximation. Furthermore, the new normalized basis functions are necessarily orthogonal and no biorthogonal set has to be constructed. In this new basis the matrix equations become simple products

$$\epsilon_{\mu\nu}(\mathbf{k}, \omega) = \delta_{\mu\nu} - \sqrt{v_\mu(\mathbf{k})} P_{\mu\nu}(\mathbf{k}, \omega) \sqrt{v_\nu(\mathbf{k})} \quad (3.38)$$

$$W_{\mu\nu}(\mathbf{k}, \omega) = \sqrt{v_\mu(\mathbf{k})} \epsilon_{\mu\nu}^{-1}(\mathbf{k}, \omega) \sqrt{v_\nu(\mathbf{k})} \quad (3.39)$$

with  $v_\mu(\mathbf{k})$  denoting the eigenvalue of the Coulomb matrix (3.31). It should be mentioned that the above definition of the matrix  $\epsilon_{\mu\nu}(\mathbf{k}, \omega)$  is a symmetrized version of the dielectric matrix. Although it is not identical with the matrix equation for the dielectric function obtained directly from the definition eq. (2.79) it can be shown that the screened interaction remains unchanged by the symmetrized formulation.

The above calculations can be further optimized, if the eigenvalues of  $v_\mu(\mathbf{k})$  are ordered according to decreasing size and those matrix elements of  $\epsilon_{\mu\nu}(\mathbf{k}, \omega)$  and  $W_{\mu\nu}(\mathbf{k}, \omega)$  are neglected, which have indices that are larger than a certain  $\mu$  defined by the threshold value  $v_{\min} = v_\mu(\mathbf{k})$ . If the eigenvalue  $v_\mu(\mathbf{k})$  is taken as a measure of the importance of the corresponding eigenfunction  $E_\mu^k(\mathbf{r})$  of  $v(\mathbf{r})$ , this procedure can be interpreted as a restriction to the dominant part of the electron-electron interaction. It will be demonstrated later on that calculations converge reasonably fast with the threshold value  $v_{\min}$ . Nevertheless, since the contributions from  $\Sigma_c^{GW}(\omega)$  are usually much smaller than those obtained from  $\Sigma_x^{GW}$  in calculations of the latter the full MPB is always employed.

With the correlation part of the screened interaction  $W_{\mu\nu}^c(\mathbf{k}, \omega') = W_{\mu\nu}(\mathbf{k}, \omega') - \delta_{\mu\nu} v_\mu(\mathbf{k})$  it is now possible to calculate matrix elements of the correlation part

of the GW self-energy

$$\begin{aligned}
& \langle \varphi_{n\mathbf{q}}^\sigma | \Sigma_c^\sigma(\omega) | \varphi_{n\mathbf{q}}^\sigma \rangle \\
&= \frac{i}{2\pi} \sum_{\mathbf{k}}^{\text{BZ}} \sum_{n'}^{\text{all}} \sum_{\mu\nu} \langle \varphi_{n'\mathbf{q}+\mathbf{k}}^\sigma | \varphi_{n\mathbf{q}}^\sigma E_\mu^{\mathbf{k}} \rangle \langle E_\nu^{\mathbf{k}} \varphi_{n\mathbf{q}}^\sigma | \varphi_{n'\mathbf{q}+\mathbf{k}}^\sigma \rangle \\
&\quad \times \int_{-\infty}^{\infty} d\omega' \frac{W_{\mu\nu}^c(\mathbf{k}, \omega')}{\omega + \omega' - \epsilon_{n'\mathbf{q}+\mathbf{k}}^\sigma + i\eta \operatorname{sgn}(\epsilon_{n'\mathbf{q}+\mathbf{k}}^\sigma)}.
\end{aligned} \tag{3.40}$$

Contrary to the corresponding expression, eq. (3.32), for the matrix elements of  $\Sigma_x^{\text{GW}}$ , eq. (3.40) comprises an explicit integration over frequencies, which has to be solved numerically. Since the integrand has a lot of structure along the real axis it is more convenient to integrate along the path depicted in figure 3.4 and to adapt the frequency argument of the integrand accordingly.

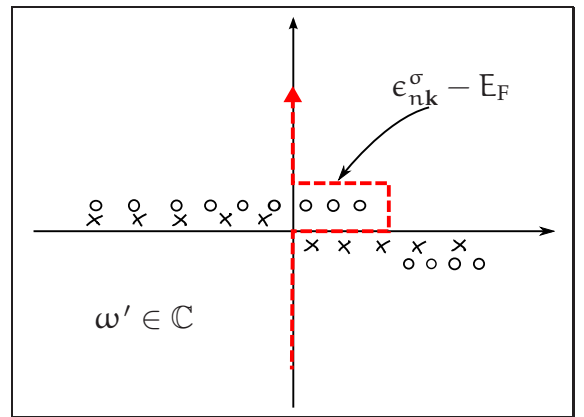
Finally, the matrix elements of  $\Sigma_c^{\text{GW}}(\omega)$  and  $\Sigma_x^{\text{GW}}$  are used to solve eq. (2.96) self-consistently to obtain the quasi-particle spectrum for a given material with a standard Newton method. Hence, no energy linearization is needed to solve eq. (2.96).

### 3.3.2. Construction of the $\mathbf{k}$ mesh

As described in the previous section, the quasi-particle spectrum is calculated for a given set of  $\mathbf{k}$  points. However, the expressions in the eqs. (3.32), (3.35) and (3.40) do not only depend on the Bloch vector  $\mathbf{k}$ . They comprise summations over other Bloch vectors  $\mathbf{q}$  as well as the vectors  $\mathbf{k} + \mathbf{q}$ , for which the KS wave functions and energies must be known, too. Only an equidistant  $\mathbf{k}$  mesh contains the vector  $\mathbf{k} + \mathbf{q}$  for each pair of vectors  $\mathbf{k}$  and  $\mathbf{q}$ . Hence, the  $\mathbf{k}$  mesh used in SPEX consisting of  $(N_x \times N_y \times N_z)$   $\mathbf{k}$  points is defined as

$$\left\{ \mathbf{k} = \frac{n_x}{N_x} \mathbf{b}_x + \frac{n_y}{N_y} \mathbf{b}_y + \frac{n_z}{N_z} \mathbf{b}_z, \quad n_i = 0, \dots, (N_i - 1) \right\} \tag{3.41}$$

**Figure 3.4:** The contour (red line) for the frequency integration in eq. (3.40) in the plane of complex frequencies. Crosses denote the position of the poles of  $W_{\mu\nu}^c(\mathbf{k}, \omega')$ . Circles correspond to the position of the zeros of the denominator of the integrand, i.e., poles of the Green function. The height of the rectangle is infinitesimally small, the width is determined by the poles of the Green function and the position of the Fermi energy  $E_F$ .



where  $N_i$  denotes the number of points in the  $i$ -th direction of space and the  $\mathbf{b}_i$  are the reciprocal lattice vectors.

The  $\mathbf{k}$  mesh used in a periodic bulk calculation with FLEUR to solve the KS equations (2.17) only contains  $\mathbf{k}$  vectors belonging to the irreducible BZ (IBZ), because the solution at any other  $\mathbf{k}' \notin \text{IBZ}$  is equivalent to a solution at a representative  $\mathbf{k}$  point contained in the IBZ. The points  $\mathbf{k}$  and  $\mathbf{k}'$  are related to the representative from the IBZ by a symmetry operation. The number of symmetry operations that leave the Hamiltonian in eq. (2.17) invariant determines the size of the IBZ, which comprises all  $\mathbf{k}$  vectors whose members are not pairwise related by such a symmetry operation.

Likewise, the SPEX code exploits time-reversal and spatial symmetries that leave the  $\mathbf{k}$  vectors defined in (3.41) unchanged to reduce the number of  $\mathbf{q}$  points used in the summations in eqs. (3.32), (3.35) and (3.40). These operations form a subset of all symmetry operations called the *little group* which, in turn, gives rise to a minimal set of non-equivalent  $\mathbf{q}$  points constituting the extended IBZ or EIBZ( $\mathbf{k}$ ) for short for a given  $\mathbf{k}$  vector. A reformulation of the three equations (3.32), (3.35) and (3.40) employing the symmetry operations from the little group can be found in ref. [20]. Furthermore, it is worth mentioning that symmetries can be exploited in a similar way to obtain the non-local exchange potential in a density-functional calculation with FLEUR employing hybrid functionals. Further details can be found in reference [85].

To determine the quasi-particle band structure, the quasi-particle energies along certain high-symmetry lines of the BZ have to be calculated. From the discussion above, it is obvious that  $\mathbf{k}$  points cannot arbitrarily be added to the  $\mathbf{k}$  mesh (3.41) used in SPEX. However, the code allows to add one additional  $\mathbf{k}$  point  $\mathbf{k}'$  in each calculation. This requires to calculate the KS wave functions and energies for all points  $\mathbf{k}' + \mathbf{k}$ . Therefore, the quasi-particle energy at  $\mathbf{k}'$  has to be determined in a separate GW calculation, if  $\mathbf{k}'$  is not contained in the mesh defined by (3.41).

### 3.3.3. Treatment of the $\Gamma$ point

The  $\Gamma$  point, i.e.  $\mathbf{k} = \mathbf{0}$ , is exceptional in the sense that the interaction potentials  $v_{IJ}(\mathbf{k})$ , eq. (3.31), and  $W_{\mu\nu}(\mathbf{k}, \omega)$ , eq. (3.39), diverge for  $\mathbf{k} \rightarrow \mathbf{0}$ . These terms for  $\mathbf{k} = \mathbf{0}$  yield an important contribution to the exchange and correlation self-energy, eqs. (3.32) and (3.40). Therefore, the  $\Gamma$  point is always part of the  $\mathbf{k}$  mesh in GW calculations with SPEX. A numerical treatment of the diverging contributions is possible, since the matrix elements in eqs. (3.32) and (3.40) have a finite value at  $\mathbf{k} = \mathbf{0}$ , because they are obtained via an integration over  $\mathbf{k}$ . Thus, the divergent terms ( $1/k^2$ ) integrate to finite volumes in three dimensions. To

evaluate eqs. (3.32) and (3.40) numerically the  $\mathbf{k}$  integration is replaced by a sum over  $\mathbf{k}$ . To enable an exact treatment of the terms containing the diverging matrix elements of  $v_{IJ}(\mathbf{k})$  and  $W_{\mu\nu}(\mathbf{k}, \omega)$  at  $\mathbf{k} = \mathbf{0}$ , the summation over  $\mathbf{k}$  is split into two parts. One part contains only non-divergent terms and can hence be treated numerically. The other part comprises all divergent terms but can be evaluated analytically. Thus, the all-electron accuracy is fully retained since no additional approximations like a projection onto plane waves is needed.

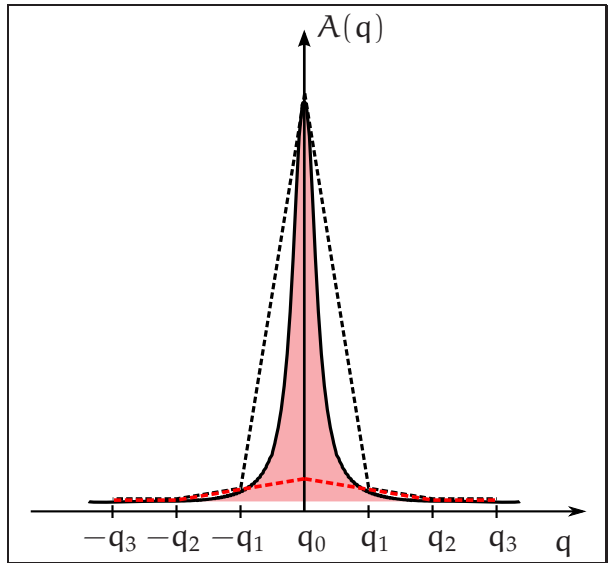
To calculate matrix elements of the correlation self-energy, eq. (3.40), the separation into parts with and without diverging matrix elements of  $W_{\mu\nu}(\mathbf{k}, \omega)$  is achieved by the basis transformation  $\{M_I^{\mathbf{k}}(\mathbf{r})\} \rightarrow \{E_{\mu}^{\mathbf{k}}(\mathbf{r})\}$  described in the previous section. In the resulting matrix expression  $W_{\mu\nu}(\mathbf{k}, \omega)$  for the screened interaction, the divergent contributions are confined to the head and wing elements of the matrix. These can be treated using  $\mathbf{k} \cdot \mathbf{p}$ -perturbation theory, ref. [98], which allows for a full treatment of the divergence. Details of the algorithm can be found in ref. [22].

To calculate matrix elements of the exchange self-energy, eq. (3.32), the matrix of the Coulomb interaction  $v_{IJ}(\mathbf{k})$  is separated according to ref. [85]

$$v_{IJ}(\mathbf{k}) = \frac{4\pi}{V} \frac{1}{k^2} \langle \tilde{M}_I^{\mathbf{k}} | e^{i\mathbf{k} \cdot \mathbf{r}} \rangle \langle e^{i\mathbf{k} \cdot \mathbf{r}} | \tilde{M}_J^{\mathbf{k}} \rangle + v'_{IJ}(\mathbf{k}). \quad (3.42)$$

The term  $v'_{IJ}(\mathbf{k})$  is finite at  $\mathbf{k} = \mathbf{0}$ . Inserted into eq. (3.32) it yields contributions to the summation over  $\mathbf{k}$ , which can be carried out numerically. The divergence of  $v_{IJ}(\mathbf{k})$  is restricted to the first term in (3.42) with the eigenfunction  $e^{i\mathbf{k} \cdot \mathbf{r}}/\sqrt{V}$ , whose  $\mathbf{k} \rightarrow \mathbf{0}$  limit can be represented exactly by the MPB by construction (cf. section 3.1.4). Therefore, it can be evaluated analytically employing again  $\mathbf{k} \cdot \mathbf{p}$ -perturbation theory. According to ref. [85]  $\mathbf{k} \cdot \mathbf{p}$ -perturbation theory

**Figure 3.5:** Typical form of the integrand in  $\langle \Sigma_x^{GW} \rangle_{\text{div}} = \int d^3q A(\mathbf{q})$  in one dimension close to  $\mathbf{q} = \mathbf{0}$ . The black curve shows the exact integrand, the dashed lines are different approximations to the true curve obtained by including (black) or neglecting (red) zeroth-order terms. Such terms originate from the products of  $1/k^2$  from the first term in (3.42) and the terms linear in  $\mathbf{k}$  in the expansion of the projections  $\langle e^{i\mathbf{k} \cdot \mathbf{r}} \varphi_{n\mathbf{q}}^{\sigma} | \varphi_{n'\mathbf{q}+\mathbf{k}}^{\sigma} \rangle / \sqrt{V}$  within  $\mathbf{k} \cdot \mathbf{p}$ -perturbation theory (see text for more details).



yields

$$\begin{aligned}\Phi_{n\mathbf{k}\mathbf{q}}^\sigma(\mathbf{r}) &= e^{-i\mathbf{k}\mathbf{r}}\varphi_{n\mathbf{q}+\mathbf{k}}^\sigma(\mathbf{r}) \\ &= \varphi_{n\mathbf{q}}^\sigma(\mathbf{r}) + \mathbf{k} \cdot \nabla_{\mathbf{k}}\Phi_{n\mathbf{k}\mathbf{q}}^\sigma(\mathbf{r}) \\ &\quad + \frac{1}{2}\mathbf{k}^T \cdot \nabla_{\mathbf{k}}\nabla_{\mathbf{k}}^T\Phi_{n\mathbf{k}\mathbf{q}}^\sigma(\mathbf{r}) \cdot \mathbf{k} + \mathcal{O}(k^3)\end{aligned}\tag{3.43}$$

with

$$\nabla_{\mathbf{k}}\Phi_{n\mathbf{k}\mathbf{q}}^\sigma(\mathbf{r}) = -i \sum_{n' \neq n} \frac{\langle \varphi_{n'\mathbf{q}}^\sigma | \nabla | \varphi_{n\mathbf{q}}^\sigma \rangle}{\epsilon_{n'\mathbf{q}}^\sigma - \epsilon_{n\mathbf{q}}^\sigma} \varphi_{n'\mathbf{q}}^\sigma(\mathbf{r}).\tag{3.44}$$

This is used to expand the projections  $\langle e^{i\mathbf{k} \cdot \mathbf{r}} \varphi_{n\mathbf{q}}^\sigma | \varphi_{n'\mathbf{q}+\mathbf{k}}^\sigma \rangle / \sqrt{V}$  which are then multiplied with  $(4\pi/V)(1/k^2)$  to yield contributions to the exchange self-energy. Due to the terms linear in  $\mathbf{k}$  in the above expansion the product of the projections with  $(1/k^2)$  will lead to terms of zeroth order in  $\mathbf{k}$ . To further analyze the effect of these zeroth-order corrections, the contributions to the exchange self-energy comprising the divergent parts of  $v_{IJ}(\mathbf{k})$  is formally written as  $\langle \Sigma_x^{\text{GW}} \rangle_{\text{div}} = \int d^3q A(\mathbf{q})$ . In figure 3.5, the integrand  $A(\mathbf{q})$  is depicted schematically in one dimension. The black curve shows the exact integrand and the red area below the curve should be integrated. The dashed lines are approximations to the integrand obtained numerically, if the true integrand is sampled on a  $q$ -point grid  $\{-q_3, \dots, q_3\}$ . The black dashed line contains corrections due to the zeroth-order term which were neglected in the calculations represented by the red dashed line. As can be seen from the graph, an integration over the area below the black dashed line would overestimate the area below the true curve whereas an integration over the area under the red line would underestimate it.

The size of the error made by neglecting zeroth-order contributions depends on the  $\mathbf{k}$ -point sampling of the IBZ and on the width of the peak. The latter is a material-dependent property (cf. discussion in ref. [20]). Hence, zeroth-order contributions improve the  $\mathbf{k}$ -point convergence for some materials whereas for others they can worsen the convergence. In general, for a reasonably converged  $\mathbf{k}$ -point sampling the contributions from  $\mathbf{k} \cdot \mathbf{p}$ -perturbation theory are small (typically  $< 0.1$  eV). In calculations of the quasi-particle band structure the contributions from  $\mathbf{k} \cdot \mathbf{p}$ -perturbation theory at the  $\Gamma$  point are completely neglected in this work, because they can lead to numerical instabilities as the energy denominator in (3.44) can become very small at certain  $\mathbf{k}$  points due to the occurrence of nearly degenerate bands.

### 3.3.4. The density of states in GW calculations

The density of states (DOS) is a very useful quantity, because it can be compared directly to spectra obtained from (inverse) photo-emission spectroscopy (PES).

This can be understood by looking at the definition of the total DOS  $D(\omega)$  in terms of the imaginary part of the many-body Green function given by

$$D(\omega) = -\text{sgn}(\omega - \epsilon_F) \frac{1}{\pi} \int d^3r \text{Im}(G(\mathbf{r}, \mathbf{r}; \omega)), \quad (3.45)$$

where  $\epsilon_F$  is the Fermi energy and the prefactor guarantees that  $D(\omega)$  is always positive. Inserting the Lehmann representation (2.60) for the Green function into the above equation leads to

$$D(\omega) = \sum_i \int d^3r |\psi_i^{N\pm 1}(\mathbf{r})|^2 \delta(\omega - \epsilon_i^{N\pm 1}). \quad (3.46)$$

Since the energies  $\epsilon_i^{N\pm 1}$  are the exact excitation energies of the electronic system, it is clear that  $D(\omega)$  is, in principle, identical to the spectrum seen in PES.

The results from a density-functional calculation can be used to approximate the photo-emission spectrum. Inserting the Kohn-Sham Green function (2.82) into eq. (3.45) yields the following expression for the DOS

$$D(\omega) = \sum_{n\sigma} \frac{1}{V_{\text{BZ}}} \int_{\text{BZ}} \underbrace{d^3r |\varphi_{n\mathbf{k}}^\sigma(\mathbf{r})|^2}_{=1} \delta(\omega - \epsilon_{n\mathbf{k}}^\sigma) d^3k, \quad (3.47)$$

where  $V_{\text{BZ}}$  is the volume of the BZ and  $\epsilon_{n\mathbf{k}}^\sigma$  and  $\varphi_{n\mathbf{k}}^\sigma(\mathbf{r})$  are the KS eigenvalues and wave function, respectively. Furthermore, a partial or projected DOS (pDOS) can be introduced. Employing the expansion of the KS wave functions in terms of the LAPW basis functions the spatial integration in (3.47) can be formally split into a contribution from the MT spheres and the interstitial region (IR)

$$\int d^3r |\varphi_{n\mathbf{k}}^\sigma(\mathbf{r})|^2 = \int_{\text{MT}} d^3r |\varphi_{n\mathbf{k}}^\sigma(\mathbf{r})|^2 + \int_{\text{IR}} d^3r |\varphi_{n\mathbf{k}}^\sigma(\mathbf{r})|^2. \quad (3.48)$$

Since the wave functions inside the MT sphere of atom  $a$  are expanded into spherical harmonics, they can be split into contributions with certain  $l$  character

$$\varphi_{n\mathbf{k}}^{a\sigma}(\mathbf{r}) = \sum_l \varphi_{nl\mathbf{k}}^{a\sigma}(\mathbf{r}). \quad (3.49)$$

The pDOS is then defined as

$$D_l^a(\omega) = \sum_{n\sigma} \frac{1}{V_{\text{BZ}}} \int_{\text{BZ}} \sum_l p_{nl\mathbf{k}}^{a\sigma} \delta(\omega - \epsilon_{n\mathbf{k}}^\sigma) d^3k \quad (3.50)$$

with  $p_{nl\mathbf{k}}^{a\sigma} = \int d^3r |\varphi_{nl\mathbf{k}}^{a\sigma}(\mathbf{r})|^2$ . Although  $D_l^a(\omega)$  cannot be measured directly in experiment it allows to analyze photo-emission spectra theoretically and helps to

better understand, which electronic states contribute to the spectrum in different energy regions.

The GW approximation yields an improved description of excitation energies. Hence, a GW calculation should also yield a better approximation of photo-emission spectra. According to the definition of the DOS, eq. (3.47), it should be calculated using the imaginary part of the GW Green function that could be in turn calculated by solving the Dyson equation (2.74). However, this is numerically expensive as the GW self-energy must be calculated at many different  $\mathbf{k}$  points to achieve a sufficient resolution in reciprocal space. To approximate the photo-emission spectrum obtained from a GW calculation the KS eigenvalues in eqs. (3.47) and (3.50) are therefore simply replaced by the real part of the quasi-particle energies thus neglecting the imaginary part of the GW self-energy corrections.

In SPEX, spatial symmetry operations are again exploited to carry out the integration over the BZ in eqs. (3.47) and (3.50) as weighted sum over  $\mathbf{k}$  points in the IBZ. This sum can be evaluated either by the tetrahedron method that interpolates between the energies  $\epsilon_{\mathbf{n}\mathbf{k}}^\sigma$  or by replacing the delta functions by a Gauss distribution function for each energy, which can then be summed over.

### 3.3.5. The dielectric function within the RPA

The effect of an external perturbation on the N-electron system of a solid, for example originating from the oscillating electric field of a beam of light in optical absorption spectroscopy, can be described by an external potential  $\phi_{\text{ext}}(\mathbf{r}, t)$ , which, in general, is time-dependent<sup>2</sup>. Assuming that  $\phi_{\text{ext}}(\mathbf{r}, t)$  can be separated according to

$$\phi_{\text{ext}}(\mathbf{r}, t) = \phi_{\text{ext}}^{(0)}(\mathbf{r}) + \phi_{\text{ext}}^{(1)}(\mathbf{r}, t) \quad (3.51)$$

and the second term is small and varies slowly, linear-response theory can be used to describe the dynamics of the N-electron system. Thus, the density is expanded in orders of  $\phi_{\text{ext}}^{(1)}(\mathbf{r}, t)$ , i.e.  $n(\mathbf{r}, t) = n^{(0)}(\mathbf{r}) + n^{(1)}(\mathbf{r}, t) + \dots$ , where the first-order correction is given by

$$n^{(1)}(\mathbf{r}_1, t_1) = \iint R(\mathbf{r}_1, \mathbf{r}_2; t_1 - t_2) \phi_{\text{ext}}^{(1)}(\mathbf{r}_2, t_2) d^3r_2 dt_2 \quad (3.52)$$

Here,  $R(\mathbf{r}_1, \mathbf{r}_2; t_1 - t_2)$  is the response function

$$R(\mathbf{r}_1, \mathbf{r}_2; t_1 - t_2) = \left. \frac{\delta n(\mathbf{r}_1, t_1)}{\delta \phi_{\text{ext}}(\mathbf{r}_2, t_2)} \right|_{\phi_{\text{ext}}(\mathbf{r}_2, t_2) = \phi_{\text{ext}}^{(0)}(\mathbf{r}_2)} \quad (3.53)$$

<sup>2</sup>Throughout this section, the external potential is denoted by  $\phi$  in accordance with the notation introduced in appendix A.1.

introduced in (A.14). Causality requires  $R(\mathbf{r}_1, \mathbf{r}_2; t_1 - t_2) = 0$  for  $t_1 < t_2$ , because the density cannot be influenced by later variations of the potential.

Changes in the density induced by the external potential lead to a polarization of the electronic system of the solid. Consequently, the total potential  $\phi_{\text{tot}}(\mathbf{r}, t)$  of the system now becomes a sum of the external potential and a potential  $\phi_{\text{ind}}(\mathbf{r}, t)$  originating from the induced changes in the density

$$\phi_{\text{tot}}(\mathbf{r}, t) = \phi_{\text{ext}}(\mathbf{r}, t) + \phi_{\text{ind}}(\mathbf{r}, t). \quad (3.54)$$

In linear-response theory, the quantity relating the total potential to the external potential is the microscopic dielectric function  $\epsilon(\mathbf{r}_1, \mathbf{r}_2; t_1 - t_2)$

$$\phi_{\text{tot}}(\mathbf{r}_1, t_1) = \iint \epsilon^{-1}(\mathbf{r}_1, \mathbf{r}_2; t_1 - t_2) \phi_{\text{ext}}(\mathbf{r}_2, t_2) d^3r_2 dt_2. \quad (3.55)$$

As demonstrated in appendix A.1, eq. (A.17), the microscopic dielectric function and the response function  $R(\mathbf{r}_1, \mathbf{r}_2; t_1 - t_2)$  are related

$$\epsilon^{-1}(\mathbf{r}_1, \mathbf{r}_2; t_1 - t_2) = \delta(\mathbf{r}_1 - \mathbf{r}_2) \delta(t_1 - t_2) + \int v(\mathbf{r}_1, \mathbf{r}_3) R(\mathbf{r}_3, \mathbf{r}_2; t_1 - t_2) d^3r_3 \quad (3.56)$$

where  $v(\mathbf{r}_1, \mathbf{r}_2) = 1/|\mathbf{r}_1 - \mathbf{r}_2|$  is the Coulomb potential. In frequency space, the response function can be expressed in terms of  $v$  and the polarization function  $P$

$$\begin{aligned} R(\mathbf{r}_1, \mathbf{r}_2; \omega) &= P(\mathbf{r}_1, \mathbf{r}_2; \omega) \\ &+ \iint P(\mathbf{r}_1, \mathbf{r}_3; \omega) v(\mathbf{r}_3, \mathbf{r}_4) R(\mathbf{r}_4, \mathbf{r}_2; \omega) d^3r_3 d^3r_4. \end{aligned} \quad (3.57)$$

according to eq. (A.15).

Here, the polarization function entering eq. (3.57) is approximated by eq. (2.83). As explained in section 2.3.3 of chapter 2, equation (2.83) is obtained from the definition of the RPA polarization function, eq. (2.78), if the Hartree Green function  $G_H$  is replaced by the KS Green function  $G_0$  defined in (2.82). Adapting the symbolical writing introduced in eq. (2.75), the polarization function becomes  $P = -iG_0G_0$  and the response function can be written as

$$R \stackrel{\text{RPA}}{=} -iG_0G_0 - (i)^2G_0G_0vG_0G_0 - (i)^3G_0G_0vG_0G_0vG_0G_0 + \dots \quad (3.58)$$

Hence, the full response function is approximated by a series of electron-hole pairs represented by the products of two KS Green functions in the above expression that interact with other electron-hole pairs via the Coulomb interaction  $v$ . In particular, the electron and the hole composing a single pair do not interact with each other. These kind of interactions could be taken into account via a vertex correction in calculations for the polarization functions according to

eq. (A.24). However, this is beyond the scope of the RPA where the vertex is set to one. Consequently, excitonic effects, i.e. bonding between an electron and a hole, are not included in the response function calculated within the RPA.

The microscopic dielectric function  $\epsilon$  is related to the macroscopic dielectric function  $\epsilon_M$ , which can be measured in absorption spectroscopy. A Fourier transform of (3.56) yields

$$\epsilon_{\mathbf{G}\mathbf{G}'}^{-1}(\mathbf{k}, \omega) = \delta_{\mathbf{G}\mathbf{G}'} + v_{\mathbf{G}}(\mathbf{k}) R_{\mathbf{G}\mathbf{G}'}(\mathbf{k}, \omega), \quad (3.59)$$

where  $\mathbf{G}$  is a reciprocal lattice vector while  $\mathbf{k}$  is a vector in the first BZ. From this expression,  $\epsilon_M(\omega)$  is obtained according to [99, 100, 101] by

$$\epsilon_M(\omega) = \lim_{\mathbf{k} \rightarrow 0} \frac{1}{[\epsilon_{\mathbf{G}\mathbf{G}'}^{-1}(\mathbf{k}, \omega)]_{\mathbf{G}\mathbf{G}'=0}}. \quad (3.60)$$

An external perturbing field inducing fluctuations on the scale of the inter-atomic distances in the material may give rise to internal density variations and thus microscopic internal fields. If these kind of density variations occur, the polarization function depends explicitly on the positions  $\mathbf{r}$  and  $\mathbf{r}'$  which leads to non-zero, off-diagonal matrix elements of  $P$  in reciprocal space. The polarization function enters eq. (3.57) for the response function which, in turn, yields the inverse of the microscopic dielectric function according to eq. (3.56). Hence, the inverse of  $\epsilon$  is also not diagonal in reciprocal space and all matrix elements contribute to  $\epsilon_M$  in (3.60). This is called local field effect (LFE). The LFE can be readily taken into account in the RPA-based calculations for  $\epsilon_M$  and is included in all calculations discussed later-on.

In SPEX, the microscopy dielectric function is calculated in matrix form according to eq. (3.38) in a representation of the eigenstates of the Coulomb matrix  $v_{IJ}(\mathbf{k})$ , eq. (3.31). Since the first eigenvector of  $v_{IJ}(\mathbf{k})$  corresponds to the projection of  $e^{i\mathbf{k} \cdot \mathbf{r}}/\sqrt{V}$  onto the biorthogonal MPB, the head element of the inverse of the dielectric matrix is equal to  $[\epsilon_{\mathbf{G}\mathbf{G}'}^{-1}(\mathbf{q}, \omega)]_{\mathbf{G}\mathbf{G}'=0}$ . Inserting the head element of the inverse of the dielectric matrix into eq. (3.60) thus leads to an estimate for  $\epsilon_M(\omega)$  within RPA.



## CHAPTER 4

# PEROVSKITES – A SHORT INTRODUCTION

The German mineralogist Gustav Rose was the first to describe the mineral with the stoichiometric composition  $\text{CaTiO}_3$  that he had discovered in the Ural Mountains in 1839 [102]. Rose gave this mineral the name "Perovskite" after the Russian politician and mineralogist L. A. Perovski. Today, the name "Perovskite" not only denotes this mineral but also the structural family of compounds with the stoichiometric composition  $\text{ABO}_3$ , where A and B are typically metals and O is oxygen. In particular, B usually stands for a transition metal, which is "an element whose atom has an incomplete d sub-shell, or which can give rise to cations with an incomplete d sub-shell" according to the definition of the International Union of Pure and Applied Chemistry (IUPAC). Consequently, the electronic d states of B play a crucial role in the formation of the valence band and the low-lying conduction-band states of perovskites.

The purpose of this chapter is twofold: the first section delivers some insight into the crystal structure of perovskites focusing in particular on the room-temperature (RT) crystal structures of the materials examined in this work. The structural composition is important because it strongly influences the formation of the electronic structure. This interplay between the crystal and the electronic structure together with various additional aspects of the latter is discussed in the remaining sections of this chapter in the context of model approaches. This will be helpful to better understand and interpret the results of calculations from first principles presented in the following chapters. Parts of this chapter were inspired by the book of Huheey [103] and the review article by Imada, Fujimori and Tokura [104].

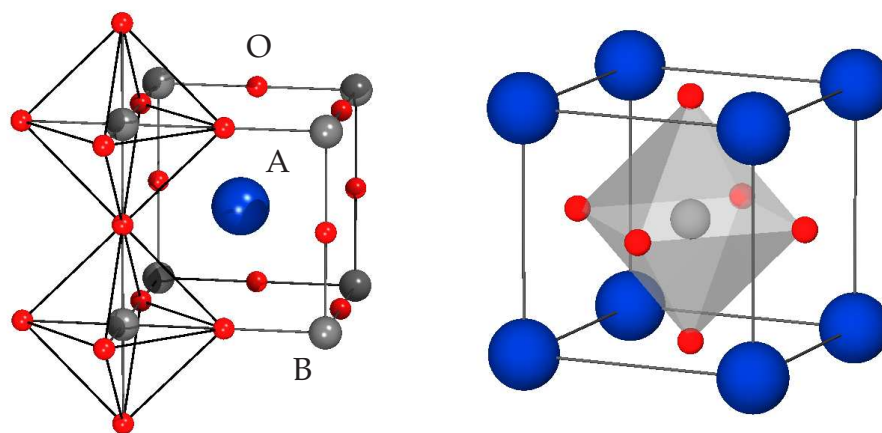


**Figure 4.1.:** Two representations of the crystal structure of the cubic perovskite composition  $ABO_3$ . The *left* picture emphasizes the formation of strings of  $BO_6$  octahedra extending infinitely in three dimensions. The *right* picture shows the unit cell used for electronic structure calculations in this work.

## 4.1. Crystal structure

The crystal structures of many  $ABO_3$  compositions were first described in the pioneering work of Goldschmidt and co-workers, who made and studied a large number of the first synthetic perovskites in 1924-26 [105]. They worked with a purely ionic model of hard spheres which will be used in this section as well. Based on this model, the cubic crystal phase of a perovskite in the following called ideal perovskite structure can be described by a very simple arrangement of ions illustrated in figure 4.1. The cubic structure is typified not by  $CaTiO_3$  for reasons discussed later on in this section but by the crystal structure of  $SrTiO_3$  at room temperature (RT). In  $SrTiO_3$  the  $Ti^{4+}$  ions (the B cations) are located at the corners, the  $Sr^{2+}$  ions (the A cations) at the center of a perfect cube. Oxygen anions are placed at the center of the twelve cube edges, giving corner-shared strings of  $TiO_6$  octahedra, which extend infinitely in three dimensions. The  $TiO_6$  octahedra are perfect with  $90^\circ$  angles and six equal Ti-O bonds, whereas a  $Sr^{2+}$  ion is surrounded by twelve equidistant oxygen anions. The crystal lattice has the space group  $Pm\bar{3}m$ .

Goldschmidt's empirical studies of the crystal structures of perovskites played a key role in formulating some very fundamental principles about the formation

of ionic crystals:

- The radius of the ions is fundamental to the structure.
- The radius ratio  $R_{\text{cation}}/R_{\text{anion}}$  determines the coordination number of the cation (= the polyhedron formed).
- The packing of polyhedra follows simple rules (later codified by Pauling [106]).

If ions are considered to be rigid spheres, the crystal structure of  $\text{SrTiO}_3$  can also be characterized as cubic close-packed layers of  $\text{Sr}^{2+}$  and oxygen ions along the cubic [111] direction and some of the resulting octahedral holes are occupied by  $\text{Ti}^{4+}$  ions. Goldschmidt then realized that the ionic radii  $R_A$ ,  $R_B$ , and  $R_O$  in the  $\text{ABO}_3$  composition of the ideal perovskite structure are related by symmetry. Based on this observation he introduced the concept of the tolerance factor  $t$  defined by

$$t = \frac{R_A + R_O}{\sqrt{2} \cdot (R_B + R_O)}, \quad (4.1)$$

where  $t = 1$  for the ideal perovskite structure in the ionic model. Based on his measurements of ionic radii Goldschmidt predicted that  $\text{ABO}_3$  compositions with  $0.8 < t \leq 1.0$  crystallize in the ideal perovskite structure, whereas perovskites with a smaller tolerance factor form orthorhombic or rhombohedral lattices.

Despite the simple form of the tolerance factor, the assumption of Goldsmith cannot be easily applied to the perovskites investigated in this work. First of all, Goldschmidt did not determine the ionic radii of all metal cations contained in the  $\text{ABO}_3$  compositions examined in this work. On the other hand, the ionic radii obtained by Shannon [118], which are considered the most accurate today, are determined differently than those by Goldsmith. The details of the two definitions of the ionic radii should not concern us here. However, it is remarkable that all  $\text{ABO}_3$  compositions investigated here, which do acquire the ideal perovskite structure at room temperature (RT), have a tol-

Material	tolerance factor	RT crystal structure.
$\text{CaTiO}_3$	0.96	orthorhombic [107]
$\text{SrTiO}_3$	1.00	cubic [108]
$\text{BaTiO}_3$	1.06	tetragonal [109]
$\text{BaZrO}_3$	1.00	cubic [110]
$\text{BaHfO}_3$	1.00	cubic [111]
$\text{PbTiO}_3$	1.01	tetragonal [112]
$\text{PbZrO}_3$	0.96	orthorhombic [113]
$\text{PbHfO}_3$	0.96	orthorhombic [114]
$\text{LaCrO}_3$	0.98	orthorhombic [115]
$\text{LaMnO}_3$	0.96	orthorhombic [116]
$\text{LaFeO}_3$	1.00	orthorhombic [117]

**Table 4.1.:** List of tolerance factors  $t$  calculated with the ionic radii after Shannon [118] and the crystal structure of the perovskite transition-metal oxides (TMOs) investigated in this work determined experimentally at room temperature (RT).

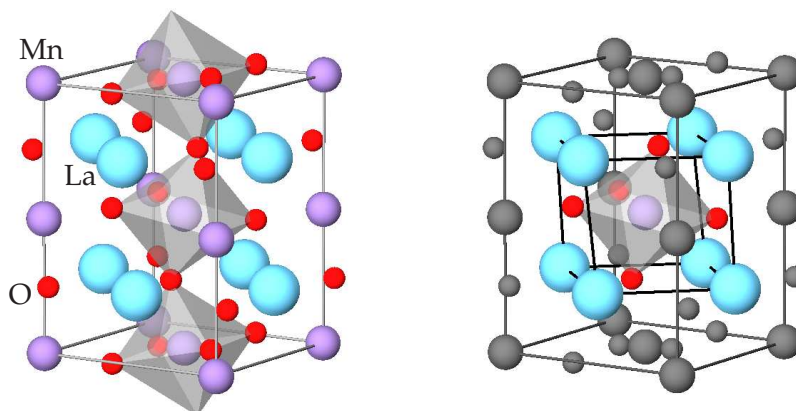
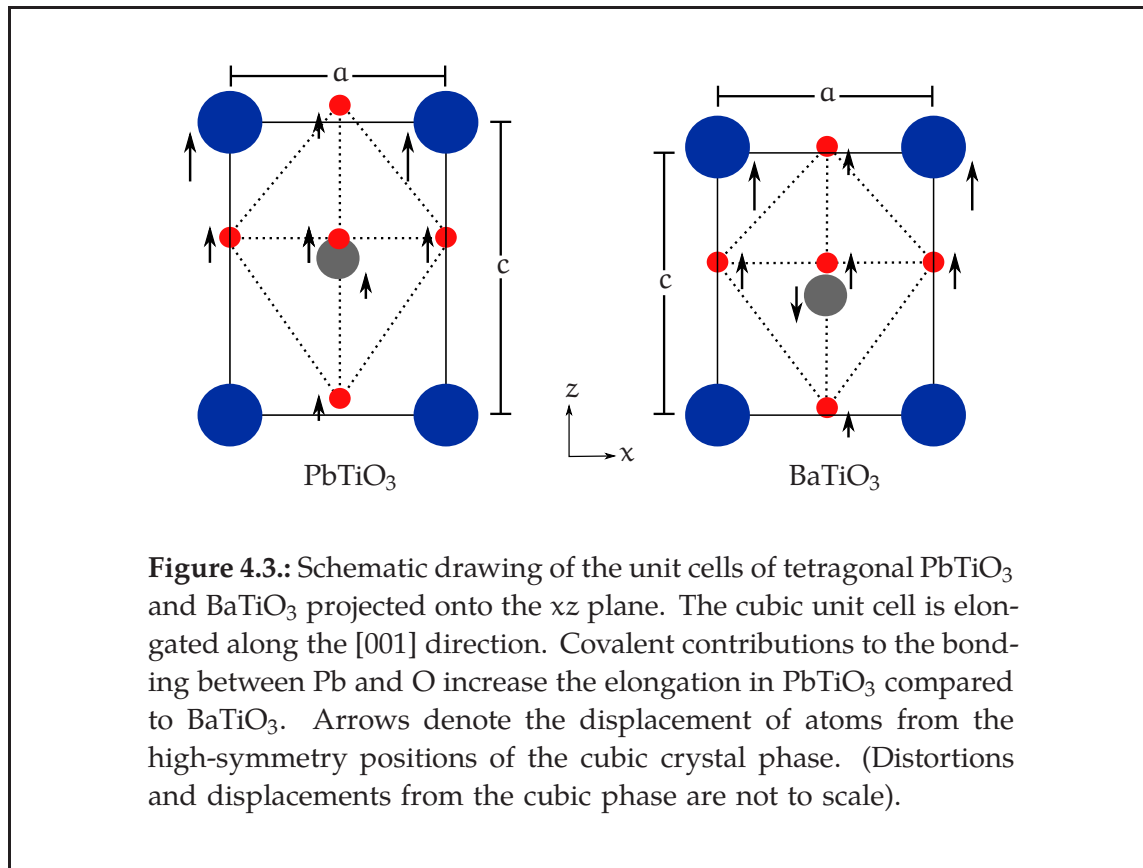


**Figure 4.2.:** Unit cell of LaMnO<sub>3</sub> in the orthorhombic crystal phase. Atomic positions were determined experimentally at RT [116]. The picture on the *left* shows the tilting and rotation of the oxygen octahedra. On the *right*, the cubic unit cell is indicated to clarify the displacement of the La atoms (A cations) from the high-symmetry position in the cubic phase.

erance factor of exactly 1.00 when calculated using the ionic radii according to Shannon. Furthermore, all perovskites listed in table 4.1 that do not crystallize in the ideal perovskite structure at RT have a tolerance factor  $t < 1.00$  in agreement with the trend observed by Goldschmidt. The only exceptions are LaFeO<sub>3</sub>, BaTiO<sub>3</sub>, and PbTiO<sub>3</sub>. The reason why the crystal structure of LaFeO<sub>3</sub> is not predicted correctly is due to the neglect of covalent contributions in the purely ionic model of Goldschmidt. The formation of the RT crystal structure of BaTiO<sub>3</sub> and PbTiO<sub>3</sub> is discussed in a later part of this section.

The formation of the orthorhombic crystal structure of the perovskites listed in table 4.1 can be at least explained qualitatively within the simple ionic model. With decreasing A-cation size a point will be reached, where the cations will be too small to remain in contact with the oxygen anions in the cubic close-packed perovskite structure. One possibility to bring at least some A cations into direct contact with the oxygen anions is the tilting of the BO<sub>6</sub> octahedra and an associated displacement of the A cation. This is exactly the situation observed in the perovskite mineral CaTiO<sub>3</sub>, where a tilt of the TiO<sub>6</sub> octahedral along the b and c axes of the cubic unit cell of the ideal perovskite structure leads to the formation of a lattice with an orthorhombic unit cell shown in figure



4.2. Tilting along all axes would reduce the symmetry even further resulting in a rhombohedral crystal structure, which is observed, e.g., in  $\text{BaTiO}_3$  below a critical temperature of 183 K [109].

To understand the formation of the tetragonal crystal structure of  $\text{BaTiO}_3$  and  $\text{PbTiO}_3$  one has to go beyond the simple ionic model and consider vibronic interactions, i.e., the coupling of electronic and nuclear motions of *pseudo-Jahn-Teller* type. A thorough discussion of the various Jahn-Teller effects is beyond the scope of this work. The discussion will therefore be restricted to a characterization of the effects determining the crystal structure of the two compounds  $\text{BaTiO}_3$  and  $\text{PbTiO}_3$ . In his work, Bersuker [119] proved that the presence of two electronic states of opposite parity close in energy of which one is filled and the other is not leads to a lattice instability favoring atomic displacement. The resulting crystal structures of  $\text{BaTiO}_3$  and  $\text{PbTiO}_3$  are drawn schematically in figure 4.3. The cubic unit cells are elongated along the  $[001]$  direction and the small arrows indicate additional shifts of the oxygen anions and the  $\text{Ti}^{4+}$  ions away from the high-symmetry positions of the ideal perovskite structure. The loss of inversion symmetry causes a spontaneous crystal polarization. Hence, the two compounds become ferroelectric. Apart from the role of the pseudo-Jahn-Teller effect, Cohen

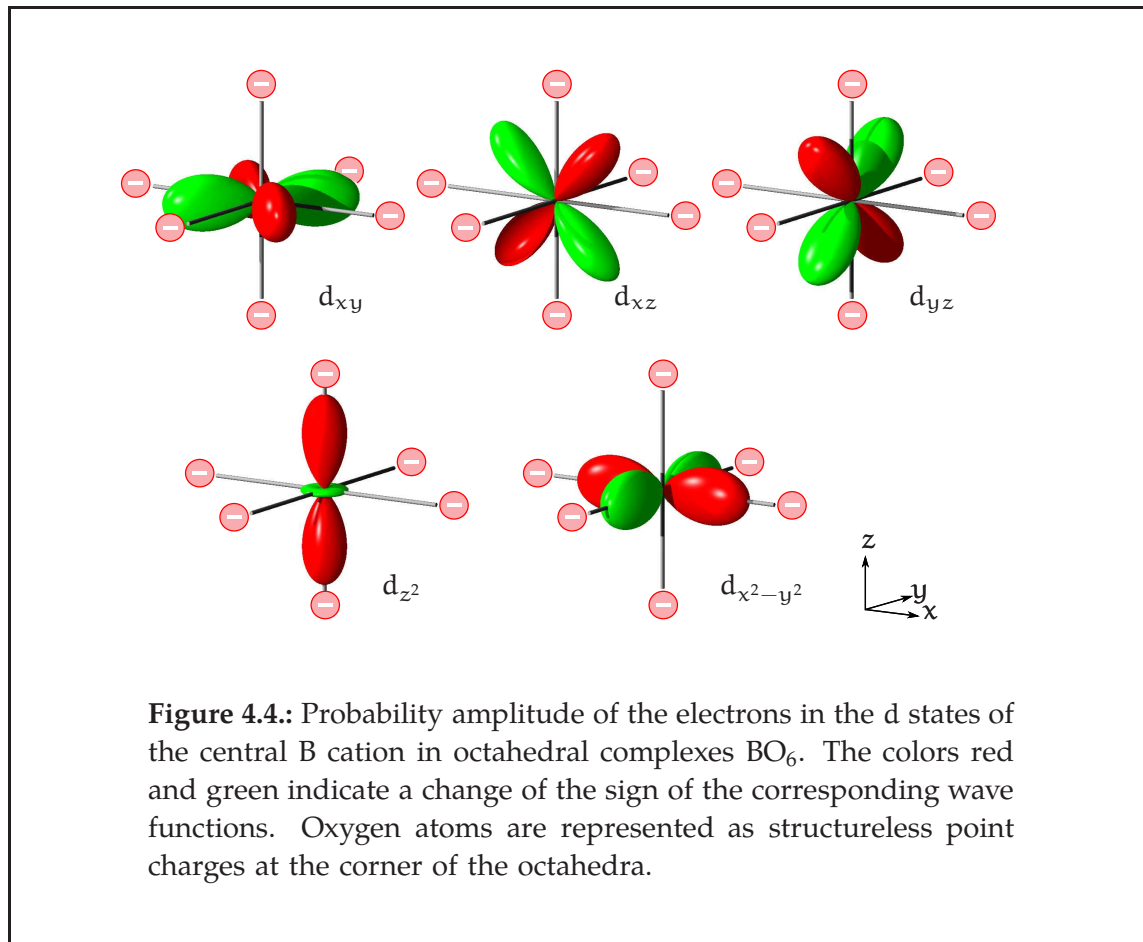
[120] emphasized the importance of the hybridization between the Ti 3d and the oxygen 2p states as well as hybridization between oxygen and lead states in  $\text{PbTiO}_3$  to stabilize the ferroelectric crystal structures of both compounds.

Finally, it should be mentioned that the tetragonal as well as the orthorhombic phases of the crystal structures of the perovskites in table 4.1 represent only small deviations from the crystal structure of the ideal perovskite. In particular, the coordination of the A and B cations is left unchanged as can be seen in figure 4.2 for the orthorhombic structure of  $\text{LaMnO}_3$ . Therefore, these non-cubic phases of the crystal structure are often called distorted perovskite structures. In the next sections, it will be discussed how the octahedral coordination of the transition metal B cation to the surrounding  $\text{O}^{2-}$  ions affects the the electronic d states of the B cation.

## 4.2. Perovskites and crystal field theory

The origins of crystal field theory (CFT) date back to the work of Bethe from 1929 [121] continued by Van Vleck in the 1930s [122, 123]. CFT is a model that describes the electronic structure of coordination complexes. These are structures consisting of a central atom or ion (usually metallic), bonded to a surrounding array of molecules or anions called ligands. In CFT, the ligands are approximated as structureless point charges whereas the central atom is described quantum-mechanically. Consequently, the ligands are considered to interact with the nucleus of the central atom solely via the electrostatic interaction. On the other hand, the electrons residing in the orbitals of the central atom will feel the repulsion from the electrostatic field, the crystal field, generated by the ligands. In the perovskites the transition metal B cation together with the oxygen  $\text{O}^{2-}$  ions form the octahedral  $\text{BO}_6$  coordination complex as shown in figure 4.1. The results of the quantum-mechanical description of the d-electronic states of the B cation as obtained from CFT will be outlined in this section.

Figure 4.4 shows the angular-dependent parts of the probability amplitude of the five 3d states of a transition metal cation. The circles symbolize the structureless point charges representing the oxygen ions of the  $\text{BO}_6$  complex in CFT. Obviously, the repulsion between these charges and an electron residing in the  $d_{z^2}$  or  $d_{x^2-y^2}$  states will be larger than for an electron in the other three states  $d_{xy}$ ,  $d_{xz}$ , and  $d_{yz}$ , because the corresponding probability amplitude of the first two states point into the direction of the position of the  $\text{O}^{2-}$  ions and those of the latter three extend into the space between them. The effect on the energy levels of the corresponding d states is illustrated in figure 4.5 and can be described in two steps: first, the five states, which are degenerate in the atom as shown in 4.5 (a), are destabilized in the electrostatic field of the ligands, figure 4.5 (b). The



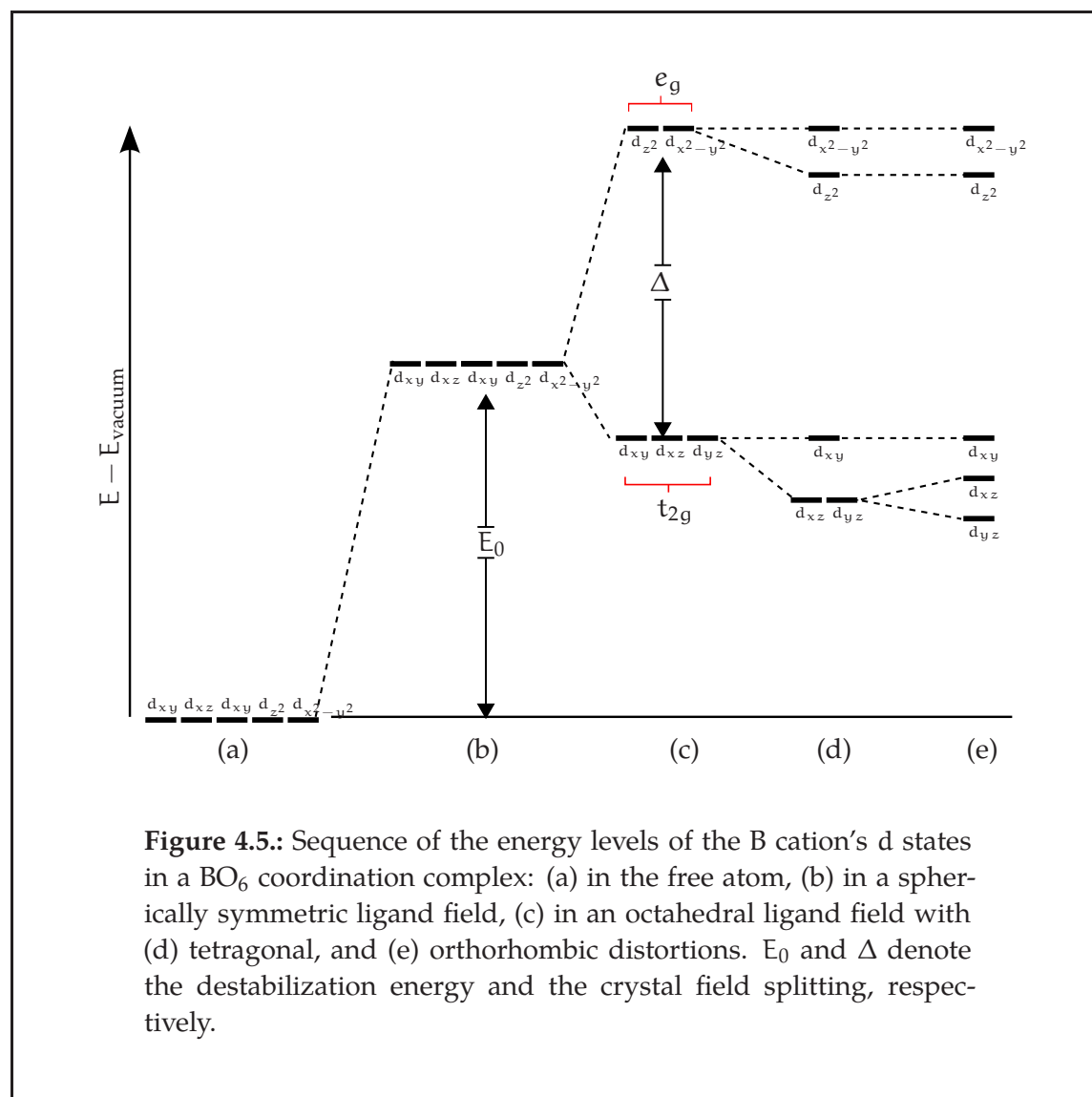
destabilization energy  $E_0$  corresponds to the repulsion of the d electrons by the ligands, assuming that they generate a spherically symmetric field around the transition metal ion. However, the electrostatic field seen by the d electrons is not spherically symmetric due to the spatial arrangement of the ligands. Consequently, the energy levels of the  $d_{z^2}$  and  $d_{x^2-y^2}$  states are further destabilized, whereas the other three states gain energy. This results in a splitting of the five degenerate levels, figure 4.5 (c). The wave functions of the threefold degenerate  $d_{xy}$ ,  $d_{xz}$ , and  $d_{yz}$  states transform according to the irreducible representation  $T_{2g}$  of the point-group symmetry  $O_h$  of the octahedral crystal field. Therefore, the corresponding d orbitals are named  $t_{2g}$  states. The wave functions of the remaining two d orbitals transform according to the irreducible representation  $E_g$  and are therefore denoted  $e_g$  states, respectively. The energy difference  $\Delta$  between the  $t_{2g}$  and  $e_g$  states is called crystal-field splitting energy.

The simple idea that the octahedral crystal field induces an energy splitting between the levels of the formally degenerated d orbitals can be easily extended to distorted perovskite structures: any distortion from the ideal perovskite structure will reduce the symmetry of the octahedral crystal field. This will in turn lift

the degeneracy between the d states labeled  $t_{2g}$  and  $e_g$ . This effect is pictured in figure 4.5 (d) and (e) for the case of the tetragonal and the orthorhombic perovskite structures introduced in the previous section. As discussed before, it is assumed that the deviations from the ideal perovskite structure are small. Hence, the deviations from the octahedral symmetry of the crystal field are also small and the induced splitting is not as big as the crystal-field splitting. In general, the strength of the crystal field and the resulting crystal field splitting depends on the following aspects:

1. *The number and geometrical arrangement of the ligands.* The importance of the geometrical arrangement was already emphasized in the discussion above. In a different geometrical arrangement orbitals other than  $d_{xy}$ ,  $d_{xz}$ , and  $d_{yz}$  can be energetically favored. For example, in a tetrahedrally coordinated complex the d states split into  $t_{2g}$  and  $e_g$  states, too, but their energetic order is reversed with respect to the octahedral case. Furthermore, a smaller number of ligands would generate a smaller electrostatic field and the resulting splitting will be smaller.
2. *The nature of the ligands.* Ligands with a larger charge or a large electronegativity induce a larger crystal field splitting. Since oxygen is the only ligand in all compounds examined in this work, this aspect will not be discussed in detail here.
3. *The oxidation state of the B cation.* If a central B cation is replaced by another cation with a higher oxidation state, the electrostatic attraction causes the ligands to move closer to the new B cation. This enlarges the repulsion between the ligands and the d-electronic states. Consequently, the crystal field splitting is enhanced.

The electronic configuration of the  $BO_6$  coordination complex can now be obtained by distributing the  $N$  d electrons of the B cation among the  $t_{2g}$  and  $e_g$  states. For  $N \leq 3$  each  $t_{2g}$  state will be singly occupied by an electron. Furthermore, the electrons' spins are supposed to align parallel maximizing the total spin and total angular momentum in agreement with Hund's rules. For the fourth, fifth etc. electron there are two possibilities: it can either occupy an  $e_g$  state paying the price of the additional energy  $\Delta$  or it can occupy a  $t_{2g}$  state. Since all  $t_{2g}$  states were already populated by one electron, the energy arising from the strong Coulomb repulsion between two electrons in the same state has to be paid in the latter case. For small  $\Delta$ , all d states first are singly occupied. In this case, Hund's first and second rule are applicable to all d states such that all electronic spins of the single electrons are aligned parallel. Therefore, this electronic configuration is called high-spin state. If  $\Delta$  is large, all  $t_{2g}$  states will be doubly occupied before  $e_g$  states will be populated. Thus, Hund's rules have to be applied to  $t_{2g}$  and  $e_g$  states separately and the resulting electronic configura-



ration is called low-spin state. Despite its simplicity, this model of the electronic structure obtained from CFT successfully described the magnetic behavior of many coordination complexes.

In CFT, it depends solely on the strength of the crystal field splitting which configuration will be favored. However, in solids there can exist other important energy contributions like the spin-orbit coupling. In heavy rare-earth elements, the spin-orbit coupling can be very strong. Furthermore, the f electrons are usually more localized than the d electrons. Therefore, they are screened from the crystal field by the outer s, p, and d electrons. Consequently, the f electrons are less affected by the crystal field than the d electrons and the spin-orbit coupling becomes larger than the crystal field splitting energy. In the compounds examined in this work, the spin-orbit coupling on the site of the B cation is

weak compared to the crystal field splitting. Therefore, the main results from the analysis of the electronic structure within CFT should hold at least qualitatively. However, it will be seen that a quantitative description of the electronic structure of perovskite TMOs also requires to take into account covalent mixing of the oxygen  $p$  wave functions with the  $d$  wave functions of the B cation. This is beyond the simple ionic model of CFT. It can be described within the ligand field theory (LFT), which can be considered an extension of CFT introduced by Hartmann and Ilse in 1951 [124]. For example, LFT allows to take into account the polarizability and field intensity of the ligands as obtained from experimental measurements and is therefore a semi-empirical theory. It can yield a much more quantitative description of the electronic structure of the central atom of a coordination complex. However, only the central atom is treated quantum-mechanically like in CFT.

Van Fleck, one of the founders of CFT, already pointed out in 1935 [123] that CFT and its descendants are only special cases of the more general molecular orbital (MO) theory yielding a fully quantum-mechanical description of the central atom and the ligands in a coordination complex. To obtain a deeper understanding of the electronic structure of perovskites, the basic results from MO theory obtained for an octahedral coordination complex will be discussed in the next section.

### 4.3. Perovskites and molecular orbital theory

The basic ideas of molecular orbital (MO) theory are quite different in spirit from those of CFT or LFT: if isolated atoms are brought together to form molecules or coordination complexes, the atomic orbitals (AOs) of the distinct atoms will begin to overlap. Thus, the AOs combine to form orbitals, which extend over the whole complex and contain the valence electrons formally occupying the distinct AOs. These new orbitals are called molecular orbitals (MOs). The electrons contained in an MO are delocalized over the whole complex. Hence, they can now move inbetween the atoms, which ties them together and thus stabilizes the molecule or coordination complex.

The first steps towards the formulation of the MO theory were made by Hund [125] and Mulliken [126] in the late 1920th. Therefore, the MO theory was first called Hund-Mulliken theory. The word "orbital" was introduced by Mulliken in 1932 [127]. However, it was Lennard-Jones, who first applied MO theory quantitatively in 1929 [128] deriving the electronic structure of the oxygen molecule. More importantly, in his later work [129, 130, 131] he established the MOs as eigenfunctions of the self-consistent field Hamiltonian of the Hartree-Fock equations. This was the point when MO theory became fully rigorous and consistent.

In Hartree-Fock theory, an N-electron wave function is computed as a single determinant of single-electron wave functions. The advantage of the Hartree-Fock method is that the single-electron wave functions are determined self-consistently. The major drawback is that the electrons apart from fulfilling the Pauli exclusion principle are treated as statistically independent. Today, there are more sophisticated wave function-based approaches that incorporate correlation effects to some degree, e.g., configuration interaction or the coupled cluster approximation. These methods are much more accurate but they are also computationally expensive because they scale unfavorably with the system size. Hence, they are mostly used for the quantitative description of the electronic structure of atoms and molecules. The main results of MO theory can be derived qualitatively from a much simpler ansatz by Lennard-Jones who suggested to construct the molecular orbitals from *linear combinations of atomic orbitals* (LCAO ansatz). Furthermore, the LCAO ansatz allows a direct graphical interpretation of the results in terms of LCAO-MO diagrams. The approach will be applied in this section to gain further insight into the electronic structure of the  $\text{BO}_6$  coordination complex of perovskites, but the basic concepts and terminologies are introduced by first looking at the simplest molecule possible: the  $\text{H}_2^+$ -molecule.

In a gedankenexperiment an  $\text{H}_2^+$ -molecule in the ground state can be constructed from an H atom with the electron in the 1s orbital and an  $\text{H}^+$  ion (a proton). In the molecule the two protons at the sites A and B are indistinguishable. The 1s orbitals at the two sites are given by

$$\phi_i(r_i) = \frac{1}{\sqrt{\pi a_0^3}} e^{-r_i/a_0}, \quad i = A, B, \quad (4.2)$$

where  $a_0$  is the Bohr radius. Here, the origin of the coordinate system is placed in the center of gravity of the two protons. Thus, the coordinates of the electron occupying  $\phi_i(r_i)$  are given by  $\mathbf{r}_i = \mathbf{r} \pm \frac{1}{2}\mathbf{R}$ , where the vector  $\mathbf{R}$  connects the two protons and  $r_i = |\mathbf{r}_i|$ . From the LCAO ansatz a MO  $\Psi(\mathbf{r}, \mathbf{R})$  for the  $\text{H}_2^+$ -molecule is obtained as linear combination of the 1s orbitals

$$\Psi(\mathbf{r}, \mathbf{R}) = c_1 \phi_A(r_A) + c_2 \phi_B(r_B) \quad (4.3)$$

with  $R = |\mathbf{R}|$ . The MO has to be normalized

$$\begin{aligned} 1 &\stackrel{!}{=} \int |\Psi(\mathbf{r}, \mathbf{R})|^2 d^3r \\ &= c_1^2 \int |\phi_A(r_A)|^2 d^3r + c_2^2 \int |\phi_B(r_B)|^2 d^3r + 2c_1c_2 S_{AB}(R). \end{aligned} \quad (4.4)$$

The overlap integral  $S_{AB}(R)$  is defined as

$$S_{AB}(R) = \int \phi_A(r_A)\phi_B(r_B) d^3r. \quad (4.5)$$

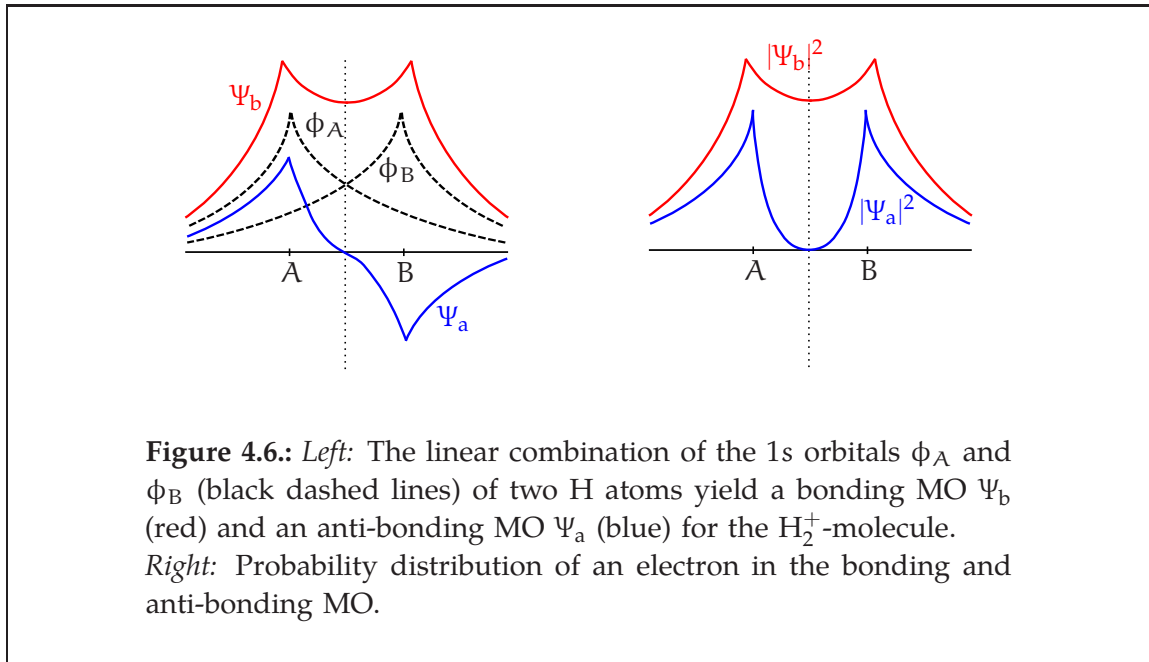


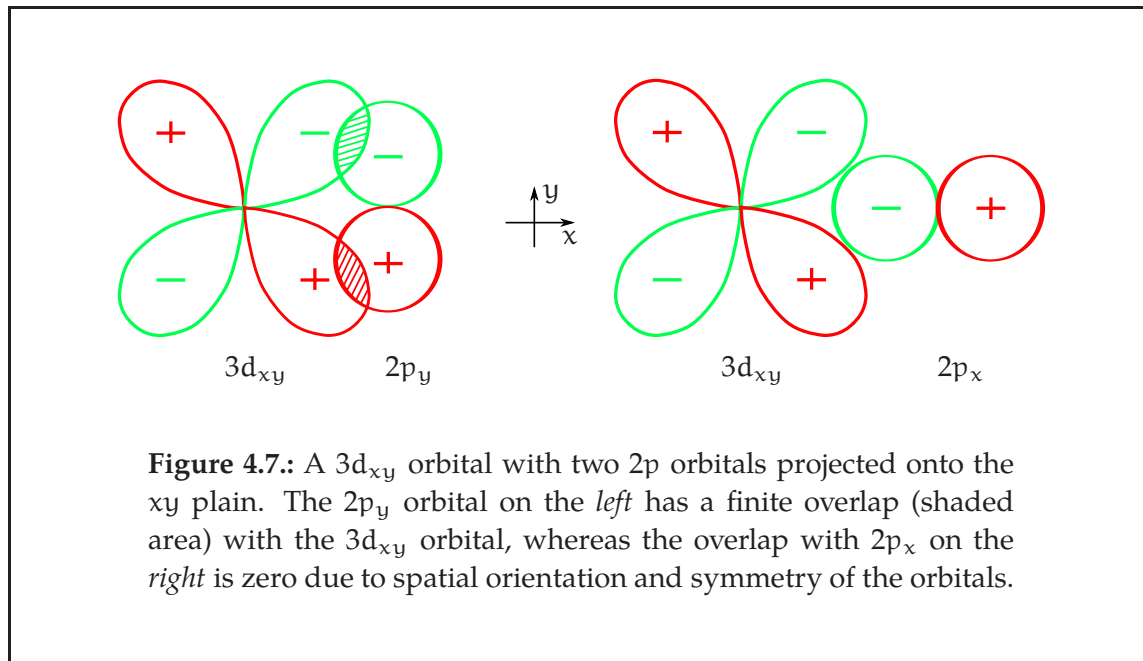
**Figure 4.6.:** *Left:* The linear combination of the 1s orbitals  $\phi_A$  and  $\phi_B$  (black dashed lines) of two H atoms yield a bonding MO  $\Psi_b$  (red) and an anti-bonding MO  $\Psi_a$  (blue) for the  $H_2^+$ -molecule. *Right:* Probability distribution of an electron in the bonding and anti-bonding MO.

Since the 1s orbitals are already normalized, the first two integrals in (4.4) equal one. Furthermore, the relation  $|c_1|^2 = |c_2|^2 = |c|^2$  holds due to the symmetry of the molecule. Since the MO  $\Psi(\mathbf{r}, R)$  has to be either symmetric or anti-symmetric with respect to the permutation of the two 1s orbitals, it follows that  $c_1 = \pm c_2$ . In a shorthand notation omitting the spacial arguments of the wave functions the resulting two MOs of the  $H_2^+$ -molecule in the ground state are

$$\Psi_b = \frac{1}{\sqrt{2 + 2S_{AB}}} (\phi_A + \phi_B), \quad (4.6)$$

$$\Psi_a = \frac{1}{\sqrt{2 - 2S_{AB}}} (\phi_A - \phi_B). \quad (4.7)$$

The indices b and a indicate that the first wave function is a *bonding* state, whereas the second one is *anti-bonding*. The terminology becomes clear by looking at the probability distribution of the single electron in the molecule given by  $|\Psi_b|^2$  and  $|\Psi_a|^2$ , which are pictured in figure 4.6. There is a finite probability to find the electron occupying  $\Psi_b$  between the two protons. The attraction between the protons and the electron thus holds the molecule together. Furthermore, the electron in  $\Psi_b$  can move in a larger region in space compared to an electron in a 1s orbital. According to the uncertainty relation this leads to a decrease of the expectation value of the momentum operator  $p = \langle \hat{p} \rangle$ . Hence, the kinetic energy of the electron is diminished which further stabilizes the  $H_2^+$ -molecule. The opposite holds for an electron occupying  $\Psi_a$ . The probability to find the electron in between the two protons is decreased and its kinetic energy is equal to or even larger than that of an electron in a 1s orbital.

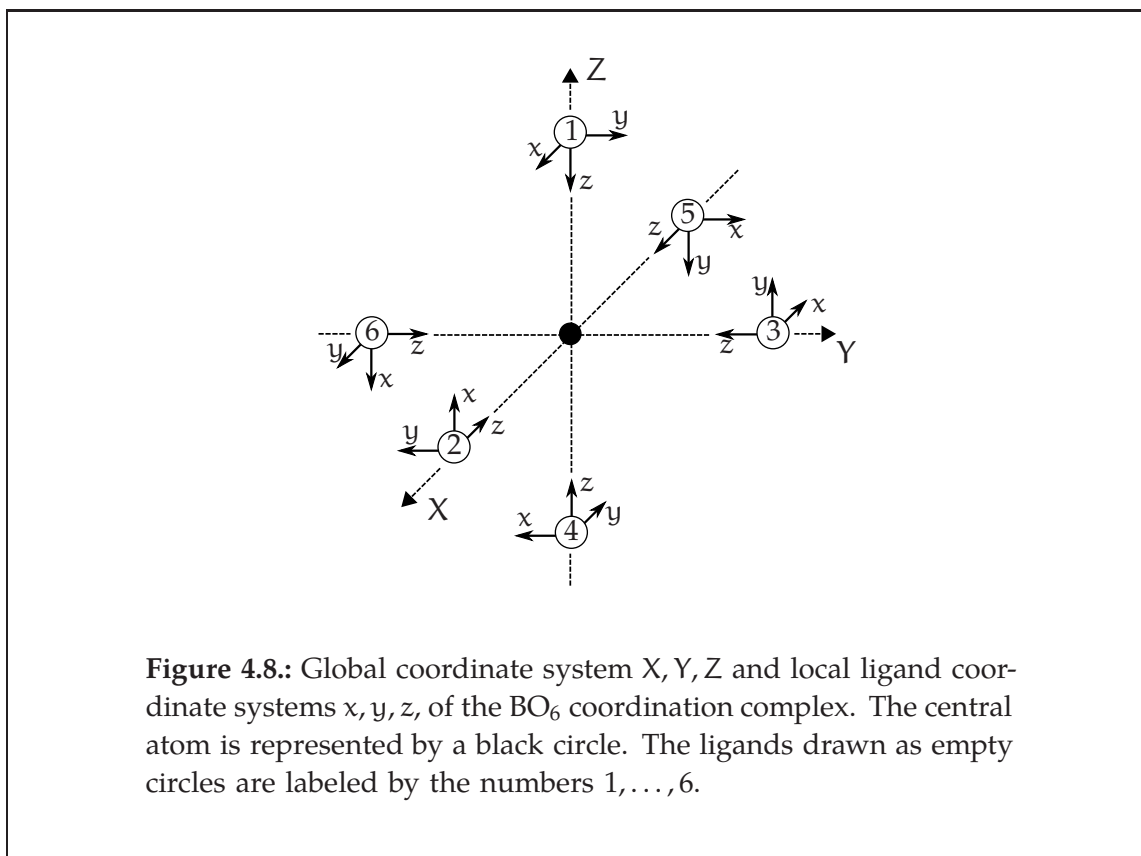


In principle, MOs for larger molecules or structures like the  $\text{BO}_6$  coordination complex in perovskites can be constructed in the same way as for the  $\text{H}_2^+$  molecule. The only difference is that the overlap between a larger number of AOs with different character  $s$ ,  $p$ ,  $d$  has to be taken into account. Typically, only the AOs constituting the valence states are considered in the LCAO ansatz. Furthermore, only those AOs with a finite overlap can form a bonding and an anti-bonding MO and it depends on the spatial orientation and the symmetry of the AOs if they have a finite overlap. An example is given in figure 4.7, where a  $3d_{xy}$  orbital and a  $2p_y$  orbital have a finite overlap due to their relative orientation, but the overlap of the  $3d_{xy}$  with the corresponding  $2p_x$  orbital is zero. Hence, the number of linear combinations of AOs in the LCAO ansatz for the MOs can be reduced if the symmetry and spatial orientation of the AOs is taken into account.

In the construction of MOs for the  $\text{BO}_6$  coordination complex of perovskites the symmetry of the AOs is exploited in the following way. First, the AOs of the ligands are combined to form MOs  $\Phi$  that transform after the irreducible representations of the symmetry group  $O_h$  of the octahedral coordination complex. In the second step, the MOs  $\Psi$  of the whole complex are constructed as linear combinations of the ligand MOs  $\Phi$  and the AOs of the central B cation  $\phi$ ,

$$\Psi = c_1 \phi + c_2 \Phi . \quad (4.8)$$

The advantage of this procedure is that the AOs  $\phi$  can also be classified according to the irreducible representations of the symmetry group  $O_h$  and only those AOs



$\phi$  and ligand MOs  $\Phi$  transforming after the same irreducible representation have a finite overlap. This can be proved rigorously using group theory (cf. [132]).

In order to explain the construction of the ligand MOs it is useful to first introduce a notation for the ligand AOs of the  $\text{BO}_6$  coordination complex. Figure 4.8 illustrates the choice of the global and local ligand coordinate systems and the ligand numeration. The  $z$  axes of the ligand coordinates are directed towards the central atom, while the orientation of the remaining axes may be chosen randomly. The  $2s$  and  $2p_z$  orbital of each oxygen ligand hybridize to form two  $sp$ -hybrid orbitals. One  $sp$  orbital is oriented along the  $z$  direction and the other points into the  $-z$  direction. Due to this spatial orientation only one  $sp$  orbital can form a  $\sigma$  bond with the AOs of the B cation. Thus, six  $sp$  orbitals, one from each ligand, are used in the construction of the ligand MOs. According to the conventions of MO theory, these orbitals are called  $\sigma$  orbitals because they are  $\sigma$  bonding. Here, the orbitals are labeled with the number of the ligand, for instance,  $\sigma_1$  means the  $\sigma$  orbital of the first oxygen ligand. The  $2p_x$  and  $2p_y$  orbitals of the oxygen ligands are not affected by the hybridization of the  $2s$  and  $2p_z$  orbital. They can form  $\pi$  bonds with the  $3d$  orbitals of the central B cation. Therefore, the  $2p_x$  orbital of the first ligand is denoted by  $\pi_{1x}$ ,  $2p_y$  is named  $\pi_{1y}$  and so on.

Type of symmetry	$\phi$	$\Phi_\sigma$	$\Phi_\pi$
$A_{1g}$	s	$(1/\sqrt{6})(\sigma_1 + \sigma_2 + \sigma_3 + \sigma_4 + \sigma_5 + \sigma_6)$	—
$A_{2u}$	—	—	—
$T_{1u}$	$p_x$	$(1/\sqrt{2})(\sigma_2 - \sigma_5)$	$\frac{1}{2}(\pi_{1x} - \pi_{4y} - \pi_{3x} + \pi_{6y})$
	$p_y$	$(1/\sqrt{2})(\sigma_3 - \sigma_6)$	$\frac{1}{2}(\pi_{1y} - \pi_{4x} - \pi_{2y} + \pi_{5x})$
	$p_z$	$(1/\sqrt{2})(\sigma_1 - \sigma_4)$	$\frac{1}{2}(\pi_{2x} - \pi_{5y} + \pi_{3y} - \pi_{6x})$
$E_g$	$d_{z^2}$	$(1/\sqrt{12})(2\sigma_1 + 2\sigma_4 - \sigma_2 - \sigma_3 - \sigma_5 - \sigma_6)$	—
	$d_{x^2-y^2}$	$\frac{1}{2}(\sigma_2 + \sigma_5 - \sigma_3 - \sigma_6)$	—
$T_{2g}$	$d_{xy}$	—	$\frac{1}{2}(\pi_{2y} + \pi_{5x} + \pi_{3x} + \pi_{6y})$
	$d_{xz}$	—	$\frac{1}{2}(\pi_{1x} + \pi_{4y} + \pi_{2x} + \pi_{5y})$
	$d_{yz}$	—	$\frac{1}{2}(\pi_{1y} + \pi_{4x} + \pi_{3y} + \pi_{6x})$
$T_{2u}$	—	—	$\frac{1}{2}(\pi_{1y} + \pi_{4x} - \pi_{3y} - \pi_{6x})$
	—	—	$\frac{1}{2}(\pi_{2x} + \pi_{5y} - \pi_{1x} - \pi_{4y})$
	—	—	$\frac{1}{2}(\pi_{3x} + \pi_{6y} - \pi_{2y} - \pi_{5x})$
$T_{1g}$	—	—	$\frac{1}{2}(\pi_{1x} - \pi_{4y} + \pi_{3x} - \pi_{6y})$
	—	—	$\frac{1}{2}(\pi_{2y} - \pi_{5x} + \pi_{1y} - \pi_{4x})$
	—	—	$\frac{1}{2}(\pi_{2x} - \pi_{5y} - \pi_{3y} + \pi_{6x})$

**Table 4.2.:** Atomic orbitals  $\phi$  of the central B cation and linear combinations  $\Phi_\sigma$  and  $\Phi_\pi$  of the ligand MOs  $\sigma$  and  $\pi$  for different types of symmetry of the  $O_h$  group for the  $BO_6$  coordination complex of perovskites (taken from reference [132]).

Altogether, the ligands contribute 18 orbitals, 6  $\sigma$  and 12  $\pi$  orbitals, which are combined to yield an equal number of ligand MOs  $\Phi$  listed in table 4.2 taken from reference [132]. Table 4.2 also lists the AOs  $\phi$  of the central B cation. All orbitals  $\phi$  and  $\Phi$  are ordered with respect to their transformation after the irreducible representation of the symmetry group  $O_h$ . Typically, the AOs and ligand MOs are labeled according to the corresponding irreducible representation, e.g., the  $s$  AO of the central B cation and the ligand MO  $(1/\sqrt{6})(\sigma_1+\sigma_2+\sigma_3+\sigma_4+\sigma_5+\sigma_6)$  are both named  $a_{1g}$  orbitals. Here, the small latter is used to distinguish the name of the MOs from the irreducible representation. All ligand MOs transforming according to the same irreducible representation are degenerate. This also applies to the AOs  $\phi$ . From the classification in table 4.2 it becomes immediately clear, which linear combinations of ligand MOs with AOs of the central B cation will have a finite overlap. They can be used to construct MOs  $\Psi$  of the  $BO_6$  coordination complex according to eq. (4.8). In particular, the three  $t_{1g}$  and the three  $t_{2u}$  ligand orbitals do not overlap with any of the AOs of the central B cation. Hence, they are not affected during the formation of the MOs and contribute only non-bonding MOs.

If the MOs  $\Psi$  of a molecule or coordination complex as well as the Hamiltonian  $\hat{H}$  of the system are known, the energy of the MOs can be calculated according to

$$E = \frac{\int \Psi^* H \Psi d\tau}{\int \Psi^* \Psi d\tau}. \quad (4.9)$$

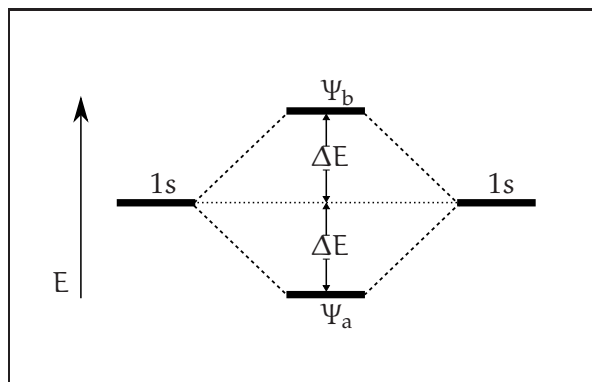
The order of the energy levels can be illustrated in a LCAO-MO diagram. This is exemplified first for the  $H_2^+$ -molecule with the Hamiltonian

$$H_{H^+} = -\frac{1}{2}\nabla_r^2 - \frac{1}{r_A} - \frac{1}{r_B} + \frac{1}{R}, \quad (4.10)$$

in the Born-Oppenheimer approximation. The energy of the electron in the states  $\Psi_b$  and  $\Psi_a$  for a certain distance between the protons can be written as

$$E_b(R) = \frac{H_{AA}(R) + H_{AB}(R)}{1 + S_{AB}(R)}, \quad E_a(R) = \frac{H_{AA}(R) - H_{AB}(R)}{1 - S_{AB}(R)} \quad (4.11)$$

**Figure 4.9:** LCAO-MO diagram of the  $H_2^+$ -molecule. Assuming that the overlap integral between the  $1s$  AOs is small (see text for further details), the energy of the bonding MO  $\Psi_b$  is lowered by an amount  $\Delta E$  with respect to that of the  $1s$  AOs and the energy of the anti-bonding MO  $\Psi_a$  is increased by the same amount.



with

$$H_{AA}(\mathbf{R}) = \int \phi_A^*(\mathbf{r}_A) H_{H^+} \phi_A(\mathbf{r}_A) d^3r, \quad (4.12)$$

$$H_{AB}(\mathbf{R}) = \int \phi_A^*(\mathbf{r}_A) H_{H^+} \phi_B(\mathbf{r}_B) d^3r. \quad (4.13)$$

Assuming that  $S_{AB}(\mathbf{R}) \ll 1$ ,  $S_{AB}(\mathbf{R})$  can be neglected in (4.11). For the ground-state equilibrium distance  $R_0$  between the protons the distribution of the resulting energies of the MOs  $\Psi_b$  and  $\Psi_a$  and the constituting 1s orbitals is shown in the LCAO-MO diagram figure 4.9. The energy of the binding MO  $E_b(R_0)$  is lowered by the energy  $\Delta E = -H_{AB}(R_0)$  with respect to the energy  $H_{AA}(R_0)$  of the 1s orbital and the energy of the anti-binding MO  $E_a(R_0)$  is increased by the same amount.

In the same manner it is possible to calculate the energies of the MOs of the  $\text{BO}_6$  coordination complex. With the knowledge of the ligand MOs and the AOs of the B cation forming the MOs of the complex and some additional considerations discussed below, it is possible to construct a LCAO-MO diagram of such a complex without detailed computations. Figure 4.10 shows the LCAO-MO diagram of the regular octahedral  $\text{TiO}_6$  coordination complex of  $\text{SrTiO}_3$ . It can be obtained from the following considerations.

- In LCAO-MO diagrams of hetero-nuclear complexes the energies of the element or ligands with larger electronegativity are pictured on the right. Thus, the oxygen ligands appear on the right side of the diagram of the  $\text{TiO}_6$  coordination complex.
- The 3d orbitals of the Ti atom are more localized than the 4p orbitals which are in turn more localized than the 4s orbital. Thus, the overlap between the  $a_{1g}$  ligand MO and the 4s orbital is larger than the overlap of the 4p orbitals and the  $t_{1u}$  ligand MOs. The overlap of 3d orbitals with  $t_{2g}$  and  $e_g$  ligand MOs is even smaller. Consequently, the energy splitting between bonding and anti-bonding MOs  $\Psi$  decreases with respect to the constituting AOs in the order 4s, 4p and 3d.
- The overlap between orbitals forming  $\sigma$  bonds is larger than the overlap between  $\pi$ -bonding orbitals. Consequently, the energy splitting between the MOs constructed from the  $3d(t_{2g})$  orbitals of Ti will be smaller than the splitting between the MOs containing contributions from the  $3d(e_g)$  orbitals.
- Anti-bonding MOs of the  $\text{TiO}_6$  coordination complex are labeled with a star to distinguish them from the bonding MOs.

In the LCAO-MO diagram of the  $\text{TiO}_6$  coordination complex, ligand MOs of oxygen are lower in energy than AOs of Ti as a consequence of the higher electronegativity of oxygen. Thus, the bonding MOs of the complex lie closer in

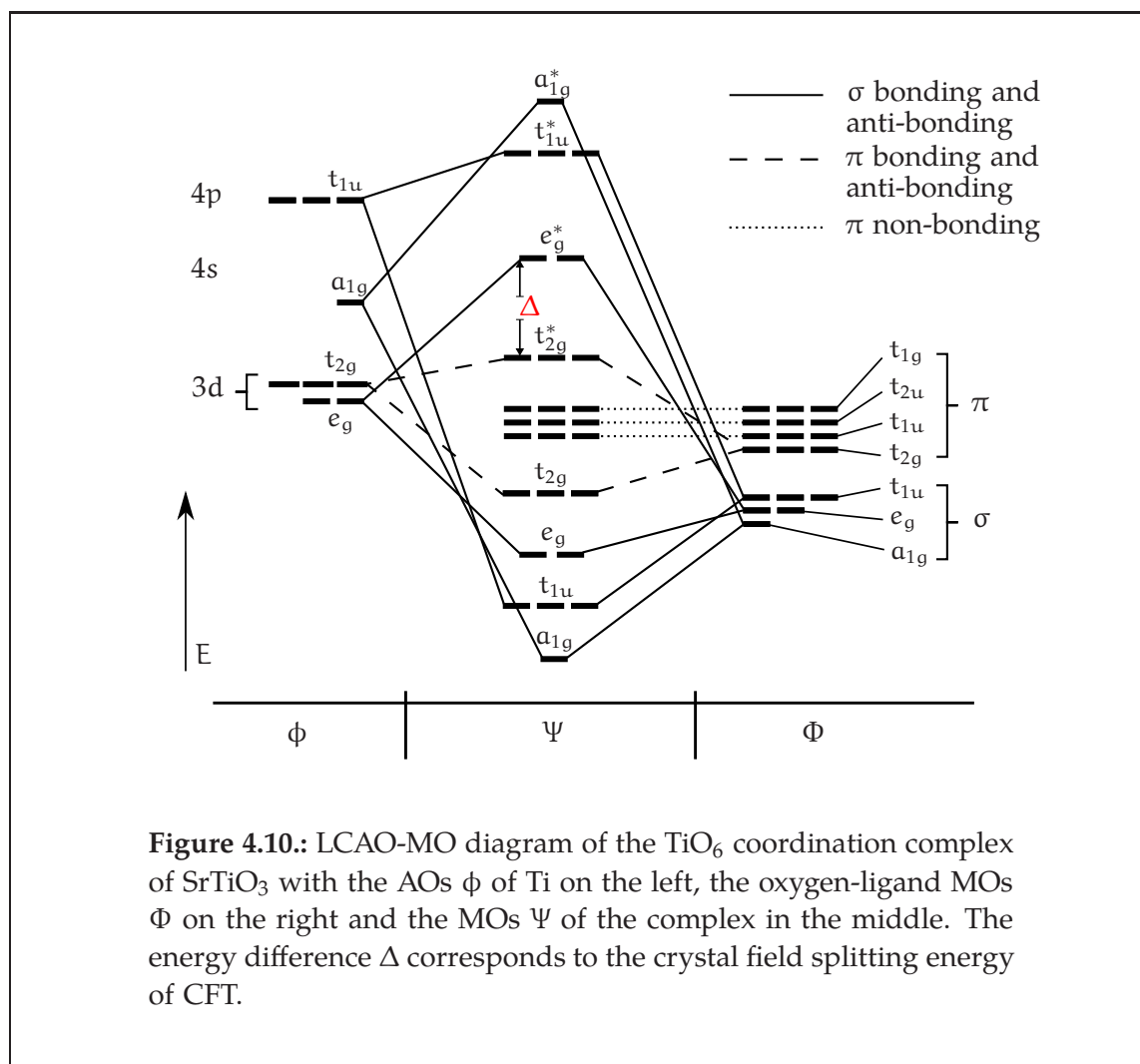


**Figure 4.10.:** LCAO-MO diagram of the  $\text{TiO}_6$  coordination complex of  $\text{SrTiO}_3$  with the AOs  $\phi$  of Ti on the left, the oxygen-ligand MOs  $\Phi$  on the right and the MOs  $\Psi$  of the complex in the middle. The energy difference  $\Delta$  corresponds to the crystal field splitting energy of CFT.

energy to the ligand MOs than to the AOs of Ti. For the anti-bonding MOs it is the other way round. Consequently, the bonding MOs have mostly ligand-MO character and the anti-bonding orbitals are mainly composed of the Ti AOs. In particular, the two anti-bonding orbitals  $t_{2g}^*$  and  $e_g^*$  have mostly Ti 3d character. Thus, the energy splitting  $\Delta$  between these MOs corresponds to the crystal field splitting in CFT. In general, the dominance of either ligand MOs or AOs of the central B cation in the composition of the MOs  $\Psi$  is interpreted as ionic character of the bonding between the ligand and the cation.

With the help of the LCAO-MO diagram the electronic configuration of the  $\text{TiO}_6$  coordination complex can now be determined by successively filling the MOs with electrons starting from the MO with the lowest energy. Due to the larger electronegativity of oxygen the 18 ligand MOs are completely filled containing in total 36 electrons, whereas the AOs of  $\text{Ti}^{4+}$  are completely empty. Thus, the electronic configuration of the  $\text{TiO}_6$  coordination complex is given by

$a_{1g}^2 t_{1u}^6 e_g^4 t_{2g}^6 t_{1u}^6 t_{1g}^6 t_{2u}^6$ . Based on this prediction of the electronic configuration of SrTiO<sub>3</sub> many spectral features seen in photo-emission experiments can be readily explained [133].

For the perovskite LaCrO<sub>3</sub> the exact same LCAO-MO diagram, figure 4.10, for the CrO<sub>6</sub> coordination complex is obtained if the orthorhombic distortions from the ideal perovskite structure are neglected. Once again, the ligand MOs of oxygen contribute 36 electrons. Chromium has the oxidation number III in the LaCrO<sub>3</sub> compound and thus contains 3 electrons in the 3d orbitals. This leads to the electronic configuration  $a_{1g}^2 t_{1u}^6 e_g^4 t_{2g}^6 t_{1u}^6 t_{1g}^6 t_{2u}^6 t_{2g}^{*3}$ . The three additional electrons are distributed evenly over the 3  $t_{2g}^*$  orbitals and their spins are aligned parallel according to Hund's rules. Hence, the CrO<sub>6</sub> coordination complex will have a total magnetic moment of 3  $\mu_B$ , which is in good agreement with 2.8  $\mu_B$  found experimentally [134].

The MO theory is capable of predicting electronic and magnetic structures of coordination complexes. It is much more reliable than CFT but calculations based on the MO theory are more cumbersome and numerically expensive. Cotton [135] quotes G. B. Shaw, who tried to characterize the different theories: CFT and LFT are "too good to be true". They are both easy to understand, but a model built solely on point charges and electrostatic interaction certainly does not describe the real physics of coordination complexes. On the other hand, MO theory is just "too true to be good". It takes into account most of the physically relevant information and conveys a much more accurate description of the electronic structure of coordination complexes. But it lacks the insightfulness of CFT. Finally, it can be ascertained that both theories – although in a very different manner – describe coordination complexes with the help of interactions between the central atom and ligands. In both cases this leads to a splitting of the d states of the central atom (cf. the LCAO-MO diagram of the TiO<sub>6</sub> coordination complex, figure 4.10). Since the crystal field splitting energy  $\Delta$  is a dominant energy scale in many of these complexes, it is after all not surprising that both theories yield a good estimate for electronic spectra and magnetic properties of perovskite TMOs.

## 4.4. Insulating properties of transition-metal oxides (TMOs)

In the previous sections, the electronic configuration of a single transition-metal cation B in a BO<sub>6</sub> coordination complex was discussed. The perovskite crystal structure can be considered as an array of BO<sub>6</sub> coordination complexes extending infinitely in three dimensions, which is embedded in a simple cubic lattice of A

cations. If  $N$  separate coordination complexes with  $M$  MOs condense into a single crystal lattice, the MOs will start to overlap forming  $M/2$  binding and  $M/2$  anti-binding MOs. For  $N \rightarrow \infty$ , the distinct energy levels of the MOs move closer in energy forming a continuum of states. This leads to the picture of energy bands in a crystal as opposed to the well separated energy levels of the single coordination complex.

Originally, the concept of energy bands was introduced in the early days of quantum mechanics and is a direct consequence of the description of the energy distribution of non-interacting electrons in the periodic potential of the atomic nuclei in a crystal lattice. It leads to the canonical distinction between metals and insulators based on the filling of the electronic bands. This will be discussed briefly in the first part of this section. Band theory successfully explains metallic and insulating behavior of many materials. However, de Boer and Verwey [136] reported already in 1937 that many TMOs with a partially filled d-electron band are poor conductors and indeed often insulators in contrast to the metallic character predicted by band theory. Following their report, Peierls [137] pointed out the importance of the electron correlation: the strong Coulomb repulsion keeps the electrons apart giving rise to the insulating behavior. The occurrence of correlation-driven insulating behavior will be discussed in more detail in the second part of this section. In the last part, the different ansatzes to explain insulating behavior will be applied to the materials examined in this work.

#### 4.4.1. Band theory

Band theory is based on the nearly-free electron (NFE) model, a modification of the free-electron gas model. It is a mean-field theory describing the valence electrons in a crystal as free particles moving independently in the periodic potential generated by the atomic nuclei. This corresponds to a neglect of the term  $V_{ee}$  in the Hamiltonian (2.6) of the  $N$ -electron Schrödinger equation (2.5). Without the term  $V_{ee}$  the  $N$ -electron eigenstates of the remaining Hamiltonian can be represented as a product of single-particle wave functions  $\phi_{\mathbf{k}\nu}(\mathbf{r})$ . Inserted into the corresponding Schrödinger equation  $N$  single-particle Schrödinger equations are obtained

$$\left[ -\frac{1}{2}\nabla_{\mathbf{r}}^2 + v^{\text{ext}}(\mathbf{r}) \right] \phi_{\mathbf{k}\nu}(\mathbf{r}) = \epsilon_{\nu}(\mathbf{k}) \phi_{\mathbf{k}\nu}(\mathbf{r}) \quad (4.14)$$

with the external potential  $v^{\text{ext}}(\mathbf{r})$  defined in eq. (2.3). For each  $\mathbf{k}$  in the BZ, there exists an infinite number of eigenvalues  $\epsilon_{\nu}(\mathbf{k})$ . The eigenvalues for a fixed  $\nu$  and all  $\mathbf{k}$  in the first BZ constitute the  $\nu$ -th band of the crystal. Thus, the index  $\nu$  is called band index. The eigenstates  $\phi_{\mathbf{k}\nu}(\mathbf{r})$  are labeled accordingly.

It is convenient to represent the external potential via its Fourier components  $\tilde{v}_{\mathbf{G}}^{\text{ext}}$

$$v^{\text{ext}}(\mathbf{r}) = \sum_{\mathbf{G}} \tilde{v}_{\mathbf{G}}^{\text{ext}} e^{-i\mathbf{G}\cdot\mathbf{r}}; \quad \tilde{v}_{\mathbf{G}}^{\text{ext}} = \frac{1}{\Omega} \int_{\Omega} v^{\text{ext}}(\mathbf{r}) e^{i\mathbf{G}\cdot\mathbf{r}} d^3r, \quad (4.15)$$

where  $\mathbf{G}$  is a reciprocal lattice vector and  $\Omega$  is the unit cell volume. Due to the periodicity of the potential, the eigenfunctions  $\phi_{\mathbf{k}\nu}(\mathbf{r})$  have to fulfill Bloch's theorem and can hence be written as

$$\phi_{\mathbf{k}\nu}(\mathbf{r}) = \sum_{\mathbf{G}} c_{\mathbf{G}} e^{-i(\mathbf{k}+\mathbf{G})\cdot\mathbf{r}}. \quad (4.16)$$

Inserting eqs. (4.15) and (4.16) into eq. (4.14) yields a set of equations for the expansion coefficients  $c_{\mathbf{G}}$

$$\left[ \frac{1}{2}(\mathbf{k} + \mathbf{G})^2 - \epsilon_{\nu}(\mathbf{k}) \right] c_{\mathbf{G}} + \sum_{\mathbf{G}'} \tilde{v}_{\mathbf{G}-\mathbf{G}'}^{\text{ext}} c_{\mathbf{G}'} = 0. \quad (4.17)$$

If  $\tilde{v}_{\mathbf{G}}^{\text{ext}} = 0 \forall \mathbf{G}$  the eigenstates are simply given by  $\epsilon_{\nu}(\mathbf{k}) = 1/2(\mathbf{k} + \mathbf{G})^2$ . The energy parabolas with origins at different  $\mathbf{G}$  have crossing points at the reciprocal unit-cell boundaries.

In the following derivation, two parabolas are considered one for  $\mathbf{G} = \mathbf{0}$  and another one with the origin at a non-zero reciprocal lattice vector  $\mathbf{G}'$ . For simplicity, it is assumed that  $\tilde{v}_0^{\text{ext}}$  and  $\tilde{v}_{\mathbf{G}'}^{\text{ext}}$  are the only non-zero Fourier components. From (4.17), the following two equations are obtained

$$0 = \left[ \frac{1}{2}\mathbf{k}^2 - \epsilon_{\nu}(\mathbf{k}) + \tilde{v}_0^{\text{ext}} \right] c_0 + \tilde{v}_{-\mathbf{G}'}^{\text{ext}} c_{\mathbf{G}'}, \quad (4.18)$$

$$0 = \left[ \frac{1}{2}(\mathbf{k} + \mathbf{G}')^2 - \epsilon_{\nu}(\mathbf{k}) + \tilde{v}_0^{\text{ext}} \right] c_{\mathbf{G}'} + \tilde{v}_{\mathbf{G}'}^{\text{ext}} c_0. \quad (4.19)$$

Since the external potential is real, the Fourier components satisfy  $\tilde{v}_{-\mathbf{G}'}^{\text{ext}} = (\tilde{v}_{\mathbf{G}'}^{\text{ext}})^*$  and the two equations above yield

$$\left[ \frac{1}{2}\mathbf{k}^2 - \epsilon_{\nu}(\mathbf{k}) + \tilde{v}_0^{\text{ext}} \right] \left[ \frac{1}{2}(\mathbf{k} + \mathbf{G}')^2 - \epsilon_{\nu}(\mathbf{k}) + \tilde{v}_0^{\text{ext}} \right] = |\tilde{v}_{\mathbf{G}'}^{\text{ext}}|^2. \quad (4.20)$$

Now, the two energy parabolas for  $\mathbf{G} = \mathbf{0}$  and  $\mathbf{G}'$  are assumed to be equal at the Brillouin-zone boundary,  $\mathbf{k}^2 = (\mathbf{k} + \mathbf{G}')^2$ . Inserted into the equation above one gets two solutions for the formally degenerate energy values

$$\epsilon_{\nu}(\mathbf{k})^{\pm} = \frac{1}{2}\mathbf{k}^2 + \tilde{v}_0^{\text{ext}} \pm |\tilde{v}_{\mathbf{G}'}^{\text{ext}}| \quad (4.21)$$

which are separated by an energy gap of the size  $2 \cdot |\tilde{v}_{\mathbf{G}'}^{\text{ext}}|$ .

The eigenstates can now be filled successively with electrons. Because of the spin-degeneracy each state can hold two electrons of opposite spin. The energy of the highest occupied state corresponds to the Fermi level of the system. If the Fermi level crosses an energy band, it only takes an infinitesimally small amount of energy to excite the electron from the highest occupied state into an unoccupied state. Consequently, the material has a high conductivity and exhibits metallic behavior. If the highest occupied state and the lowest unoccupied state are separated by an energy gap, the material is insulating. Depending on the size of the gap, the material is either called a semiconductor for  $E_{\text{gap}} < 2\text{eV}$  or an insulator for  $E_{\text{gap}} \geq 2\text{eV}$ .

The occurrence of metallic behavior in the NFE model is the consequence of the periodicity of the potential on the one hand and the filling of the bands on the other. In particular, a material with an unpaired electron per unit cell is predicted to be metallic because the Fermi energy in such a system crosses a band. However, there are prominent examples among the TMOs, e.g.,  $\text{LaTiO}_3$ , which is insulating at low temperature, although there is only a single electron per unit cell occupying a Ti 3d state. The origin of the insulating behavior in such materials can be explained if the electron-electron interaction term  $V_{ee}$  in the Hamiltonian (2.6) is taken into account explicitly as will be seen in the next section. Mean-field theories such as the NFE model which employ the independent-particle picture to describe the electrons in a solid are therefore not suited to describe this kind of correlation-driven insulating behavior because they do not take the two-particle term  $V_{ee}$  explicitly into account.

DFT-based calculations employ the KS or gKS schemes which treat the electrons as independent particles moving in an effective potential which is constructed in such a way that the exact density of the interacting N-electron system is obtained. In particular, the KS or gKS single-particle energies are not related to the exact eigenspectrum of the N-electron system apart from the highest occupied state. In practice, the eigenspectrum of the (g)KS system is frequently interpreted as approximation for the ground-state eigenspectrum of the interacting N-electron system<sup>1</sup>. As the (g)KS eigenspectrum is obtained from a mean-field type description in the same sense as discussed above, i.e., the term  $V_{ee}$  is not included explicitly in the calculations, the (g)KS approach predicts a metallic ground-state for materials like  $\text{LaTiO}_3$ . It is important to realize that this is neither a failure of DFT nor the (g)KS formalism which are exact theory. However, it is an indication that the single-particle picture employed in the (g)KS approach is not sufficient to describe all properties of materials where electron-electron interactions are large.

---

<sup>1</sup>This has been discussed in detail in section 2.2.3 of chapter 2.

### 4.4.2. Correlation-driven insulating behavior

It was already discussed in the introduction to chapter 2 that the N-electron Schrödinger equation (2.5) cannot be solved exactly due to the electron-electron term  $V_{ee}$ . However, there are numerous model approaches that allow to study the influence of the term  $V_{ee}$  in (2.5). Here, two models are introduced, namely the Hubbard model [26, 27, 28, 29, 30] and the p-d model. Whereas the first is most suited to explain the occurrence of correlation-driven insulating behavior, the second one is more suitable to model the electronic structure of TMOs.

Before the two models are introduced, it is instructive to first consider the many-electron Hamiltonian in second quantization, eq. (2.64), written in terms of field operators  $\hat{\psi}_\sigma^\dagger(\mathbf{r})$ ,  $\hat{\psi}_\sigma(\mathbf{r})$  defined in section 2.3. Here, the spin of the electron denoted by  $\sigma$  is taken into account explicitly. If a new set of creation and annihilation operators  $\hat{c}_{i\sigma}^\dagger, \hat{c}_{i\sigma}$  is introduced that acts on the AOs<sup>2</sup> denoted by  $\phi_i(\mathbf{r})$ , the field operators can be written as

$$\hat{\psi}_\sigma(\mathbf{r}) = \sum_i \phi_i(\mathbf{r}) \hat{c}_{i\sigma}. \quad (4.22)$$

Inserted into (2.64), the Hamiltonian acquires the form of a fermionic lattice model

$$\hat{H} = \sum_{i\sigma} \epsilon_i n_{i\sigma} - \sum_{\substack{ij,\sigma \\ i \neq j}} t_{ij} \hat{c}_{i\sigma}^\dagger \hat{c}_{j\sigma} + \frac{1}{2} \sum_{ijkl} \sum_{\sigma\sigma'} U_{ijkl} \hat{c}_{i\sigma}^\dagger \hat{c}_{j\sigma'}^\dagger \hat{c}_{k\sigma'} \hat{c}_{l\sigma} \quad (4.23)$$

with  $n_{i\sigma} = \hat{c}_{i\sigma}^\dagger \hat{c}_{i\sigma}$ . The energy levels  $\epsilon_i$  of the orbitals are given by

$$\epsilon_i \equiv \int \phi_i^*(\mathbf{r}) H_1(\mathbf{r}) \phi_i(\mathbf{r}) d^3r, \quad (4.24)$$

with  $H_1(\mathbf{r}) = -\frac{1}{2}\nabla_r^2 + v^{\text{ext}}(\mathbf{r})$  and  $v^{\text{ext}}(\mathbf{r})$  defined in (2.3). The second term in (4.23) describes the "hopping" of electrons between different orbitals with the hopping matrix elements

$$-t_{ij} \equiv \int \phi_i^*(\mathbf{r}) h(\mathbf{r}) \phi_j(\mathbf{r}) d^3r \quad (4.25)$$

and the last term yields the electron-electron interaction with matrix elements of the Coulomb interaction

$$U_{ijkl} \equiv \iint \phi_i^*(\mathbf{r}) \phi_j^*(\mathbf{r}') v(\mathbf{r}, \mathbf{r}') \phi_k(\mathbf{r}') \phi_l(\mathbf{r}) d^3r d^3r' \quad (4.26)$$

with  $v(\mathbf{r}, \mathbf{r}')$  defined in (2.4). Equation (4.23) is an exact representation of the many-electron Hamiltonian if the basis of the single-electron wave functions  $\phi_i(\mathbf{r})$  is complete. The many-electron Hamiltonian written in the above form, eq. (4.23), can be considered as the theoretical background of various lattice models suggested during the last decades.

<sup>2</sup>The AOs used in this context must form a complete basis.

### The Hubbard model

One of the most celebrated and simple lattice models is the Hubbard model [26, 27, 28, 29, 30]. It only considers electrons in a single band that can move from a single orbital  $i$  at one site to an orbital  $j$  at neighboring sites. Two electrons occupying the same orbital will repel each other due to the Coulomb interaction. The corresponding Hamiltonian is given by

$$\hat{H}_{\text{Hub}} = \epsilon \sum_{i\sigma} n_{i\sigma} - t \sum_{\langle ij \rangle \sigma} \hat{c}_{i\sigma}^\dagger \hat{c}_{j\sigma} + U \sum_i n_{i\sigma} n_{i-\sigma}. \quad (4.27)$$

Formally, it can be obtained from eq. (4.23) by retaining only the terms with hopping matrix elements between neighboring sites and the electron-electron interaction term with the on-site Coulomb interaction  $U_{\text{iii}}$ . However, if the Hubbard model is used to simulate a band in a solid, the effective Coulomb interaction  $U$  is smaller than the bare Coulomb integral  $U_{\text{iii}}$  by roughly one order of magnitude, because it is screened by the presence of other electrons in the system. Although constraint RPA<sup>3</sup> [84], in principle, yields an exact expression for the screened Coulomb interaction in a subspace,  $U$  can only be approximately determined for real materials. In practice, it is often taken as a parameter obtained from the analysis of photo-emission spectra.

Clearly, the Hubbard Hamiltonian neglects multiband effects. If this model is used to describe d-electron systems, it is implicitly assumed that the orbital degeneracy is lifted, e.g., due to a strong crystal-field splitting, such that low-energy excitations can be described within a single band. Furthermore, the inter-site Coulomb force is neglected. It has already been discussed in the first chapter that the long-range part of the Coulomb interaction is screened in solids which justifies the neglect of the Coulomb interaction beyond a certain screening radius. However, ignoring the inter-site interaction in the short-range part of the Coulomb force is a crude approximation that will lead to erroneous characterizations of the electronic structure of certain materials.

Despite these drastic simplifications, the Hubbard model has been studied extensively, in particular because it predicts a correlation-driven phase transition from a metallic to an insulating phase due to a correlation-induced splitting of the single band considered in eq. (4.27). Indeed, if two electrons occupy the same orbital  $i$ , the on-site Coulomb interaction  $U$  has to be paid. Mott [138] argued that this splits the band in two: the lower band is formed by electrons occupying an empty orbital and the upper one by electrons that populate an orbital already taken by another electron. With one electron per site (half-filling), the lower band would be completely filled. If the ratio  $U/t$  is larger or equal to one, the hopping between neighboring sites will be suppressed because there

<sup>3</sup>Constraint RPA is discussed in more detail in chapter 7.

is not enough energy available to bridge the energy gap between the lower and upper band. Consequently, the system becomes an insulator. For less or more than one electron per site at least one of the bands is only partially filled and the system is metallic. Hence, by manipulating the occupation of the AOs a metal-insulator transition can be induced if  $U/t \geq 1$ . The insulating state is called a Mott insulator. Today, the existence of Mott-insulating phases in real materials has been widely accepted and was observed experimentally in various transition-metal compounds (see [104] and references therein).

### Zaanen-Sawatzky-Allen classification scheme

The Hubbard model, eq. (4.27), only yields a reasonable description of the electronic d states in TMOs if the ligand p bands are far from the d states or they are strongly hybridized allowing for a description in terms of a single band. To model the electronic structure of most perovskites investigated in this work,  $\hat{H}_{\text{Hub}}$  will certainly not be sufficient, because it was already shown in the LCAO-MO description of the  $\text{TiO}_6$  coordination complex of  $\text{SrTiO}_3$  that the upper valence band states of the majority of these compounds have oxygen 2p character and only the lower conduction bands are composed of transition-metal d states. In fact, it is demonstrated in the first-principles calculations presented later-on that only in the  $\text{LaBO}_3$  series with  $B = \text{Cr}, \text{Mn}$  or  $\text{Fe}$  both valence and conduction bands are composed of d states. A more realistic description of the remaining materials is obtained from the p-d model, where the Hamiltonian takes the form

$$\hat{H}_{\text{pd}} = \hat{H}_{\text{pdt}} + \hat{H}_{\text{pdU}} + \hat{H}_{\text{pdV}} \quad (4.28)$$

with

$$\hat{H}_{\text{pdt}} = \epsilon_d \sum_{i\sigma} n_{i\sigma}^d + \epsilon_p \sum_{j\sigma} n_{j\sigma}^p - t_{\text{pd}} \sum_{\langle ij \rangle \sigma} (\hat{d}_{i\sigma}^\dagger \hat{p}_{j\sigma} + \hat{d}_{i\sigma} \hat{p}_{j\sigma}^\dagger), \quad (4.29)$$

$$\hat{H}_{\text{pdU}} = U_{\text{dd}} \sum_i n_{i\sigma}^d n_{i-\sigma}^d + U_{\text{pp}} \sum_i n_{i\sigma}^p n_{i-\sigma}^p, \quad (4.30)$$

$$\hat{H}_{\text{pdV}} = V_{\text{pd}} \sum_{\langle ij \rangle \sigma, \sigma'} n_{i\sigma}^p n_{i-\sigma'}^d. \quad (4.31)$$

It describes the hopping of electrons between p and d orbitals of a single p and a single d band located at the energies  $\epsilon_d$  and  $\epsilon_p$ . Electrons occupying a state in the d or p band that is already taken by another electron experience the on-site Coulomb repulsion  $U_{\text{dd}}$  and  $U_{\text{pp}}$ , respectively. The last term describes the Coulomb repulsion between a d and a p electron. The creation and annihilation operators  $\hat{c}_{i\sigma}^\dagger, \hat{c}_{i\sigma}$  were renamed  $\hat{d}_{i\sigma}^\dagger, \hat{d}_{i\sigma}$  and  $\hat{p}_{i\sigma}^\dagger, \hat{p}_{i\sigma}$  according to the orbitals they act on. For simplicity, it will be assumed in the further discussion that  $U_{\text{dd}} \gg U_{\text{pp}}$  such that  $U_{\text{pp}}$  can be neglected.

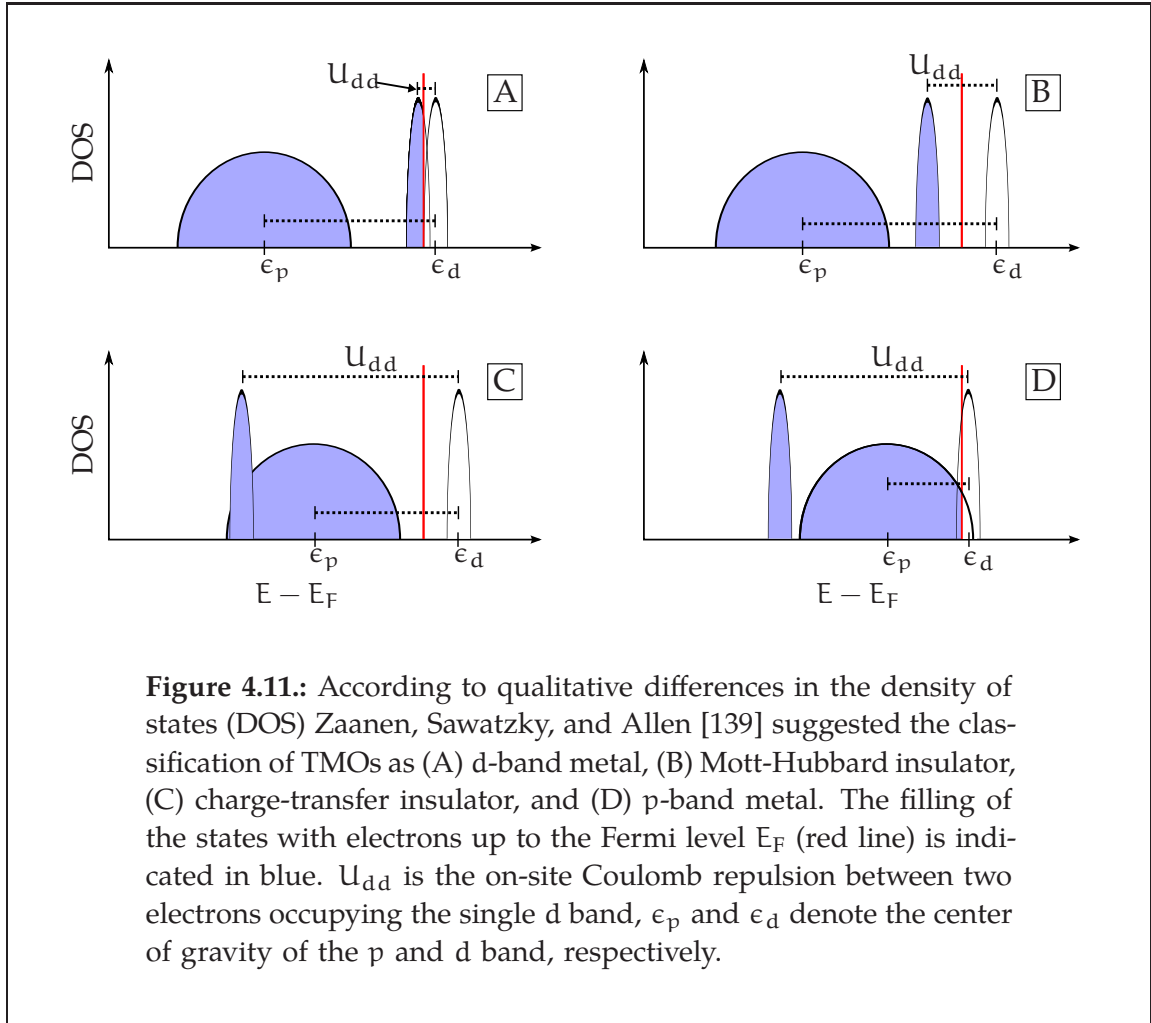


**Figure 4.11.:** According to qualitative differences in the density of states (DOS) Zaanen, Sawatzky, and Allen [139] suggested the classification of TMOs as (A) d-band metal, (B) Mott-Hubbard insulator, (C) charge-transfer insulator, and (D) p-band metal. The filling of the states with electrons up to the Fermi level  $E_F$  (red line) is indicated in blue.  $U_{dd}$  is the on-site Coulomb repulsion between two electrons occupying the single d band,  $\epsilon_p$  and  $\epsilon_d$  denote the center of gravity of the p and d band, respectively.

Zaanen, Sawatzky, and Allen (ZSA) demonstrated for a similar lattice fermionic model<sup>4</sup> that the conductivity gap and the nature of the electron and hole states in TMOs mainly depend on the relation between  $U_{dd}$  and the charge-transfer energy  $\Delta_{dp} = |\epsilon_d - \epsilon_p|$  [139]. They proposed a phase diagram allowing to classify the TMOs according to their distinct electronic structure and the nature of their conductivity gaps in particular. The phase diagram allows to distinguish between four different types of electronic structures, of which two exhibit metallic and two insulating behavior. The densities of states (DOS) of these four structures are drawn schematically in figure 4.11, where the filling of the states with electrons up to the Fermi level is indicated in blue. If the width of the p and d band denoted by  $w_p$  and  $w_d$  is defined as the distance between the middle and the edge of the band  $\epsilon_p$  or  $\epsilon_d$ , the relation between the different structures can be

<sup>4</sup>Zaanen, Sawatzky, and Allen based their discussion and calculations on the Anderson impurity model [140], which can be formally obtained from the p-d model if  $U_{pp}$  is set to zero and the term  $\hat{H}_{pdV}$  is neglected.

expressed in terms of the four model parameters  $w_p$ ,  $w_d$ ,  $U_{dd}$ , and  $\Delta_{pd}$ :

- (A) d-band metal:  $U_{dd} < 2w_d < \Delta_{dp}$ ;  $E_{\text{gap}} = 0$ .
- (B) Mott-Hubbard insulator (MHI):  $2w_d < U_{dd} < \Delta_{dp}$ ;  $E_{\text{gap}} = U_{dd} - 2w_d$ .
- (C) charge-transfer insulator (CTI):  $w_d + w_p < \Delta_{dp} < U_{dd}$ ;  $E_{\text{gap}} = \Delta_{pd} - (w_p + w_d)$ .
- (D) p-band metal:  $\Delta_{dp} < w_p + w_d < U_{dd}$ ;  $E_{\text{gap}} = 0$ .

The parameter  $\Delta_{pd}$  should not be confused with the crystal-field splitting energy  $\Delta$  introduced in the previous sections. In particular, the splitting of the d band in this model is not due to the crystal field of the ligands but it is a consequence of the Coulomb interaction between the d electrons themselves. The correlation-induced splitting leads to an energy splitting of the single d band in the model into two bands usually called lower and upper Hubbard band. Contrary to that, the crystal field induces an energy splitting between previously degenerate d orbitals. Finally, it should be mentioned that the terms MHI and CTI are sometimes used with slightly different connotations in the literature (see for example [104]). In this work, MHI and CTI will always be used as defined within the ZSA classification scheme.

#### 4.4.3. Classification of the perovskite TMOs investigated in this work

The first-principles calculations presented in the next chapter predict the d bands of the compounds with an iso-electronic configuration of the  $\text{BO}_6$  coordination complex to the  $\text{TiO}_6$  coordination complex in  $\text{SrTiO}_3$  to be completely empty. The valence bands are formed by oxygen 2p states. According to the ZSA classification scheme these materials are CTIs. However, no lower Hubbard band in the occupied part of the spectrum has been observed experimentally. This suggests that the experimental data are either not accurate enough or it indicates that correlation effects are not that strong in these materials. The latter interpretation is supported by the good agreement between experiment and the first-principles calculations. This implies that the band gaps result from the periodicity of the effective KS potential and do not result from the interplay between the charge-transfer energy  $\Delta_{dp}$  and the on-site Coulomb repulsion  $U_{dd}$ .

A detailed analysis of the band structures of the compounds  $\text{LaBO}_3$  with  $B = \text{Cr, Mn or Fe}$  presented in chapter 6 reveals that the highest occupied and the lowest unoccupied bands both have d character. According to the ZSA classification scheme these materials are MHIs. However, their insulating behavior is also described correctly in *ab initio* calculations based on the KS formalism. As discussed previously, KS-derived eigenspectra do not incorporate correlation-driven

splitting of the bands resulting directly from the term  $V_{ee}$ . On the other hand, in the model used by ZSA the splitting of the d states results from the approximate treatment of  $V_{ee}$ . In chapter 6, it is demonstrated that the splitting of the d bands is caused by the crystal field in combination with the corporate Jahn-Teller effect. As the model used by ZSA neglects these kind of effects, it does not yield a proper bases for a qualitative description of the electronic structure of these compounds.

## CHAPTER 5

# TRENDS IN THE ELECTRONIC STRUCTURE OF SELECTED PEROVSKITE TMOs

In this chapter, results from all-electron DFT (GGA) and GW calculations for band-insulating perovskite TMOs are presented that are contained in the three series  $ATiO_3$ ,  $BaBO_3$ , and  $PbBO_3$  with  $A = Ca, Sr, \text{ and } Ba$  and  $B = Ti, Zr, \text{ and } Hf$ . Numerous applications of these materials in microelectronics as dielectrics in capacitors, as the dielectric layer in dynamic random access memories (DRAMs), as substrates for high  $T_c$  superconductors, as piezoelectric materials in actuators or as non-linear optics detection devices [141, 142, 143, 144, 145, 146] can be taken as an indication for the different physical behavior of these materials in an external electric field:  $BaTiO_3$  and  $PbTiO_3$  are ferroelectric and piezoelectric at room temperature (RT),  $SrTiO_3$  and  $CaTiO_3$  are conventional dielectrics,  $BaZrO_3$  and  $BaHfO_3$  are coined high- $\kappa$  dielectrics, i.e., they are materials with an exceptionally large imaginary part  $\kappa$  of the dielectric function, and  $PbZrO_3$  and  $PbHfO_3$  are antiferroelectrics. On the other hand, optical experiments measuring the transition energies or absorption coefficients of these compounds exhibit a number of similarities of the electronic structures [147, 148, 149, 150, 146, 151]. In particular, the size of the optical band gap of all materials is comparable except for  $BaZrO_3$  and  $BaHfO_3$ , where the band gap is at least 1 eV larger than in the other materials.

A thorough understanding of many material properties can be obtained from theoretical investigations of their bulk-electronic structures. For some of the compounds of the series  $ATiO_3$ ,  $BaBO_3$ , and  $PbBO_3$ , first-principles calculations have been reported based on pseudo-potentials, e.g., references [152, 153] as well as all-electron calculations using the LAPW method, e.g., [120, 154] within the LDA and GGA and, more recently, calculations using hybrid functionals

[85, 155, 150, 15]. These investigations focused on certain aspects of the electronic structures. Results from DFT calculations using LDA or GGA underestimate the band gaps of all compounds compared to experimental data. On the other hand, hybrid-functional-based calculations yield band gaps that are too large. Although GW calculations for the two compounds BaTiO<sub>3</sub> [15] and SrTiO<sub>3</sub> [16] yield better agreement with experimental data, no GW calculations for the other compounds from the series ATiO<sub>3</sub>, BaBO<sub>3</sub>, and PbBO<sub>3</sub> have been reported so far.

The purpose of this chapter is twofold: In the first part, results from a systematic study are presented, which was carried out to investigate changes in the electronic structure of all compounds contained in the series ATiO<sub>3</sub>, BaBO<sub>3</sub>, and PbBO<sub>3</sub> originating from changes in the composition of the compounds. Results of DFT (GGA) and GW calculations employing the all-electron implementations FLEUR and SPEX are analyzed, to reveal trends in electronic structure of the valence- and low-lying conduction-band region as well as changes of the energy levels of high-lying core states (semicore states). In addition, the influence of spin-orbit coupling on the valence- and conduction-band spectra of compounds from the PbBO<sub>3</sub> series is analyzed. Secondly, the electronic structure of the compounds is described within DFT (GGA) and the GWA assuming the RT crystal phase. Deviations of the electronic structures of the compounds in the RT crystal phases from those obtained for the cubic phase are discussed. The resulting band gaps as well as energy levels of semicore states are compared to experimental data.

The chapter is organized as follows. After discussing the convergence of the numerical schemes implemented in the FLEUR and SPEX code in the calculations for perovskite TMOs in section 5.1, section 5.2 illustrates the trends in the electronic structure of the compounds from the series ATiO<sub>3</sub>, BaBO<sub>3</sub>, and PbBO<sub>3</sub>. In section 5.3, the results from DFT and GW calculations of these compounds calculated in the RT crystal structure are presented and compared to experimental data. All results are summarized and discussed in the last section.

## 5.1. Numerical aspects

To carry out electronic structure calculations with FLEUR and SPEX, a set of input parameters for each material has to be determined. In all calculations presented in this work, the lattice constants are taken from experiment. All other input parameters are obtained from the results of convergence tests. DFT calculations for perovskite TMOs with all-electron implementations similar to the FLEUR code are already well documented in the literature [120, 154]. Hence, only those aspects of FLEUR calculations are discussed corresponding to modifications of the standard procedures of DFT calculations, which are necessary to

generate data for a subsequent GW calculation with SPEX. Thus, the first part of this section primarily focuses on convergence tests of the GW results carried out with the SPEX code. The convergence of QP transition energies in SrTiO<sub>3</sub> and PbTiO<sub>3</sub> with respect to selected input parameters is analyzed in detail. Due to the chemical and structural similarities, the other perovskite TMOs show similar convergence behavior. The second part of this section deals with the representation of the unoccupied states with the help of additional LOs in FLEUR and its influence on GW calculations with SPEX.

In all convergence tests, the cubic crystal phase with 5 atoms in the unit cell is used (figure 4.1, chapter 4), because the input parameters do not explicitly depend on the geometry of the lattice. Unless noted otherwise, the BZ is sampled by a mesh of  $2 \times 2 \times 2$   $\mathbf{k}$  points and the PBE functional within the GGA is used at the DFT level. The resulting input parameters for calculations with FLEUR and SPEX are tabulated in appendix B.1 for all compounds.

### 5.1.1. Convergence of input parameters

For numerical calculations employing the LAPW basis, eq. (3.3), the plane-wave cutoff  $G_{\max}$  and the cutoff  $l_{\max}$  for the angular momentum of the LAPW basis functions have to be determined. To guarantee a smooth matching of the basis functions across the MT border these two parameters may not be chosen independently. As pointed out in section 3.2.1, chapter 3, a reasonable choice of the  $l$  cutoff is  $l_{\max}^a = s_a G_{\max}$ , where  $s_a$  denotes the MT radius of the  $a$ -th atom in the unit cell. For all materials studied here, a choice of  $G_{\max} = 4.4 \text{ bohr}^{-1}$  is sufficient to converge the KS eigenvalues of the valence and low-lying conduction bands to within 0.01 eV. However, in GW calculations the knowledge of the unoccupied KS eigenvalues and eigenstates up to high energies is also required. They enter into the equation for the correlation self-energy, eq. (3.40), through the Green function  $G$ , eq. (2.82), as well as the screened interaction  $W$ , eq. (2.77). To generate enough eigenfunctions and eigenstates a  $G_{\max}$  of at least  $5 \text{ bohr}^{-1}$  has to be chosen and the values for  $l_{\max}$  have to be modified accordingly. Furthermore, the flexibility of the basis in the MT spheres must be improved to guarantee an accurate description of the high-lying KS eigenstates. In this work, LOs located in the unoccupied bands are added to the LAPW basis to enhance its flexibility. These changes in the LAPW basis can have a large impact onto the results of FLEUR and SPEX calculations and are therefore discussed separately in the next section. Convergence tests from SPEX calculations will be discussed in the following.

The test results from SPEX calculations for SrTiO<sub>3</sub> and PbTiO<sub>3</sub> shown in the first row of figure 5.1 emphasize the importance of unoccupied states. At least

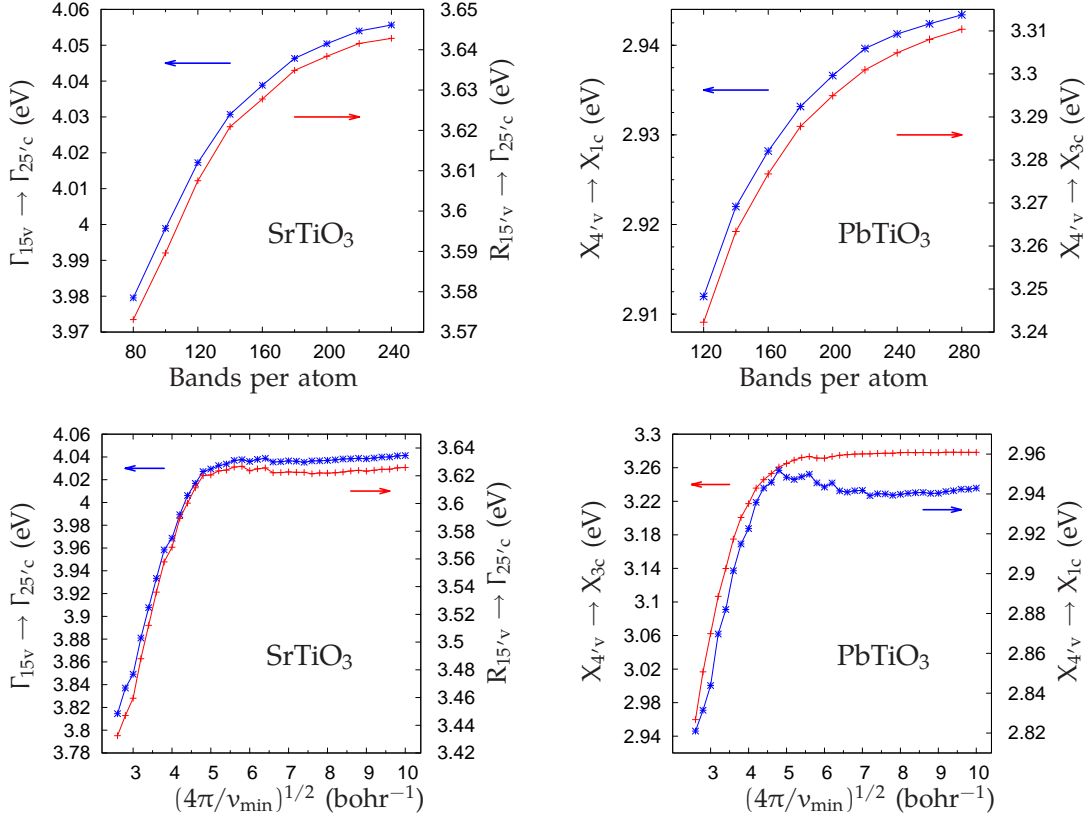


**Figure 5.1.:** Top row: Convergence of the  $\Gamma_{15v} \rightarrow \Gamma_{25'c}$  and  $R_{15'v} \rightarrow \Gamma_{25'c}$  gaps of SrTiO<sub>3</sub> (left) and the  $X_{4'v} \rightarrow X_{1c}$  and  $X_{4'v} \rightarrow X_{3c}$  gaps of PbTiO<sub>3</sub> (right) with respect to the number of bands per atom. Bottom row: Convergence of the same gaps as in the top row as functions of  $(4\pi/v_{\min})^{1/2}$ .

180 bands per atoms are necessary to converge the QP transitions  $\Gamma_{15v} \rightarrow \Gamma_{25'c}$  and  $R_{15'v} \rightarrow \Gamma_{25'c}$  in SrTiO<sub>3</sub> and  $X_{4'v} \rightarrow X_{3c}$  in PbTiO<sub>3</sub> to within 0.01 eV, but only the first 20 bands of SrTiO<sub>3</sub> and 22 bands of PbTiO<sub>3</sub> are occupied in the ground state. The transition  $X_{4'v} \rightarrow X_{1c}$  in PbTiO<sub>3</sub> is exceptional, because it converges much faster than the other three with respect to the maximal number of bands  $n_{\max}$ . A closer look at the final states of the transitions reveals that  $X_{1c}$  has mostly Pb 6p character whereas  $\Gamma_{25'c}$ ,  $\Gamma_{25'c}$  in SrTiO<sub>3</sub> and  $X_{3c}$  in PbTiO<sub>3</sub> all are nearly pure Ti 3d states. The test calculations for all materials show that the self-energy correction for d states converges much slower with respect to  $n_{\max}$  than the respective correction for the s and p state. As the initial states of the transitions in SrTiO<sub>3</sub> and PbTiO<sub>3</sub> all have oxygen 2p character, the discrepancy in the speed of convergence originates from the different characters of the conduction band states.

As mentioned previously, the unoccupied states enter into GW calculations in

the evaluation of matrix elements of the correlation self-energy via the Green function and the screened interaction  $W$ . The calculations of the matrix  $W$  can be optimized by introducing a threshold value  $v_{\min}$  as explained in section 3.3.1, chapter 3, which leads to a reduction of the rank of the matrix. This speeds up calculations considerably and also decreases the amount of storage necessary to save the matrix during calculations. According to reference [20], the threshold value  $v_{\min}$  can be reformulated in terms of a cutoff value in reciprocal space  $|\mathbf{k}+\mathbf{G}| = \sqrt{4\pi/v_{\min}}$  similar to the plane-wave cutoff for the LAPW basis functions. In the second row of figure 5.1 the convergence of QP transitions of SrTiO<sub>3</sub> and PbTiO<sub>3</sub> as functions of  $\sqrt{4\pi/v_{\min}}$  is shown. As explained in reference [20], steps in the curves can be interpreted as the contribution from additional shells of reciprocal lattice vectors. For example, the step at 5.8 bohr<sup>-1</sup> in the curve of SrTiO<sub>3</sub> for the transition  $\Gamma_{15v} \rightarrow \Gamma_{25'c}$  is caused by a shell of reciprocal lattice vectors entering between 5.5 and 6.0 bohr<sup>-1</sup>. Convergence of the transitions of SrTiO<sub>3</sub> to within 0.01 eV is attained for  $\sqrt{4\pi/v_{\min}} = 5.5$  bohr<sup>-1</sup>, and the rank of the matrix  $W$  is 708 for this choice of the cutoff radius. For comparison,  $\sqrt{4\pi/v_{\min}} = 10.0$  bohr<sup>-1</sup> corresponds to a rank of 1473. The results for PbTiO<sub>3</sub> converge more slowly. The rank of the matrix  $W$  can be reduced to 1000 with the choice  $\sqrt{4\pi/v_{\min}} = 6.5$  bohr<sup>-1</sup> (1454 for  $\sqrt{4\pi/v_{\min}} = 10.0$  bohr<sup>-1</sup>). Furthermore, a qualitative difference in the curves for the two QP transitions of PbTiO<sub>3</sub> can be observed, but convergence of both transitions to within 0.01 eV is reached around the same value of  $\sqrt{4\pi/v_{\min}}$ . (Note the different energy scales for both transitions.)

To determine the polarization function given by eq. (2.83) as well as the exchange self-energy, eq. (3.32), products of KS wave functions have to be calculated. These products are represented in terms of the MPB in SPEX, which consists of radial functions for the regions in space occupied by MT spheres and plane waves in the interstitial region called interstitial plane waves (IPWs). The radial functions of the MPB are constructed from products of radial functions contained in the LAPW basis according to eqs. (3.12) and (3.14). For each atom, a cutoff value  $L_{\max}$  for the angular momentum of the MPB radial functions has to be chosen. Furthermore, a plane-wave cutoff  $G'_{\max}$  for the IPWs has to be determined.

For convenience, the cutoff values for  $L_{\max}$  of the radial functions of Ti, O, Sr, and Pb were set to the same value in all test calculations. An exact representation of the products of LAPW basis functions would require to choose the cutoff values  $L_{\max}$  to be twice as large as the corresponding  $l$  cutoff of the LAPW radial functions. However, the test results in figure 5.2 show that a value of  $L_{\max} = 6$  for Sr and  $L_{\max} = 7$  for Pb is sufficient to attain convergence of the QP transitions as opposed to  $l_{\max} = 12$  for Sr and  $l_{\max} = 14$  for Pb in the respective FLEUR calculation. Likewise, a plane-wave cutoff  $G'_{\max} = 2G_{\max}$  would be necessary to

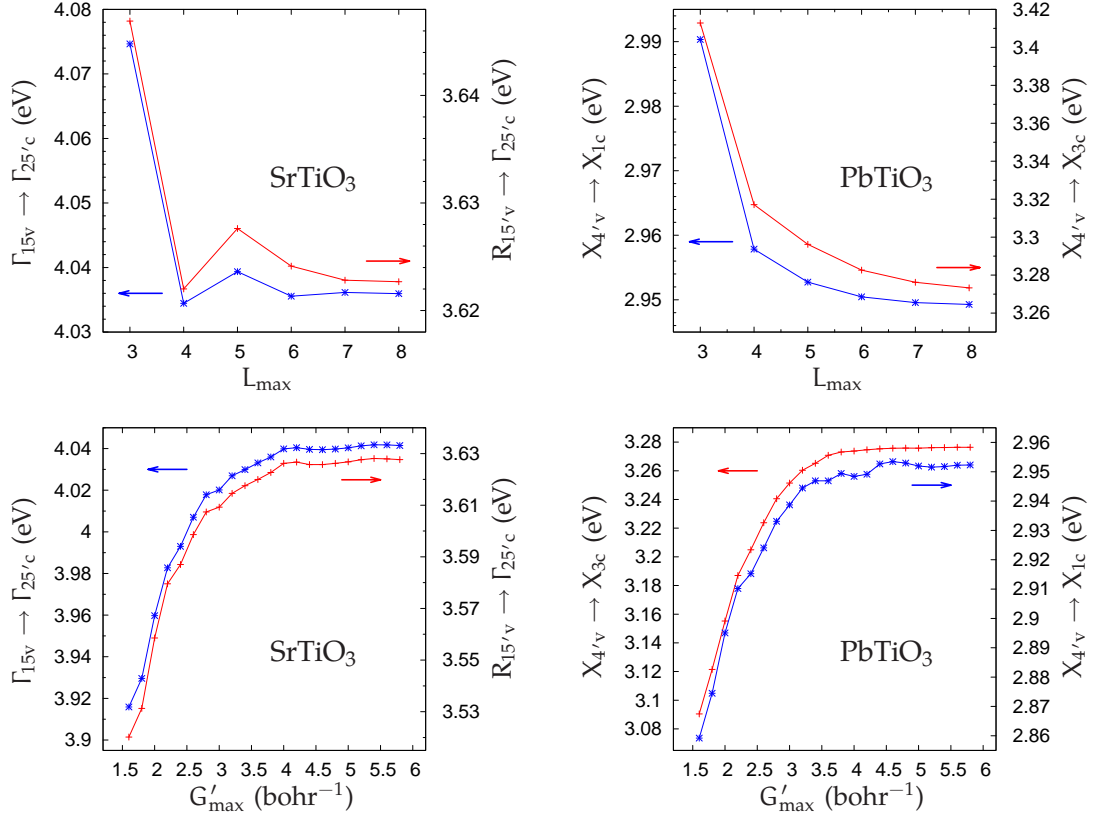


**Figure 5.2.:** Top row: Convergence of the  $\Gamma_{15v} \rightarrow \Gamma_{25c}$  and  $R_{15/v} \rightarrow \Gamma_{25c}$  gaps of  $\text{SrTiO}_3$  (left) and the  $X_{4/v} \rightarrow X_{1c}$  and  $X_{4/v} \rightarrow X_{3c}$  gaps of  $\text{PbTiO}_3$  (right) as functions of the MPB cutoff parameter  $L_{\text{max}}$  for the angular momentum. **Bottom row:** Convergence of the same gaps as in the top row as functions of the MPB cutoff parameter  $G'_{\text{max}}$  for the IPWs.

exactly represent wave-function products in the interstitial region, but  $4.0 \text{ bohr}^{-1}$  and  $5.0 \text{ bohr}^{-1}$  suffice to converge the QP transitions of  $\text{SrTiO}_3$  and  $\text{PbTiO}_3$  as demonstrated in the second row of figure 5.2. In contrast, plane-wave cutoffs of  $G_{\text{max}} = 5.8 \text{ bohr}^{-1}$  and  $G_{\text{max}} = 6.0 \text{ bohr}^{-1}$  for the LAPW basis functions were chosen. The same trends in the convergence of the representation of wave-function products in terms of the MPB were reported in references [20, 85] and a detailed discussion can be found there. Here, it is yet worth mentioning that the LOs contained in the LAPW basis can be selected manually in the construction of the MPB, which can help to further reduce the number of MPB basis functions. Furthermore, the energy derivatives of the radial functions contained in the LAPW basis can be omitted in the construction of the MPB in all calculations without any loss of accuracy.

Since the GW self-energy is a non-local operator, eqs. (3.32) and (3.40) yielding matrix elements of the exchange and correlation self-energy calculated at a given

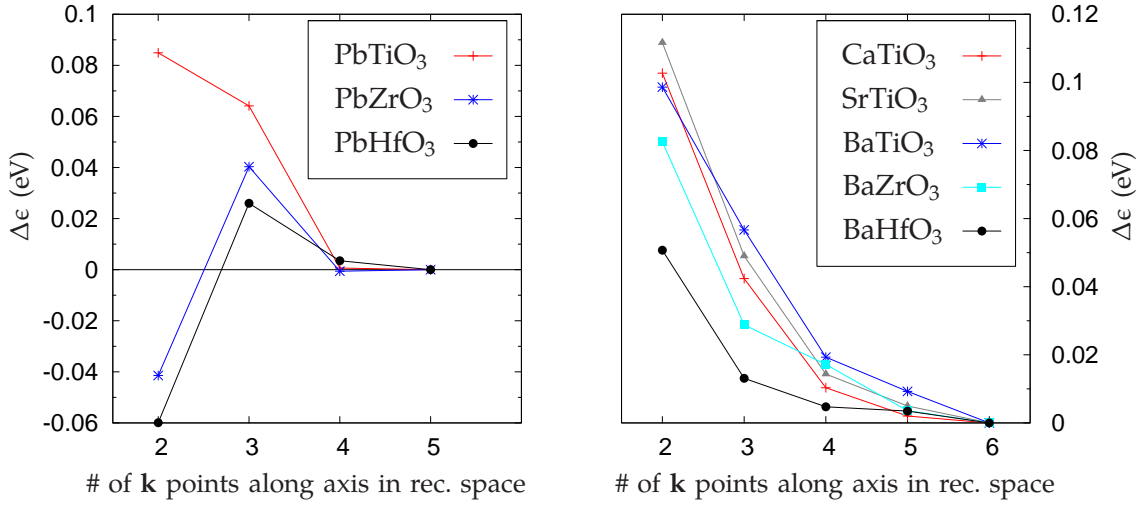


**Figure 5.3.:** The graphs show the QP gaps  $E_{\text{gap}}^{\text{QP}}$  at the X (*left*) and  $\Gamma$  (*right*) point as functions of the number of  $\mathbf{k}$  points  $N$  used to sample the BZ by  $N \times N \times N$   $\mathbf{k}$ -point meshes. The energy differences are calculated according to  $\Delta\epsilon = E_{\text{gap}}^{\text{QP}}(N) - E_{\text{gap}}^{\text{QP}}(N_{\text{max}})$  with  $N_{\text{max}} = 5$  (*left*) and  $N_{\text{max}} = 6$  (*right*).

$\mathbf{k}$  point comprise summations over all other  $\mathbf{k}$  points in the BZ. Thus, the QP transitions become a function of the number of  $\mathbf{k}$  points used to sample the BZ. The  $\mathbf{k}$ -point meshes used in SPEX calculations are defined in eq. (3.41). In all test calculations,  $N_x \times N_y \times N_z$   $\mathbf{k}$ -point meshes were used with  $N_x = N_y = N_z = N$ . For the perovskite TMOs containing Pb the energy of the QP transition  $X_{4'v} \rightarrow X_{3c}$  was determined for  $N = 5$ . The left graph in figure 5.3 shows the energy differences  $\Delta\epsilon$  between this transition energy and the energies obtained from calculations employing  $\mathbf{k}$ -point meshes with  $N < 5$ . Convergence of the gaps of all three materials to within 0.01 eV is attained with a  $4 \times 4 \times 4$   $\mathbf{k}$ -point mesh. On the right side in figure 5.3 the results of similar test calculations for the remaining perovskite TMOs are illustrated. Here, the energy of the QP transition  $\Gamma_{15v} \rightarrow \Gamma_{25'c}$  obtained with  $N = 6$  is compared to the transition energies from calculations with less numbers of  $\mathbf{k}$  points. To converge the results for these materials a mesh of at least  $5 \times 5 \times 5$   $\mathbf{k}$  points has to be used.

Finally, input parameters for SPEX calculations are required, which determine the number of frequencies used in the evaluation of the Hilbert transformation in eq. (3.37) as well as the frequency mesh used for the representation of the resulting matrix elements of the polarization function  $P_{IJ}(\mathbf{k}, \omega)$ . The choice of these parameters has already been discussed in section 3.3.1, chapter 3. Some comments on the choice of frequency intervals necessary to solve the integral in eq. (3.40) have been given there as well. The QP transitions converge quickly as functions of these parameters.

As mentioned at the beginning of this section, the input parameters do not depend on the number of atoms per unit cell. Hence, the parameters obtained for the cubic crystal phases should be used in calculations for the same materials in the room-temperature crystal phases presented in section 5.3. However, it was not possible in calculations for materials with 20 ( $\text{CaTiO}_3$ ) or 40 ( $\text{PbZrO}_3$ ,  $\text{PbHfO}_3$ ) atoms per unit cell to use as many bands per atom as in the calculations for the cubic crystal phases with 5 atoms per unit cell, because it would require more working memory than provided by the conventional personal computer used in this work. Therefore, the input parameters had to be changed for these calculations (see appendix B.1) such that convergence of QP transition energies to within 0.05 eV instead of 0.01 eV was achieved for these systems. In this context, it is worth mentioning that the present GW implementation in SPEX only runs on a single processor. As the unoccupied states only enter in the calculation of the correlation contribution to the self-energy, a simple parallelization of this particular part of the code, which redistributes this task between several processors, should allow to include more unoccupied states in calculations for large systems or speed up calculations for smaller systems.

### 5.1.2. Convergence of the representation of the unoccupied states

The LAPW basis functions, eq. (3.3), are defined by an expansion around fixed energy parameters  $\epsilon_{\alpha l}^{\sigma}$  such that an accurate representation of the KS wave functions is only obtained in the neighborhood of these energies. Typically, the energy parameters are located in the valence band close to the Fermi level such that valence states are described accurately. Note that only occupied states are needed to calculate the electron density which is the central ingredient of DFT. Unoccupied states are described less accurately by the conventional LAPW basis, which might lead to errors in the QP energies obtained from the GWA, because the correlation self-energy, eq. (3.40), and the screened interaction  $W$ , eq. (2.77), depend on the unoccupied states up to high energies.

In order to enhance the basis-set flexibility, it is not sufficient to simply increase the plane-wave cutoff  $G_{\max}$ , since this only improves the basis set in the interstitial region but not within the MT spheres. Krasovskii demonstrated [96] that a fairly small  $G_{\max}$  is sufficient to provide enough flexibility in the interstitial region. However, the MT part of the LAPW basis quickly deteriorates the more the wave-function energies deviate from the parameter  $\epsilon_{\alpha l}^{\sigma}$ . This inadequacy cannot be overcome by increasing  $G_{\max}$ .

In this work LOs located in the conduction bands are used to enhance the flexibility of the MT part of the LAPW basis functions. The construction of these

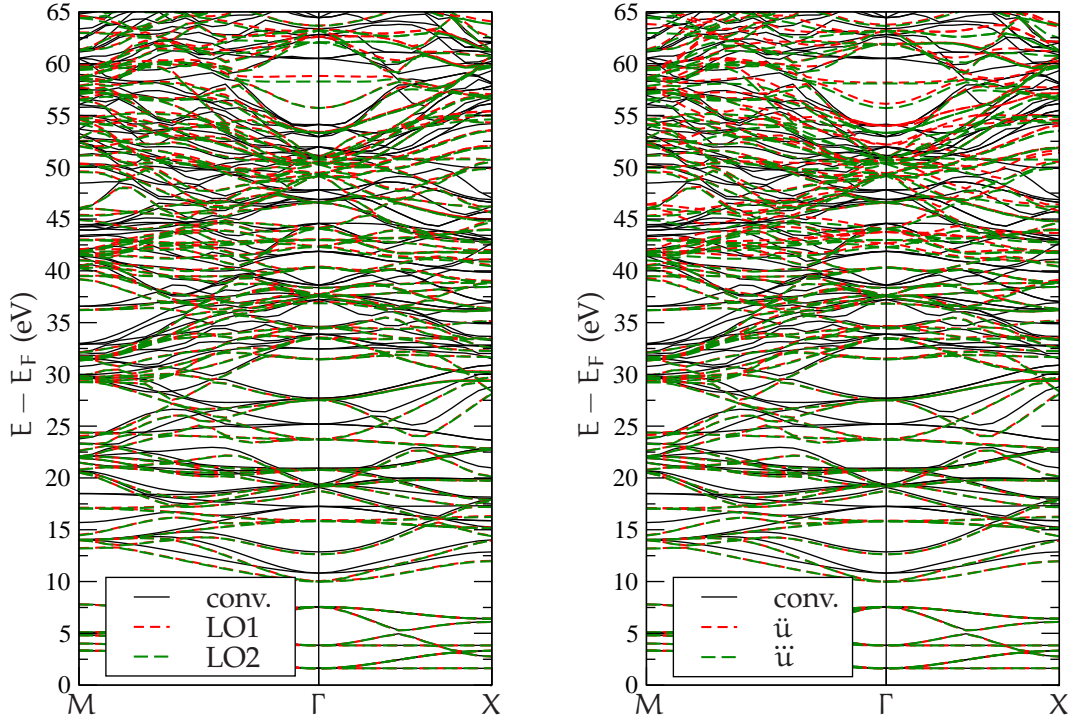


**Figure 5.4.:** Comparison of KS band structures of  $\text{PbTiO}_3$  calculated in the cubic unit cell with two different  $\text{LAPW}^{\text{unocc}}$  basis sets LO1 and LO2 on the *left* and basis sets  $\ddot{u}$  and  $\ddot{u}\ddot{u}$  comprising LOs, which represent higher-order energy derivatives of the radial functions in the LAPW basis, on the *right*. Black lines illustrate the results obtained from the conventional LAPW basis.

LOs and the determination of their energy parameters  $\epsilon_{\text{al}}^{\sigma, \text{lo}}$  is described in section 3.1.3, chapter 3. In the further discussion, the LAPW basis sets including LOs located in the unoccupied part of the energy spectrum are called  $\text{LAPW}^{\text{unocc}}$  basis. These basis sets are similar to those used in [96] although no energy derivatives of the LOs are included here. Alternative approaches to enhance the flexibility of the LAPW basis were introduced by Friedrich *et al.* [156] as well as Boss and Fehrenbach [157]. The latter used spline functions to gain more flexibility whereas Friedrich *et al.* added LOs to the conventional LAPW basis defined as second and higher energy derivatives of solutions of the scalar-relativistic KS Dirac equation, eq. (3.27).

To compare the ansatz of Friedrich *et al.* with the scheme employing  $\text{LAPW}^{\text{unocc}}$  basis sets, DFT (GGA) calculations for  $\text{PbTiO}_3$  were conducted employing four different basis sets. The  $\text{LAPW}^{\text{unocc}}$  basis denoted LO1 contains LOs for the lowest unoccupied  $s$ ,  $p$ ,  $d$ , and  $f$  states of each atom in the unit cell. The basis  $\ddot{u}$

comprises the same number of LOs representing second-order energy derivatives of the solutions of the scalar-relativistic KS Dirac equation for the corresponding  $l$  quantum numbers. Likewise, LO2 is constructed by adding LOs for the lowest and second-lowest unoccupied  $s$ ,  $p$ ,  $d$ , and  $f$  states and  $\ddot{u}$  by adding second- and third-derivative LOs to the conventional LAPW basis. To compare the representation of the unoccupied states obtained from the four different basis sets figure 5.4 shows parts of the KS band structure of  $\text{PbTiO}_3$  calculated in the cubic unit cell. Apart from the differences in the basis sets, the same input parameters listed in appendix B.1 were used in all calculations. For comparison, the band structure calculated with the conventional LAPW basis is also shown.

Direct band gap at $\Gamma$ point				
	without LOs		with LOs	
	DFT	GW	DFT	GW
$\text{CaTiO}_3$	2.34	4.05	2.34	4.11
$\text{SrTiO}_3$	2.24	3.91	2.23	3.96
$\text{BaTiO}_3$	1.91	3.39	1.91	3.46
$\text{BaZrO}_3$	3.43	4.82	3.43	5.20
$\text{BaHfO}_3$	3.77	5.17	3.76	5.58

Direct band gap at X point				
	without LOs		with LOs	
	DFT	GW	DFT	GW
$\text{PbTiO}_3$	1.62	2.94	1.63	2.98
$\text{PbZrO}_3$	2.46	3.19	2.44	3.28
$\text{PbHfO}_3$	2.47	3.31	2.47	3.37

**Table 5.1.:** Comparison of DFT and QP band gaps obtained from calculations using basis sets with and without additional LOs located in the conduction band.

of Friedrich *et al.*, because the energies obtained from LO1 deviate from those using LO2 only above 58 eV. In contrast, deviations in the energies calculated with  $\ddot{u}$  and  $\ddot{u}$  already occur above 43 eV.

Friedrich *et al.* demonstrated that the representation of the unoccupied states can be converged to the results of an APW-like approach, which contains no energy-linearization errors, by systematically including higher-order energy derivatives of the radial functions into the LAPW basis. In figure 5.4, the energies obtained with LO2 and  $\ddot{u}$  illustrated by green dashed lines in each graph are almost identical in the whole energy range displayed here. Hence, basis-set completeness can be attained by augmenting the conventional LAPW basis with LOs either located in the conduction bands or defined as higher energy derivatives. The single-particle energies tend towards smaller values in the basis-set limit as a consequence of the variational principle. Furthermore, figure 5.4 shows that the representation in terms of  $\text{LAPW}^{\text{unocc}}$  basis sets converges faster with respect to the number of additional LOs than the ansatz

For a quantitative analysis of these results, figure 5.5 shows the energy differences of the single-particle energies at the  $\Gamma$  point between results obtained with  $\ddot{u}$  and  $\ddot{u}$  (A), LO1 and LO2 (B), and between LO2 and  $\ddot{u}$  (C). The latter proves, that both schemes indeed converge to the same results. Furthermore, (A) and (B) illustrates that the results from  $\ddot{u}$  deviate much more from the reference energies obtained with  $\ddot{u}$  than the energies calculated with LO1 differ from those obtained with LO2. Since  $\ddot{u}$  and LO1 contain the same number of additional LOs, it can be concluded that less LOs are needed in the construction of an  $\text{LAPW}^{\text{unocc}}$  basis than in the ansatz by Friedrich *et al.* to achieve the same level of accuracy. This makes the  $\text{LAPW}^{\text{unocc}}$  basis set more efficient, which is especially important for the investigation of materials with many atoms per unit cell. Therefore,  $\text{LAPW}^{\text{unocc}}$  basis sets are used throughout this work. For the sake of completeness it should be mentioned that an advantage of the approach of Friedrich *et al.* is that no additional energy parameters are needed other than those already used in the construction of the conventional LAPW basis functions.

To analyze the effect of the representation of the unoccupied states in terms of  $\text{LAPW}^{\text{unocc}}$  basis sets on the QP energies obtained within the GWA, the QP band gaps of the cubic crystal phases of all perovskite TMOs studied in this chapter are listed in table 5.1. For comparison, results from calculations employing the conventional LAPW basis as well as the band gaps resulting from the corresponding DFT calculations are shown. The input parameters for the DFT and the GW calculations including the number of local orbitals used in the construction of the  $\text{LAPW}^{\text{unocc}}$  basis sets can be found in appendix B.1.

The KS band gaps of all materials in table 5.1 obtained from the two basis sets differ by less than 0.02 eV although the unoccupied states do not enter explicitly in the self-consistent solution of the KS equation (2.17). However, the additional LOs in the  $\text{LAPW}^{\text{unocc}}$  basis do not only affect the representation of the unoccupied states but also slightly improve the representation of the occupied states. This leads in turn to small deviations in the single-particle density,

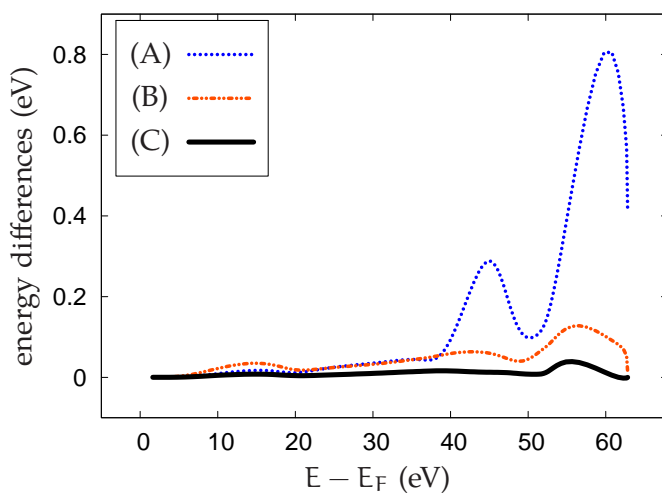


**Figure 5.5:** Deviations between the KS eigenvalues of  $\text{PbTiO}_3$  at the  $\Gamma$  point obtained from different basis sets. The curve (A) represents the energy differences between results from calculations using  $\ddot{u}$  and  $\ddot{u}$ , (B) and (C) the differences employing LO1 and LO2 and LO2 and  $\ddot{u}$ , respectively. The curves are smoothed using a Bezier algorithm for clarity.

eq. (2.18). Since the density reenters into the self-consistency cycle, the changes in the basis-set representation of the KS eigenstates also have a small influence on the KS band gaps.

Apart from the KS eigenvalues, expectation values  $\langle V_{xc} \rangle$  and  $\langle \Sigma_x \rangle$  of the exchange correlation potential, eq. (2.16), and the exchange self-energy, eq. (3.32) as well as expectation values of the correlation self-energy, eq. (3.40), enter into the evaluation of the QP equation, eq. (2.93). The exchange-correlation potential and the exchange self-energy are both independent of the unoccupied states. Hence, changes in  $\langle V_{xc} \rangle$  and  $\langle \Sigma_x \rangle$  are smaller than 0.02 eV and originate from the changes in the basis-set representation described above. The main effect on the QP energies is due to the expectation values of the correlation self-energy, which depends explicitly on the unoccupied part of the spectrum through the Green function  $G$ , eq. (2.82), and the screened interaction  $W$ , eq. (3.39). In particular, the effect on  $G$  due to changes in the representation of the unoccupied states is larger than the effect on  $W$ . A calculation of the QP band gap of  $\text{BaZrO}_3$  yields a value of 5.01 eV if additional LOs located in the conduction bands are only taken into account to obtain  $G$ . On the other hand, a value of 4.86 eV is obtained if the LOs are only included in the calculation of  $W$ . Table 5.1 shows that the effects from the augmentation of the conventional LAPW basis on the QP band gaps are strongest for the large-gap insulators  $\text{BaZrO}_3$  and  $\text{BaHfO}_3$ .

In practice, the number of additional LOs used in the construction of the  $\text{LAPW}^{\text{unocc}}$  basis sets and the MPB has yet to be determined. This is done in two steps. First, the maximum number of bands  $n_{\text{max}}$  necessary to converge the QP spectrum in a GW calculation with SPEX is obtained from convergence tests. The number  $n_{\text{max}}$  directly determines the highest KS eigenvalue  $\epsilon_{\text{max}}$  entering into the GW calculations. In a second step, the basis representation of the KS eigenstates up to the energy  $\epsilon_{\text{max}}$  is converged in FLEUR calculations by adding LOs to the LAPW basis. As a rule of thumb, convergence of the basis-set representation is attained if all LOs with energy parameters  $\epsilon_{\text{al}}^{\sigma, \text{lo}} \leq 0.7\epsilon_{\text{max}}$  are taken into account. However, test calculations for the materials listed in table 5.1 show that it is usually not necessary to include all of these LOs in the construction of the MPB as well. It is sufficient to only include few LOs for the lowest unoccupied states in the construction of the MPB to achieve convergence of QP band gaps to within 0.01 eV.

The input parameters obtained from the test calculations discussed in the previous section together with the improved LAPW and mixed-product basis sets were applied in DFT and GW calculations for the perovskite TMOs comprising the series  $\text{ATiO}_3$ ,  $\text{BaBO}_3$ , and  $\text{PbBO}_3$  to study trends in their electronic structures. The results of these calculations are presented in the next part of this chapter.

## 5.2. Trends in the electronic structure

In this section, KS and QP spectra obtained from DFT (GGA) and GW calculations are analyzed to reveal, which changes in the electronic structure of the perovskite TMOs can be related to changes in their chemical composition. In the first part of the section, the valence- and low-lying conduction-band spectra of the following three series are analyzed: the series  $ATiO_3$  with  $A = Ca, Sr,$  and  $Ba$ , the series  $BaBO_3$  with  $B = Ti, Zr,$  and  $Hf$ , and finally the series  $PbBO_3$  with  $B = Ti, Zr,$  and  $Hf$ . All compounds in the series crystallize in the cubic crystal phase (figure 4.1, chapter 4) at high temperatures. To suppress changes in the electronic structure due to lattice distortions all calculations were carried out for this phase. The second part deals with additional changes in the valence- and conduction-band spectra of compounds from the  $PbBO_3$  series that may arise from the influence of spin-orbit coupling (SOC). Although GW calculations, which fully incorporate the SOC, are not feasible for these materials at present, the results from DFT-based calculations allow to estimate the influence of the SOC on the valence- and conduction-band spectra. In the third and last part of the section, trends in the position of the energy levels of semicore states obtained from DFT calculations are compared to results from GW and non-self-consistent Hartree-Fock (HF) calculations.

### 5.2.1. Valence- and conduction-band spectra

Before the KS and QP band structures of the perovskite TMOs are compared in detail, general trends observed for all materials shall be summarized: At first sight, the KS band structures illustrated by the blue dots in the three figures 5.6, 5.9, and 5.12 reveal that the valence bands of all compounds are largely composed of oxygen 2p states, whereas the d states of the transition metals Ti, Zr, and Hf strongly contribute to the formation of the low-lying conduction bands. This composition of the valence and conduction bands has been predicted with the help of MO theory using the simplified LCAO ansatz to describe the electronic structure of the  $TiO_6$  octahedra summarized in the LCAO-MO diagram in figure 4.10, chapter 4. However, the first-principle calculations also show that Pb 6s and 6p states yield dominant contributions in the formation of the valence- and conduction-band spectra of the three compounds  $PbTiO_3$ ,  $PbZrO_3$ , and  $PbHfO_3$ . This cannot be described by the simple ansatz used to derive the qualitative picture of the valence- and conduction-band spectra illustrated in the LCAO-MO diagram.

The analysis of the QP correction  $\Delta E_{nk\sigma}^{GW}$  obtained from the GW calculations, which is illustrated in figures 5.8, 5.11, and 5.14 for selected  $\mathbf{k}$  points, reveals that the valence bands are lowered in energy, whereas the energy levels of the

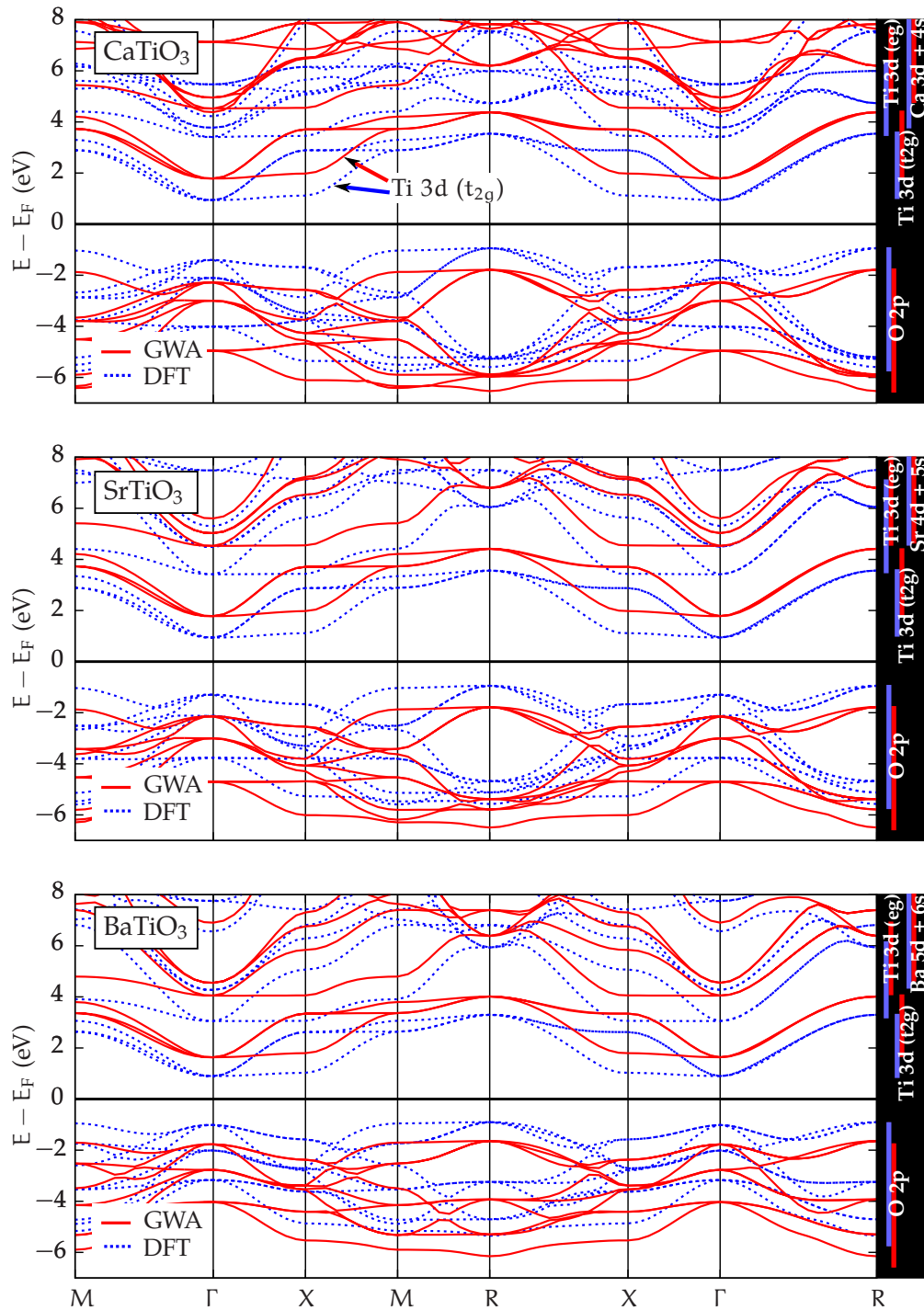


**Figure 5.6.:** KS (blue) and QP (red) band structures of CaTiO<sub>3</sub> (top), SrTiO<sub>3</sub> (middle) and BaTiO<sub>3</sub> (bottom). The Fermi energy is placed in the middle of the KS and QP gap, respectively. The bars on the right indicate the orbital character of the bands.

conduction-band states are raised, which leads to an increase of the band gap of all compounds. To illustrate the two effects graphically, the Fermi energy was placed in the middle of the calculated KS and QP band gaps in figures 5.6, 5.9, and 5.12. To understand the origin of the two effects, a closer look at eq. (2.96) for the QP energies as obtained within the GWA is necessary. Rewriting this equation in the following form

$$E_{nk}^{\sigma} = \epsilon_{nk}^{\sigma} + \Delta E_{nk\sigma}^{\text{GW}} \quad (5.1)$$

emphasizes that the QP spectra  $E_{nk}^{\sigma}$  calculated within the GWA is obtained from the KS band structure  $\epsilon_{nk}^{\sigma}$  due to an energy shift  $\Delta E_{nk\sigma}^{\text{GW}}$  for each band  $n$  at each  $\mathbf{k}$  point and for each spin direction  $\sigma$ . This energy shift leads to

- *a partial correction of the self-interaction error* inherent to the conventional KS scheme within GGA by including contributions from the exchange energy, eq. (2.41), in  $\Delta E_{nk\sigma}^{\text{GW}}$  which leads to the decrease of the energies of the valence band states in the QP band structure, as well as
- *a partial compensations of the lack of the exchange-correlation discontinuity* in GGA (cf. section 2.2.4, chapter 2), which results in the increase of the energy levels of the conduction band states.

Furthermore, a thorough analysis of the QP band structures reveals that the size of the energy correction  $\Delta E_{nk\sigma}^{\text{GW}}$  for a certain band  $n$  at a given  $\mathbf{k}$  point strongly depends on the character of the orbitals contributing to the formation of this band. In the following, details of the KS and QP band structures will be discussed.

### **ATiO<sub>3</sub>, A = Ca, Sr, Ba**

Figure 5.6 shows that the KS band structures of all three compounds ATiO<sub>3</sub>, A = Ca, Sr, Ba are virtually identical in the energy range between  $-6$  and  $+3$  eV. From the projection of the KS eigenfunctions  $\varphi_{nk}(\mathbf{r})$  onto the LAPW basis functions, the eigenfunctions at each  $\mathbf{k}$  point and for each band index  $n$  can be decomposed into an interstitial and a MT part [eq. (3.48), chapter 3]. The MT contributions can be further divided into contributions from radial functions representing the atomic-like orbitals of the distinct atomic species [eq. (3.49), chapter 3]. This analysis reveals that the bands of all three compounds between  $-6$  and  $-1$  eV are mostly composed of oxygen 2p states. Furthermore, the three conduction bands lowest in energy have almost pure Ti 3d character. In reference to the CF and MO theory, these states are labeled  $t_{2g}$ . Consequently, the two bands at higher energies between  $+3$  and  $+5$  eV, which also primarily consist of contributions from the Ti 3d states, are labeled  $e_g$  states. As in CF or MO theory these bands are completely separated. The smallest band gap in all three compounds corresponds to the indirect transition between R and  $\Gamma$ . The smallest direct transition occurs

at the  $\Gamma$  point. Moreover, the hysteresis-like shape originating from the  $t_{2g}$  states of the transition metal, which is formed along the high-symmetry lines between  $\Gamma$  to X and X to M of the BZ, is a characteristic feature of  $t_{2g}$  bands and is present in the electronic structure of all perovskites in the cubic crystal phase studied in this section.

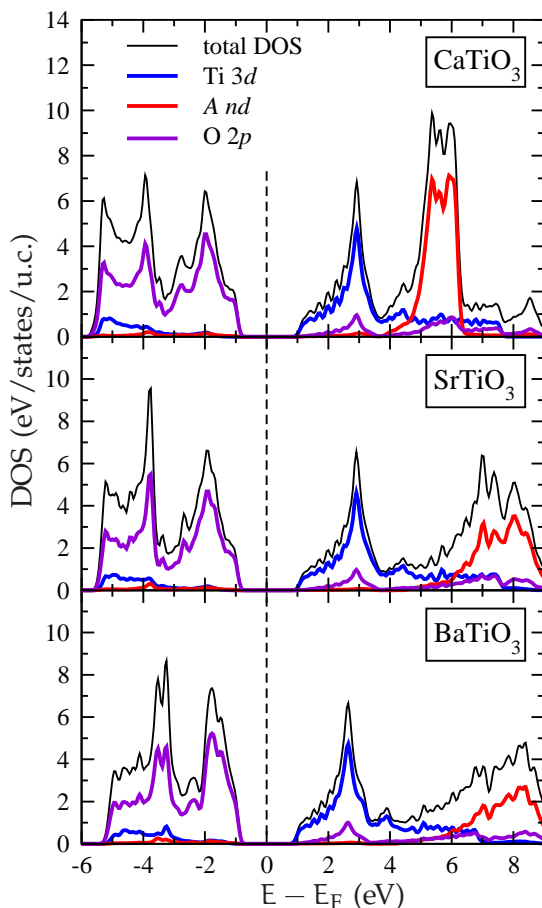


**Figure 5.7.:** Total DOS (black) of  $\text{CaTiO}_3$  (top),  $\text{SrTiO}_3$  (middle), and  $\text{BaTiO}_3$  (bottom) and the pDOS of Ti 3d (blue), O 2p (violet), and of the d states of Ca, Sr, and Ba (red) obtained from DFT calculations.

increases throughout the series  $\text{ATiO}_3$ . As this increase translates into an increase of the distance between the Ti cation and the oxygen anions it should reduce the electrostatic repulsion between electrons occupying the orbitals of oxygen and Ti. However, there are additional effects such as changes in the crystal potential due to substitution of the A cation which may also influence the size of the band gaps. The complexity of the first-principles scheme does not allow to attribute

The d and s states of the A cations of Ca, Sr and Ba only yield significant contributions to the formation of the bands above +4 eV. Hence, the shape as well as the energy positions of the valence and low-lying conduction bands are nearly identical in all three materials. In particular, the d states of the A cations do not hybridize with the states constituting the valence-band maximum (VBM) or the conduction-band minimum (CBM) in any of the three compounds. This is demonstrated in figure 5.7, where the contribution of the A cation's d state to the total DOS is illustrated. Figure 5.7 also shows that there is no hybridization between the Ti 3d states and the oxygen 2p states at the VBM or the CBM.

A comparison of the direct KS band gaps of all three materials (cf. table 5.1) shows a decrease of the gap of 0.11 eV from  $\text{CaTiO}_3$  to  $\text{SrTiO}_3$  and of 0.32 eV between the gaps of the latter and of  $\text{BaTiO}_3$ . The lack of hybridization implies that these changes might originate solely from electrostatic effects. In this context, it is worth noticing that the radii of the A cation increases throughout the series  $\text{ATiO}_3$ .

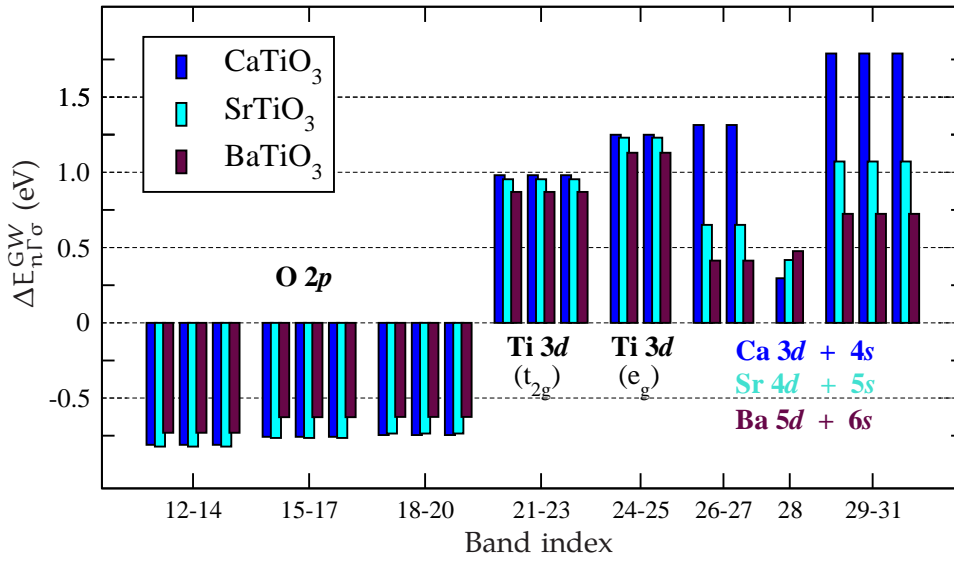


**Figure 5.8.:** QP corrections obtained from GW calculations at the  $\Gamma$  point for the bands 12 through 31 for CaTiO<sub>3</sub>, SrTiO<sub>3</sub>, and BaTiO<sub>3</sub>.

the origin of these changes to a single cause.

The QP band structures of the three compounds in 5.6 exhibit the aforementioned downwards and upwards shift of the valence and conduction bands with respect to (w.r.t.) the KS band structure. However, the bands are not shifted uniformly. This can be observed directly in the band structure of CaTiO<sub>3</sub>, where the different size of the QP correction  $\Delta E_{nk\sigma}^{GW}$  obtained for the three KS bands located at roughly +4 eV at the  $\Gamma$  point leads to a reordering of the bands in the QP band structure at +5 eV.

To further analyze the QP correction, figure 5.8 lists  $\Delta E_{nk\sigma}^{GW}$  at the  $\Gamma$  point for the nine valence bands 12-20 and the conduction bands 21-31 of all three compounds corresponding to the bands in the band structures in figure 5.6. In the cubic phase, the 9 valence bands consists of 3 sets of triply degenerate states. The QP corrections for the degenerate bands 12-14, 15-17, and 18-20 for each compound are identical. Likewise, the QP correction of the degenerate conduction bands are of equal size but the corrections for distinct sets of degenerate bands differ. Furthermore, there is a decrease in the size of the energy correction in the series ATiO<sub>3</sub> except for the QP correction for band 28, for which the energy correction increases systematically throughout the series and which gives rise to the already mentioned band reordering in CaTiO<sub>3</sub>.

To understand the trends in the QP corrections, it is instructive to look again at the DOS of the compounds in figure 5.7. In the energy interval between -5 and

–3 eV, the Ti 3d states hybridize with the O 2p states forming the valence band, between –4 and –2 eV the d states of the *A* cation also mix with the oxygen states, whereas the VBM has pure oxygen character as mentioned previously. It stands to reason that the differences in the composition of the valence bands in the different energy regions lead to the slight differences between QP corrections for the three distinct sets of triply degenerate valence bands. Furthermore, the pDOS of the *A* nd states in the conduction-band regime become more extended and move to higher energies throughout the series as illustrated in figure 5.7. This indicates that the Ca 3d states are bound more strongly than the Sr 4d states and the Ba 5d states are even bound less strongly. However, correlation effects are strongest between highly localized electrons or holes. Thus, the decrease in the localization of the *A* nd states throughout the series might be responsible for the decrease of the QP correction for the *A* nd states.

### **BaBO<sub>3</sub>, B = Ti, Zr, Hf**

This series results from replacing Ti in BaTiO<sub>3</sub> by Zr and Hf. Since the conduction bands lowest in energy in BaTiO<sub>3</sub> are mainly composed of Ti 3d states the largest changes in the band structure of this series are expected to be observed in the conduction-band regime. Indeed, for energies below  $E_F$  the KS band structures of BaZrO<sub>3</sub> and BaHfO<sub>3</sub> shown in figure 5.9 are both very similar to that of BaTiO<sub>3</sub> in figure 5.6. However, the conduction bands lowest in energy in BaZrO<sub>3</sub> and BaHfO<sub>3</sub> are located at higher energies than the corresponding bands in BaTiO<sub>3</sub>, which is the reason for the observed increase in the band gaps of the first two compounds compared to the gap of the latter one. On the other hand, the spectra of BaZrO<sub>3</sub> and BaHfO<sub>3</sub> are very similar in the whole energy region shown in figure 5.9. Apart from the upwards shift of the conduction bands in BaZrO<sub>3</sub> and BaHfO<sub>3</sub>, the fundamental gap is indirect and corresponds to the transition between R and  $\Gamma$  like in BaTiO<sub>3</sub>. The smallest direct transition occurs at the  $\Gamma$  point in all three materials.

In the series BaBO<sub>3</sub>, the valence bands mostly consist of O 2p states. This explains the similarities of the band structures in the valence-band regime. Furthermore, the first three bands above  $E_F$  are composed of the d states of the *B* cation of the transition metals Ti, Zr, and Hf, respectively. The Zr 4d and the Hf 5d states are more extended and less strongly bound than the Ti 3d states. This is demonstrated in figure 5.10 comparing the total and partial DOS of all three compounds as obtained within DFT (GGA). The consequences are twofold: first, the conduction bands formed out of the Zr 4d and the Hf 5d states are located at higher energies than the bands originating from Ti 3d states. Second, the Zr 4d and Hf 5d orbitals hybridize much more with the Ba 5d states than the Ti 3d states, since the first two are much closer in energy to the Ba 5d states,

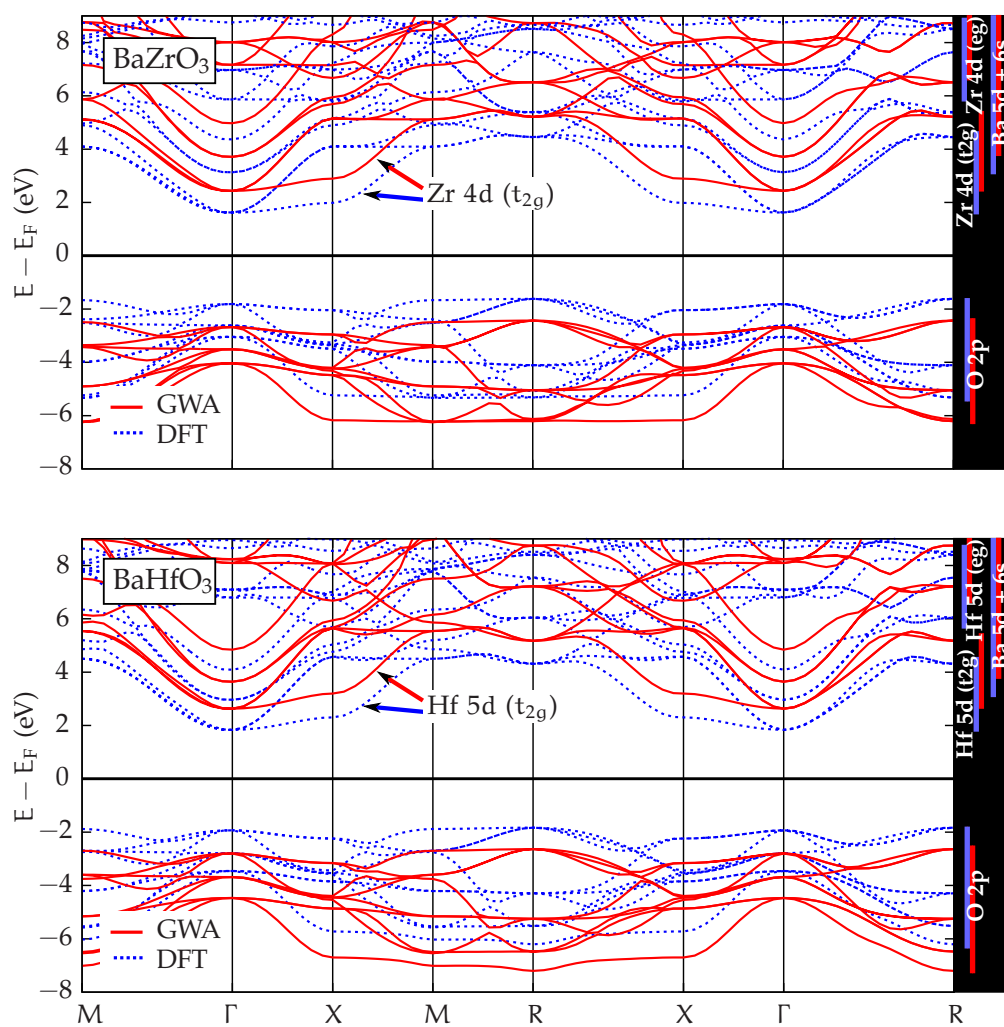


**Figure 5.9.:** KS (blue) and QP (red) band structures of BaZrO<sub>3</sub> (top) and BaHfO<sub>3</sub> (bottom). The Fermi energy is placed in the middle of the KS and QP gap, respectively. The bars on the right indicate the orbital character of the bands.

than the Ti 3d states. This can also be seen in figure 5.10 and explains, why the hysteresis-like feature in the conduction-band regime between  $\Gamma$  and M in the band structures of BaZrO<sub>3</sub> and BaHfO<sub>3</sub> in figure 5.9 are less flat than the corresponding feature in the band structure of BaTiO<sub>3</sub> in figure 5.8.

The close resemblance of the band structure of BaHfO<sub>3</sub> to that of BaZrO<sub>3</sub> is attributed to the influence of the lanthanide contraction. This term denotes the large decrease of the atomic as well as the ionic radii of elements in the lanthanide series resulting from the poor shielding of the charge of the nucleus by the 4f electrons. It leads to an increase in the attraction between the nucleus and the valence electrons occupying the outer states in the 5th or 6th shell resulting in a decrease of the ionic radii. Consequently, the size of the ions of the period-6 transition metals is significantly smaller than would be expected if there were no lanthanides. In fact, they are very similar to the ionic radii of the period-5 transition metals. In the case of Zr and Hf, the size of the ionic radii of Zr<sup>4+</sup> and Hf<sup>4+</sup> with coordination number IV are 72 pm and 71 pm, respectively [118]. Furthermore, the 5d states of Hf are located at similar energies as the Zr 4d states in BaZrO<sub>3</sub> and BaHfO<sub>3</sub> as demonstrated in figure 5.10. In general, many chemical properties of the elements Zr and Hf or of compounds containing either one of the elements are known to be similar.

The QP corrections determined within the GWA for BaZrO<sub>3</sub> and BaHfO<sub>3</sub> lead to shifts of the valence bands to lower energies and of the conduction bands to higher energies. The resulting QP band structures are shown in red in figure 5.9. The QP corrections calculated at the  $\Gamma$  point for the bands 12 to 31 of BaZrO<sub>3</sub> and BaHfO<sub>3</sub> are shown in figure 5.11. A comparison of these energies with the QP correction of BaTiO<sub>3</sub> for the same bands at the  $\Gamma$  point listed in figure 5.8 reveals that the size of the correction for the valence-band states strongly increases from BaTiO<sub>3</sub> to BaZrO<sub>3</sub>, whereas the increase of the energy corrections from BaZrO<sub>3</sub> to BaHfO<sub>3</sub> is much more moderate. The largest increase from BaTiO<sub>3</sub> to BaZrO<sub>3</sub> of almost 0.3 eV can be observed for the bands 12 to 14. The QP correction for the Ba 5d and 6s states also slightly increases, whereas the correction for the transition-metal d states decreases throughout the series.

Due to the large increase in the KS transition energies obtained for BaTiO<sub>3</sub> and BaZrO<sub>3</sub>, the contribution of screening to the QP correction is reduced as energy differences between the occupied and unoccupied states of the KS eigenspectra enter the denominator of the polarization function, eq. (2.83). A closer look at the correlation contribution to the GW self-energy, calculated at the KS energies of the transition-metal d states of Ti, Zr, and Hf, shows that the contribution decreases throughout the BaBO<sub>3</sub> series. In addition, the exchange contribution to the self-energy exhibits the same trend for these states such that the QP corrections for the transition-metal d states become smaller throughout the series. For the other valence- and conduction-band states, changes in the contributions to

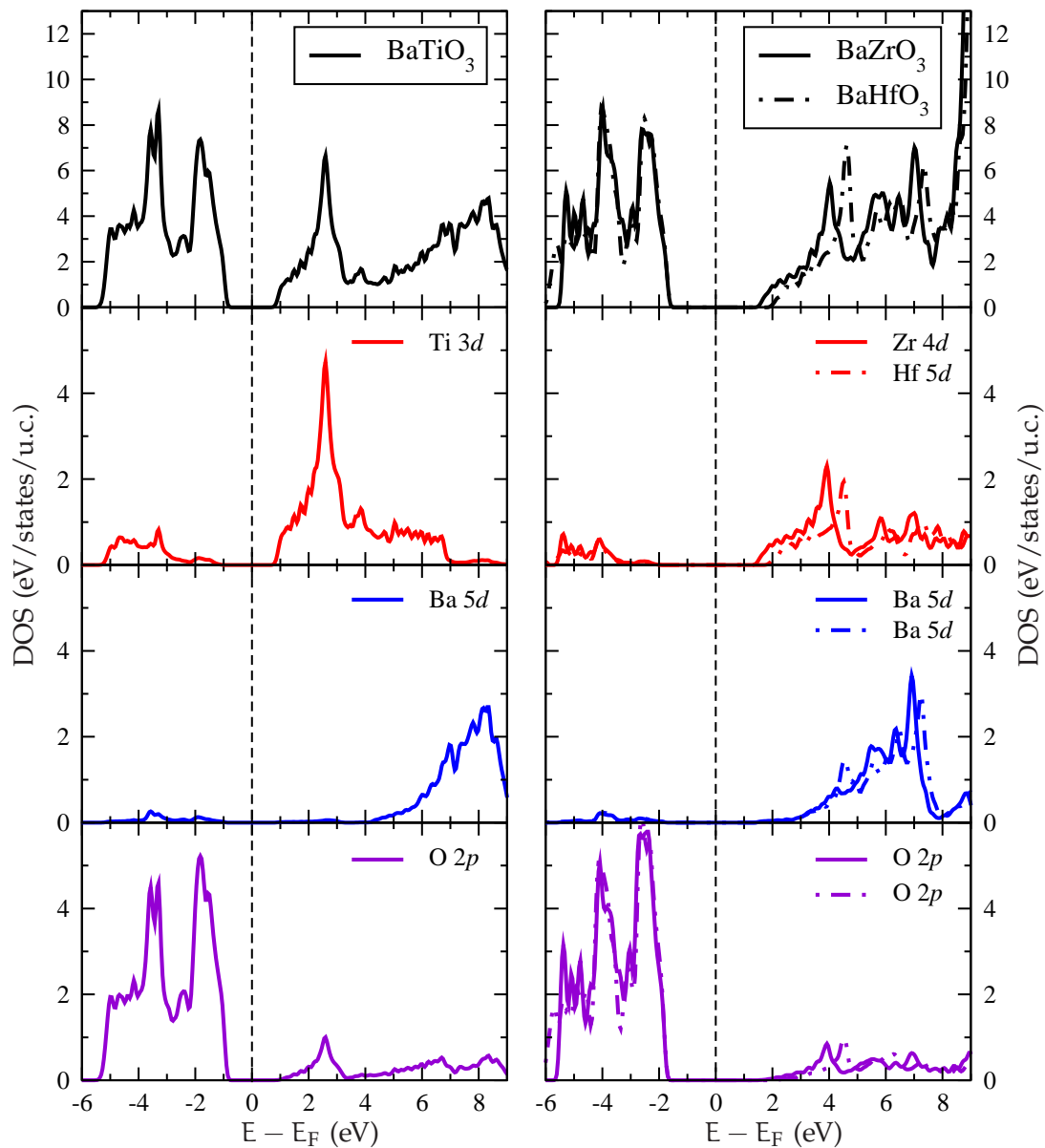


**Figure 5.10.:** The DOS obtained from DFT calculations.

*Left:* Total DOS (black) of BaTiO<sub>3</sub> (top) and pDOS of Ti 3d (red), Ba 5d (blue), and O 2p (violet) from top to bottom.

*Right:* Total and partial DOS of BaZrO<sub>3</sub> (straight lines) and BaHfO<sub>3</sub> (dashed-dotted lines). From top to bottom: total DOS, Zr or Hf nd pDOS (red), Ba 5d (blue), and O 2p (violet) pDOS.

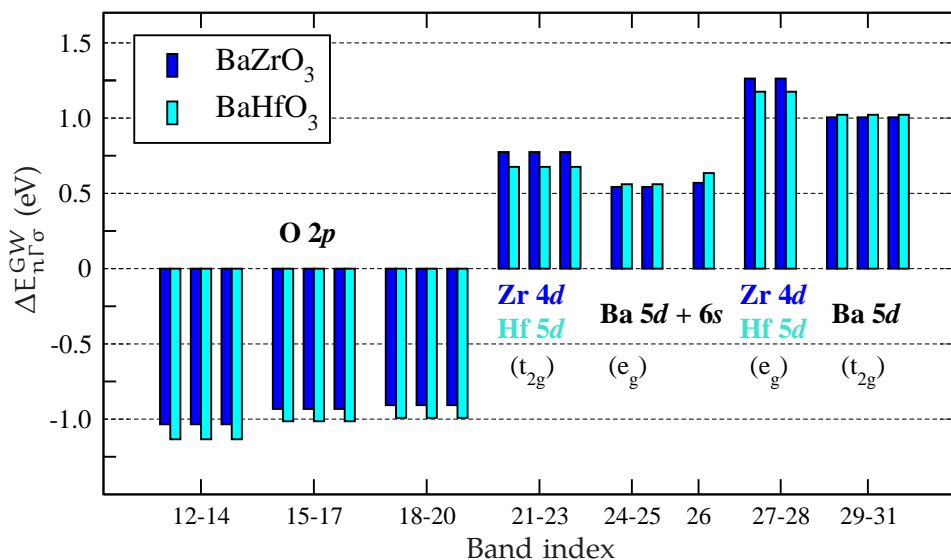


**Figure 5.11.:** QP corrections obtained from GW calculations at the  $\Gamma$  point for the bands 12 through 31 for BaZrO<sub>3</sub> and BaHfO<sub>3</sub>.

the self-energy are less pronounced and partially compensate each other. Furthermore, there are other aspects that may have influence on the size of the QP correction, e.g., the differences in the KS wave functions of the distinct materials which are used to calculate matrix elements of the GW self-energy to obtain the QP correction. However, none of these aspects influencing the QP corrections of the remaining states are as predominant as the changes in the correlation and exchange contributions to the GW self-energy observed for the transition-metal d states.

### PbBO<sub>3</sub>, B = Ti, Zr, Hf

The last series analyzed in this chapter is formally obtained, if Ba is replaced by Pb in the compounds discussed in the previous section. The KS and QP band structures of the resulting series displayed in figure 5.12 exhibit a number of changes and new features, which cannot be found in the spectra of the materials discussed previously: in all three compounds, a new valence band is formed in the energy interval from  $-9$  to  $-7$  eV in the KS band structures. The other valence bands above  $-7$  eV are of similar form as in the compounds of the series BaBO<sub>3</sub>. However, additional conduction bands can be found in the energy interval from  $+1$  to  $+7$  eV in the KS spectra of PbTiO<sub>3</sub> and between  $+1$  and  $+5$  eV in the spectra of PbZrO<sub>3</sub> and PbHfO<sub>3</sub>. They cross the bands formed by the transition-metal d states, which yield the hysteresis-like structure in the conduction-band regime

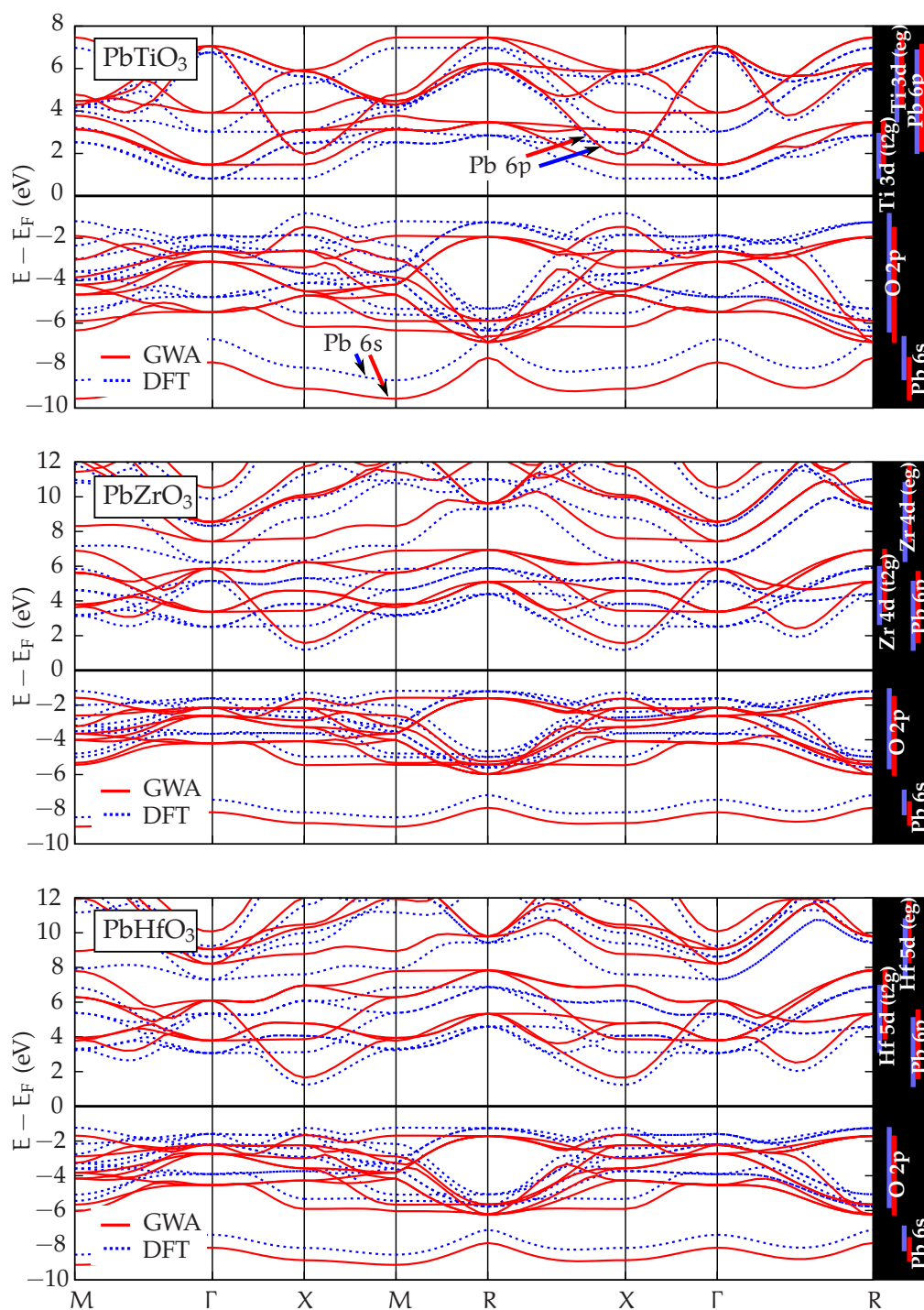


**Figure 5.12.:** KS (blue) and QP (red) band structures of  $\text{PbTiO}_3$  (top),  $\text{PbZrO}_3$  (middle), and  $\text{PbHfO}_3$  (bottom). The Fermi energy is placed in the middle of the KS and QP gap, respectively. The bars on the right indicate the orbital character of the bands.

between  $\Gamma$  and  $M$  observed previously in the band structure of other compounds. One of these new bands forms the CBM of  $\text{PbZrO}_3$  and  $\text{PbHfO}_3$  located at the  $X$  point. In  $\text{PbTiO}_3$ , the CBM is formed by states, which can be identified as Ti 3d from comparison to the KS band structures discussed in previous sections and it is also located at the  $X$  point. All states of the lowest conduction band along the high-symmetry line between  $\Gamma$  and  $X$  are very close in energy in all three compounds. The fundamental band gap in  $\text{PbTiO}_3$  corresponds to the indirect transition between the  $X$  and the  $\Gamma$  point whereas in  $\text{PbZrO}_3$  it is the indirect transition between  $R$  and  $X$ . In  $\text{PbHfO}_3$ , the fundamental band gap corresponds to the direct transition at the  $X$  point.

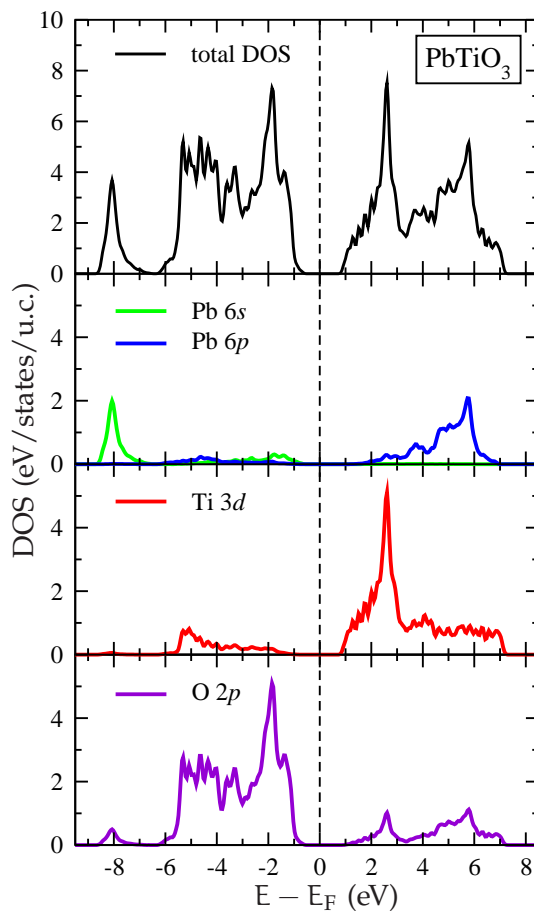


**Figure 5.13.:** From top to bottom: total DOS (black) of  $\text{PbTiO}_3$  and partial DOS of the states Pb 6s and 6p (green and blue), Ti 3d (red), and O 2p (violet) obtained from DFT calculations.

The changes and new features in the KS band structures of  $\text{PbBO}_3$  can all be related to the contributions from the valence states of Pb. This is illustrated in figure 5.13 showing the total DOS of  $\text{PbTiO}_3$  as well as the pDOS from those states of Ti, Pb, and oxygen that yield the largest contributions to the total DOS within the energy interval displayed here. Hence, the additional valence band evolving around  $-8$  eV is mostly formed by Pb 6s states with small contributions from the oxygen 2p states. Furthermore, it is worth noticing that the Pb 6s states also yield a non-negligible contribution to the formation of the upper valence bands and the VBM, which are primarily composed of oxygen 2p states as in the materials discussed earlier. In addition, the Pb 6p states hybridize with the valence-band states between  $-6$  and  $-4$  eV. However, the dominant contribution of the Pb 6p to the total DOS can be found between  $+1.5$  and  $+7$  eV above  $E_F$ , where it leads to the formation of the additional conduction bands observed in the KS band structures, figure 5.12.

The other conduction bands are again composed of the transition-metal d states as in the compounds of the  $\text{BaBO}_3$  series. Hence, replacing Ti by Zr or Hf leads

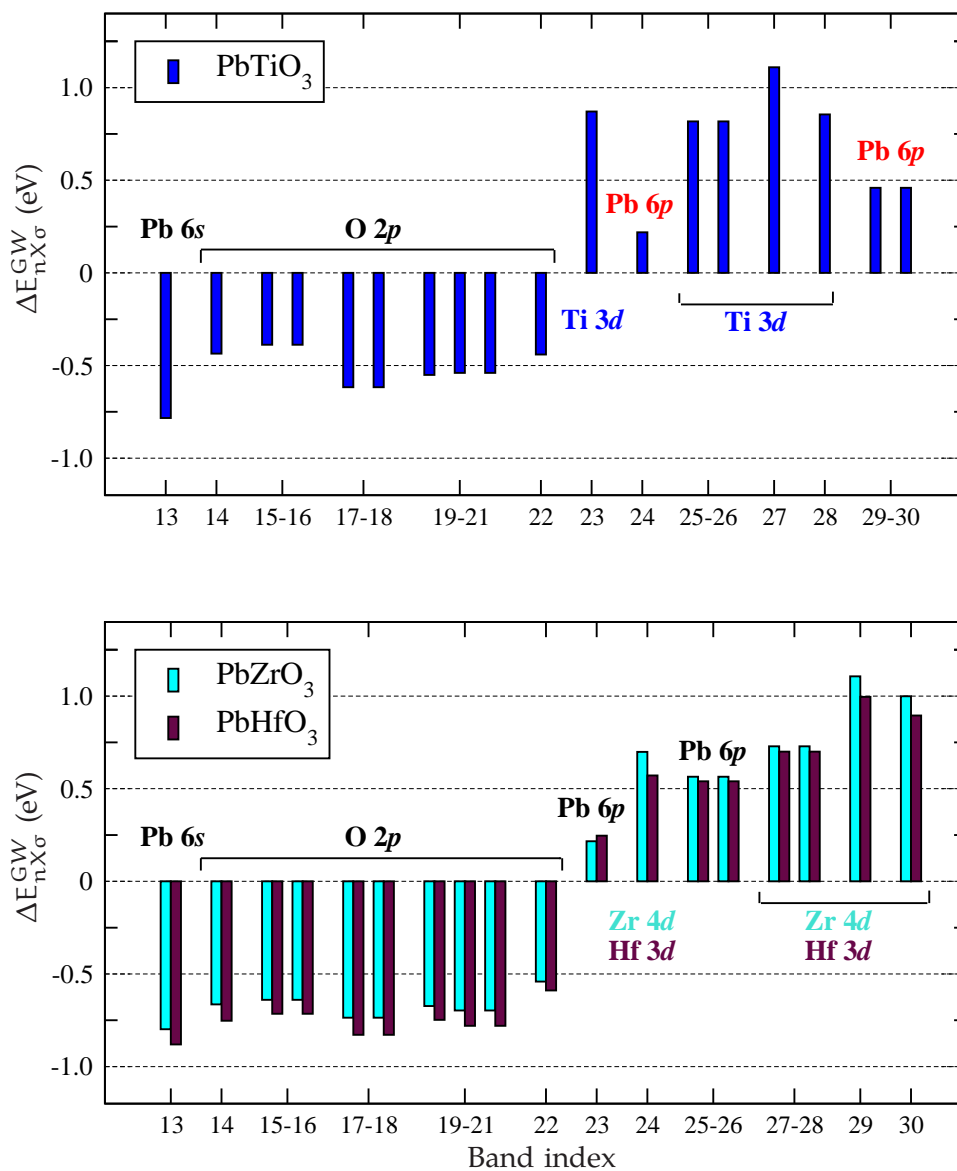


**Figure 5.14.:** QP corrections obtained from GW calculations at the X point for the bands 13 through 30 of  $\text{PbTiO}_3$  (top) and of  $\text{PbZrO}_3$  and  $\text{PbHfO}_3$  (bottom).

to the same shift of these bands to higher energies in the KS band structure of  $\text{PbZrO}_3$  and  $\text{PbHfO}_3$  like the one observed in the series  $\text{BaBO}_3$  upon replacing Ti by Zr or Hf. Likewise, the close resemblance between the band structures of  $\text{PbZrO}_3$  and  $\text{PbHfO}_3$  can again be related to the similar physical and chemical properties of Zr and Hf discussed previously.

The QP bands of the compounds  $\text{PbBO}_3$  with  $B = \text{Ti, Zr, and Hf}$  in figure 5.12 are shifted downwards in the valence-band regime and upwards in the conduction-band regime w.r.t. the KS band structures in agreement with previously observed trends. Again, the size of the energy shifts for the distinct bands is not identical. For a quantitative analysis of the QP corrections, the observed energy shifts obtained for the bands 13 to 30 at the X point for all three compounds of the  $\text{PbBO}_3$  series are illustrated in figure 5.14.

The largest deviation of the valence bands and the corresponding QP corrections of the series  $\text{PbBO}_3$  from those observed in the other two series of compounds results from the presence of Pb 6s and p states. The smallness of the QP correction for the conduction band 24 of  $\text{PbTiO}_3$  at the X point and 23 in  $\text{PbZrO}_3$  and  $\text{PbHfO}_3$ , which is mostly composed of Pb 6p states, is mainly attributed to the fact that this band is extended over a large energy interval. Electrons occupying the corresponding states are very delocalized. Since correlation effects between delocalized electrons are small so is the QP correction obtained for these states.

For the other valence- and conduction-band states, the same trends in the QP corrections can be observed like in the  $\text{BaBO}_3$  series. It is discussed in the following section that additional changes in the spectra of the compounds from the  $\text{PbBO}_3$  series may arise if the influence of spin-orbit coupling is taken into account.

### 5.2.2. Influence of SOC in $\text{PbBO}_3$ , $B = \text{Ti, Zr, and Hf}$

In the photo-emission spectrum of Pb, a two-peak structure can be observed [158] in the energy interval comprising the valence bands. First-principles calculations [158] indicate that this feature originates from the effect of spin-orbit coupling on the Pb 6p states. Quantitative agreement of the calculated spectrum with the experimental data can thus only be attained, if SOC is included in the calculation. It was discussed in detail in the previous sections that the Pb 6p states yield a dominant contribution to the formation of the conduction bands in the three compounds  $\text{PbBO}_3$ ,  $B = \text{Ti, Zr, and Hf}$ . Therefore, the influence of SOC on the valence- and conduction-band spectra of these compounds will be investigated in this section. First, the influence of the SOC on the KS band structure of the three compounds is discussed.

Figure 5.15 shows the KS band structure of  $\text{PbTiO}_3$  obtained from a calculation without SOC on the left and with SOC on the right. The spin-orbit interaction induces several changes: at the R point around  $-7$  eV and  $+3$  eV, at the X point at  $-4$  eV and at the  $\Gamma$  point at  $-5$  eV the degeneracy between bands is lifted due to small shifts in energy of the KS eigenstates. Close to the X point at  $+5$  eV, the curvature of bands changes such that the bands do not cross each other any more. However, these changes are of the order of meV at the most. On the contrary, larger shifts on the scale of one eV can be observed in the conduction bands above  $+3$  eV.

The SOC term, eq. (2.29), induces a splitting between degenerate bands composed of orbitals with  $l \geq 1$ . The magnitude of the splitting reflects the spin-orbital coupling strength. As discussed in section 2.2.2, chapter 2, the influence of SOC is expected to be strongest for p orbitals of heavy atoms, since the spin-orbit coupling strength is enhanced as the atomic number increases. Therefore, the largest changes in the KS band structure of  $\text{PbTiO}_3$  can be observed for the bands above  $+3$  eV, since they are mostly composed of Pb 6p states. In particular, the KS eigenstates located roughly at  $+6$  eV at the R point are degenerate if SOC is neglected but they are separated by more than 1 eV if the SOC term is included in the DFT calculations. In contrast, the influence of SOC on the

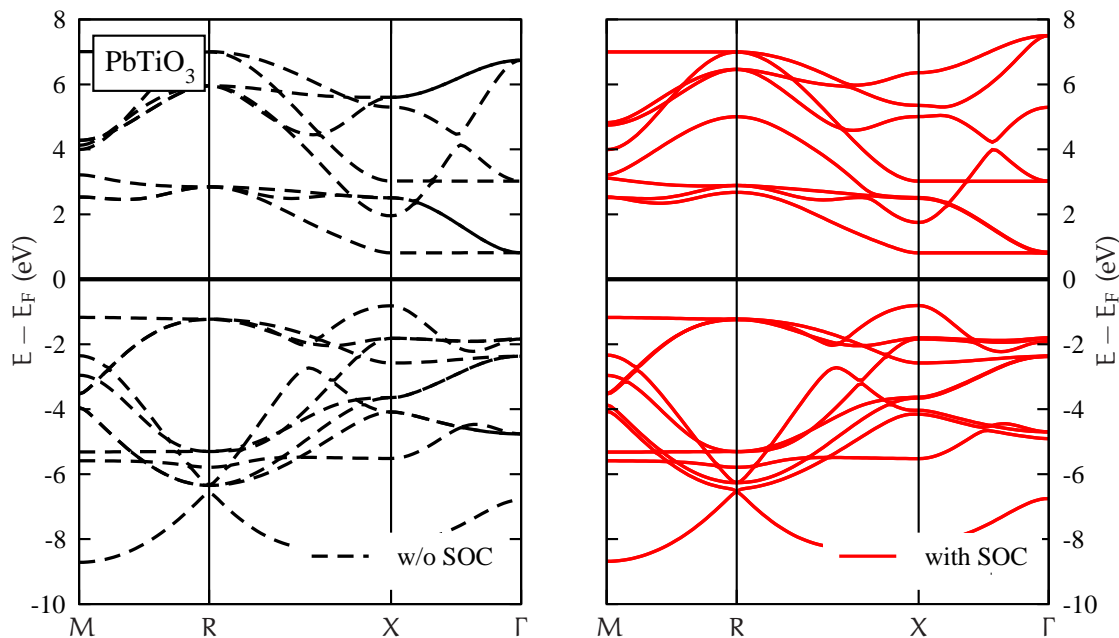


**Figure 5.15.:** KS band structures of  $\text{PbTiO}_3$  calculated without SOC (left) and with SOC (right) included in second variation. The Fermi energy is placed in the middle of the band gap.

conduction bands below +3 eV consisting of Ti 3d states and on the valence bands which are mainly composed of oxygen 2p states is much smaller. Hence, the fundamental gap at the X point in  $\text{PbTiO}_3$  is only slightly affected by the changes originating from the SOC.

Along the same line of arguments, changes in the KS band structures of  $\text{PbZrO}_3$ , figure 5.16, can be related to the influence of SOC on eigenstates with different orbital character. Moreover, it follows immediately that SOC has a larger influence on the position of the CBM in  $\text{PbZrO}_3$  than in  $\text{PbTiO}_3$ , since the conduction band of  $\text{PbZrO}_3$  lowest in energy is composed of Pb 6p states as opposed to the conduction band lowest in energy in the KS band structure of  $\text{PbTiO}_3$ . Since the KS band structures of  $\text{PbHfO}_3$  and  $\text{PbZrO}_3$  are practically identical in the energy interval from  $-9$  to  $+6$  eV (cf. figure 5.12), the SOC leads to similar modifications of the band structure of  $\text{PbHfO}_3$  than those observed for  $\text{PbZrO}_3$  in figure 5.16.

For the sake of completeness, it should be mentioned that SOC can also lift the spin-degeneracy at certain  $\mathbf{k}$  points in systems without inversion symmetry. Prominent examples of such changes in crystals lacking inversion symmetry are the Dresselhaus effect and the Rashba splitting. In a lattice with inversion symmetry, the energy eigenvalues of the two spin states at a given  $\mathbf{k}$  point have to be

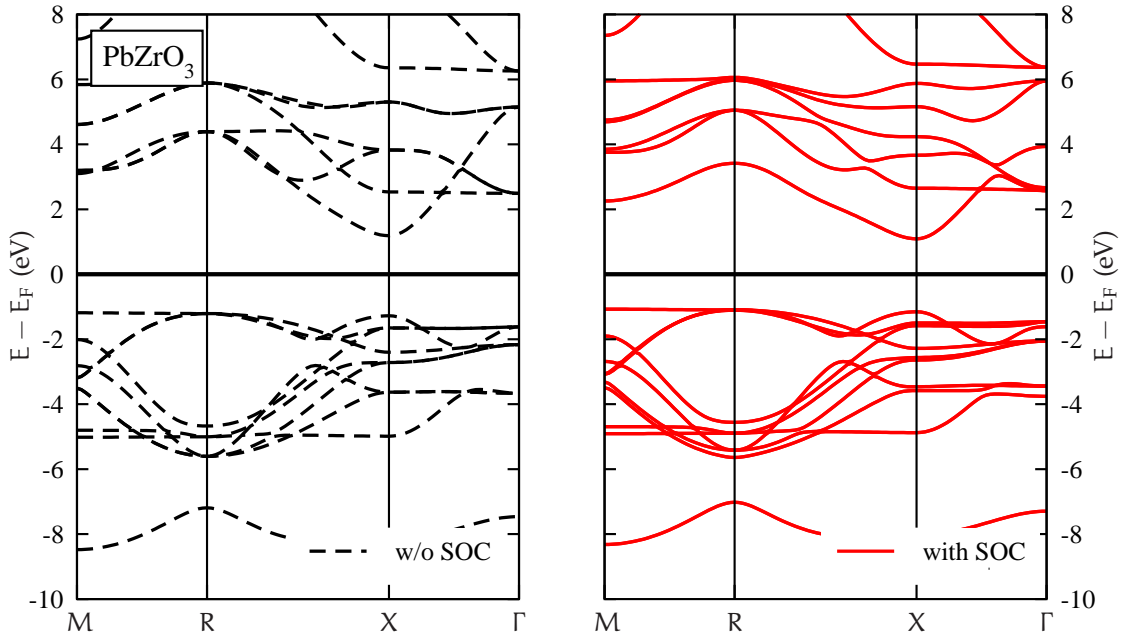


**Figure 5.16.:** KS band structures of  $\text{PbZrO}_3$  calculated without SOC (left) and with SOC (right) included in second variation. The Fermi energy is placed in the middle of the band gap.

degenerate, because time-reversal symmetry requires a spin state at an arbitrary  $\mathbf{k}$  point to have the same energy as the opposite-spin state at  $-\mathbf{k}$ <sup>1</sup>. Hence, the SOC does not induce a splitting between the different spin states in the band structures of the cubic crystal phases studied here.

In reference [159], it is described how the SOC can be included in the GWA. However, GW calculations for complex oxide materials such as the compounds from the  $\text{PbBO}_3$  series, which fully incorporate the SOC, are not feasible at present. To estimate the influence of the SOC on the QP energies  $E_{nk}$ , new QP energies  $E_{nk}^{\text{SOC}}$  are calculated according to

$$E_{nk}^{\text{SOC}} = E_{nk} + (\epsilon_{nk}^{\text{SOC}} - \epsilon_{nk}), \quad (5.2)$$

where  $\epsilon_{nk}$  denotes the KS eigenvalues obtained from calculations without the SOC term and  $\epsilon_{nk}^{\text{SOC}}$  represents the KS eigenvalues which are calculated including the SOC term in second variation. Similar schemes [160, 161] employed in calculations for binary semiconductors yield better agreement with experimental data than calculations which do not take into account the effects of the SOC.

To determine the quantitative changes caused by SOC, table 5.2 lists the direct KS and QP gaps between the highest occupied and lowest unoccupied states at

<sup>1</sup>This is also referred to as Kramers degeneracy.

Material	Transitions	KS gaps (eV)		QP gaps (eV)	
		w/o SOC	with SOC	w/o SOC	with SOC
PbTiO <sub>3</sub>	X → X	1.62	1.61	2.98	2.97
	Γ → Γ	2.64	2.61	4.15	4.12
	M → M	3.70	3.69	5.07	5.06
PbZrO <sub>3</sub>	X → X	2.46	2.23	3.28	3.05
	Γ → Γ	4.11	4.03	5.63	5.55
	M → M	4.34	3.33	5.34	4.33
PbHfO <sub>3</sub>	X → X	2.48	2.25	3.37	3.14
	Γ → Γ	4.64	4.39	6.14	5.89
	M → M	4.50	3.49	5.59	4.58

**Table 5.2.:** Influence of SOC on the transition energies between the highest occupied and lowest unoccupied KS and QP states of PbTiO<sub>3</sub>, PbZrO<sub>3</sub>, and PbHfO<sub>3</sub> at selected  $\mathbf{k}$  points. The QP energy including contributions from the SOC are obtained from the definition (5.2).

the  $X$ ,  $\Gamma$  and  $M$  points of the BZ of the compounds  $\text{PbBO}_3$ , with  $B = \text{Ti, Zr, Hf}$  calculated with and without inclusion of the SOC term. The values for the KS band gaps confirm that the changes in  $\text{PbTiO}_3$  are much smaller than in the other two compounds for the reasons discussed above. The fundamental KS gaps of  $\text{PbZrO}_3$  and  $\text{PbHfO}_3$  are diminished by 0.23 eV due to the influence of the SOC, whereas in  $\text{PbTiO}_3$  it is only decreased by 0.01 eV. In general, the transition energies of all three materials systematically decrease upon inclusion of SOC in the DFT calculations.

As the QP energies incorporating the corrections from the SOC are calculated according to eq. (5.2), the reduction of the transition energies observed for the KS gaps directly translates into a decrease of the QP transition energies listed in table 5.2. However, the resulting new QP gaps have to be dealt with carefully, because, strictly speaking, it is not correct to predict the size of energy corrections in the QP band structures due to SOC based on the changes observed in the KS band structures. The SOC does not only change the eigenvalues. It also alters the KS wave function. Eigenvalues and eigenstates both enter in the calculation of the Green function  $G_0$ , eq. (2.82), and the polarization function  $P$ , eq. (2.83), which, in turn, enter the calculations to determine the GW self-energy. The SOC leads to sizable changes in the KS eigenspectra of  $\text{PbZrO}_3$  and  $\text{PbHfO}_3$  and it is doubtful that these changes are negligible in calculations of  $G_0$  or  $W$ . Further investigations will be necessary to prove that eq. (5.2) yields a good estimate for the influence of the SOC on the QP energies obtained from the GWA.

After the detailed analysis of trends in valence- and conduction-band spectra of the perovskite TMOs the energies of semicore states will be compared in the next section.

### 5.2.3. Semicore states

In this section, trends in the spectra of the perovskite TMOs in the energy interval between  $-70$  and  $-10$  eV are discussed. In all compounds, energy bands resulting from high-lying core states, called semicore states, are present in this energy regime. As a semicore state is well separated in energy from the core and valence states, it does not hybridize neither with the core or valence states nor with other semicore state. Hence, the resulting bands have nearly pure orbital character and are almost dispersionless. Therefore, only the energies of these bands at the  $\Gamma$  point are compared here. All energies are aligned w.r.t. the energy  $E_{\text{VBM}}$  of the highest occupied state.

Figure 5.17 shows the KS as well as the QP energies of the semicore states at the  $\Gamma$  point calculated within the GGA and GWA, respectively. For almost all states, the KS and the QP energies are very similar. In general, the QP corrections

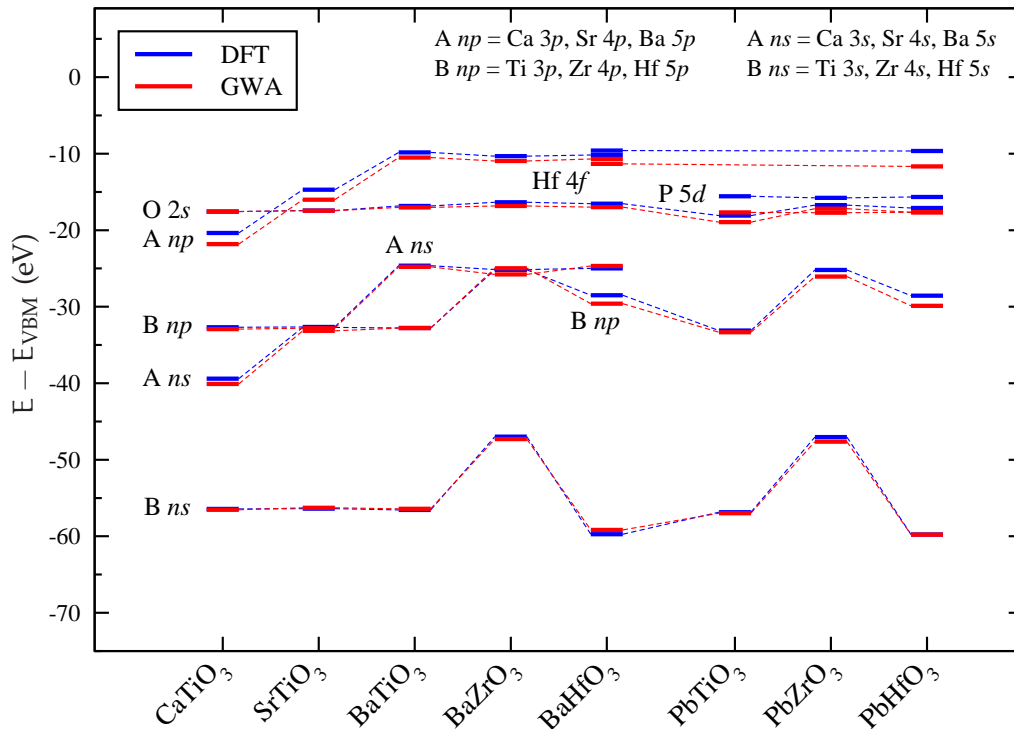


**Figure 5.17.:** Comparison of the energies of the semicore states at the  $\Gamma$  point obtained from DFT (GGA) and GW calculations.

shifts the semicore states to slightly lower energies. In the KS and QP spectra of all materials, oxygen 2s states form bands located roughly at  $-17$  eV. Likewise, the semicore states originating from elements, which are contained in more than one of the compounds, like the Ti 3s and p states as well as the Pb 5d or the Hf 4f states, are all located at about the same energies in all compounds.

For the sake of completeness, it should be mentioned that the bands resulting from the oxygen 2s states are not dispersionless. There are three oxygen atoms in the unit cell. The 2s states of these atoms form three bands which are very close in energy at all points of the BZ and extend over an energy interval of only 2 eV. In order not to overburden the graphs in figure 5.17 and 5.18 only the position of the band lowest in energy is displayed.

For the position of the semicore states formed by the  $B$  cation's s and p states with  $B = \text{Ti, Zr and Hf}$  and the  $A$  cation's s and p states with  $A = \text{Ca, Sr and Ba}$  two trends are observed: states attributed to shells with larger quantum numbers are more extended and less tightly bound. This leads to a systematic increase of the energies of the s and p states from Ca over Sr to Ba. For the same reason, the Zr 4s and p states are located at higher energies than the corresponding states

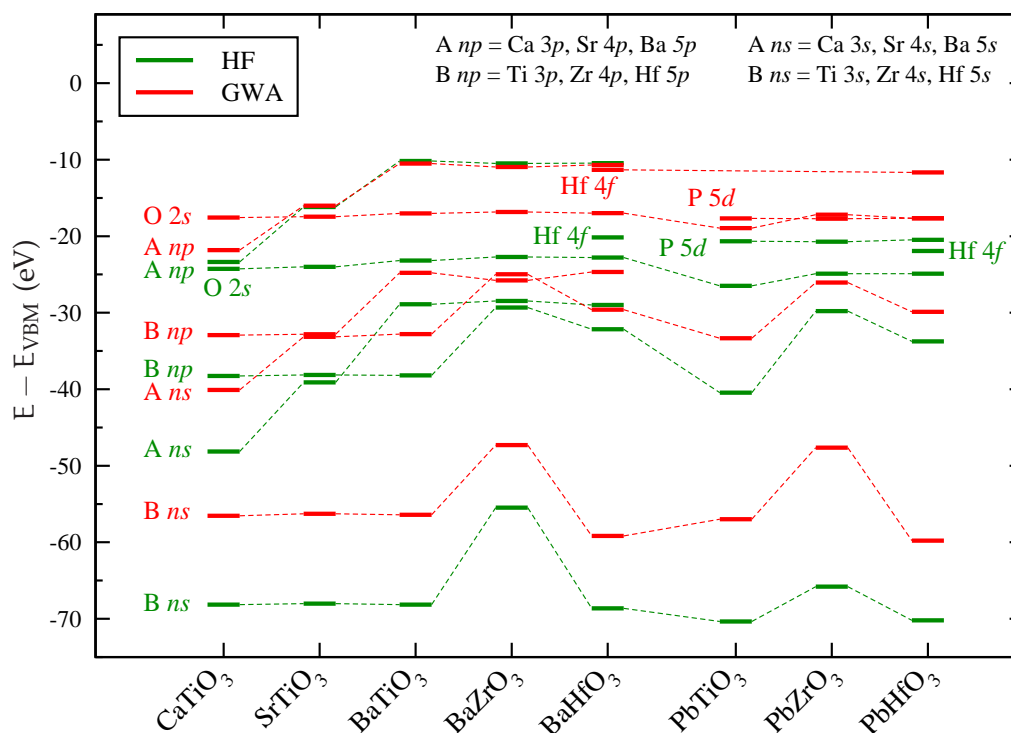


**Figure 5.18.:** Comparison of the QP energies of the semicore states at the  $\Gamma$  point obtained from the full QP correction from the GWA with spectra obtained by including only the non-selfconsistent HF correction.

of Ti. On the other hand, the Hf 5s and p states are located at lower energies than the 4s and p states of Zr in both compounds  $\text{BaHfO}_3$  and  $\text{PbHfO}_3$ . This second trend originates from the extended 4f states of Hf that screen the nuclear charge only partially such that the Hf 5s and p states feel more of the nuclear charge, which leads to a contraction of the orbitals (lanthanide contraction) and a stronger binding of these states.

To further analyze the QP spectra of the semicore states, figure 5.18 compares the energies obtained from the full QP correction calculated in the GWA with the spectra, which are calculated by adding only the contribution of the exchange term to the GW QP correction. As this contribution compensates the self-interaction error, the resulting spectra are shifted to lower energies. This effect is strongest for the B ns states as they are the most tightly bound ones of all semicore states discussed here. The effect is also strong for the 4f states of Hf. The contribution from the screening to the QP correction compensates this shift such that the resulting QP spectra are again close in energy to the KS spectra.

Since the screening does not fully compensate the effect of the contribution from the exchange term the QP states are, in general, located at slightly lower energies than the KS eigenstates.

In summary, trends in the valence- and conduction-band spectra as well as in the position of semicore states can be related to changes in the chemical composition of the perovskite TMOs in first-principles calculations. In the next part of the chapter, the influence of changes in the crystal structure on the electronic spectra is analyzed and the resulting KS and QP gaps are compared with experimental data.

### 5.3. GWA results versus experiment

In the third part of this chapter, band gaps, positions of semicore states and dielectric functions obtained from GW calculations are compared to experimental data. These data are typically measured at room temperature. As the majority of the perovskite TMOs investigated in this part of the thesis does not crystallize in the cubic phase at RT, the first section deals with changes occurring in the band structures upon phase transitions from the cubic to the RT crystal phase. After some brief comments on the experimental procedures used to determine the aforementioned quantities, the results of measurements are compared with the results of DFT (GGA) and GW calculations for the RT crystal phases. The influence of contributions missing in the GWA, i.e., the neglect of excitonic effects due to the neglect of the vertex, are revised briefly and the shortcomings of the theoretical approach are contrasted with possible flaws in the interpretation of the experimental data. Finally, the results of the whole chapter are summarized.

#### 5.3.1. Room temperature crystal and electronic structures

Table 5.3 lists the crystal phases of the perovskite TMOs and the corresponding transition temperatures that are known from experiment. Only the three compounds  $\text{SrTiO}_3$ ,  $\text{BaZrO}_3$ , and  $\text{BaHfO}_3$  crystallize in the cubic phase at RT (space group  $\text{Pm}\bar{3}\text{m}$ ). Their KS band structures illustrated in figure 5.6 and 5.9, respectively, have already been analyzed in detail in the previous sections.

The two compounds  $\text{BaTiO}_3$  and  $\text{PbTiO}_3$  form a tetragonal lattice (space group  $\text{P4mm}$ ). Furthermore, they are ferroelectric at RT, which implies that they crystallize in a non-centrosymmetric structure. The crystal phase is obtained from an elongation of the cubic unit cell along the  $c$  axis accompanied by small shifts of the Ti cations and oxygen anions away from their high-symmetry positions (cf. figure 4.3, chapter 4). The  $c/a$  ratio of  $\text{PbTiO}_3$  is given by 1.062 and is larger

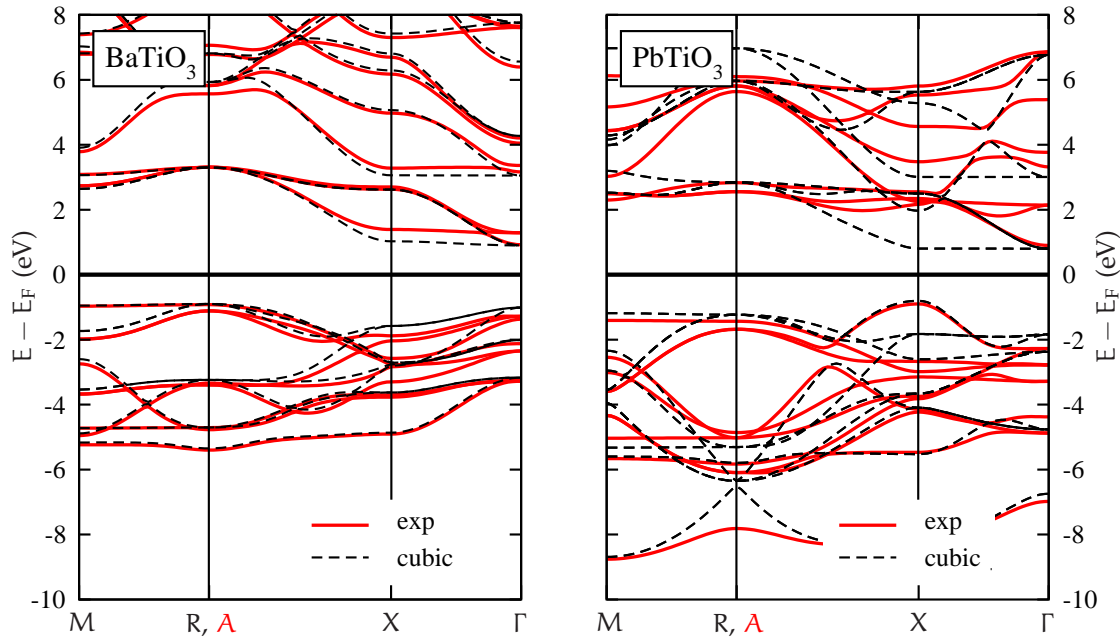
than  $c/a = 1.011$  in  $\text{BaTiO}_3$ .

Figure 5.19 shows parts of the KS band structures of  $\text{BaTiO}_3$  and  $\text{PbTiO}_3$  in red obtained for the tetragonal, ferroelectric structure. For comparison, the KS band structures for the cubic crystal phases are also displayed. All four band structures agree well with spectra published in the literature [166]. Whereas the electronic structure of the RT crystal phase of  $\text{BaTiO}_3$  only exhibits small deviations from that of the cubic phase, the differences between the electronic structures of the crystal phases of  $\text{PbTiO}_3$  are much larger. A direct comparison of the changes in the band structures of both materials is hampered by the previously discussed differences in the composition of the bands: in  $\text{PbTiO}_3$ , the Pb 6s states hybridize with the valence bands composed of oxygen 2p states and the Pb 6p states lead to the formation of additional conduction bands. In contrast, the valence bands of  $\text{BaTiO}_3$  have nearly pure oxygen 2p character and the low-lying conduction bands are composed of Ti 3d states. Furthermore, the shifts of the atoms away from the high-symmetry points are larger in  $\text{PbTiO}_3$ . This is the reason why the differences between the electronic structures of the cubic and tetragonal phase of  $\text{PbTiO}_3$  are more pronounced than the differences between the electronic structures of the corresponding crystal phases of  $\text{BaTiO}_3$ .

The three compounds  $\text{CaTiO}_3$ ,  $\text{PbZrO}_3$ , and  $\text{PbHfO}_3$  attain an orthorhombic crystal phase at RT. In  $\text{CaTiO}_3$ , the resulting unit cell (space group  $\text{Pbnm}$ ) contains 4 chemical units which corresponds to 20 atoms. The number of atoms per unit cell in  $\text{PbZrO}_3$  and  $\text{PbHfO}_3$  (space group  $\text{Pbam}$ ) amounts to 40, which is equivalent to 8 chemical units.

Material	Crystal phases (transition temperatures in K)	Ref.
$\text{CaTiO}_3$	cubic $\xrightarrow{(1634)}$ tetragonal $\xrightarrow{(1498)}$ <u>orthorhombic</u>	[107]
$\text{SrTiO}_3$	<u>cubic</u> $\xrightarrow{(106)}$ tetragonal	[162]
$\text{BaTiO}_3$	cubic $\xrightarrow{(393)}$ <u>tetragonal</u> $\xrightarrow{(278)}$ orthorhombic $\xrightarrow{(183)}$ rhombohedral	[109]
$\text{BaZrO}_3$	<u>cubic</u>	[110]
$\text{BaHfO}_3$	<u>cubic</u>	[111]
$\text{PbTiO}_3$	cubic $\xrightarrow{(766)}$ <u>tetragonal</u>	[163]
$\text{PbZrO}_3$	cubic $\xrightarrow{(508)}$ <u>orthorhombic</u>	[164]
$\text{PbHfO}_3$	cubic $\xrightarrow{(477)}$ <u>orthorhombic</u>	[165]

**Table 5.3.:** Crystal phases of the perovskite TMOs. The RT phases are underlined.



**Figure 5.19.:** Comparison of the KS band structures of  $\text{BaTiO}_3$  and  $\text{PbTiO}_3$  calculated in the RT crystal phase (red) and the cubic phase (black).

The KS band structures of  $\text{CaTiO}_3$  and  $\text{PbZrO}_3$  are illustrated in figure 5.20. Since the number of atoms per unit cell is increased compared to the cubic phases a larger number of valence and conduction bands close in energy is formed by the oxygen 2p and the transition-metal d states than in the KS spectra of the cubic phase, figure 5.6 and 5.12. Again, contributions from the Pb 6s and p states can be identified in the band structure of  $\text{PbZrO}_3$ . In contrast to the band structures of the cubic phase, the fundamental band gap now corresponds to the direct transition at the  $\Gamma$  point in all three materials with orthorhombic crystal phase at RT including  $\text{PbHfO}_3$ . For the reasons discussed previously, the KS spectrum of  $\text{PbHfO}_3$  is very similar to that of  $\text{PbZrO}_3$ . Therefore, the band structure of the former is not displayed here.

### 5.3.2. Transition energies and band gaps in experiment

Photo-emission spectroscopy (PES)<sup>2</sup> is an excellent tool to determine the core and semicore level spectra of solids. Semicore states form nearly dispersionless bands well separated in energy such that the position of these bands can be directly determined from the peak positions in the spectra obtained from X-ray

<sup>2</sup>The basic mechanism of PES is explained in section 2.3 of chapter 2.

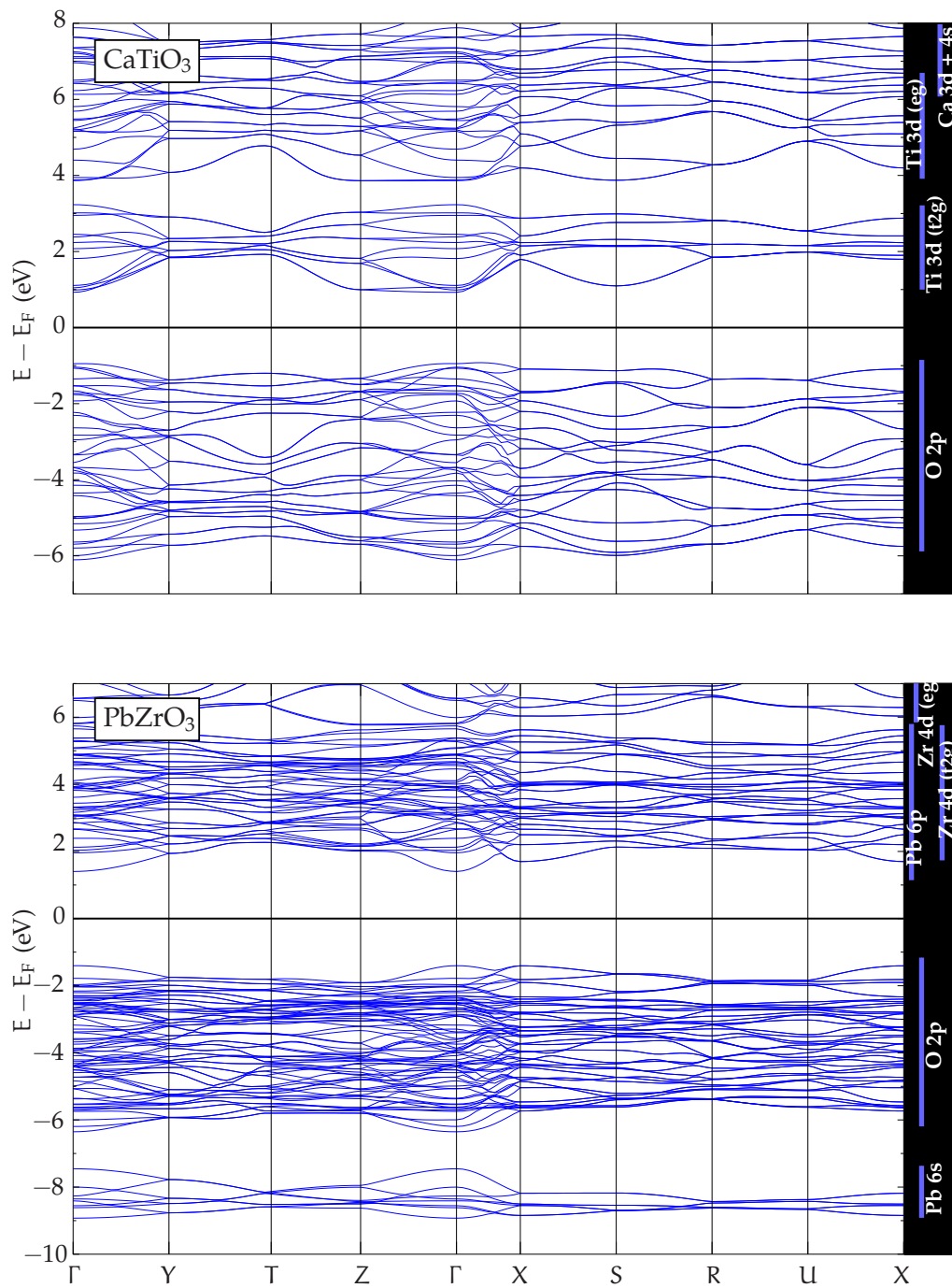


**Figure 5.20.:** KS band structures of orthorhombic  $\text{CaTiO}_3$  (top) with 20 atoms per unit cell and of orthorhombic  $\text{PbZrO}_3$  (bottom) with 40 atoms per units. The Fermi energy is placed in the middle of the KS band gaps.

photo-emission spectroscopy (XPS). In contrast, it is much more difficult to determine energies of transitions between valence- and conduction-band states by PES. On the one hand, there are usually many states close in energy in this energy regime, which are difficult to resolve in PES. On the other hand, the occupied and unoccupied parts of the QP spectra cannot be probed simultaneously in PES but have to be studied by complementary techniques, i.e., PES and inverse PES, yielding two separate spectra for the occupied and unoccupied part of the QP spectrum. These spectra from different measurements have to be aligned to determine transition energies which may lead to additional inaccuracies. Therefore, optical spectroscopies are usually preferred to probe the transition energies between states pertaining to the valence- and conduction-band spectrum of solids.

Optical experiments like absorption, transmission, and reflectance spectroscopy allow to directly measure the fundamental band gap and transition energies between the occupied and unoccupied part of the QP spectrum. In both spectroscopies, a detector first measures the spectrum from the radiation generated by a source, which emits light in the energy regime to be probed experimentally. To probe the valence- and conduction-band spectra of the perovskite TMOs radiation with frequencies of near infrared (NIR), visible (vis), and ultra violet (UV) light is used. The spectrum is then re-measured after placing the material of interest in between the source and the detector. The two measured spectra can then be combined to either determine the transmittance  $T$  corresponding to the fraction of radiation refracted by the material or the reflectance  $R$ , which is the fraction of the incident radiation that is reflected from the surface of the material. The sample spectrum alone is not sufficient to determine transmission or reflectance spectra, because they will be affected by the experimental conditions, such as the spectrum of the source, the spectra of other materials in between the source and detector and the wavelength-dependent characteristics of the detector. The reference spectrum will be affected in the same way, though, by these experimental conditions and therefore the combination of both spectra yields the spectrum of the material alone.

In recent years, spectroscopic ellipsometry (SE) has evolved to a powerful, alternative optical technique to measure dielectric properties of thin films. Ellipsometry measures the change in the polarization of the radiation upon reflection. The polarization state of the radiation incident upon the sample may be decomposed into a component  $p$  parallel to the plane of incidence and a component  $s$  (from German "senkrecht") perpendicular to that plane. The amplitudes of the  $s$  and  $p$  components, after reflection and normalized to their initial value, are denoted by  $r_s$  and  $r_p$ . Ellipsometry measures the complex reflectance ratio  $\rho$  given by

$$\rho = \frac{r_p}{r_s} = \tan(\Psi)e^{i\Delta}, \quad (5.3)$$

where the amplitude ratio  $\tan(\Psi)$  upon reflection and the phase shift  $\Delta$  are the two quantities determined experimentally. Since ellipsometry measures an intensity ratio instead of pure intensities no reference measurement is needed.

The basic mechanism exploited in all optical spectroscopies is the excitation of electrons from an occupied to an unoccupied state by absorbing the energy  $\hbar\omega$  of an incident photon or the deexcitation by emitting a photon, where the energy of the photon has to match the energy difference between the initial and the final state. If the reflectance or transmittance are plotted as functions of the energy of the incident photons, maxima of  $R(\omega)$  or minima of  $T(\omega)$  can thus be identified as transition energies between occupied and unoccupied states. However, an electron which has been excited into an empty state of the conduction band can couple via the Coulomb interaction to the hole in the valence band created upon the excitation. The combined electron-hole pair is called exciton. The excitation of excitons may effect optical spectra in two ways: the formation of bound excitons with energies smaller than that of the fundamental gap  $E_{\text{gap}}$  may hamper the determination of  $E_{\text{gap}}$  in optical spectroscopies. Secondly, the formation of excitons with energies larger than  $E_{\text{gap}}$  usually leads to a shift of the peaks in transmission or reflectance spectroscopy to lower energies compared to the energy differences between the actual QP states [167, 168].

Transmittance or reflectance are directly related to the real part  $n(\omega)$  of the complex refractive index

$$\tilde{n}(\omega) = n(\omega) + i\kappa(\omega) \quad (5.4)$$

via the Fresnel equations. The imaginary part  $\kappa(\omega)$  of  $\tilde{n}(\omega)$  describes the loss through absorption of light propagating through the material and is therefore also called extinction coefficient. If  $n(\omega)$  is measured over a wide range of frequencies,  $\kappa(\omega)$  can be obtained from a Kramers-Kronig transformation. If birefringence is negligible in the material of interest, the macroscopic dielectric function  $\epsilon_M(\omega)$  introduced in section 3.3.5, chapter 3, is related to the complex refractive index by

$$\epsilon_M(\omega) = \tilde{n}^2(\omega). \quad (5.5)$$

From transmission spectroscopy, the absorption coefficient  $\alpha(\omega)$  of a material can also be directly determined, as it is related to the intensities  $I_0(\omega)$  of the incident light and  $I(\omega, z)$  of the transmitted light according to the Beer-Lambert law

$$I(z, \omega) = I_0(\omega) \cdot e^{-\alpha(\omega)z}, \quad (5.6)$$

where  $z$  is the thickness of the sample. The absorption coefficient, in turn, is related to the extinction coefficient by

$$\alpha(\omega) = \frac{4\pi\kappa(\omega)}{\lambda}, \quad (5.7)$$

where  $\lambda$  is the wavelength of the incident light. Moreover, Tauc [169] as well as Davis and Mott [170] established that the absorption coefficients of semiconductors are related to the energy of their fundamental gaps  $E_{\text{gap}}$  by

$$\alpha(\omega) \cdot \hbar\omega \sim (\hbar\omega - E_{\text{gap}})^2. \quad (5.8)$$

This relation is frequently used to derive the energy of the fundamental gap by a linear fit to the plot of the square root of the absorption coefficient obtained from transmission spectroscopy.

The quantities measured in SE, i.e., the amplitude ratio  $\tan(\Psi)$  and phase shift  $\Delta$ , can, in general, not be converted directly into the optical constants of the sample. Usually, a layer model is established, which considers the optical constants and thickness parameters of all individual layers of the sample including the correct layer sequence. Based on an iterative procedure, unknown optical constants and thickness parameters are varied and  $\tan(\Psi)$  and  $\Delta$  are calculated using the Fresnel equations. The calculated  $\tan(\Psi)$  and  $\Delta$  values, which match the experimental data best, provide the optical constants and thickness parameters of the sample. Further details on the procedures used to extract material properties from results of SE can be found in reference [171, 172].

### 5.3.3. Band gaps, semicore states, and dielectric functions

In table 5.4, energies of interband transitions between the QP states obtained from GW calculations for the RT crystal phases of the perovskite TMOs comprising the series  $\text{ATiO}_3$ ,  $\text{BaBO}_3$ , and  $\text{PbBO}_3$  are compared to transition energies determined experimentally. In addition, the transition energies obtained from the KS band structures of the RT crystal phases as well as the results from DFT (GGA) and GW calculations for the cubic lattices are listed. Whereas the results from DFT calculations systematically underestimate the energies measured in experiment, the QP band gaps are in much better agreement with the experimental data for all materials. Furthermore, explicit changes can be observed in the results obtained for the different crystal phases. The sizes of the fundamental band gaps calculated for the different crystal phases differ by as much as 1.09 eV in  $\text{PbTiO}_3$ . In  $\text{CaTiO}_3$ ,  $\text{PbZrO}_3$ , and  $\text{PbHfO}_3$ , the positions of the fundamental band gaps in the RT crystal phases differ from those in the cubic lattices and the size of the gaps for the RT crystal phases is significantly smaller as for the cubic phases. In contrast, the transition energies obtained for the RT phases of  $\text{BaTiO}_3$  and  $\text{PbTiO}_3$  are larger compared to those of the cubic phases. For all materials, the energy differences between QP states calculated for the RT crystal phases agree best with the experimental data. Thus, it is vitally important to consider the correct RT crystal phase explicitly in theoretical investigations to attain a quantitative description of the spectra observed in experiment.

Material	Interband Transition	Energy gaps (eV) of the cubic phase		Energy gaps (eV) of the crystal phase at RT		
				<i>cubic</i>		
				DFT	GWA	Exp.
SrTiO <sub>3</sub>	R → $\Gamma$	–	–	1.88	3.61	3.20* [151]
	$\Gamma$ → $\Gamma$	–	–	2.23	3.96	3.88# [151]
BaZrO <sub>3</sub>	R → $\Gamma$	–	–	3.24	4.94	4.86* [150]
	$\Gamma$ → $\Gamma$	–	–	3.41	5.20	–
BaHfO <sub>3</sub>	R → $\Gamma$	–	–	3.67	5.40	5.7+ [146]
	$\Gamma$ → $\Gamma$	–	–	3.76	5.58	–
		<i>cubic</i>		<i>tetragonal</i>		
		DFT	GWA	DFT	GWA	Exp.
BaTiO <sub>3</sub>	R/A → $\Gamma$	1.80	3.32	1.84	3.45	3.27# [149]
	$\Gamma$ → $\Gamma$	1.91	3.46	2.20	3.81	3.92# [149]
PbTiO <sub>3</sub>	X → X	(1.63)	(2.98)	3.06	3.98	3.81# [148]
	X → X'	2.77	3.51	(3.14)	(4.61)	–
	Z → Z	–	–	(2.15)	(3.68)	–
	Z → Z'	–	–	3.12	4.02	4.11# [148]
		<i>cubic</i>		<i>orthorhombic</i>		
		DFT	GWA	DFT	GWA	Exp.
CaTiO <sub>3</sub>	R → $\Gamma$	1.88	3.62	2.29	3.86	–
	$\Gamma$ → $\Gamma$	2.34	4.11	1.88	3.44	3.57* [147]
PbZrO <sub>3</sub>	X → X	2.44	3.28	3.06	3.80	–
	$\Gamma$ → $\Gamma$	4.12	5.63	2.78	3.47	3.86# [148]
PbHfO <sub>3</sub>	X → X	2.48	3.37	3.00	3.79	–
	$\Gamma$ → $\Gamma$	4.65	6.14	2.73	3.45	–

\* UV-vis absorption spectroscopy

# Spectroscopic ellipsometry (SE)

+ Ultraviolet photo emission (UPS) and x-ray absorption (XAS) spectroscopy

**Table 5.4.:** Energies of interband transitions in the KS and QP band structures of perovskite TMOs obtained from calculations for the cubic and RT crystal structures compared to experimental data. Transition energies of PbTiO<sub>3</sub> listed in brackets are dipole-forbidden. (See text for further details.)

Apart from the significant improvement over the DFT result, smaller deviations between the QP transition energies obtained from the GWA and the experimental data can yet be observed. In  $\text{SrTiO}_3$ ,  $\text{BaTiO}_3$ , and  $\text{PbTiO}_3$  as well as  $\text{BaZrO}_3$  the GWA predicts transition energies that are slightly larger than the ones observed in experiment, whereas it underestimates the fundamental gaps of  $\text{CaTiO}_3$ ,  $\text{BaZrO}_3$  and  $\text{PbZrO}_3$ . As a large effort was made to converge the GW calculation for the RT crystal phases of  $\text{CaTiO}_3$ ,  $\text{PbZrO}_3$ , and  $\text{PbHfO}_3$  to within 0.05 eV and the calculations for the other five compounds to within 0.01 eV, these deviations must either originate from the approximations inherent to the first-principles calculations or from inaccuracies in the experimental data or from a combination of both. In general, it is important to note the difference between optical and photo-emission spectra. Although the spectra might be close in energy and yield similar values for the transition energies in solids, the physical mechanisms exploited in the two spectroscopic procedures are different. The QP spectra obtained from the GWA yields approximations to photo-emission spectra as described in section 2.3, chapter 3. It is not to be expected that the QP spectrum describes an optical spectrum correctly, because they represent a different kind of excitation spectrum. Nevertheless, it is instructive to critically revise the approximations used in the GW calculations as well as the procedures used to determine the transition energies in experiment to identify and better understand possible causes of the discrepancies between the QP transition energies and the experimental data.

In the single-shot GW calculations for the perovskite TMOs, energy differences of KS eigenvalues describing the occupied and unoccupied states, respectively, enter into the calculation of the polarization function, eq. (3.34), which, in turn, is used to determine the screened Coulomb potential, eq. (3.38). The systematic underestimation of the transition energies in DFT (GGA) leads to an overestimation of contributions from low-energy transitions to the polarization function. Hence, the screening of the bare Coulomb potential can become too large. Therefore, single-shot GW calculations for binary semiconductors often underestimate the fundamental band gaps (cf. figure 2.3, chapter 2). Hence, the underestimation of the band gaps of  $\text{CaTiO}_3$  and  $\text{PbZrO}_3$  can be attributed to an overestimation of the screening in these two compounds. It has been demonstrated for binary semiconductors that the size of the band gaps is usually increased [74, 75] if GW calculations are carried out self-consistently, i.e., by replacing the KS eigenvalues in the calculation of the polarization function by the QP energies obtained from the GWA. However, self-consistent calculations are beyond the scope of this work.

The overestimation of the transition energies, in particular in  $\text{SrTiO}_3$  and  $\text{BaTiO}_3$ , are most likely related to the neglect of the influence of phonons in the GW calculations. The momentum of the radiation used in the optical experiments is

too small to directly induce indirect transitions. Hence, these types of transitions can only be observed in optical experiments due to a coupling between electronic and phononic excitations and the latter is not taken into account in the GW calculations. In reference [151], the temperature dependence of the absorption edge of SrTiO<sub>3</sub> was determined. Cooling of the samples resulted in a shift of the absorption edge to higher energies. This substantiates the influence of phonons on the transition energies measured in experiment. Furthermore, it may suggest that the QP gaps obtained from the GWA are in better agreement with the actual electronic energy gaps of these compounds than indicated by the comparison to the optical gaps.

Furthermore, fundamental gaps, i.e., the indirect transitions lowest in energy of SrTiO<sub>3</sub> and BaZrO<sub>3</sub>, are frequently derived from experimental data by a linear fit to the curve  $[\alpha(\omega)\hbar\omega]^2$  exploiting the relation in eq. (5.8). As pointed out by Benthem *et al.* [173], who investigated the absorption spectrum of SrTiO<sub>3</sub>, these band-gap energies can vary depending on the range of absorption coefficients used for the linear fit. For example, this technique was applied in references [150] and [174] to determine the fundamental gap of BaZrO<sub>3</sub>. In reference [150], a gap of 4.86 eV was determined whereas in [174] a gap of 5.4 eV was derived. Furthermore, it is already known since the middle of the eighties [175] that the absorption edge of these materials has a long exponential tail not described by eq. (5.8). The origin of this behavior first observed by Urbach [176] has not been fully clarified yet, but its existence in many different materials has been confirmed in numerous experiments. According to the Urbach rule, the absorption coefficient in the energy region close to the fundamental absorption edge is described by

$$\alpha(\omega, T) = \alpha_0 \exp\{(\hbar\omega - E_{\text{gap}})/k_B(T - T_0)\} \quad (5.9)$$

where  $k_B$  is the Boltzmann constant,  $T$  denotes the temperature and  $T_0$  and  $\alpha_0$  are material-specific constants. It was pointed out by Wemple [177], who reported an Urbachian tail in BaTiO<sub>3</sub> extending down to nearly 2.5 eV, that  $E_{\text{gap}}$  and  $\alpha_0$  cannot be determined simultaneously from the absorption spectrum in the energy region of the Urbachian tail. Wemple emphasized the importance to measure the absorption edge in those energy regime, where the Urbachian tail blends in with the region, where the behavior predicted by eq. (5.8) is dominant, in order to minimize the influence of the temperature and to guarantee reliable results from the linear fit to  $[\alpha(\omega)\hbar\omega]^2$ . In more recent publications, e.g., in reference [174], these aspects have not been discussed and it is not clear if they have been taken into account in the analysis of the experimental data. Hence, the reliability of the value for the band gap of BaZrO<sub>3</sub> taken from reference [174] is questionable.

Likewise, the reliability of the experimentally determined band gaps of BaHfO<sub>3</sub> and CaTiO<sub>3</sub> in table 5.4 is also questionable. The value of BaHfO<sub>3</sub> was determined

from a combination of spectra obtained from direct and inverse PES. As already mentioned, the alignment of the two spectra is delicate and the resulting band-gap value taken from reference [146] must be taken with a grain of salt. In reference [147], the value of the band gap is identified as the optical absorption edge without any further definition or explanation. The existence of an Urbachian tail or a temperature dependence of the absorption spectrum is not discussed. Unfortunately, no other experiments could be found that measured the band gaps of BaHfO<sub>3</sub> and CaTiO<sub>3</sub> whereas the values listed for the other materials in table 5.4 have been confirmed by several groups [178, 179, 173, 180, 181, 182].

For the cubic crystal phase of PbTiO<sub>3</sub>, Lee *et al.* [153] calculated the dipole transition-matrix elements squared which are denoted by  $p_{i \rightarrow f}$  in this work according to

$$p_{i \rightarrow f} = |\langle \varphi_{n\mathbf{k}}^{(f)} | \nabla | \varphi_{n'\mathbf{k}'}^{(i)} \rangle|^2 \quad (5.10)$$

where the initial (i) and final (f) states correspond to the KS eigenstates from DFT calculations. With  $\mathbf{k} = \mathbf{k}'$  and  $n, n'$  denoting a band below and above  $E_F$ , respectively,  $p_{i \rightarrow f}$  can be taken as an estimate for the optical transition probability between the two state. Lee found that the matrix element calculated for the lowest direct transition at the X point between the electronic eigenstates obtained for the cubic crystal structure is zero.

For this work, dipole transition-matrix elements between initial and final states taken from the electronic structure of the cubic as well as the tetragonal, ferroelectric crystal phase were calculated. For the cubic lattice, the results of Lee could be confirmed, i.e., for the transition lowest in energy denoted by  $X \rightarrow X$  in table 5.4  $p_{X \rightarrow X} = 0$ . The transition second lowest in energy also occurs at the X point in the electronic structure of the cubic crystal phase and is labeled  $X \rightarrow X'$  in table 5.4. As  $p_{X \rightarrow X'}$  is larger than zero, it is concluded in reference [153] that this is the transition corresponding to the fundamental gap measured in optical spectroscopies.

In the RT crystal phase, the lowest direct transition occurs at the Z point. However, the transition probability  $p_{Z \rightarrow Z}$  is also zero. On the other hand, the transition second lowest in energy can again be found between the highest occupied and lowest unoccupied states located at the X point. As  $p_{X \rightarrow X} > 0$  for the electronic structure of the RT crystal phase, the value of 3.98 eV listed in table 5.4 is identified as the most probable transition measured in SE. In addition, the energy of the transition at the Z point between the highest occupied and the unoccupied state second lowest in energy, which is denoted by  $Z \rightarrow Z'$  in table 5.4, also agrees well with the transition energy measured by SE.

Last but not least, the influence of the SOC term on the conduction-band states of PbZrO<sub>3</sub> and PbHfO<sub>3</sub> was already emphasized in the previous part of this chapter. However, GW calculations fully incorporating the influence of the

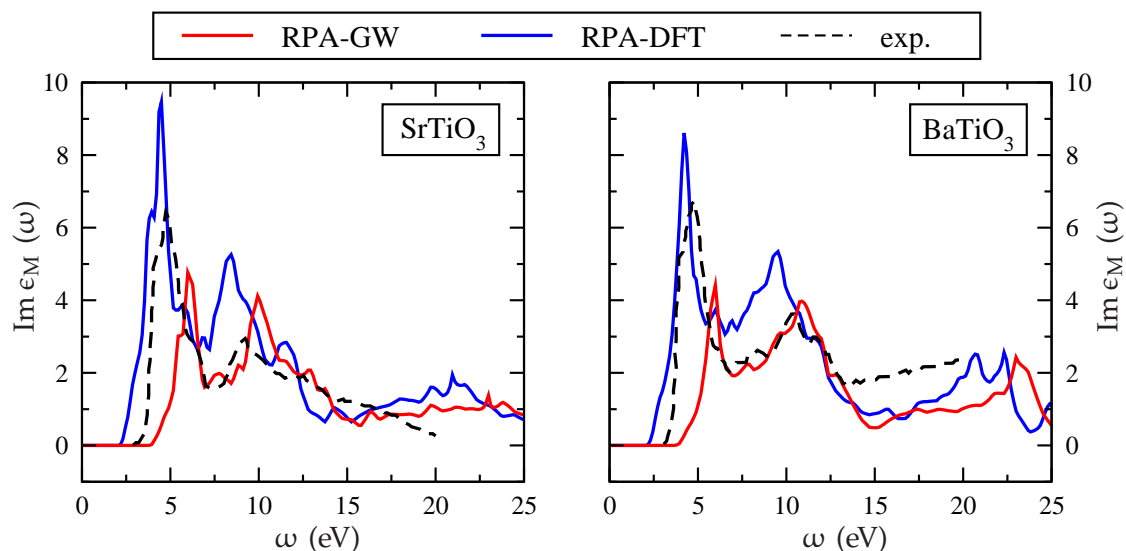


**Figure 5.21.:** The imaginary part of the macroscopic dielectric function of SrTiO<sub>3</sub> and BaTiO<sub>3</sub> calculated within RPA using the KS eigenvalues (RPA-DFT) and the QP energies from a GW calculation (RPA-GW) as input are compared to the dielectric function obtained from reflectance spectroscopy [178].

SOC for these materials are not feasible at the moment. As the SOC leads to sizable changes in the spectra of these two compounds it should be taken into account in the GW calculations to obtain an accurate estimate of the QP gaps.

The fundamental difference between QP and optical spectra mentioned previously can be illustrated best by looking directly at the optical absorption spectrum. Figure 5.21 compares the imaginary part of the macroscopic dielectric function of SrTiO<sub>3</sub> and BaTiO<sub>3</sub> obtained from reflectance spectroscopy [178] with two curves obtained from first principles calculations. The results coined RPA-DFT (blue lines) were obtained from calculations of the dielectric function within the RPA (section 3.3.5, chapter 3) using the KS eigenvalues to calculate the polarization function. Although the resulting spectra agree qualitatively with the experimental curves of both materials they are both shifted to lower energies, because the transition energies are underestimated within DFT (GGA). Replacing the KS eigenvalues by the QP energies obtained within GWA in the calculation of the polarization function results in the red curves in figure 5.21 labeled RPA-GW. The resulting spectra shift to higher energies but overcompensate the underestimation of the GGA. This is most easily seen in the onset of the absorption. Furthermore, relative peak heights of the RPA-GW spectra, which can be taken as measures of the absorption strength, differ from those observed in experiment.

Semicore state	Method	$E - E_{\text{VBM}}$ (eV)		
		CaTiO <sub>3</sub>	SrTiO <sub>3</sub>	BaTiO <sub>3</sub>
Ti 3p	DFT	-39.41	-32.70	-32.78
	GWA	-40.10	-33.14	-32.79
	exp.	-	-34 [183]	-34 [183]
A ns (A = Ca, Sr, Ba)	DFT	-32.69	-32.65	-24.64
	GWA	-32.92	-32.82	-24.78
	exp.	-33.43 [184]	-34 [183]	-27 [183]
A np (A = Ca, Sr, Ba)	DFT	-20.36	-14.70	-9.83
	GWA	-21.82	-16.01	-10.51
	exp.	-22.43 [184]	-16 [183]	-12 [183]
O 2s	DFT	-17.03	-16.94	-16.50
	GWA	-17.18	-17.14	-16.53
	exp.	-18.43 [184]	-19.5 [183]	-19 [183]

**Table 5.5.:** Energy levels of semicore states of CaTiO<sub>3</sub>, SrTiO<sub>3</sub>, and BaTiO<sub>3</sub> at the  $\Gamma$  point obtained from DFT (GGA) and GW calculations are compared to results from XPS.

Both discrepancies, the blue shift as well as the underestimation of the absorption strength in the low-energy part of the spectra can be attributed to the neglect of excitons in the description of the optical spectra calculated within the GWA [167]. Excitonic effects can be included in the first-principles description of optical spectra, e.g., by an approximate solution of the Bethe-Salpeter equation [167, 168]. In particular, it was demonstrated by Rohlfing and Louie [168] that a proper description of optical spectra is not obtained by simply shifting the QP energies by the amount of the binding energies of the excitons. It rather leads to a renormalization of the whole QP spectrum calculated within the GWA, which results in a much better agreement between the theoretical and experimental optical spectra.

However, the poor resemblance of the RPA-GW dielectric function with the optical spectra does not indicate that the approximation of the true QP spectrum obtained from the GWA is erroneous. It only emphasizes that QP and optical spectra are not alike. Optical excitations measured by absorption spectroscopy are neutral excitations, i.e., the number of electrons in the solid is unchanged.

This can be described by the Bethe-Salpeter equation in the context of many-body perturbation theory. In photo-emission spectroscopy, the number of electrons is raised or reduced by one. This kind of excitation is model by QP spectra obtained from the GWA. Excitonic effects can, in principle, be incorporated in the GW calculations of the QP spectra in terms of vertex correction, but this is beyond the scope of the calculations presented here. However, it was already mentioned in section 2.3.4 of chapter 2 that the vertex corrections employed so far only result in small or no changes of the QP spectra [76, 77].

Last but not least, the energies of semicore states of  $\text{CaTiO}_3$ ,  $\text{SrTiO}_3$ , and  $\text{BaTiO}_3$  obtained from DFT (GGA) and GW calculations are compared to results from XPS. As observed previously, the DFT and GW results are very close in energy. They agree best with the energies measured in  $\text{CaTiO}_3$  and are slightly worse for  $\text{SrTiO}_3$  and  $\text{BaTiO}_3$ . Furthermore, all energies obtained from DFT and GW calculations are larger than the ones observed in experiment. Since QP energies from the GWA are slightly lower than the KS eigenstates, the QP corrections from GW calculations at least yield a small improvement over the DFT results.

In the previous section, the influence of the different contributions to the QP correction for the semicore states was analyzed. It was demonstrated that the exchange part yields a large negative contribution to the QP correction, whereas the screening of the Coulomb potential leads to a positive correction which almost cancels the former contribution. Hence, the overestimation of the screening discussed earlier in this section might be responsible for the observed deviations between the QP energies and the XPS results. In addition, the exchange contribution might also be too small, since it ought to correct the self-interaction error, which effects the KS eigenvalues as well as the KS eigenstates. Since the latter are used in the evaluation of the matrix elements of the exchange contribution to the QP correction, the self-interaction is not removed completely in the GWA.

## 5.4. Discussion and Summary

In this chapter, results from all-electron DFT (GGA) and GW calculations for the perovskite TMOs  $\text{CaTiO}_3$ ,  $\text{SrTiO}_3$ ,  $\text{BaTiO}_3$ ,  $\text{PbTiO}_3$ ,  $\text{BaZrO}_3$ ,  $\text{BaHfO}_3$ ,  $\text{PbZrO}_3$ , and  $\text{PbHfO}_3$  obtained from the FLAPW-based implementations FLEUR and SPEX have been analyzed. Detailed convergence test for these materials demonstrate that more than 180 unoccupied states per atom in the unit cell are needed to converge the QP corrections from the GWA of the lower-lying conduction bands to within 0.01 eV. This emphasizes the necessity to improve the representation of the unoccupied states, because the conventional LAPW basis does not yield an accurate description of high-lying states. It was shown that this deficiency can be removed by adding LOs to the conventional LAPW basis, which are located in

the unoccupied part of the KS eigenvalue spectrum. The efficiency of the ansatz in comparison to other methods [156] has been demonstrated. Moreover, only a small number of LOs has to be retained in the construction of the MPB used in the GW calculations to obtain an accurate description of the unoccupied states, which makes this scheme fast and efficient.

The investigation of the KS and QP band structures of the perovskite TMOs has revealed trends in the electronic structures of the cubic crystal phases in the series  $ATiO_3$  with  $A = Ca, Sr$  and  $Ba$ ,  $BaBO_3$ , and  $PbBO_3$  with  $B = Ti, Zr$ , and  $Hf$  due to changes in the chemical compositions. The valence bands of all compounds are mainly composed of oxygen 2p states. Furthermore, the conduction bands lowest in energy in the series  $ATiO_3$  and  $BaBO_3$  exhibit transition-metal d character. Hence, the band gaps in the series  $ATiO_3$  are very similar. In the series  $BaBO_3$ , band gaps become larger if Ti is replaced by Zr or Hf, because the more extended Zr 4d and Hf 5d are located at higher energies.

In the  $PbBO_3$  series, the Pb 6p states lead to the formation of additional conduction bands. In contrast to the compounds from the  $ATiO_3$  and  $BaBO_3$ , the conduction-band minimum (CBM) is formed by the Pb 6p states instead of d states of Zr and Hf, whereas in  $PbTiO_3$  the Ti 3d states make up the CBM. As the Ti 3d-derived bands in  $PbTiO_3$  are located in the same energy interval as the Pb 6p-derived bands lowest in energy in  $PbZrO_3$  and  $PbHfO_3$ , only small changes in the band gaps are observed in the  $PbBO_3$  series.

Moreover, it is illustrated that the shape as well as the positions of conduction bands, which are composed of Pb 6p states, are altered significantly if SOC is included in the DFT calculations for compounds in the series  $PbBO_3$  in second variation. However, it is questionable whether changes in KS band structures resulting from SOC can be translate directly into changes in the QP spectra by simply adding the difference between the KS eigenstates obtained with and without the corrections from the SOC to the QP energies, because the transition energies between the occupied part of the KS eigenvalue spectrum and a large number of unoccupied states up to high energy enter the equation for the GW self-energy. As the SOC changes the positions of the conduction-band states in a broad energy region the effect on the screening of the Coulomb interaction calculated within the GWA cannot be predicted without further investigations. GW calculations fully taking into account the effect of SOC will be necessary to answer the question how the SOC changes the QP states.

In general, the QP corrections obtained from the GWA lead to downward shifts of the occupied part of the KS spectrum and to upward shifts of the unoccupied parts. However, the size of these energy shifts strongly depends on the orbital composition of the KS eigenstates. For example, in  $PbTiO_3$ , the QP corrections obtained at the X point for the first two conduction bands above  $E_F$

with prevalent Ti 3d and Pb 6p character, respectively, differ by a factor of three. This demonstrates clearly that a quantitative description of the QP spectra of the perovskite TMOs cannot be obtained from a uniform shift of the conduction bands to higher energies, e.g., by applying a scissors operator but may only be attained if the QP corrections for each band at each  $\mathbf{k}$  point are calculated explicitly.

For all perovskite TMOs investigated in this chapter, good agreement has been found between the QP gaps in the band structures of the RT crystal phases with transition energies measured in experiment. In particular, the QP gaps agree much better with the experimental data than the corresponding transition energies between KS eigenstates. Furthermore, significant deviations between the QP band structures of the high-temperature cubic lattices and the RT crystal phases emphasize the necessity to consider the RT crystal structure in theoretical studies to attain quantitative agreement with experimental data. In addition, the GW calculations also lead to a small but systematic improvement of the energies of semicore states with respect to experimental data.

Smaller deviations between the QP gaps and experimental data could be related to approximations inherent to the GW calculation, i.e., the neglect of electron-phonon coupling and the vertex function or the use of the KS eigenstates in the evaluation of the polarization functions. The latter is considered to result in an overestimation of the screening which, in turn, might lead to an underestimation of band gaps. Self-consistent GW calculations typically lead to larger band gaps. The reason for the increase is usually attributed to a reduction of the screening as the KS eigenvalues are replaced by the QP energies in the self-consistent calculations. Furthermore, the QP wave functions are approximated by the KS wave functions in single-shot GW calculations. A better estimate for the QP states might be obtained if off-diagonal elements of the GW self-energy neglected in the present approach are included in the calculations. In addition, the results from the present approach do depend on the choice of the DFT starting point as will be demonstrated in the following chapter. Although the comparison between the QP band gaps and experimental data imply that DFT (GGA) calculations yield a good starting point to apply many-body perturbation theory in terms of the GWA to describe the electronic structure of the perovskite TMOs discussed in this chapter, it could be educational to use input data obtained from DFT-based calculations employing hybrid functional or OEP.

Last but not least, the transition energies and band gaps reported for the valence- and conduction-band regime were mainly determined in optical spectroscopies. Due to the fundamental difference between optical and QP excitations, a one-to-one agreement of the experimental data and the QP gaps should not be expected. In particular, excitonic excitations not taken into account in GW calculations may alter the transition energies between QP states considerably. This

has been demonstrated by comparing the RPA dielectric functions of SrTiO<sub>3</sub> and BaTiO<sub>3</sub> to absorption spectra determined in experiment.



## CHAPTER 6

# FIRST-PRINCIPLES CALCULATIONS FOR LaCrO<sub>3</sub>, LaMnO<sub>3</sub>, AND LaFeO<sub>3</sub>

Since the middle of the 1990s, the rare-earth compounds of the series LaBO<sub>3</sub> with  $B = \text{Sc, Ti, V, Cr, Mn, Fe, Co, Ni, and Cu}$  have attracted a lot of attention both experimentally and theoretically [185, 186, 187, 17, 188, 189, 190]. From the experimental point of view, the series is most suitable to investigate the systematic variation of the electronic structure with the  $B$  species, since all of these compounds can be synthesized. Optical and electron spectroscopies reveal a wide spectrum of electronic and magnetic ground state properties throughout the series such as Mott-insulating, charge-transfer type and metallic behavior as well as antiferromagnetism and paramagnetism. This diversity originates from the competition between two opposing trends: the presence of a strong electron-electron interaction strength within the transition-metal  $d$  manifold tends to localize the electrons and stabilize a magnetic moment at the transition-metal site whereas the hybridization between oxygen  $2p$  and transition-metal  $d$  states enhances the delocalization of electrons.

The scope of strong correlation effects on the one hand and delocalized electrons on the other makes it difficult to describe the compounds of this series by first-principles calculations. Band-structure calculations within the LDA or GGA only predict some of the ground state properties of these compounds correctly. In particular, they fail to describe the Mott-insulating phase of LaTiO<sub>3</sub> and LaVO<sub>3</sub> due to the underestimation of correlation effects originating from strong electron-electron repulsion. For the remaining compounds of the series, the mean-field like treatment of correlation within LDA or GGA results in too small magnetic moments. Furthermore, band gaps and conduction-band spectra do not agree well with experimental data [185, 191]. The LSDA+U method

[192, 193], which introduces a static on-site Coulomb repulsion  $U$  felt by two electrons of opposite spins occupying the same KS orbitals, removes some of the deficiencies of the standard LDA or GGA in calculations for some of the compounds of the  $\text{LaBO}_3$  series [186]. Recently, an approach coined  $U+GW$  was introduced [17], which combines the LSDA+ $U$  description with a subsequent GW calculation, to take into account dynamic contributions of the correlation missing in LSDA+ $U$ . Moreover, photo-emission spectra of  $\text{LaTiO}_3$  and  $\text{LaVO}_3$  have been described successfully by a combination of LDA with dynamical mean-field theory [34]. However, the results of these approaches all depend on the choice of the effective Coulomb interaction strength  $U$ . Since there is no unique way to determine  $U$  as indicated by the variety of different values of  $U$  used in the literature [186, 194], the effective Coulomb interaction strength has to be viewed as a parameter in these calculations. A parameter-free description of the compounds of the  $\text{LaBO}_3$  series from first principles is still missing.

In this chapter, results from first-principles GW calculations for the three compounds  $\text{LaCrO}_3$ ,  $\text{LaMnO}_3$ , and  $\text{LaFeO}_3$  are presented. For all GW calculations, results of DFT calculations were used as a starting point employing the PBE functional [25] within the GGA as well as the hybrid functional HSE [23, 24]. This allows for a parameter-free description of the three materials. It is demonstrated that this ansatz improves the description of band gaps and photo-emission spectra of the conduction bands compared to the LDA and GGA results.

In the first part of the chapter, crystal and magnetic structures of the three compounds are introduced. Secondly, the discussion of the KS band structures calculated within GGA yield qualitative insight into their electronic structures. Afterwards, it is demonstrated, how GW calculations employing PBE and HSE results as starting points improve the quantitative agreement of the GGA results with experimental data. A similar trend is observed for the spin-magnetic moments of the transition metals. Finally, some concluding remarks will be given in the last section of the chapter.

## 6.1. Crystal and magnetic structures

The RT crystal structure of  $\text{LaMnO}_3$  [116] was already illustrated in figure 4.2 in chapter 4. The compounds  $\text{LaCrO}_3$  and  $\text{LaFeO}_3$  form similar crystal lattices at RT [115, 117]. All compounds attain an orthorhombic crystal structure at RT, where the oxygen octahedra are tilted and rotated compared to the octahedra in the unit cell of the cubic crystal phases (figure 4.1, chapter 4). The resulting crystal lattices (space group  $\text{Pbnm}$ ) are composed of unit cells containing four chemical units of  $\text{LaBO}_3$ , which corresponds to a total of 20 atoms per unit cell. All calculations presented later-on were carried out for the RT crystal structures

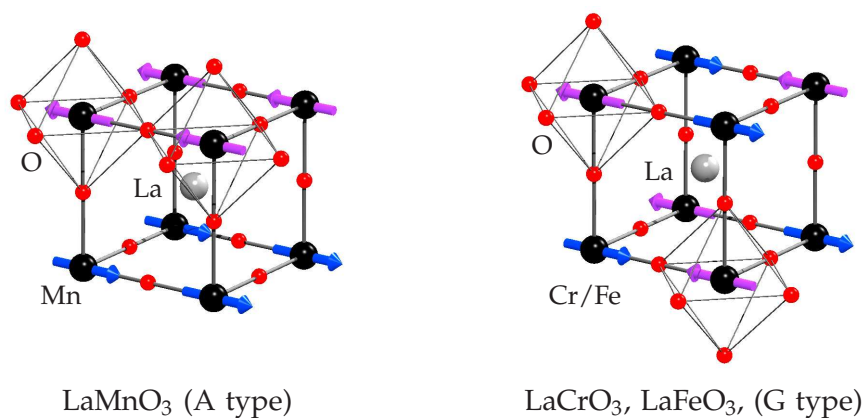


**Figure 6.1.:** Ground-state magnetic structures of LaBO<sub>3</sub> with  $B = \text{Cr}$ , Mn, and Fe (black spheres) and La and O represented by gray and red spheres, respectively. Up and down spin-magnetic moments of Cr, Mn, and Fe are illustrated by blue and pink arrows.

of the three compounds. Lattice constants and atomic positions were taken from experiment (see appendix B.2).

Regarding the magnetic structure of the three compounds, it was discussed briefly in chapter 4 that the spins of electrons occupying the  $d$  states of the transition metals  $B$  in LaBO<sub>3</sub> align in parallel according to Hund's rule. In the ground state, the  $d$  states of the transition metals of all three compounds LaCrO<sub>3</sub>, LaMnO<sub>3</sub>, and LaFeO<sub>3</sub> are partially filled and the alignment of the spins leads to a finite magnetic moment proportional to the total spin of the electrons at each transition-metal site. For all three compounds, an antiferromagnetic (AFM) ordering of the spin-magnetic moments in the ground state has been reported [134]. Different types of AFM spin ordering were categorized in reference [195]. LaMnO<sub>3</sub> exhibit an A-type AFM order, i.e., planes of ferromagnetically ordered spins couple antiferromagnetically to neighboring planes. In LaCrO<sub>3</sub> and LaFeO<sub>3</sub>, a G-type ordering was reported: the total spin-magnetic moment at one transition-metal site couples antiferromagnetically to the magnetic moments at all neighboring sites. The corresponding magnetic structures are illustrated in figure 6.1. For simplicity, cubic unit cells were chosen in figure 6.1 with the transition metal cations occupying the eight corners of a cube. In the first-principles calculations, the experimental geometry and the antiferromagnetic structures were fully taken into account.

## 6.2. KS band structures

Apart from their different magnetic structures,  $\text{LaCrO}_3$ ,  $\text{LaMnO}_3$ , and  $\text{LaFeO}_3$  were all found to be insulators in optical conductivity measurements [188]. Conventional band-structure calculations within the LSDA qualitatively reproduce the magnetic as well as the insulating properties of all three compounds [185, 191]. Furthermore, it was demonstrated by Sarama *et al.* [196] that the valence-band spectra of  $\text{LaMnO}_3$  and  $\text{LaFeO}_3$  obtained from LSDA calculations agree well with photo-emission data. In this section, KS band structures of  $\text{LaCrO}_3$ ,  $\text{LaMnO}_3$ , and  $\text{LaFeO}_3$  in the RT crystal phase obtained from the GGA using the PBE functional are illustrated in figures 6.2 and 6.3 to gain qualitative insight into the electronic structure of the three compounds. In all calculations, the FLEUR code was used. Input parameters are listed in appendix B.2.

The band structure of all three compounds differ from those of the perovskite TMOs discussed in the previous chapter in several ways: the highest-lying valence bands in all three compounds are composed of transition-metal d states. Secondly, there is a large number of bands close in energy located at about 1 eV, 2.5 eV, and 4 eV above the Fermi energy in the conduction-band regime of  $\text{LaCrO}_3$ ,  $\text{LaMnO}_3$ , and  $\text{LaFeO}_3$ , respectively. These bands are composed of La 4f states. Similarly to the band structures of the materials discussed earlier, the main contribution to the valence bands originates from the oxygen 2p states. In contrast to the other materials, these states hybridize more strongly with the transition-metal d states in  $\text{LaCrO}_3$ ,  $\text{LaMnO}_3$ , and  $\text{LaFeO}_3$  in the lower part of the valence band spectra. This is indicated on the right side of the band structures illustrated in figures 6.2 and 6.3, where the main contributions to the distinct bands in certain energy regions are denoted by blue bars.

For a detailed analysis of the band structures, it is helpful to first consider the electronic structure of the cubic crystal phases. As discussed in detail in chapter 4, the transition-metal d states split into triply degenerate  $t_{2g}$  and doubly degenerate  $e_g$  states in the cubic phase due to the interaction of the transition-metal states with the crystal field generated by the surrounding oxygen atoms. In accordance with Hund's rule, the electronic configuration of the  $\text{Cr}^{3+}$  and  $\text{Fe}^{3+}$  cations in  $\text{LaCrO}_3$  and  $\text{LaFeO}_3$  are given by  $t_{2g\uparrow}^3 t_{2g\downarrow}^0 e_{g\uparrow}^0 e_{g\downarrow}^0$  and  $t_{2g\uparrow}^3 e_{g\uparrow}^2 t_{2g\downarrow}^0 e_{g\downarrow}^0$ , respectively, where  $\uparrow$  and  $\downarrow$  denote majority- and minority-spin states. Due to the deviations from the cubic lattice, which lead to the formation of the orthorhombic crystal phases of the two compounds, the degeneracy of the  $t_{2g}$  and  $e_g$  states is lifted. However, the energy splitting between the two subsets of the transition-metal d manifold is substantially larger than the splitting among the distinct  $t_{2g}$  and  $e_g$  states. (Figure 4.5 in chapter 4 illustrates the splitting of the energy levels schematically.) Consequently, the Cr 3d-derived bands in the energy interval between  $-0.5$  eV and  $-1.5$  eV in figure 6.2 can be identified as  $t_{2g\uparrow}$ -like bands in

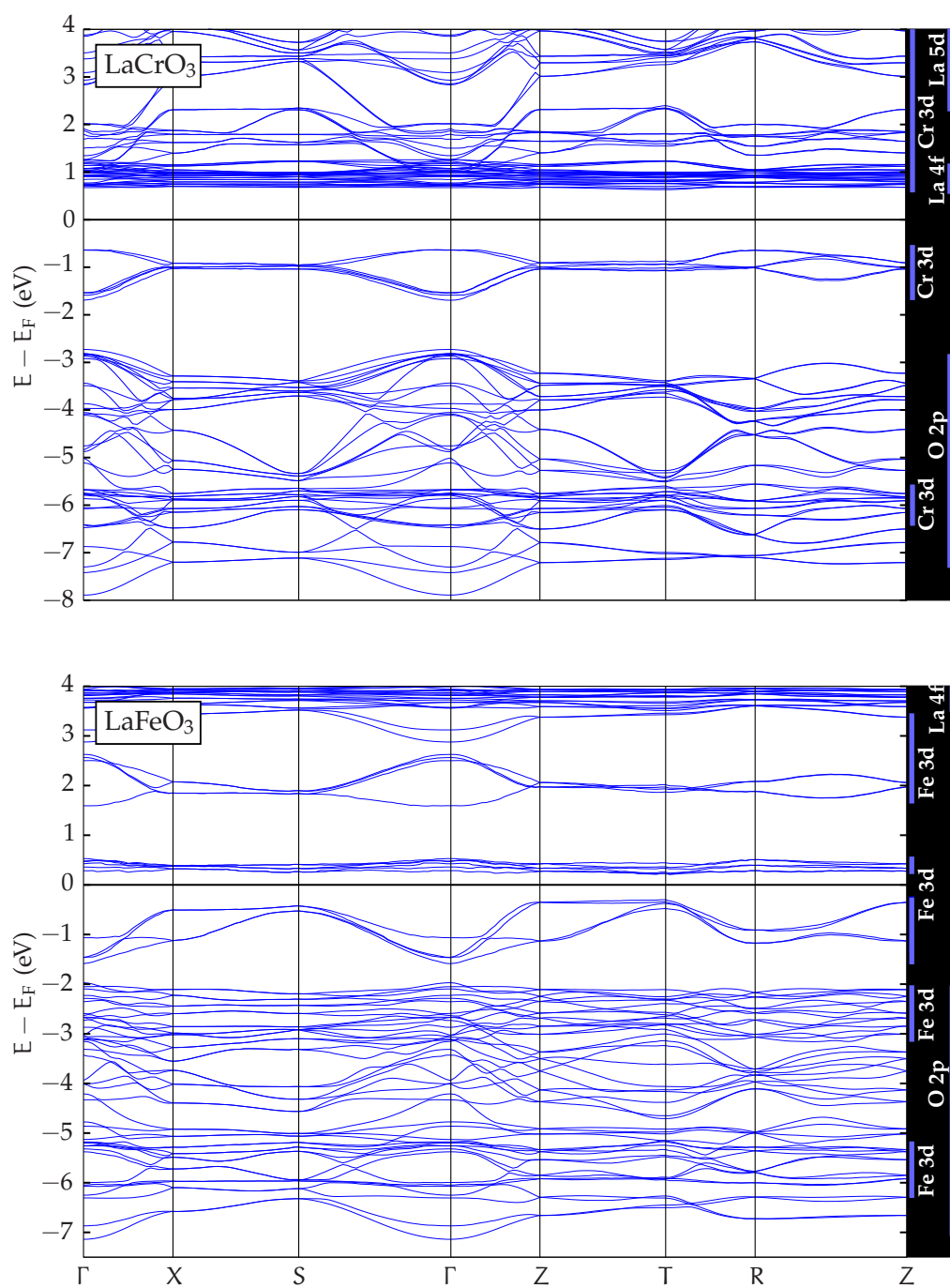


**Figure 6.2.:** KS band structures of orthorhombic LaCrO<sub>3</sub> (top) and LaFeO<sub>3</sub> (bottom) calculated within GGA using the PBE functional. The Fermi energy is placed in the middle of the band gap. The bars on the right indicate the orbital character of the bands.

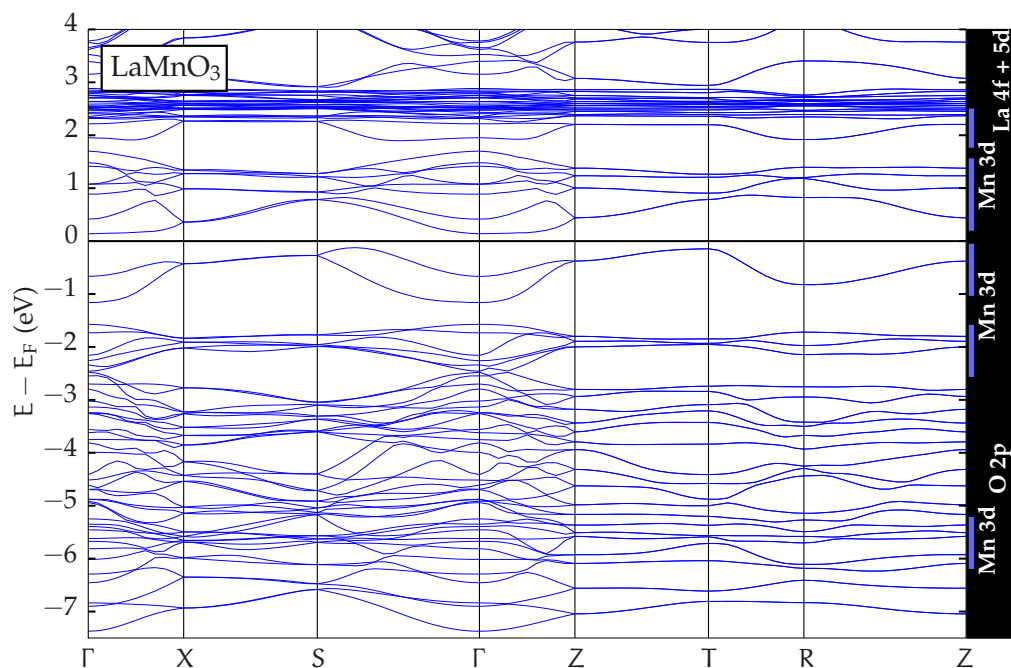


**Figure 6.3.:** KS band structure of orthorhombic  $\text{LaMnO}_3$  calculated within GGA using the PBE functional. The Fermi energy is placed in the middle of the band gap. The bars on the right indicate the orbital character of the bands.

accordance with the electronic configuration of the  $\text{Cr}^{3+}$  cation in cubic  $\text{LaCrO}_3$ . The  $t_{2g\downarrow}$ -like bands and those conduction bands originating from the  $e_g$ -like states cannot be identified directly in figure 6.2, since they are located in the same energy interval above the Fermi energy as those conduction bands composed of La 4f and 5d states. In  $\text{LaFeO}_3$  in figure 6.2, the occupied  $t_{2g\uparrow}$ -like states hybridize with the oxygen 2p states forming bands in the energy interval between  $-3$  eV and  $-2$  eV whereas the highest-lying valence bands consist of Fe  $e_{g\uparrow}$ -like states. The conduction bands lowest in energy consist of  $t_{2g\downarrow}$ -like states, which are well separated from the bands in the interval between  $1.5$  eV and  $2.5$  eV due to the crystal field splitting. The latter are composed of  $e_{g\downarrow}$ -like states.

The electronic structure of  $\text{LaMnO}_3$  differs from that of the other two compounds, because the electronic configuration of the  $\text{Mn}^{3+}$  cation corresponds to  $t_{2g\uparrow}^3 e_{g\uparrow}^1 t_{2g\downarrow}^0 e_{g\downarrow}^0$  in the cubic crystal phase. Since the crystal field only lifts the degeneracy between the  $t_{2g}$  and  $e_g$  states, cubic  $\text{LaMnO}_3$  should be metallic in the ground state, i.e., the Fermi energy crosses the  $e_g$ -derived valence bands. Indeed, Pari *et al.* [185] obtained a metallic ground state from their LSDA calculations for cubic  $\text{LaMnO}_3$  and concluded that the insulating ground state cannot be described correctly within LSDA. However, it was demonstrated shortly after by

Pickett and Singh [191] that the insulating ground state is well attained within LSDA if the experimentally observed crystal and magnetic structure is assumed in the DFT calculation. In the same year, it was suggested [197] that the opening of the gap originates from a splitting between the two bands composed of  $e_{g\uparrow}$ -type states, which is caused by a cooperative Jahn-Teller effect. The crucial contribution of the Jahn-Teller effect to the formation of an insulating phase has been confirmed recently [198]. Hence, the insulating phase of  $\text{LaMnO}_3$  can only be described in first-principle calculation if the distortions originating from the Jahn-Teller effect are properly taken into account, e.g., by assuming the RT crystal structure in the calculation. The resulting KS band structure is shown in figure 6.3. It exhibits a small gap between the two bands composed of the  $e_{g\uparrow}$ -type states. The other Mn 3d-derived valence bands lower in energy have  $t_{2g\uparrow}$  character, the higher-lying conduction bands are of  $t_{2g\downarrow}$  and  $e_{g\downarrow}$  type. The splitting between the latter again results from the influence of the crystal field.

After gaining qualitative insight into the electronic structure of  $\text{LaCrO}_3$ ,  $\text{LaMnO}_3$ , and  $\text{LaFeO}_3$ , the next section deals with the quantitative analysis of band gaps and densities of states obtained from both DFT and GW calculations.

### 6.3. Band gaps and photo-emission spectra

In this section, results from GW calculations for  $\text{LaCrO}_3$ ,  $\text{LaMnO}_3$ , and  $\text{LaFeO}_3$  are presented, which were carried out with the SPEX code. Input data for these calculations were generated by DFT calculations with the FLEUR code, where the PBE functional within the GGA as well as the hybrid functional HSE have been employed. Similar to calculations for the perovskite TMOs discussed in the previous chapter, LOs located in the unoccupied part of the KS eigenvalue spectra have been added to the conventional LAPW basis to improve the description of the unoccupied states in the DFT calculations. For further details on technical aspects of these calculations the reader is referred to the discussion in section 5.1 of the previous chapter. A list of the input parameters for the DFT and the GW calculations can be found in appendix B.2.

Table 6.1 lists the fundamental band gaps of all three compounds determined from optical conductivity measurements [188] as well as the band gaps obtained from DFT and GW calculations. The PBE results systematically underestimate the band gaps of all materials. The GWA using input data from the PBE calculations leads to an opening of the gaps of all compounds. However, only the resulting QP gap of  $\text{LaMnO}_3$  is in good agreement with the experimental data, but the QP gaps of  $\text{LaCrO}_3$ , and  $\text{LaFeO}_3$  obtained from the PBE+GW scheme still underestimate the results from the optical spectroscopy. On the other hand, DFT calculations employing the hybrid functional HSE systematically overestimate

Material	Transition	Band gaps (eV)				
		PBE	PBE+GW	HSE	HSE+GW	Exp.
$\text{LaCrO}_3$	$\Gamma \rightarrow \Gamma$	1.36	2.22	3.71	3.66	3.4
$\text{LaMnO}_3$	$T \rightarrow \Gamma$	0.31	0.84	2.30	2.69	–
	$\Gamma \rightarrow \Gamma$	0.80	1.15	2.57	2.93	1.1
$\text{LaFeO}_3$	$T \rightarrow T$	0.63	1.54	3.61	4.13	2.1

**Table 6.1.:** Fundamental band gaps and smallest direct transitions in the KS and QP spectra obtained from calculations employing the PBE and HSE functionals including corrections from GW calculations compared to data from optical conductivity measurements [188].

the optical gaps. A GW calculation using HSE results as input data leads to a decrease of the gap of  $\text{LaCrO}_3$ . The gap calculated with this HSE+GW scheme agrees well with the data from the optical spectroscopy. In contrast, the QP gaps of  $\text{LaMnO}_3$ , and  $\text{LaFeO}_3$  obtained from the HSE+GW calculations are even larger than the HSE results such that the agreement with experimental data becomes worse.

To further analyze the results from the first-principles calculations, the total and partial densities of states of  $\text{LaCrO}_3$ ,  $\text{LaMnO}_3$ , and  $\text{LaFeO}_3$  have been calculated from the QP energies as described in section 3.3.4 of chapter 3. On the one hand, this allows to systematically investigate changes in the DOS obtained from DFT calculations upon inclusion of the corrections from the GWA in a broader energy range. On the other hand, the DOS can be compared directly to spectra from PES, as the GWA yields an approximate description of the physical processes exploited in photo-emission experiments. Therefore, it is, in principle, favorable to compare the QP spectra from GW calculations to results from PES instead of optical spectroscopies<sup>1</sup>.

For the three materials discussed here, PES, namely x-ray photo-emission (XPS) and ultra-violet photo-emission (UPS) spectroscopy, has been used to analyze the occupied states of the QP spectra [189, 199, 200], whereas the unoccupied parts were probed by Bremsstrahlung isochromat spectroscopy (BIS) in the case of  $\text{LaCrO}_3$  [189] and by oxygen K-edge x-ray absorption spectroscopy (XAS) in  $\text{LaMnO}_3$  and  $\text{LaFeO}_3$  [199, 200]. As it is not possible to probe the occupied and unoccupied parts of the QP spectra simultaneously by PES, the authors from the above references aligned the occupied and unoccupied parts of the spectra

<sup>1</sup>The link between the Green-function formalism and photo-emission spectroscopy is discussed in more detail in section 2.3 of chapter 2 and section 5.3.2 of chapter 5

manually. In reference [200], the gap between the two parts of the spectrum of  $\text{LaFeO}_3$  is adjusted to match the size of the optical gap listed in table 6.1, whereas the spectra of  $\text{LaMnO}_3$  presented in [199] are aligned according to the band gap obtained from a DFT-based calculation. The reference energy used to align the spectrum of  $\text{LaCrO}_3$  obtained from XAS illustrated in reference [189] remains undefined. Hence, a direct comparison of results from our first-principles calculations to the spectra presented in the above references does not allow for a consistent interpretation of the calculated spectra. Therefore, the experimental data were aligned in this work such that the position of the first peaks in the occupied and unoccupied part of the spectra match the position of the first peak in the calculated DOS. This allows to determine how well the calculated spectra can reproduce the shape as well as the relative positions of spectral features observed in experiment. In order to better match the results from PES the calculated spectra were broadened with Gaussian functions to simulate the instrumental broadening.

A comparison of the DOS of the three compounds  $\text{LaCrO}_3$ ,  $\text{LaMnO}_3$ , and  $\text{LaFeO}_3$  shown in figures 6.4, 6.5, and 6.6 reveals that the La 4f states form a large, sharp peak in the unoccupied part of the DOS of all compounds. A similar spectral feature is observed for  $\text{LaCrO}_3$  in BIS but these kind of features do not show in the spectra of  $\text{LaMnO}_3$  and  $\text{LaFeO}_3$  probed by XAS. It was already discussed in the previous section that the La 4f states form a number of very flat bands close in energy, i.e., the La 4f states scarcely hybridize with other states. As pointed out by Sarma *et al.* [189], XAS only probes the oxygen p admixture in the unoccupied parts of the spectra due to dipole selection rules. In particular, it was demonstrated in reference [189] that the dominant peak in the Bremsstrahlung isochromat spectrum of  $\text{LaCrO}_3$  is missing in the spectra of  $\text{LaCrO}_3$  measured by XAS. Therefore, it stands to reason that similar features originating from La 4f state do not show in the x-ray absorption spectra of  $\text{LaMnO}_3$  and  $\text{LaFeO}_3$ . Hence, the spectra obtained from XAS are not suitable to determine the contributions of La 4f states to the QP spectra. However, they do yield information about features originating from other states such as the transition-metal d states and the La 5d states. Keeping this in mind, the spectra of the three compounds  $\text{LaCrO}_3$ ,  $\text{LaMnO}_3$ , and  $\text{LaFeO}_3$  are now discussed in detail.

The best estimate for the optical band gaps listed in table 6.1 has been obtained from the combination of HSE results with the GWA in the case of  $\text{LaCrO}_3$  or GW calculation using PBE results as input in the case of  $\text{LaMnO}_3$  and  $\text{LaFeO}_3$ . Figures 6.4, 6.5, and 6.6 illustrate that the same combinations also yield the best estimate for the photo-emission spectrum of the corresponding material.

In  $\text{LaCrO}_3$ , the highest occupied states mainly contributing to the formation of the first peak below  $E_F$  in the total DOS of  $\text{LaCrO}_3$  in figure 6.4, have  $t_{2g}$ -like Cr 3d character, whereas the lower part of the valence spectrum is primarily

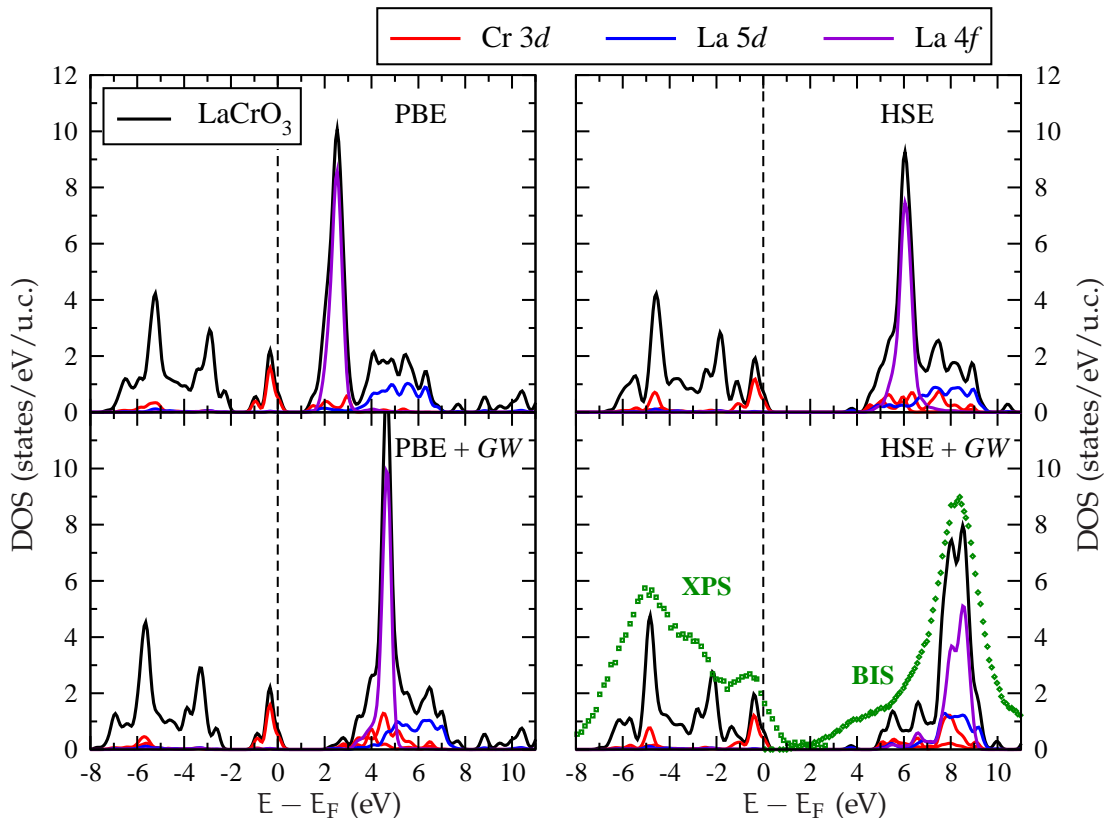


**Figure 6.4.** Total DOS of  $\text{LaCrO}_3$  and pDOS of Cr 3d, La 4f and 5d states. Top row: Results from DFT calculations using the functionals PBE (*left*) and HSE (*right*). Bottom row: DFT spectra shifted by the energy corrections obtained from GW calculations as well as the results from PES (XPS and BIS [189]).

composed of oxygen 2p states. The overall shape of the DOS in the occupied part of the spectrum is identical in all calculations. It consists of three large peaks and a smaller one at the low end of the energy range displayed in figure 6.4. As the 3d states of Cr are more localized than the oxygen 2p states, the self-interaction error (SIE) for the d states in PBE is larger. The partial correction of the SIE by HSE may lead to a larger shift of the Cr 3d states down in energy than for the oxygen 2p states. Consequently, the first peak below  $E_F$  moves closer to the oxygen 2p-derived spectral features in the HSE calculation.

The changes in the unoccupied part of the spectrum of  $\text{LaCrO}_3$  resulting from the GWA using PBE input data are much more pronounced. They are even larger if the HSE functional is used instead of the PBE functional on the DFT level and in HSE+GW calculations. The peak formed by La 4f states moves to higher energies and the unoccupied Cr 3d states are redistributed over a broader energy range than in the PBE calculation. The redistribution of the Cr 3d states

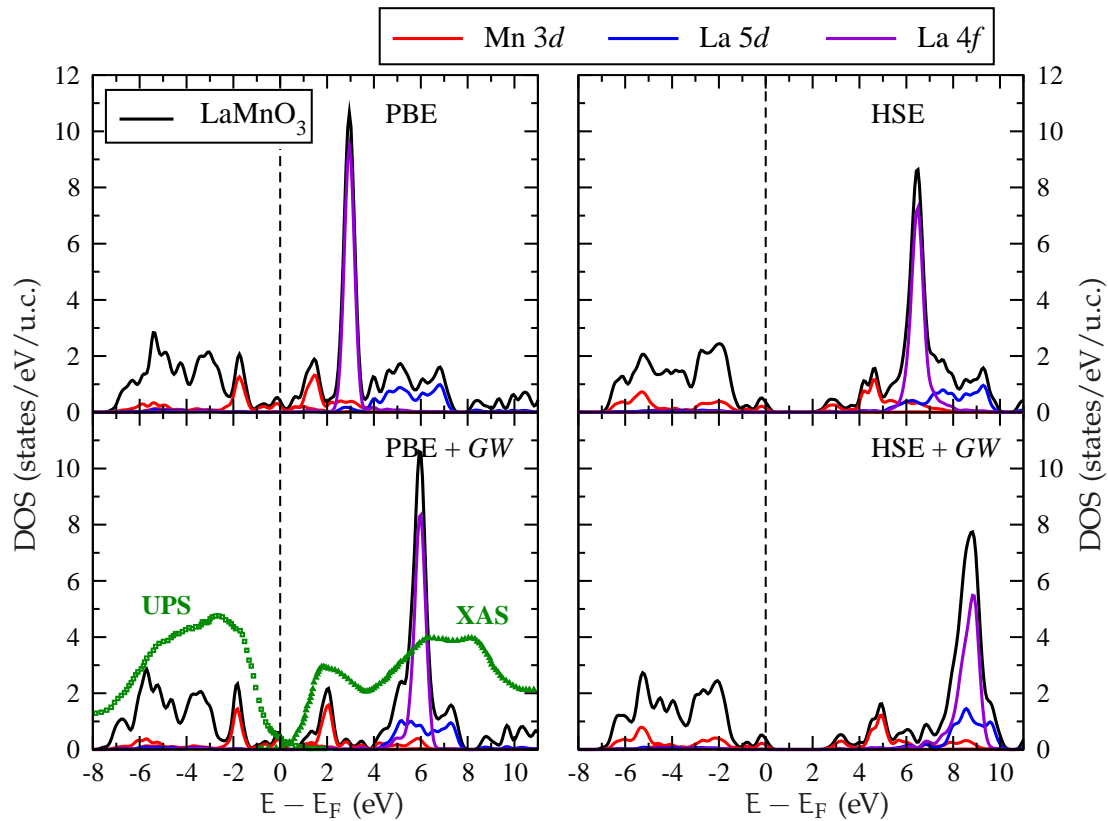


**Figure 6.5.:** Total DOS of  $\text{LaMnO}_3$  and pDOS of Mn 3d, La 4f and 5d states. Top row: Results from DFT calculations using the functionals PBE (*left*) and HSE (*right*). Bottom row: DFT spectra shifted by the energy corrections obtained from GW calculations as well as the results from PES (UPS and XAS [199]). Note, that La 4f-derived features cannot be probed by XAS. (See text for more detail)

enhances the hybridization with La 5d states especially in the HSE calculations. The peak lowest in energy in the spectra obtained with PBE+GW and HSE is composed of La 5d states. Whereas the La 4f-derived features in the DOS move to even higher energies if corrections from GW calculations are added to the HSE results, the hybridized Cr 3d and La 5d states stay in the same energy range and the peak lowest in energy moves slightly down in energy. The DOS obtained from the HSE+GW calculations agrees best with the spectra determined by XPS and BIS. In particular, the broad shoulder on the low-energy side of the the large peak in the BIS spectrum between 3 and 7 eV above  $E_F$  is only reproduced by the HSE+GW results.

For  $\text{LaMnO}_3$  and  $\text{LaFeO}_3$ , the band gaps in the PBE DOS in figures 6.5 and 6.6 are small and barely visible due to the broadening of the calculated spectra with Gaussian functions. In the PBE+GW calculations, the band gaps become larger

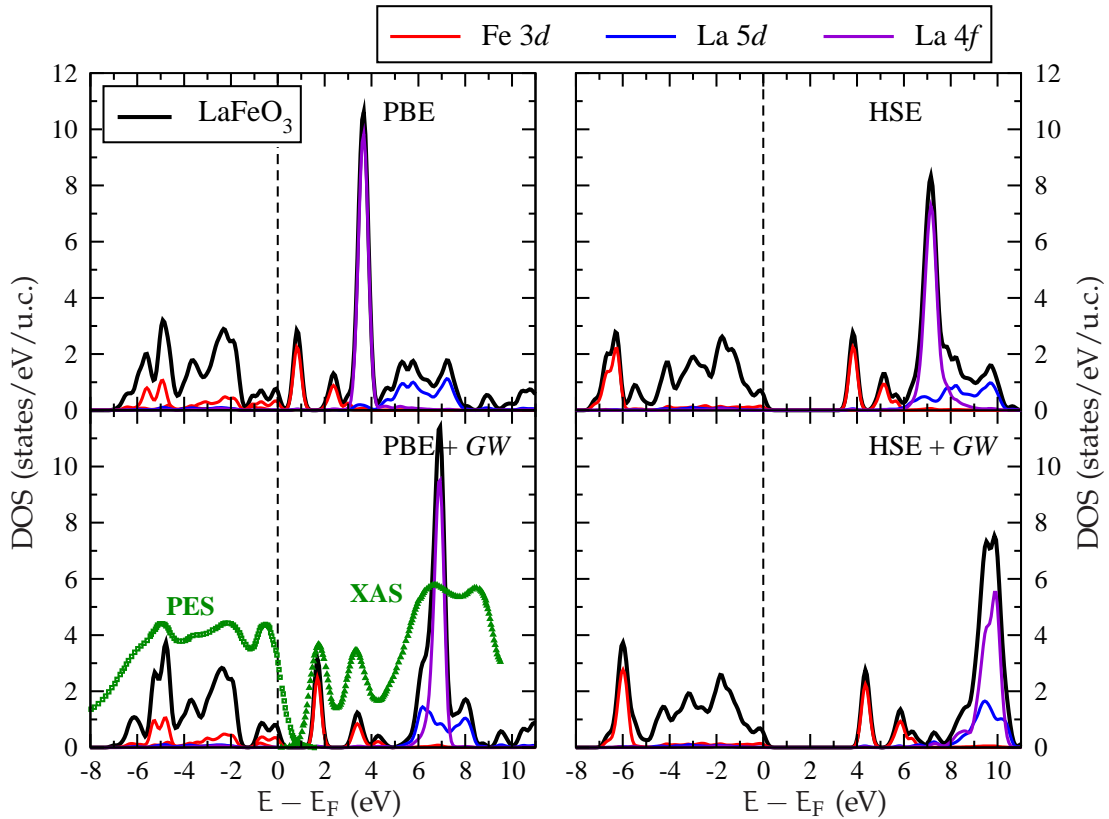


**Figure 6.6.:** Total DOS of  $\text{LaFeO}_3$  and pDOS of Fe 3d, La 4f and 5d states. Top row: Results from DFT calculations using the functionals PBE (*left*) and HSE (*right*). Bottom row: DFT spectra shifted by the energy corrections obtained from GW calculations as well as the results from PES and XAS [200]. Note, that La 4f-derived features cannot be probed by XAS. (See text for more detail.)

but the occupied parts of the PBE spectra are only slightly changed. There is a good overall agreement of the width and positions of spectral features between the calculated PBE+GW valence spectra and the experimental data. In contrast, spectral weight from the transition-metal d states located at the top of the valence spectrum obtained from PBE and PBE+GW calculations is shifted to the lower part of the valence band spectrum in HSE and HSE+GW calculations. The resulting spectra do not agree well with the data measured by UPS and PES especially in the case of  $\text{LaFeO}_3$ .

In the unoccupied part of the spectra of  $\text{LaMnO}_3$  and  $\text{LaFeO}_3$ , the most pronounced change induced by adding corrections from the GWA to the PBE results or by switching to the HSE functional is the upwards shift of the La 4f-derived peak as in  $\text{LaCrO}_3$ . However, it is not possible to obtain information about the actual position of such features from the spectra measured by XAS for the rea-

sons discussed earlier. However, XAS can probe the spectral features resulting from the partial density of states of the transition-metal d states and the La 5d states. For both materials, the positions as well as the shapes of these features are best reproduced by the PBE+GW results. In contrast, the pDOS from Mn 3d in LaMnO<sub>3</sub>, figure 6.5, splits into two separate peaks in HSE and HSE+GW calculations and the shape of the pDOS from the La 5d states changes w.r.t. the PBE+GW results. Similar changes can also be observed in the pDOS from the La 5d of LaFeO<sub>3</sub>. Hence, the pDOS resulting from the HSE and HSE+GW calculations of LaMnO<sub>3</sub> and LaFeO<sub>3</sub> for the unoccupied states do not reproduce the spectra obtained from XAS.

Several aspects should be considered in order to better understand, why HSE+GW calculations yield the best estimate for both the band gap and the photo-emission spectrum of LaCrO<sub>3</sub>, whereas band gaps and spectra of LaMnO<sub>3</sub> and LaFeO<sub>3</sub> are better described by PBE+GW. As pointed out in reference [17], the main contribution to the screening of the electrons occupying the states close to  $E_F$  in LaMnO<sub>3</sub> and LaFeO<sub>3</sub> originates from transitions between occupied and unoccupied transition-metal d states. Thus, the size of the RPA screening strongly depends on the relative positions of the occupied and unoccupied d states. For example, if the screened interaction  $W$  in a HSE+GW calculation for LaFeO<sub>3</sub> is replaced by the  $W$  obtained from a PBE+GW calculation, the QP band gap of 4.13 eV is reduced to 2.67 eV. In contrast, the screening due to transitions from the occupied part of the valence spectrum into empty La 4f states has little effect on the size of the QP band gaps. If these transitions are omitted in the calculation of the screened interaction  $W$ , the QP band gap of LaFeO<sub>3</sub> obtained from the corresponding PBE+GW calculation amounts to 1.58 eV as opposed to 1.54 eV if these transitions are taken into account. Even if the La 4f states might be located at much too low energies in the PBE spectra of LaFeO<sub>3</sub> and LaMnO<sub>3</sub> like in the case of LaCrO<sub>3</sub>, the influence on the size of the QP band gap obtained from PBE+GW calculations is negligible.

As the band gaps of both LaMnO<sub>3</sub> and LaFeO<sub>3</sub> are strongly overestimated in DFT calculations employing the HSE functional, the effect of screening as described by the RPA polarization function within the GWA is underestimated. This effect might be responsible for the further increase of the band gaps in HSE+GW calculations. In contrast, the band gaps obtained from PBE calculations are too small. This typical underestimation has been attributed to the missing exchange-correlation discontinuity in the generalized-gradient approximation [201, 202]. The too small band gaps in PBE lead to an overscreening in the PBE+GW calculation. This might be the reason why the QP band gaps obtained from PBE+GW calculations are smaller than the gaps measured by optical conductivity. Moreover, the transition-metal d states are filled up and become more localized throughout the series LaBO<sub>3</sub>. Therefore, additional cor-

relation effects not contained in the GWA might yield an important contribution to the screening of the electrons in LaMnO<sub>3</sub> and LaFeO<sub>3</sub>. Further calculations employing methods beyond the GWA are necessary to clarify this issue.

#### 6.4. Magnetic moments of $B = \text{Cr, Mn, and Fe}$ in LaBO<sub>3</sub>

The representation of the particle density in terms of the FLAPW basis functions, eq. (3.48), allows to separate the former into contributions from the IR and the MT spheres. The latter can be further split into the contributions from majority and minority spin states denoted by  $\uparrow$  and  $\downarrow$  of each atom  $a$  according to

$$n_a^\sigma = \int_{\text{MT}} d^3r \sum_n \frac{1}{V_{\text{BZ}}} \int_{\text{BZ}} d^3k |\varphi_{n\mathbf{k}}^{\alpha\sigma}(\mathbf{r})|^2, \quad \sigma = \uparrow, \downarrow. \quad (6.1)$$

This allows to approximate the magnetic moment at each atomic site  $\mathbf{R}_a$  by the magnetic moment inside the MT sphere of atom  $a$  given by

$$m_a = n_a^\uparrow - n_a^\downarrow. \quad (6.2)$$

The magnetic moments of Cr, Mn, and Fe in LaCrO<sub>3</sub>, LaMnO<sub>3</sub> and LaFeO<sub>3</sub> were calculated according to eqs. (6.1) and (6.2) using the KS and gKS eigenstates obtained from DFT calculations, where the functionals PBE and HSE were employed.

Material	Magnetic moment ( $\mu_B$ )		
	PBE	HSE	Exp.
LaCrO <sub>3</sub>	2.50	2.75	2.8±0.2
LaMnO <sub>3</sub>	3.50	3.75	3.9±0.2
LaFeO <sub>3</sub>	3.85	4.19	4.6±0.2

**Table 6.2.:** Magnetic moments of  $B = \text{Cr, Mn, and Fe}$  in LaBO<sub>3</sub> calculated with PBE and HSE compared to data from neutron-diffraction experiments [134].

Table 6.2 shows the calculated magnetic moments at the transition-metal sites of LaCrO<sub>3</sub>, LaMnO<sub>3</sub>, and LaFeO<sub>3</sub> as well as the magnetic moments determined by neutron-diffraction experiments [134]. The PBE results systematically underestimate the experimental data, whereas in calculations employing the HSE functional the magnetic moment of each compound becomes larger. The HSE result for LaCrO<sub>3</sub> agrees well with the neutron-diffraction measurement but the magnetic moments of Mn and Fe in LaMnO<sub>3</sub> and LaFeO<sub>3</sub> are still smaller

than the experimental data. In general, the calculations employing the HSE functionals improve the agreement with the experimental data for all three compounds.

However, the results from calculations listed in table 6.2 have to be dealt with carefully. It was already mentioned that the above definition (6.2) employed to calculate the magnetic moments only yields an estimate for the latter. The contributions to the particle density from parts of the wave function which are contained in the IR are not taken into account because the formalism does not allow to attribute them to one of the atoms. Thus, the MT radii of the transition metals must be chosen large enough such that the wave functions composing the d states are mostly contained inside the MT spheres. Otherwise, the resulting magnetic moments might strongly depend on the choice of the MT radius but the value of that observable should not depend on the artificial partitioning of space used in the FLAPW method.

In the first test calculations for the magnetic moments using the PBE functional, input data generated by the FLEUR code were used where the value of the MT radii of the transition metals Cr and Fe in  $\text{LaCrO}_3$  and  $\text{LaFeO}_3$  were smaller by 14% and 17%, respectively, as the values used for the calculations that yield the magnetic moments in table 6.2. The resulting magnetic moments obtained from this choice of the radii amount to  $2.37 \mu_B$  and  $3.69 \mu_B$  for Cr and Fe, respectively. This indicates that the size of the magnetic moments is by no means independent of the choice of the MT radii. However, the MT radii cannot be chosen large enough such that the d states are fully contained inside the MTs. Although the MT radii have been chosen as large as possible, a decomposition of the wave functions into MT and IR contributions according to (3.48) reveals that up to 12% of the wave function is contained outside the MT sphere in the case of  $\text{LaCrO}_3$ . In  $\text{LaMnO}_3$  and  $\text{LaFeO}_3$  even 20% and 24% of the wave function are not inside the MT spheres. Moreover, the contributions to the wave functions which are localized inside the MT spheres change if the HSE functional is used instead of the PBE functional. In  $\text{LaFeO}_3$ , it becomes larger whereas in the other two compounds it gets smaller. As this effect is not directly translated into an increase or a decrease of the magnetic moments listed in table 6.2 there must be other effects which also lead to changes in the magnetic moments. However, the origin of these effects cannot be derived solely from these numbers. In summary, the above analysis implies that the results exhibit an unphysical dependence on the choice of the MT radii of the transition metals. Therefore, the indication that HSE improves the PBE results should not be over-interpreted.

## 6.5. Discussion and Summary

In this chapter, first-principles GW calculations for the perovskite TMOs  $\text{LaCrO}_3$ ,  $\text{LaMnO}_3$ , and  $\text{LaFeO}_3$  have been presented. Results from DFT calculations were used as starting points for the GWA, where two different functionals have been

used to approximate the exchange-correlation potential: the PBE functional within the GGA and the hybrid functional HSE. Whereas the insulating and antiferromagnetic ground-state electronic structures of all three compounds are reproduced qualitatively in PBE calculations, quantitative agreement with experimental data such as band gaps, magnetic moments at the transition-metal sites and photo-emission spectra cannot be attained. The HSE results increase the size of the magnetic moments and lead to better agreement with neutron-diffraction data. On the other hand, the band gaps of all three compounds are overestimated in HSE calculations. Nevertheless, HSE results constitute a good starting point for GW calculations in the case of  $\text{LaCrO}_3$ . The QP gap and the DOS obtained from a HSE+GW calculation match the experimental data. On the other hand, it is illustrated for  $\text{LaMnO}_3$  and  $\text{LaFeO}_3$  that the band gaps obtained from HSE+GW are even larger than the HSE results in disagreement with experimental data. Furthermore, the resemblance of the DOS with photo-emission spectra is also poor. For these two compounds, PBE results yield a better starting point for a subsequent GW calculation. In  $\text{LaMnO}_3$ , good quantitative agreement with photo-emission spectra and the optical band gap is attained in PBE+GW calculations although the latter is slightly underestimated. In the PBE+GW calculation for  $\text{LaFeO}_3$ , the optical gap is more strongly underestimated. Nevertheless, the GWA yields a sizable improvement over the PBE result. Furthermore, the relative positions of spectral features and the shape of the spectrum obtained from PES is well reproduced by the DOS obtained from the PBE+GW calculation.

Further analysis of the photo-emission spectra and magnetic moments yield several indications as to why the HSE and HSE+GW calculations yield the best results for  $\text{LaCrO}_3$ , whereas in  $\text{LaMnO}_3$  and  $\text{LaFeO}_3$  the results from PBE and PBE+GW calculations lead to better agreement with data from optical and photo-emission spectroscopies. It is discussed that the data from PBE calculations may lead to an overestimation of the screening in a subsequent GW calculation, whereas for GW calculations employing HSE results as input data an underestimation is to be expected. This might lead to the too small and too large band gaps in PBE+GW and HSE+GW calculations, respectively. Furthermore, a dependence of the calculated magnetic moments on the choice of the MT radii of the transition metals Cr, Mn, and Fe in  $\text{LaCrO}_3$ ,  $\text{LaMnO}_3$ , and  $\text{LaFeO}_3$  is illustrated which is why these results should be dealt with carefully. Apart from these minor discrepancies, it has been demonstrated that the parameter-free scheme employing the GWA on top of results from DFT calculations improves the DFT results substantially and good agreement between the theoretical results and several quantities observed in experiment is achieved for all three compounds  $\text{LaCrO}_3$ ,  $\text{LaMnO}_3$ , and  $\text{LaFeO}_3$ .

## CHAPTER 7

# MODELING SPECTRA OF SUBSPACES – A CASE STUDY BEYOND THE GWA

The GW approximation (GWA) yields quasiparticle spectra in very good agreement with experiments for a large variety of material classes. However, two serious difficulties hamper further progress in *ab initio* calculations employing the GWA: first, the size of the unit cell of many materials is still too large for realistic GW calculations, despite the rapid growth of computational power in the last decades. Second, the GWA may not be sufficient to treat correlation effects especially in those materials with partially filled narrow bands. Such materials exhibit many intriguing properties, for example, they may become Mott-insulating at low temperatures. However, the description of the phase transition from a metallic to a Mott-insulating phase is beyond the scope of perturbation theory used in *ab initio* calculations employing the GWA. Thus, the growing interest in modeling the electronic structure of these kind of systems translates into the need to develop theories beyond the GWA.

The traditional approach to analyze spectra of materials with large unit cells and, in particular, to study strongly correlated materials is to introduce a model Hamiltonian, focusing on a small subspace of the full Hilbert space that is considered to yield the dominant contributions to the spectrum in the energy range to be investigated. One of the most successful model Hamiltonians describing strongly correlated materials, the Hubbard model, was already presented in chapters 4, section 4.4.2. It approximates the electron-electron interaction in a given subspace of the full Hilbert space by a local, statically screened effective Coulomb interaction known as the Hubbard  $U$ . In recent years, the Hubbard model has been frequently applied to real materials in the context of LDA + DMFT [32, 33] reproducing the experimental spectra of selected materials rather accurately [34].

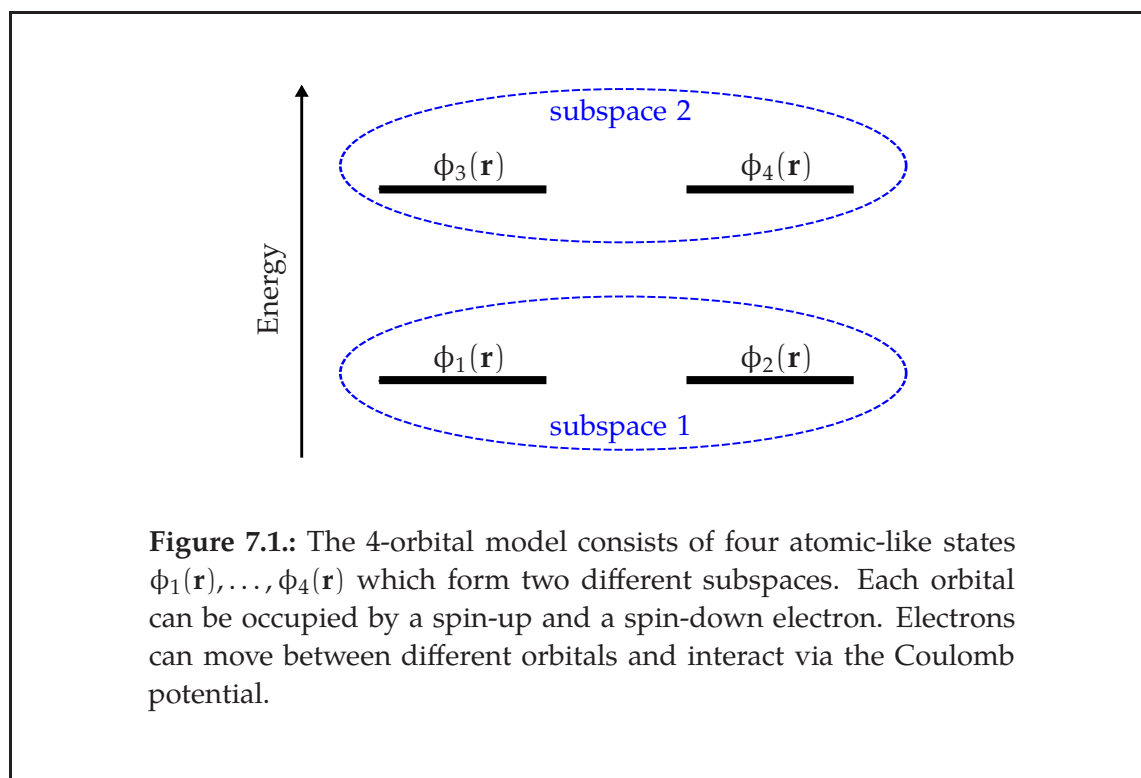
Furthermore, a combined GW + DMFT scheme has been proposed in reference [203]. It describes the states in a correlated subspace via a Hubbard-type model and the remaining parts of the Hilbert space within the GWA thus exploiting the advantages of both approaches. However, the Hubbard Hamiltonian cannot be strictly derived from the many-body Hamiltonian, eq. (2.64). Therefore, it is not entirely clear, which features of the excitation spectra of real materials can be reproduced and which are not accessible in a Hubbard-model based approach.

In this chapter, results from a case study for a simple toy model are presented to reveal possible limitations of a Hubbard-model based approach. The toy model may simulate partially filled valence states in the presence of fully occupied or completely empty states. The exact many-body spectrum of the toy model is compared to the results from an effective, Hubbard-type model, which is designed to reproduce the spectrum of the subspace composed of the partially occupied states. In the first part of the chapter, the toy model is introduced and the effective, Hubbard-type model will be constructed. Then, results of calculations for two different setups of the toy model will be presented. Finally, possible indications for the applicability of Hubbard-model based approaches in *ab initio* calculation for real materials are discussed. The theoretical considerations presented in the first part of the chapter were motivated by the work of F. Aryasetiawan and coworkers and, in particular, by the idea of the downfolded self-energy of many-electron systems introduced in reference [204].

## 7.1. Theory

In this part of the chapter the setup of the model is introduced, which is the basis for all calculation presented later on. The model is drawn schematically in figure 7.1 and will be referred to as "4-orbital model" for apparent reasons. It consists of four orbitals  $\phi_1(\mathbf{r}), \dots, \phi_4(\mathbf{r})$ , which are considered to be atomic-like states. Each orbital can be occupied by one spin-up electron and one spin-down electron. Electrons can move between the different orbitals and interact via the Coulomb interaction. As indicated in figure 7.1, the states  $\phi_1(\mathbf{r})$  and  $\phi_2(\mathbf{r})$  as well as  $\phi_3(\mathbf{r})$  and  $\phi_4(\mathbf{r})$  are degenerate. Each pair of degenerate states forms a subspace.

In the first part of this section, it is described how the exact many-body spectrum of the 4-orbital model for a fixed number of N electrons occupying the orbitals can be obtained using the occupation number formalism. In the second part of the section, an effective, Hubbard-type model for one of the two subspaces labeled d space will be constructed. The remaining subspace is then called r space. The effective model only treats those two states explicitly, that form the subspace d. Interactions between electrons in d space with those in



subspace  $r$  must be included implicitly in the construction of the model. The spectrum of the  $d$  space obtained from this effective model will then be compared to the exact solution in later parts of this chapter.

For the sake of clarity and brevity the theoretical concepts introduced in this section are all discussed within the context of the 4-orbital model. However, it should be pointed out that these concepts are completely general and could thus be equally applied to more sophisticated models and, in principle, even within the context of first-principles calculations.

### 7.1.1. The 4-orbital model

#### Hamiltonian

To derive a Hamiltonian describing the 4-orbital model it is convenient to start from the Hamiltonian of the  $N$ -electron Schrödinger equation in second quan-

tized form given by

$$\begin{aligned}\hat{H} &= \sum_{\sigma} \int \hat{\psi}_{\sigma}^{\dagger}(\mathbf{r}) H^{\text{H}}(\mathbf{r}) \hat{\psi}_{\sigma}(\mathbf{r}) d^3r \\ &+ \frac{1}{2} \sum_{\sigma\sigma'} \iint \hat{\psi}_{\sigma}^{\dagger}(\mathbf{r}) \hat{\psi}_{\sigma'}^{\dagger}(\mathbf{r}') v(\mathbf{r}, \mathbf{r}') \hat{\psi}_{\sigma'}(\mathbf{r}') \hat{\psi}_{\sigma}(\mathbf{r}) d^3r d^3r' \\ &- \sum_{\sigma} \int \hat{\psi}_{\sigma}(\mathbf{r}) H^{\text{d.c.}}(\mathbf{r}) \hat{\psi}_{\sigma}(\mathbf{r}) d^3r.\end{aligned}\quad (7.1)$$

Here, the Hamiltonian is written in a form which is slightly different form that in eq. (2.64) to emphasize the resemblance with the Hamiltonian of the effective, Hubbard-type model, eq. (7.26), derived later-on. The first term of (7.1) contains the Hartree Hamiltonian  $H^{\text{H}}(\mathbf{r})$ , which is the sum of the one-particle Hamiltonian  $h(\mathbf{r}) = -\frac{1}{2}\nabla_{\mathbf{r}}^2 + v^{\text{ext}}(\mathbf{r})$  and the Hartree potential  $V^{\text{H}}(\mathbf{r})$ . The latter is given by

$$V^{\text{H}}(\mathbf{r}) = \int v(\mathbf{r}, \mathbf{r}') \rho(\mathbf{r}') d^3r', \quad \rho(\mathbf{r}) = -i \sum_{\sigma} G_{\sigma}(\mathbf{r}, t; \mathbf{r}, t^+), \quad (7.2)$$

where the exact one-particle density  $\rho(\mathbf{r})$  is obtained from the many-body Green function  $G_{\sigma}(\mathbf{r}, t; \mathbf{r}, t^+)$  defined in eq. (7.21). The Hartree potential  $V^{\text{H}}(\mathbf{r})$  is also implicitly contained in the second term describing the interaction between two electrons via the Coulomb potential  $v(\mathbf{r}, \mathbf{r}')$ . Hence, a third term has to be introduced in order to subtract the contributions that are counted twice. This double-counting correction for the 4-orbital model is by construction identical to the Hartree potential itself

$$H^{\text{d.c.}}(\mathbf{r}) = V^{\text{H}}(\mathbf{r}). \quad (7.3)$$

The four orbitals of the model form a complete basis set for the electronic states. Hence, creation and annihilation operators  $\hat{c}_{\alpha\sigma}^{\dagger}$  and  $\hat{c}_{\alpha\sigma}$  can be defined, which create or annihilate an electron with spin  $\sigma$  in one of the orbitals labeled by  $\alpha$ . Then, the field operators in formula (7.1) are replaced by linear combinations of the new operators and the orbitals

$$\hat{\psi}_{\sigma}(\mathbf{r}) = \sum_{\alpha=1}^4 \phi_{\alpha}(\mathbf{r}) \hat{c}_{\alpha\sigma}, \quad \alpha \in \{1, 2, 3, 4\}. \quad (7.4)$$

Consequently, the Hamiltonian of the 4-orbital model takes on the following form

$$\hat{H} = \sum_{\alpha\beta} \sum_{\sigma} [H_{\alpha\beta}^{\text{H}} - H_{\alpha\beta}^{\text{d.c.}}] \hat{c}_{\alpha\sigma}^{\dagger} \hat{c}_{\beta\sigma} + \frac{1}{2} \sum_{\alpha\beta\mu\nu} \sum_{\sigma\sigma'} u_{\alpha\beta\mu\nu} \hat{c}_{\alpha\sigma}^{\dagger} \hat{c}_{\beta\sigma'}^{\dagger} \hat{c}_{\mu\sigma'} \hat{c}_{\nu\sigma} \quad (7.5)$$

$$= - \sum_{\alpha\beta} \sum_{\sigma} t_{\alpha\beta} \hat{c}_{\alpha\sigma}^{\dagger} \hat{c}_{\beta\sigma} + \frac{1}{2} \sum_{\alpha\beta\mu\nu} \sum_{\sigma\sigma'} u_{\alpha\beta\mu\nu} \hat{c}_{\alpha\sigma}^{\dagger} \hat{c}_{\beta\sigma'}^{\dagger} \hat{c}_{\mu\sigma'} \hat{c}_{\nu\sigma}. \quad (7.6)$$

The matrices  $\mathbf{H}^H$  and  $\mathbf{H}^{d.c.}$  are defined as

$$H_{\alpha\beta}^H \equiv \int \phi_{\alpha}^*(\mathbf{r}) H^H(\mathbf{r}) \phi_{\beta}(\mathbf{r}) d^3r, \quad (7.7)$$

$$H_{\alpha\beta}^{d.c.} \equiv \int \phi_{\alpha}^*(\mathbf{r}) H^{d.c.}(\mathbf{r}) \phi_{\beta}(\mathbf{r}) d^3r. \quad (7.8)$$

Hence, the matrix elements of the hopping matrix  $\mathbf{t}$  are given by

$$-t_{\alpha\beta} \equiv \int \phi_{\alpha}^*(\mathbf{r}) h(\mathbf{r}) \phi_{\beta}(\mathbf{r}) d^3r. \quad (7.9)$$

Finally,  $\mathbf{U}$  is the matrix calculated from the Coulomb interaction according to

$$U_{\alpha\beta\mu\nu} \equiv \iint \phi_{\alpha}^*(\mathbf{r}) \phi_{\beta}^*(\mathbf{r}') v(\mathbf{r}, \mathbf{r}') \phi_{\mu}(\mathbf{r}') \phi_{\nu}(\mathbf{r}) d^3r d^3r'. \quad (7.10)$$

All calculations for the 4-orbital model presented later-on employ the Hamiltonian given by eq. (7.6). In this notation, the four orbitals are fully determined by the diagonal elements  $-t_{\alpha\alpha}$  of the hopping matrix, which can be interpreted as atomic-like energy levels. The movement of an electron from an orbital  $\phi_{\alpha}(\mathbf{r})$  into another orbital  $\phi_{\beta}(\mathbf{r})$  translates into the hopping from the energy level  $\alpha$  to  $\beta$  in the above notation. The probability of such a process to take place depends on the value  $-t_{\alpha\beta}$  of the corresponding hopping matrix element. In all calculations, the matrix elements of both  $\mathbf{t}$  and  $\mathbf{U}$  were treated as parameters and were not obtained by evaluating eqs. (7.9) and (7.10) explicitly. Hence, the wave functions  $\phi_{\alpha}(\mathbf{r})$  did not enter explicitly in the calculations and were therefore never determined. In section 7.2, it will be discussed that a certain choice of the matrix elements together with a fixed number of electrons in the system allows to model different physical problems. Therefore, the actual choice of the matrix elements is presented together with the results from the corresponding calculations in section 7.2.

### Exact solution

To obtain the eigenvalue spectrum of the 4-orbital model if  $N \leq 8$  electrons occupy the four orbitals, the following Schrödinger equation is to be solved

$$\hat{H} |\Psi_J^N\rangle = E_J^N |\Psi_J^N\rangle \quad (7.11)$$

where  $|\Psi_J^N\rangle$  are the eigenstates of the  $N$ -electron system labeled by  $J$  and the  $E_J^N$  are the corresponding eigenvalues. In order to determine  $|\Psi_J^N\rangle$  and  $E_J^N$  eq. (7.11) is transformed into a matrix equation. The construction of the Hamilton matrix with elements  $H_{ab}$  will be described in the following.

First, all possible many-body wave functions for the given number of electrons are constructed. Here, the occupation number formalism is used, where each many-body wave function is represented by a vector of the following form

$$|N, a\rangle = |n_1^\uparrow, n_2^\uparrow, n_3^\uparrow, n_4^\uparrow; n_1^\downarrow, n_2^\downarrow, n_3^\downarrow, n_4^\downarrow\rangle, \quad (7.12)$$

and  $a$  labels the different many-body states. Each entry of the vector represents one energy level  $\alpha$  corresponding to one of the four atomic orbitals. If an electron with spin up ( $\uparrow$ ) occupies orbital  $\alpha$ ,  $n_\alpha^\uparrow$  is set to one. Otherwise, it is zero. Likewise,  $n_\alpha^\downarrow$  is set to one if a spin-down electron ( $\downarrow$ ) can be found in orbital  $\alpha$  and otherwise it is zero. For example, if the system contains three up and zero down electrons there exist four different many-body wave functions, which are represented by

$$|1110;0000\rangle, |1101;0000\rangle, |1011;0000\rangle, |0111;0000\rangle. \quad (7.13)$$

In the next step, it is defined how the creation and annihilation operators  $\hat{c}_{\alpha\sigma}^\dagger$  and  $\hat{c}_{\alpha\sigma}$  act on a many-body state given by (7.12)

$$\begin{aligned} \hat{c}_{\alpha\uparrow}^\dagger |N, a\rangle &= (-1)^{\Sigma_\alpha^\uparrow} (1 - n_\alpha^\uparrow) |N + 1, b\rangle, \\ \hat{c}_{\alpha\uparrow} |N, a\rangle &= (-1)^{\Sigma_\alpha^\uparrow} n_\alpha^\uparrow |N - 1, b\rangle, \end{aligned} \quad (7.14)$$

and

$$\begin{aligned} \hat{c}_{\alpha\downarrow}^\dagger |N, a\rangle &= (-1)^{\Sigma_\alpha^\downarrow} (1 - n_\alpha^\downarrow) |N + 1, b\rangle \\ \hat{c}_{\alpha\downarrow} |N, a\rangle &= (-1)^{\Sigma_\alpha^\downarrow} n_\alpha^\downarrow |N - 1, b\rangle, \end{aligned} \quad (7.15)$$

with

$$\Sigma_\alpha^\uparrow = n_1^\uparrow + n_2^\uparrow + \dots + n_{\alpha-1}^\uparrow, \quad \Sigma_\alpha^\downarrow = N_\uparrow + n_1^\downarrow + n_2^\downarrow + \dots + n_{\alpha-1}^\downarrow. \quad (7.16)$$

Here,  $N_\uparrow$  represents the total number of electrons with spin up. The factors  $n_\alpha^\uparrow, n_\alpha^\downarrow$  and  $(1 - n_\alpha^\uparrow), (1 - n_\alpha^\downarrow)$  are necessary to enforce the Pauli exclusion principle, whereas the factors  $(-1)^{\Sigma_\alpha^\uparrow}, (-1)^{\Sigma_\alpha^\downarrow}$  account for the Fermionic nature of the electrons. The above definitions in (7.14) and (7.15) allow to calculate matrix elements  $H_{ab}$  of the Hamiltonian (7.6) with respect to many-body states constructed according to the definition in (7.12). Thus, eq. (7.11) can be transformed into a matrix equation

$$H_{ab} C_{bJ}^N = E_J^N C_{bJ}^N. \quad (7.17)$$

Diagonalizing the matrix  $\mathbf{H}$  yields the eigenvalues  $E_J^N$  and the coefficients  $C_{aJ}^N$  that determine the many-body eigenstate  $|\Psi_J^N\rangle$  according to

$$|\Psi_J^N\rangle = \sum_a C_{aJ}^N |N, a\rangle. \quad (7.18)$$

### Formal definition of the d and r space

For all further considerations, it is necessary to define the subspaces d and r. This can be done with the help of the wave functions  $\phi_\alpha(\mathbf{r})$  representing the four orbitals of the model. The field operators can be split into a d field and an r field

$$\hat{\psi}_\sigma(\mathbf{r}) = \hat{\psi}_\sigma^d(\mathbf{r}) + \hat{\psi}_\sigma^r(\mathbf{r}) = \sum_{i \in d} \phi_i(\mathbf{r}) \hat{c}_{i\sigma}^d + \sum_{j \in r} \phi_j(\mathbf{r}) \hat{c}_{j\sigma}^r \quad (7.19)$$

where

$$d = \{1, 2\}, r = \{3, 4\} \quad \text{or} \quad d = \{3, 4\}, r = \{1, 2\}. \quad (7.20)$$

The operator  $\hat{\psi}_\sigma^\dagger(\mathbf{r})$  can be separated in the same way. Definition (7.20) indicates that the d space is either formed by the lower two orbitals  $\phi_1(\mathbf{r})$ ,  $\phi_2(\mathbf{r})$  and  $\phi_3(\mathbf{r})$ ,  $\phi_4(\mathbf{r})$  from the r space or vice versa. The operators  $\hat{c}_{i\sigma}^d$ ,  $\hat{c}_{j\sigma}^r$  are identical to the operators  $\hat{c}_{\alpha\sigma}$  defined previously but they act only on the states of the corresponding subspace.

### Green functions

The spectral representation of the many-body one-particle Green function has been given in eq. (2.60) and is restated below in a slightly different form

$$\begin{aligned} G_\sigma(\mathbf{r}, \mathbf{r}'; \omega) &= \sum_J \frac{\langle \Psi_0^N | \hat{\psi}_\sigma(\mathbf{r}) | \Psi_J^{N+1} \rangle \langle \Psi_J^{N+1} | \hat{\psi}_\sigma^\dagger(\mathbf{r}') | \Psi_0^N \rangle}{\omega - (E_J^{N+1} - E_0^N) + i\eta} \\ &+ \sum_{J'} \frac{\langle \Psi_0^N | \hat{\psi}_\sigma^\dagger(\mathbf{r}') | \Psi_{J'}^{N-1} \rangle \langle \Psi_{J'}^{N-1} | \hat{\psi}_\sigma(\mathbf{r}) | \Psi_0^N \rangle}{\omega + (E_{J'}^{N-1} - E_0^N) - i\eta}. \end{aligned} \quad (7.21)$$

Here, the many-body eigenstates  $|\Psi_J^N\rangle$ ,  $|\Psi_J^{N\pm 1}\rangle$  and eigenvalues  $E_J^N$ ,  $E_J^{N\pm 1}$  are obtained from the solution of the Schrödinger equation (7.11) with N and (N±1) electrons occupying the four orbitals.

By inserting the expansion for the field operators, eq. (7.4), into eq. (7.21) for the Green function a  $(4 \times 4)$  matrix  $\mathbf{G}$  is obtained with matrix elements defined by

$$G_\sigma(\mathbf{r}, \mathbf{r}'; \omega) = \sum_{\alpha\beta} \phi_\alpha^*(\mathbf{r}) G_{\alpha\beta, \sigma}(\omega) \phi_\beta(\mathbf{r}'). \quad (7.22)$$

Furthermore, it follows from the decomposition of the field operators into the d and r space, eq. (7.19), that the matrix of the Green function can be decomposed into four blocks of  $(2 \times 2)$  matrices

$$\mathbf{G}_\sigma(\omega) = \left( \begin{array}{c|c} \mathbf{G}_\sigma^r(\omega) & \mathbf{G}_\sigma^{rd}(\omega) \\ \hline \mathbf{G}_\sigma^{dr}(\omega) & \mathbf{G}_\sigma^d(\omega) \end{array} \right), \quad (7.23)$$

where the two matrices  $\mathbf{G}_\sigma^d(\omega)$  and  $\mathbf{G}_\sigma^r(\omega)$  represent the projection of the Green function onto the states forming the d and r space, respectively. Consequently, the partial density of states (pDOS) of the d and r space is given by

$$\text{pDOS}(\omega) = \sum_{i \in P} \sum_{\sigma} \text{Im}(G_{\sigma}^P(\omega))_{ii}, \quad P = d, r. \quad (7.24)$$

Equation (7.24) yields the exact many-body spectra of the d and r space consisting of  $\delta$ -function like peaks. For numerical calculations, the infinitesimal positive number  $\eta$  in the denominator of the Green function, eq. (7.21), is set to 0.05 transforming the  $\delta$ -like excitations into Lorentzians of finite height and width.

### 7.1.2. Hubbard Hamiltonian for a subspace

In this section, an effective, Hubbard-type model for the d space is constructed. This requires to determine the Hartree potential, eq. (7.2), which, in turn, requires the knowledge of the exact one-particle density  $\rho(\mathbf{r})$ . In addition, the one-particle density  $\rho^d(\mathbf{r})$  in d space enters in the construction of the effective model. According to the definition of the density in terms of the Green function, eq. (7.2),  $\rho(\mathbf{r})$  can be calculated as

$$\rho(\mathbf{r}) = \sum_{\sigma} \langle \Psi_0^N | \hat{\rho}(\mathbf{r}) | \Psi_0^N \rangle, \quad \hat{\rho}(\mathbf{r}) \equiv \sum_{\sigma} \hat{\psi}_{\sigma}^{\dagger}(\mathbf{r}) \hat{\psi}_{\sigma}(\mathbf{r}) \quad (7.25)$$

and  $\rho^d(\mathbf{r})$  can be obtained by substituting  $\hat{\psi}_{\sigma}^{d\dagger}(\mathbf{r})$  and  $\hat{\psi}_{\sigma}^d(\mathbf{r})$  in the above equation thus defining an operator  $\hat{\rho}^d(\mathbf{r})$ . Replacing the field operators in the definition of the density operators using (7.4) and (7.19) yields matrices of the densities with elements  $\rho_{\alpha\beta}$  and  $\rho_{\alpha\beta}^d$ , which can be calculated using the solution of the Schrödinger equation (7.11).

#### Hamiltonian and Schrödinger equation

Within the basis representation of the atomic-like orbitals  $\phi_{\alpha}(\mathbf{r})$  a Hamiltonian of an effective, Hubbard-type model for the d space is given by

$$\hat{H}^{\text{Hub}} = \sum_{ij \in d} \sum_{\sigma} [\tilde{H}_{ij}^H - \tilde{H}_{ij}^{d.c.}] \hat{c}_{i\sigma}^{d\dagger} \hat{c}_{j\sigma}^d + \frac{1}{2} \sum_{ijkl \in d} \sum_{\sigma\sigma'} W_{ijkl}^r \hat{c}_{i\sigma}^{d\dagger} \hat{c}_{j\sigma'}^{d\dagger} \hat{c}_{k\sigma'}^d \hat{c}_{l\sigma}^d. \quad (7.26)$$

This Hamiltonian is formally identical to that of the 4-orbital model, eq. (7.6). However, the summations in both terms comprise only those two states forming the d space and the matrices  $\tilde{\mathbf{H}}^H$ ,  $\tilde{\mathbf{H}}^{d.c.}$  and  $\mathbf{W}^r$  have yet to be determined. In the remaining parts of this section it is described how these matrices can be

calculated to yield the most accurate, effective model for the d space of the 4-orbital model.

If the matrices in the three terms of the above Hamiltonian have been calculated, the same methods used in previous parts of this section can be employed to obtain the spectrum of the d space. In particular, many-body states have to be constructed from the two orbitals forming the d space

$$|N, \tilde{\alpha}\rangle = |n_1^\uparrow, n_2^\uparrow; n_1^\downarrow, n_2^\downarrow\rangle, \quad n_i^\sigma \in \{0, 1\}, \quad i = 1, 2, \quad \sigma = \uparrow, \downarrow. \quad (7.27)$$

Then, matrix elements  $H_{\tilde{\alpha}\tilde{\beta}}^{\text{Hub}}$  of the Hamiltonian (7.26) with respect to these states are calculated. Diagonalizing the resulting matrix yields the eigenvalues  $\tilde{E}_J^N$  and the coefficients  $C_{\tilde{\alpha}J}^N$  of the Schrödinger equation

$$H_{\tilde{\alpha}\tilde{\beta}}^{\text{Hub}} C_{\tilde{\beta}J}^N = \tilde{E}_J^N C_{\tilde{\alpha}J}^N. \quad (7.28)$$

The corresponding eigenstates are given by

$$|\tilde{\Psi}_J^N\rangle = \sum_{\tilde{\alpha}} C_{\tilde{\alpha}J}^N |N, \tilde{\alpha}\rangle. \quad (7.29)$$

### Screened interaction $W^r$

The interaction between a quasiparticle and a test charge is described by the screened interaction  $W(\mathbf{r}, \mathbf{r}'; \omega)$ , which is defined by the Dyson-type equation (A.19). From the expression for  $W(\mathbf{r}, \mathbf{r}'; \omega)$  obtained within the random-phase approximation (RPA), where the exact expression for the polarization function  $P(\mathbf{r}, \mathbf{r}'; \omega)$  entering into eq. (A.19) is replaced by eq. (2.78), it can be seen directly that the bare Coulomb interaction in eq. (A.19) is screened due to transitions between all states of the Hilbert space, since eq. (2.78) comprises a summation over all these states.

In [84], the effective interaction  $W^r(\mathbf{r}, \mathbf{r}'; \omega)$  between electrons in a subspace d in a Hubbard model is introduced as

$$W^r(\mathbf{r}, \mathbf{r}'; \omega) = v(\mathbf{r}, \mathbf{r}') + \iint v(\mathbf{r}, \mathbf{r}'') P^r(\mathbf{r}'', \mathbf{r}'''; \omega) W^r(\mathbf{r}''', \mathbf{r}'; \omega) d^3r'' d^3r'''. \quad (7.30)$$

The above equation is formally identical to eq. (A.19) for the fully screened interaction except that the full polarization function is replaced by  $P^r(\mathbf{r}, \mathbf{r}'; \omega)$ . The latter is constructed in such a way, that it does not include the polarization from d-d transitions, since the corresponding screening channels are treated explicitly within the Hubbard model due to the inclusion of the two-particle term. However,  $P^r(\mathbf{r}, \mathbf{r}'; \omega)$  accounts for all screening channels resulting from transitions r-r in r space as well as r-d and d-r transitions between both subspaces d and r. Hence,  $P^r(\mathbf{r}, \mathbf{r}'; \omega)$  is defined as

$$P^r(\mathbf{r}, \mathbf{r}'; \omega) = P(\mathbf{r}, \mathbf{r}'; \omega) - P^d(\mathbf{r}, \mathbf{r}'; \omega), \quad (7.31)$$

where  $P(\mathbf{r}, \mathbf{r}'; \omega)$  is the full polarization and  $P^d(\mathbf{r}, \mathbf{r}'; \omega)$  the polarization in  $d$  space, which can both be obtained from

$$R^{(d)}(\mathbf{r}, \mathbf{r}'; \omega) = P^{(d)}(\mathbf{r}, \mathbf{r}'; \omega) + \iint P^{(d)}(\mathbf{r}, \mathbf{r}''; \omega) v^{(d)}(\mathbf{r}'', \mathbf{r}''') R^{(d)}(\mathbf{r}''', \mathbf{r}'; \omega) d^3 r'' d^3 r''' . \quad (7.32)$$

For the 4-orbital model, the above equation for  $P(\mathbf{r}, \mathbf{r}'; \omega)$  and  $P^d(\mathbf{r}, \mathbf{r}'; \omega)$  can be solved exactly since the exact response functions  $R(\mathbf{r}, \mathbf{r}'; \omega)$  and  $R^d(\mathbf{r}, \mathbf{r}'; \omega)$  can be calculated according to

$$R^{(d)}(\mathbf{r}, \mathbf{r}'; \omega) = \sum_J \frac{\langle \Psi_0^N | \hat{\rho}^{(d)}(\mathbf{r}) | \Psi_J^N \rangle \langle \Psi_J^N | \hat{\rho}^{(d)}(\mathbf{r}') | \Psi_0^N \rangle}{\omega - (E_J^N - E_0^N) + i\eta} - \sum_{J'} \frac{\langle \Psi_0^N | \hat{\rho}^{(d)}(\mathbf{r}') | \Psi_{J'}^N \rangle \langle \Psi_{J'}^N | \hat{\rho}^{(d)}(\mathbf{r}) | \Psi_0^N \rangle}{\omega + (E_{J'}^N - E_0^N) - i\eta} , \quad (7.33)$$

where  $|\Psi_J^N\rangle$  and  $E_J^N$  are the eigenvalues and eigenstates obtained from the solution of eq. (7.11) and the density operators  $\hat{\rho}(\mathbf{r})$  and  $\hat{\rho}^d(\mathbf{r})$  are given by (7.25).

Before applying the above formalism to the 4-orbital model, it should be mentioned that the ansatz to calculate  $W^r(\mathbf{r}, \mathbf{r}'; \omega)$  using eq. (7.30) is frequently referred to as constraint RPA (cRPA). However, this name is a little misleading, since eq. (7.30) for  $W^r(\mathbf{r}, \mathbf{r}'; \omega)$  is formally exact. In reference [84],  $P^r(\mathbf{r}, \mathbf{r}'; \omega)$  is calculated within RPA to obtain  $W^r(\mathbf{r}, \mathbf{r}'; \omega)$ , since reference [84] focuses on calculations for real materials, for which  $P^r(\mathbf{r}, \mathbf{r}'; \omega)$  cannot be determined exactly. For the 4-orbital model, eq. (7.30) for  $W^r(\mathbf{r}, \mathbf{r}'; \omega)$  is solved without any additional approximations, since eq. (7.33) yields the exact expressions for  $R(\mathbf{r}, \mathbf{r}'; \omega)$  and  $R^d(\mathbf{r}, \mathbf{r}'; \omega)$ .

To calculate  $R(\mathbf{r}, \mathbf{r}'; \omega)$  and  $R^d(\mathbf{r}, \mathbf{r}'; \omega)$  for the the 4-orbital model, the field operators in the definition of the density operators in eq. (7.33) are again replaced by the expansion (7.4) transforming the response functions into matrices defined by

$$R(\mathbf{r}, \mathbf{r}'; \omega) = \sum_{\alpha\beta\mu\nu} \phi_\alpha^*(\mathbf{r}) \phi_\beta(\mathbf{r}) R_{\alpha\beta\mu\nu}(\omega) \phi_\mu^*(\mathbf{r}') \phi_\nu(\mathbf{r}') \quad (7.34)$$

$$R^d(\mathbf{r}, \mathbf{r}'; \omega) = \sum_{ijkl \in d} \phi_i^*(\mathbf{r}) \phi_j(\mathbf{r}) R_{ijkl}^d(\omega) \phi_k^*(\mathbf{r}') \phi_l(\mathbf{r}') . \quad (7.35)$$

For further calculations, a multiindex  $I = (\alpha\beta)$  is introduced to rewrite the matrices  $\mathbf{R}$  and  $\mathbf{R}^d$ . Formally, this step corresponds to the introduction of a product basis

$$R_{IJ}^{(d)}(\omega) = \iint M_I^{(d)}(\mathbf{r}) R^{(d)}(\mathbf{r}, \mathbf{r}'; \omega) M_J^{(d)}(\mathbf{r}') d^3 r d^3 r' , \quad M_I^{(d)}(\mathbf{r}) = \phi_\alpha^*(\mathbf{r}) \phi_\beta(\mathbf{r}) . \quad (7.36)$$

Now, matrices of the polarization functions  $P_{IJ}(\omega)$  and  $P_{IJ}^d(\omega)$  can be obtained from eq. (7.31) using regular matrix operations. Likewise, a matrix of the screened interaction  $W_{IJ}^r(\omega)$  can be calculated from eq. (7.30) and a back transformation yields  $W_{ijkl}^r(\omega)$ .

Since the Coulomb interaction is screened due to dynamical many-body effects incorporated into the polarization functions the matrix  $W_{ijkl}^r(\omega)$  of the screened interaction is frequency dependent. While this frequency dependence is naturally taken into account in the Green function formalism, the Hamiltonian of the Schrödinger equation (7.28) must not be frequency dependent. Here, the matrix elements  $W_{ijkl}^r$  in (7.26) are obtained from the screened interaction  $W_{ijkl}^r(\omega)$  at  $\omega = 0$ . This neglect of the frequency dependence of  $W_{ijkl}^r(\omega)$  is an approximation that will only yield accurate results if the frequency dependence is weak. In particular, it will be demonstrated in section 7.2 that the approximation to the spectrum of the d space resulting from the Hubbard-type model becomes increasingly inaccurate if  $W_{ijkl}^r(\omega) \neq W_{ijkl}^r(0)$  for frequencies close to zero. Nevertheless, this approximation is inevitable in the formalism used here and could only be avoided by using other theoretical concepts like Green functions or the path integral formalism to calculate the spectral function of the d space.

### Effective Hartree Hamiltonian $\tilde{\mathbf{H}}^H$

If electrons occupy orbitals in r space, the resulting charge density yields a contribution to the Hartree potential, which is felt by the electrons in d space as well. This effect is not accounted for by the two-particle term of the Hamiltonian (7.26), since this term only describes interactions between electrons in d space. However, the Hartree potential can be included in the single-particle term of the Hamiltonian (7.26) as demonstrated already for the Hamiltonian of the full Hilbert space of the 4-orbital model, eq. (7.6). Hence, the effective Hartree Hamiltonian  $\tilde{\mathbf{H}}^H$  of the Hubbard-type model is to be constructed in such a way that it reproduces the eigenvalue spectrum of the Hartree Hamiltonian  $\mathbf{H}^H(\mathbf{r})$  of the 4-orbital model in d space. Therefore, the eigenvalue spectrum of  $\mathbf{H}^H(\mathbf{r})$  has first to be determined.

Within the basis representation of the atomic-like orbitals  $\phi_\alpha(\mathbf{r})$ ,  $\mathbf{H}^H(\mathbf{r})$  becomes a  $(4 \times 4)$  matrix, whose matrix elements are given by

$$H_{\alpha\beta}^H = -t_{\alpha\beta} + V_{\alpha\beta}^H, \quad (7.37)$$

where  $t_{\alpha\beta}$  are the matrix elements of the hopping matrix defined in eq. (7.9) and  $V_{\alpha\beta}^H$  are the matrix elements of the Hartree potential, eq. (7.2). Diagonalizing the matrix  $\mathbf{H}^H$  yields the eigenvalues  $\epsilon_\alpha$  and eigenvectors  $\mathbf{C}_\alpha = (c_{1\alpha}, c_{2\alpha}, c_{3\alpha}, c_{4\alpha})^T$  of the corresponding eigenvalue problem

$$H_{\alpha\beta}^H \mathbf{C}_\beta = \epsilon_\beta \mathbf{C}_\beta. \quad (7.38)$$

Although it is defined clearly at the beginning of each calculations, which of the four orbitals constitute the d space, it has yet to be determined which of the four eigenvalues of the Hartree Hamiltonian correspond to the eigenvalue spectrum in d space. Therefore, the contribution of each of the four orbitals to a Hartree eigenvector  $C_\alpha$  is weighted by  $w_{j\alpha} = |c_{j\alpha}|^2$ . The two eigenvalues belonging to the eigenstates containing the largest contribution from the two states spanning the d space are taken as the Hartree eigenvalue spectrum of the d space. They will be referred to as  $\epsilon_1^d$  and  $\epsilon_2^d$  in the remaining part of this section.

The search for an effective Hartree Hamiltonian  $\tilde{\mathbf{H}}^H$  can now be reformulated as the search for a matrix  $\tilde{\mathbf{T}}$  transforming the effective Hamiltonian into a diagonal matrix  $\mathbf{D}^d$  with elements  $\epsilon_1^d$  and  $\epsilon_2^d$  according to the following definition

$$\mathbf{D}^d = \tilde{\mathbf{T}} \tilde{\mathbf{H}}^H (\tilde{\mathbf{T}})^{-1}, \quad \mathbf{D}^d = \begin{pmatrix} \epsilon_1^d & 0 \\ 0 & \epsilon_2^d \end{pmatrix}. \quad (7.39)$$

To determine  $\tilde{\mathbf{T}}$ , the Hartree Hamiltonian  $\mathbf{H}^H$  of the full Hilbert space of the 4-orbital model, eq. (7.37), is written as

$$\mathbf{H}^H = \left( \begin{array}{c|c} \mathbf{H}^r & \mathbf{H}^{rd} \\ \hline \mathbf{H}^{dr} & \mathbf{H}^d \end{array} \right), \quad (7.40)$$

where  $\mathbf{H}^d$  and  $\mathbf{H}^r$  are  $(2 \times 2)$  matrices corresponding to the projections of  $\mathbf{H}^H$  onto the states spanning the d and r space, respectively. Since the matrix  $\mathbf{H}^d$  is known, a matrix  $\mathbf{T}^d$  diagonalizing  $\mathbf{H}^d$  can be determined

$$\tilde{\mathbf{D}} = \mathbf{T}^d \mathbf{H}^d (\mathbf{T}^d)^{-1}, \quad \tilde{\mathbf{D}} = \begin{pmatrix} \tilde{\epsilon}_1 & 0 \\ 0 & \tilde{\epsilon}_2 \end{pmatrix}. \quad (7.41)$$

Furthermore, it can be shown that a matrix  $\tilde{\mathbf{H}}^H$  with the desired properties is obtained if  $\tilde{\mathbf{T}}$  is set equal to  $\mathbf{T}^d$

$$\tilde{\mathbf{H}}^H = (\mathbf{T}^d)^{-1} \mathbf{D}^d \mathbf{T}^d. \quad (7.42)$$

(In appendix C.1, it is proved that the effective Hartree Hamiltonian  $\tilde{\mathbf{H}}^H$  with the desired properties can be calculated using the transformation matrix  $\mathbf{T}^d$ .) If  $\mathbf{H}^{rd} \neq \mathbf{0}$ , then  $\tilde{\mathbf{D}} \neq \mathbf{D}^d$ . Therefore  $\tilde{\mathbf{H}}^H$  is, in general, not identical to  $\mathbf{H}^d$ . Nevertheless, the effective Hartree Hamiltonian defined by eq. (7.42) will reproduce the Hartree eigenvalue spectrum of  $\mathbf{H}^H$  in d space.

#### Double-counting correction $\tilde{\mathbf{H}}^{d.c.}$

If the matrix  $\tilde{\mathbf{H}}^H$  is calculated according to eq. (7.42), the one-particle term of (7.26) not only contains the Hartree potential originating from charges in r space

but also the contributions to the Hartree potential from electrons in the d space. However, the latter is already included in the two-particle term of the Hamiltonian (7.26). Thus, a double-counting correction is introduced to subtract the contributions contained in both terms. The exact double-counting correction is given by

$$\tilde{H}^{\text{d.c.}}(\mathbf{r}) = -i \int W^r(\mathbf{r}, \mathbf{r}') \tilde{\rho}(\mathbf{r}') d^3r' \quad (7.43)$$

where  $W^r(\mathbf{r}, \mathbf{r}')$  corresponds to  $W^r(\mathbf{r}, \mathbf{r}'; \omega)$ , defined in eq. (7.30), with  $\omega = 0$  and the density  $\tilde{\rho}(\mathbf{r})$  is given by

$$\tilde{\rho}(\mathbf{r}) = \sum_{\sigma} \langle \tilde{\Psi}_0^N | \hat{\rho}^d(\mathbf{r}) | \tilde{\Psi}_0^N \rangle. \quad (7.44)$$

Unfortunately, in general  $\tilde{\rho}(\mathbf{r})$  cannot be determined, since the eigenstates  $|\tilde{\Psi}_j^N\rangle$  are solutions of the Schrödinger equation (7.28), which can only be solved if the exact double-counting correction is known.

To work with the effective, Hubbard-type model Hamiltonian, (7.26), it is inevitable to approximate expression (7.43) for  $\tilde{H}^{\text{d.c.}}(\mathbf{r})$ . In search for an adequate approximation, the Hamiltonian (7.6) of the 4-orbital model is analyzed. Just like the Hartree Hamiltonian in eq. (7.37), the hopping matrix  $\mathbf{t}$  entering the Hamiltonian (7.6) can be written as

$$\mathbf{t} = \left( \begin{array}{c|c} \mathbf{t}^r & \mathbf{t}^{\text{rd}} \\ \hline \mathbf{t}^{\text{dr}} & \mathbf{t}^d \end{array} \right). \quad (7.45)$$

Furthermore, all contributions to the two-particle term of the Hamiltonian (7.6) can be identified, for which the matrix elements  $U_{\alpha\beta\mu\nu}$  of the Coulomb interaction fulfill the following constraint

$$\alpha \in d, \nu \in r \quad \text{or} \quad \alpha \in r, \nu \in d \quad \text{or} \quad \beta \in d, \mu \in r \quad \text{or} \quad \beta \in r, \mu \in d. \quad (7.46)$$

For the remainder of the section, the subset of matrix elements fulfilling eq. (7.46) is denoted by  $U_{\alpha\beta\mu\nu}^{\text{rd}}$ . If the following assumption holds for the corresponding matrix elements of  $\mathbf{t}$  and  $\mathbf{U}$

$$\mathbf{t}^{\text{rd}} = \mathbf{t}^{\text{dr}} = \mathbf{0} \quad \text{and} \quad U_{\alpha\beta\mu\nu}^{\text{rd}} = 0, \quad (7.47)$$

the eigenstates  $|\Psi_j^N\rangle$  of the Schrödinger equation (7.11) of the 4-orbital model can be separated into contributions  $|\Psi_j^N, d\rangle$  and  $|\Psi_j^N, r\rangle$  from the d and r space, respectively

$$|\Psi_j^N\rangle = |\Psi_j^N, d\rangle \otimes |\Psi_j^N, r\rangle. \quad (7.48)$$

Then, the following identity holds

$$|\tilde{\Psi}_j^N\rangle = |\Psi_j^N, d\rangle \quad (7.49)$$

and

$$\tilde{\rho}(\mathbf{r}) = \rho^d(\mathbf{r}), \quad (7.50)$$

where  $\rho^d(\mathbf{r})$  is the density of the d space defined in eq. (7.25). Therefore, the following approximation to the exact double-counting correction, eq. (7.43), will be used in this work

$$\tilde{H}^{d.c.}(\mathbf{r}) \approx -i \int W^r(\mathbf{r}, \mathbf{r}') \rho^d(\mathbf{r}') d^3r'. \quad (7.51)$$

From eq. (7.51), a double-counting correction for the effective Hubbard-type model can now be calculated, since all terms on the right-hand side are known. A matrix  $\tilde{H}^{d.c.}$  of  $\tilde{H}^{d.c.}(\mathbf{r})$  as defined by (7.51) is obtained from the matrix expressions for  $W^r(\mathbf{r}, \mathbf{r}')$  and  $\rho^d(\mathbf{r})$  derived earlier.

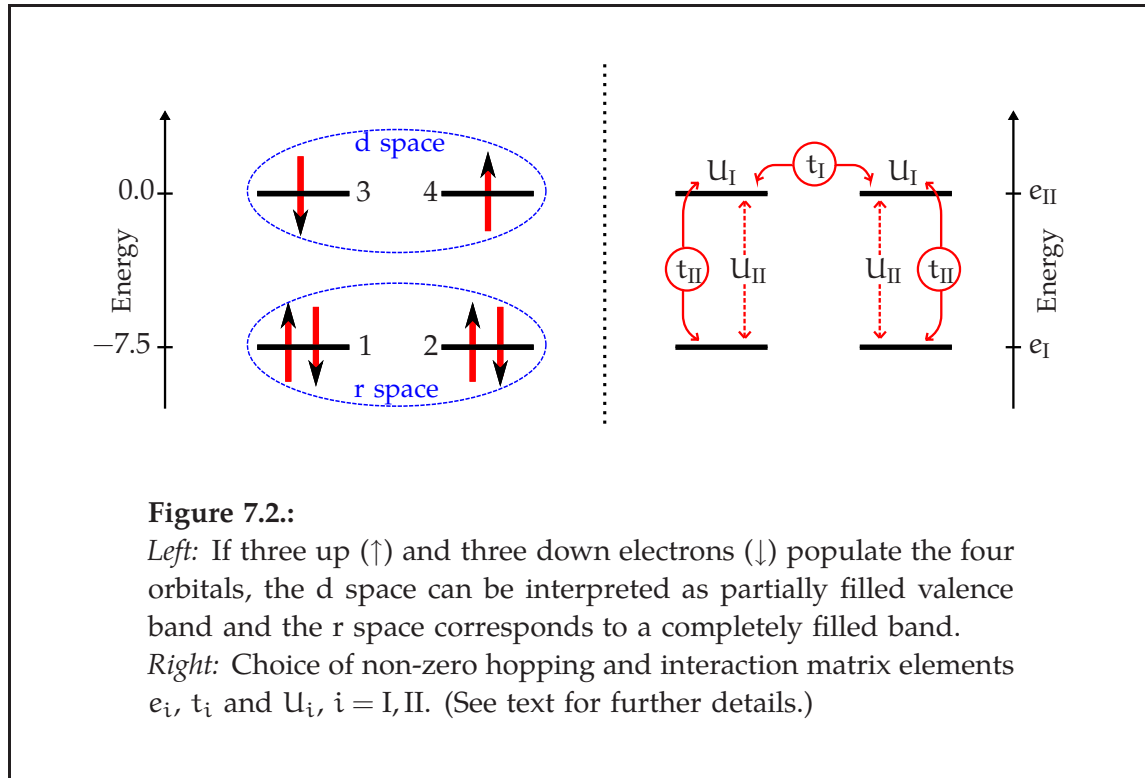
All matrices determining the Hamiltonian (7.26) can now be calculated. The spectra obtained from the solutions of the two Schrödinger equations (7.11) and (7.28) are compared in the next section.

## 7.2. Results

### 7.2.1. Influence of fully occupied states on valence electrons

In the first part of this section, results are presented from calculations with three up and three down electrons occupying the energy levels of the 4-orbital model. The resulting orbital occupation is shown schematically in the left picture of figure 7.2. As indicated in the picture, the upper two orbitals form the d space and the lower two the r space. The orbitals of the d space can be interpreted as partially filled valence states in the presence of completely filled valence states modeled by the orbitals in r space. Thus, the present setup of the 4-orbital model exhibits some similarities to the electronic structure of the compounds  $\text{LaBO}_3$  with  $B = \text{Cr, Mn, Fe}$ , discussed in chapter 6, where the 3d states of the transition metals form partially filled valence bands whereas the valence bands formed by oxygen 2p states are completely filled with electrons in the ground state. Hence, the analysis of the 4-orbital model might help to gain further insight into the electronic structure of real materials.

To carry out calculation for the 4-orbital model, the hopping matrix elements  $t_{\alpha\beta}$  formally defined in (7.9) as well as the interaction matrix elements  $U_{\alpha\beta\mu\nu}$ , eq. (7.10), constituting the Hamiltonian (7.6) of the 4-orbital model have yet to be determined. These matrix elements enter into the model calculations as parameters. Features in the many-body spectra of the 4-orbital model can then be related to one parameter of the model or to certain combinations of selected parameters. In general, it is one of the big advantage of model calculations



that the origin of spectral features although manifold in their appearance can be clearly determined.

This work focuses on changes in the many-body spectrum originating from the interaction between the charges in the two subspaces r and d. Therefore, most matrix elements of  $\mathbf{t}$  and  $\mathbf{U}$  are set to zero keeping only a subset of six non-zero elements. The six parameters are labeled  $e_i$ ,  $t_i$ ,  $U_i$  with  $i \in I, II$  and their influence on the electrons occupying the different energy levels of the 4-orbital model is indicated in figure 7.2 on the right side. A definition of these parameters is given below:

- The diagonal elements of the hopping matrix  $\mathbf{t}$  correspond to the energy levels of the four orbitals. The values of the elements were fixed in all calculations and are given in arbitrary units by

$$e_I \equiv -7.5 = -t_{11} = -t_{22}, \quad (7.52)$$

$$e_{II} \equiv 0.0 = -t_{33} = -t_{44}. \quad (7.53)$$

- In all calculations

$$t_I \equiv -t_{34} = -1.0. \quad (7.54)$$

If  $t_I \neq 0$ , the two orbitals in the d space hybridize forming a bonding and an anti-bonding state. Since there are 6 electrons in the system, the bonding

state will be completely filled and the anti-bonding state will be empty in the single-particle picture. Consequently, the system becomes insulating.

- Due to the choice

$$t_{II} \equiv -t_{13} = -t_{24} \neq 0 \quad (7.55)$$

electrons can hop between the two subspaces d and r.

- The electrons in d space are thought to be strongly correlated like electrons occupying a narrow 3d band. Thus, two electrons occupying the same orbital in d space feel a strong on-site Coulomb repulsion given by

$$U_I \equiv U_{3333} = U_{4444} \neq 0. \quad (7.56)$$

- Charges in d and r space should repel each other. This can be simulated choosing  $U_{II}$  to be non-zero, where  $U_{II}$  is defined as

$$U_{II} \equiv U_{1331} = U_{2442} \neq 0. \quad (7.57)$$

In the following, the pDOS of the d and r space obtained for different choices of the six parameters defined above are analyzed. Furthermore, the exact pDOS of the d space is compared to the spectrum obtained from the effective, Hubbard-type model. Throughout the whole chapter the pDOS of occupied states is always plotted with a positive sign and the pDOS of unoccupied states has a negative sign such that occupied and unoccupied states can be better distinguished graphically. The discussion of results starts by analyzing the influence of the parameters  $t_I$ ,  $U_I$  and  $U_{II}$  on the many-body spectra.

### Effect of $t_I$ , $U_I$ and $U_{II}$ on the spectra of the d and r space

In all calculations presented in this section, the parameter  $t_{II}$  was set to zero in order to demonstrate that distinct features of the many-body spectrum can be directly related to the parameters  $t_I$ ,  $U_I$  and  $U_{II}$ . On the left side of figure 7.3 the pDOS of the d and r space are displayed. These spectra were obtained from calculations with three different choices of the parameters  $t_I$ ,  $U_I$  and  $U_{II}$ . The pDOS are aligned at the Fermi energy, which is identified as the energy in the middle of the gap between the highest occupied and the lowest unoccupied state. On the right side of of figure 7.3, the exact spectrum of the d space is compared to the description obtained from the effective, Hubbard-type model for the given choice of the parameters  $t_I$ ,  $U_I$  and  $U_{II}$ . The resulting spectra are not aligned at the Fermi level to check how well the effective model reproduces the absolute many-body eigenvalues of the exact solution.

The spectra in figure 7.3 A were obtained by choosing  $t_I = -1.0$  and  $U_I$  and  $U_{II}$  were set to zero. Only the hybridization between the two orbitals in d space

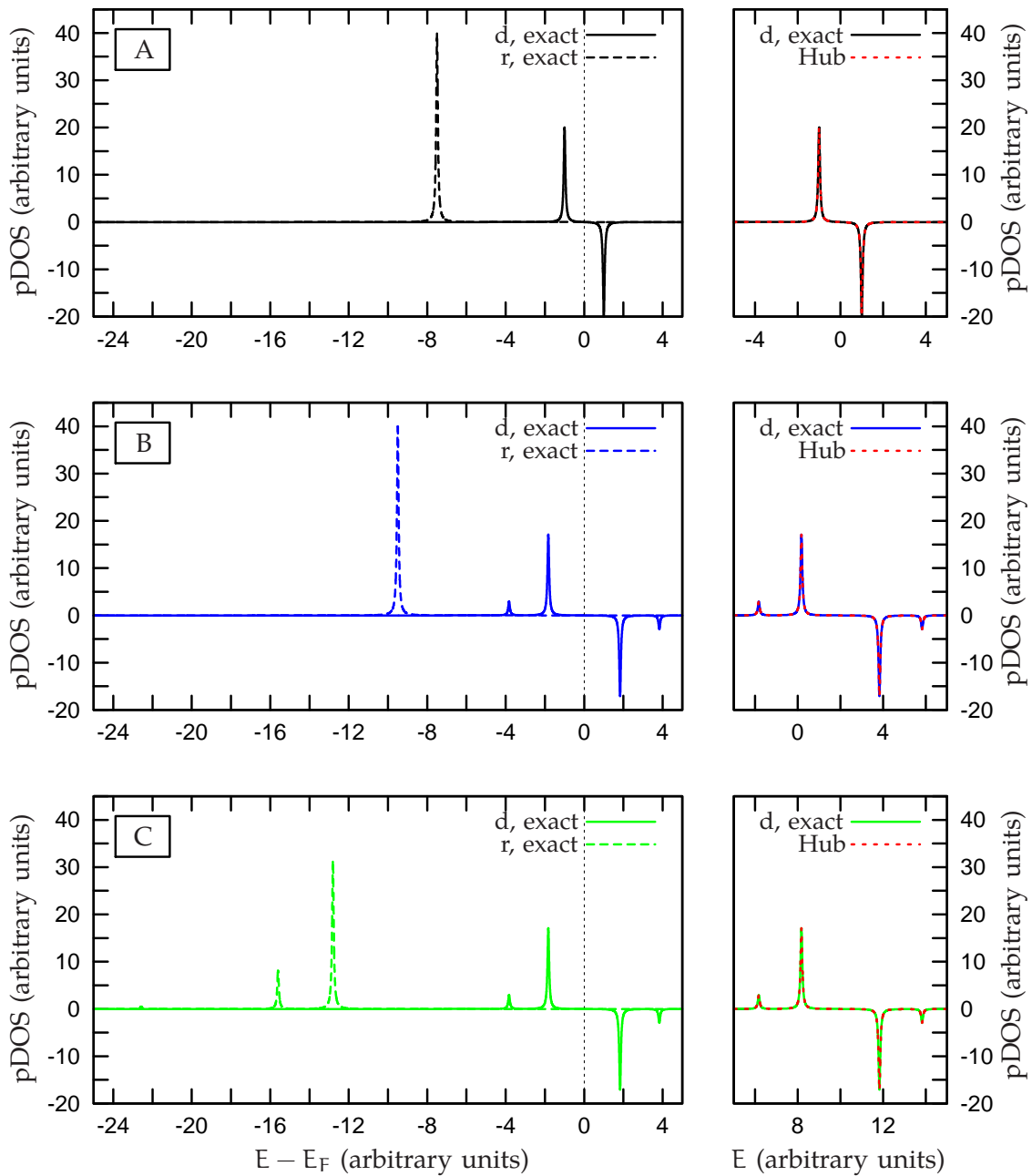


**Figure 7.3.:**

*Left:* pDOS of the  $r$  and  $d$  space obtained from the exact solution of the 4-orbital model demonstrating the influence of the parameters  $t_I$ ,  $U_I$  and  $U_{II}$  on the many-body spectrum. In A,  $t_I = -1.0$  and  $U_I$  and  $U_{II}$  equal 0. In B,  $U_I = 4.0$  is added and in C  $U_{II} = 4.0$  is included additionally.

*Right:* The same pDOS of the  $d$  space displayed in the graphs on the left are compared to the spectra obtained from the effective, Hubbard-type model (Hub). In all cases the two curves are indistinguishable

already described above is observed resulting in a bonding and anti-bonding contribution to the pDOS of the d space. Hence, for this particular choice of parameters all electrons are treated as independent particles. Consequently, the pDOS of the r space consists of only one peak located at the energy  $-7.5$  due to the choice of the parameter  $e_1$  determining the position of the two orbitals in r space. The effective model exactly reproduces the pDOS in d space, because the given choice of parameters leads to  $\tilde{\mathbf{H}}^{\text{H}} = \mathbf{H}^{\text{d}} = \mathbf{t}^{\text{d}}$  and all matrix elements of  $\tilde{\mathbf{H}}^{\text{d.c.}}$  and  $\mathbf{W}^{\text{r}}$  are exactly zero, since  $\mathbf{U} = \mathbf{0}$ .

For the calculations yielding the spectra labeled B in figure 7.3 the value of  $U_{\text{I}}$  was raised to 4.0. All other parameters were the same as in the calculations yielding the spectra in figure 7.3 A. The on-site Coulomb interaction  $U_{\text{I}}$  leads to the formation of satellites called Hubbard bands in the pDOS of the d space. For  $U_{\text{I}} = 4.0$  the Hubbard bands are located at energies 2.0 and  $-2.0$  with respect to the Fermi level. The shape of the pDOS in r space is unchanged, but the peak is shifted to lower energies with respect to the Fermi level. This is a consequence of the Hartree potential felt by the electrons in d space, which originates from the non-zero value of  $U_{\text{I}}$  and which leads to a shift of the energetic positions of the peaks in the pDOS of the d space to higher energies. Due to the alignment of the spectra at the Fermi energy, this shift gives rise to a downwards shift of the pDOS of the r space.

The upwards shift of energetic d positions can be seen in the graph to the right of figure 7.3 B. Furthermore, it is seen that this shift and all other spectral features are again exactly reproduced by the effective model. As a direct consequence of the choice of the parameters the two subspaces are still completely separated. Therefore, the approximation (7.51) for the double-counting correction (7.43) becomes exact. Furthermore, the double-counting correction cancels the contribution of the Hartree potential in  $\tilde{\mathbf{H}}^{\text{H}}$  exactly such that the identity  $\tilde{\mathbf{H}}^{\text{H}} = \mathbf{t}^{\text{d}}$  still holds. In addition, the only non-zero matrix elements of  $\mathbf{W}^{\text{r}}$  are identical to the only non-zero matrix elements of  $\mathbf{U}$  given by  $U_{\text{I}}$ . In general, there is no screening of the Coulomb potential in d space from charges in the r space as long as electrons cannot move between the two subspaces, i.e.  $t_{\text{II}} = 0$ . This can be understood by looking at the definition of the response function  $R(\mathbf{r}\mathbf{t}, \mathbf{r}'\mathbf{t}') \equiv \delta n(\mathbf{r}, \mathbf{t}) / \delta \phi(\mathbf{r}', \mathbf{t}')|_{\phi=0}$ , eq. (A.14). If electrons cannot leave the r space, the density in r space is constant and the response function is zero. As long as the r-space charge is not polarizable, it will not screen the Coulomb potential in d space.

There is still no screening of the Coulomb potential in the d space if  $U_{\text{II}}$  is set to 4.0 as long as  $t_{\text{II}} = 0$  and  $t_{\text{I}}$  and  $U_{\text{I}}$  have the same values as in the previous calculations. The resulting spectra are shown in figure 7.3 C. The choice of  $U_{\text{II}} = 4.0$  leads to the formation of two satellites in the pDOS of the r space, of which the smaller satellite located around  $-23$  is barely visible in the spectrum.

Furthermore, it yields an additional contribution to the Hartree potential such that the relative distance between the peak positions of the pDOS of the d and r space is increased further. Apart from this shift in the peak positions, the shape of the pDOS in d space is unchanged.

The graph on the right of figure 7.3 C again compares the exact spectra of the d space with that from the Hubbard-type model. The matrix elements of the  $\mathbf{W}^r$  are again identical to the matrix elements given by  $U_I$  due to the lack of screening. However,  $\tilde{\mathbf{H}}^H \neq \mathbf{H}^d$  since  $U_{II} \neq 0$ ; but the effective Hartree Hamiltonian constructed according to eq. (7.42) can exactly reproduce the shift of the peaks of the pDOS to higher energies due to the additional contribution to the Hartree potential originating from  $U_{II}$ . Furthermore, eq. (7.51) for the double-counting correction is still exact, since condition (7.47) is fulfilled for the given choice of parameters. Thus, the effective model can reproduce the spectrum of the d space correctly if all three parameters  $t_I$ ,  $U_I$  and  $U_{II}$  are non-zero. In the next section, it is demonstrated that a one-to-one agreement of the spectra from the effective model with those from the exact solution cannot be achieved if the two subspaces are coupled, i.e.  $t_{II} \neq 0$ .

### The parameter $t_{II}$ – if subspaces communicate

To demonstrate the effect of  $t_{II}$  itself on the many-body spectrum,  $U_I$  and  $U_{II}$  were again set to zero. The pDOS of the d and r space obtained from a calculation with  $t_I = -1.0$  and  $t_{II} = -3.0$  is shown in figure 7.4 on the left side. The largest qualitative change compared to the spectra in figure 7.3 A, where  $t_{II} = 0$ , occurs in the pDOS of the r space, since the hybridization between the states in d and r space resulting from  $t_{II} \neq 0$  leads to the formation of a bonding and an anti-bonding state in the r space. Thus, the single peak in the spectrum of the r space observed in figure 7.3 A is split into two peaks.

A closer look at the spectra in figure 7.4 reveals that charge density from the r space is shifted to the d space. This can be observed due to the emergence of small peaks in the spectra of each subspace d and r, which are located at the position of the main peaks of the spectrum of the other subspace. The formation of two additional peaks in the pDOS of the d space can be seen more clearly in the right graph of figure 7.4, where the exact pDOS is compared to the spectrum obtained from the solution of the effective, Hubbard-type model. Furthermore, it can be seen directly that these two features in the exact solution are missing in the spectrum of the effective model. Since the Hilbert space of the effective model is constructed from those states forming the d space, the electrons have to stay in d space because they have nowhere else to go. Therefore, the additional peaks seen in the pDOS of the exact solution are not reproduced. Furthermore, the height of the peaks in the spectrum from the effective model are unchanged

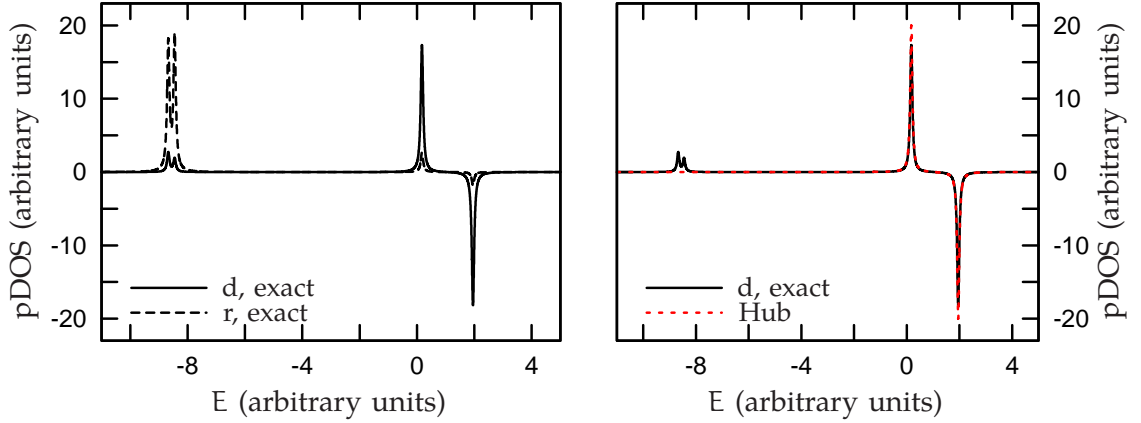


**Figure 7.4.:**

*Left:* The exact pDOS of the d and r space, where  $t_I = -1.0$ ,  $t_{II} = -3.0$  and  $U_I$  and  $U_{II}$  were set to zero.

*Right:* The pDOS of the d space compared to the spectrum of the effective, Hubbard-type model (Hub) for the same choice of parameters.

compared to the spectrum in 7.3 A, because the number of particles occupying the states in d space in calculations employing the effective, Hubbard-type model is 2 by construction. However, the actual number of particles in the d space given by the trace of the exact matrix of the density  $\rho^d(\mathbf{r})$ , eq. (7.25), turns out to be larger than 2.

The discrepancies between the spectra obtained from the exact solution and the effective model result from the particular construction of the effective model. Therefore, these deficiencies cannot be easily cured without changing the model itself. However, the model was chosen in the first place in order to check how well it reproduces the exact solution, because in the present form it resembles the Hubbard models employed in calculations for real materials. Furthermore, it should be emphasized that the deviations do not result from an inaccuracy of the treatment of correlations, which can only be approximated in calculations for real materials. They originate from the single-particle term of the Hamiltonian (7.6). In particular, the matrices  $\tilde{\mathbf{H}}^{d,c}$  and  $\mathbf{W}^r$  in the Hamiltonian (7.26) of the effective model are exactly zero in the example discussed here, since  $\mathbf{U} = \mathbf{0}$ . Last but not least, it should be pointed out that the effective model is at least able to reproduce the exact positions of the two main peaks in the spectrum of the d space, since  $\tilde{\mathbf{H}}^H$  calculated according to (7.42) readily accounts for the small shifts of the two main peaks in the spectrum of the d space resulting from  $t_{II} \neq 0$ .

For the calculations discussed next,  $U_I$  was set again to 4.0. The remaining parameters were kept constant, in particular,  $U_{II}$  is still zero. The resulting spectra

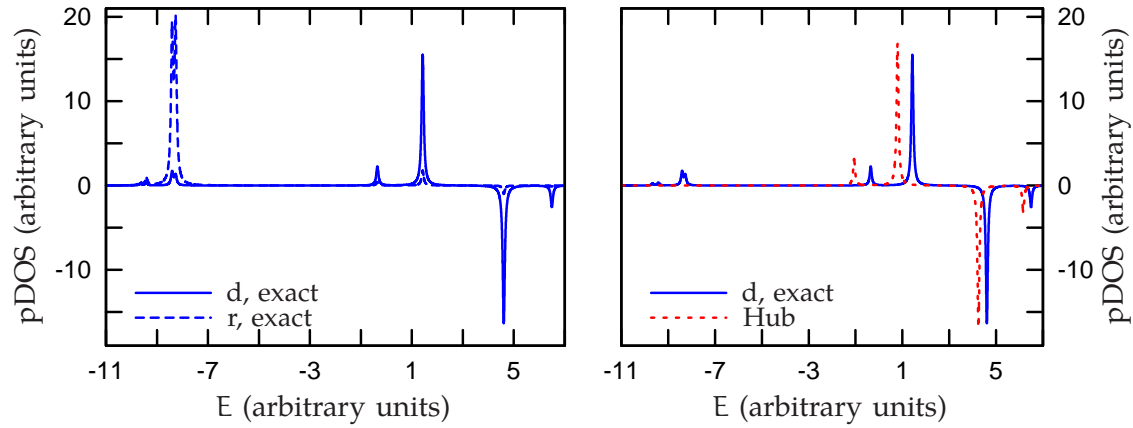


**Figure 7.5.:**

*Left:* The exact pDOS of the d and r space, where  $t_I = -1.0$ ,  $t_{II} = -3.0$  and  $U_I = 4.0$ . Here,  $U_{II}$  is zero.

*Right:* The exact pDOS of the d space compared with the spectrum of the effective, Hubbard-type model (Hub) for the same parameters.

are displayed in figure 7.5. Compared to figure 7.3 B, the only new features in the spectra obtained from the exact solution of the 4-orbital model are two additional satellites in the spectra of the r and the d space located at roughly  $-10$ . The hybridization between the states in d and r space originating from  $t_{II} \neq 0$  combined with  $U_I \neq 0$  result in a potential  $U^{\text{ind}}$  induced in the r space. Similar to the effect of  $U_{II}$  demonstrated in figure 7.3 C,  $U^{\text{ind}}$  generates satellites in the spectrum of the r space. Due to the hybridization between the states of the two subspaces, part of the charges forming the satellite is shifted to the d space such that two satellites at the same position can be found in the pDOS of the d space. From the previous discussion it is clear that these satellites cannot be reproduced by the effective model whereas the two Hubbard bands do show in the spectrum of the effective model in figure 7.6. However, the energetic positions of both the two main peaks as well as the Hubbard bands are not exactly reproduced by the Hubbard-type model.

The treatment of the two-particle term and particularly the construction of the interaction matrix elements  $\mathbf{W}^r$  in the Hamiltonian (7.26) of the effective model are not the origin of the observed discrepancies between the spectra. In fact, the only non-zero matrix elements of  $\mathbf{W}^r$  are again identical to  $U_I$  for the given choice of parameters, since the effect of screening is zero. The corresponding proof is lengthy and is therefore deferred to appendix C.2. Since  $\mathbf{W}^r$  is known exactly and the single-particle term of the Hubbard-type model is constructed to reproduce the one-particle contributions to the many-body spectrum exactly, the deviations between the exact spectrum and the results from the effective model

must be related to the double-counting correction.

For the given choice of parameters, the condition in (7.47) indeed is no longer fulfilled and (7.51) is merely an approximation to the exact double-counting correction (7.43). As a result of the hybridization between the two subspaces, it was observed that the true number of particles obtained from  $\rho^d(\mathbf{r})$  is larger than the number of particles occupying the states in  $d$  space in calculations employing the effective model. Consequently, the double-counting correction becomes too large if the density  $\tilde{\rho}(\mathbf{r})$  entering the exact double-counting term is replaced by  $\rho^d(\mathbf{r})$ . Therefore, the spectrum obtained from the effective model is shifted downwards in energy with respect to the peak positions of the exact pDOS of the  $d$  space in figure 7.6.

To demonstrate that the hybridization between the subspaces is the main source of the differences between the spectra, a series of calculations was carried out for  $t_{II} = -3.0$ ,  $t_{II} = -5.0$  and  $t_{II} = -7.0$  with  $t_I = -1.0$  and  $U_I = 4.0$  in all calculations. In figure 7.6, the resulting spectra of the effective model and the exact pDOS of the  $d$  space are displayed in the graphs labeled A1, A2, A3. Obviously, the differences between the eigenvalues of the exact solution and those from the Hubbard-type model, which determine the position of the peaks in the spectra, become larger if  $t_{II}$  increases. For comparison, another series of spectra denoted by B1, B2 and B3 is shown in figure 7.6, which was obtained by changing  $U_I$  from 6.0 to 9.0 and to 12.0 keeping the non-zero hopping matrix elements  $t_I$  and  $t_{II}$  at a constant value of  $-1.0$  in all calculations. Since there is still a small hybridization between the two subspaces, the spectra from the effective model still deviate from those obtained from the exact solution. However, the increase in the deviations between the spectra due to changes of  $U_I$  is much smaller than the changes due to an increase of  $t_{II}$ . These small changes can again be related to the double-counting correction, since changes of  $U_I$  lead to different eigenstates  $|\Psi_J^N\rangle$  of the Schrödinger equation (7.11). These eigenstates enter the calculations of the density  $\rho^d(\mathbf{r})$ , eq. (7.25), which in turn enters eq. (7.51) for the double-counting correction. On the other hand, the majority of the changes originating from the increase of  $U_I$  are reproduced qualitatively and quantitatively by the effective model, since  $\mathbf{W}^r = \mathbf{U}$ .

Finally, the effect of the combination of the parameters  $t_{II}$  and  $U_{II}$  on the many-body spectrum is analyzed. The calculations were carried out with  $t_I = -1.0$ ,  $t_{II} = -5.0$  and  $U_{II} = 4.0$ . Furthermore,  $U_I$  was set to zero in all calculations. The resulting spectra are shown in figure 7.7. As demonstrated previously in figure 7.3 C,  $U_{II}$  leads to the formation of satellites in the pDOS of the  $r$  space. Due to the hybridization between the two subspaces, satellites at the same positions can now also be found in the pDOS of the  $d$  space. In addition, the formation of two small Hubbard bands located roughly at 9.0 and 13.0 can be observed in the spectrum of the  $d$  space although  $U_I = 0$ . The emergence of Hubbard bands

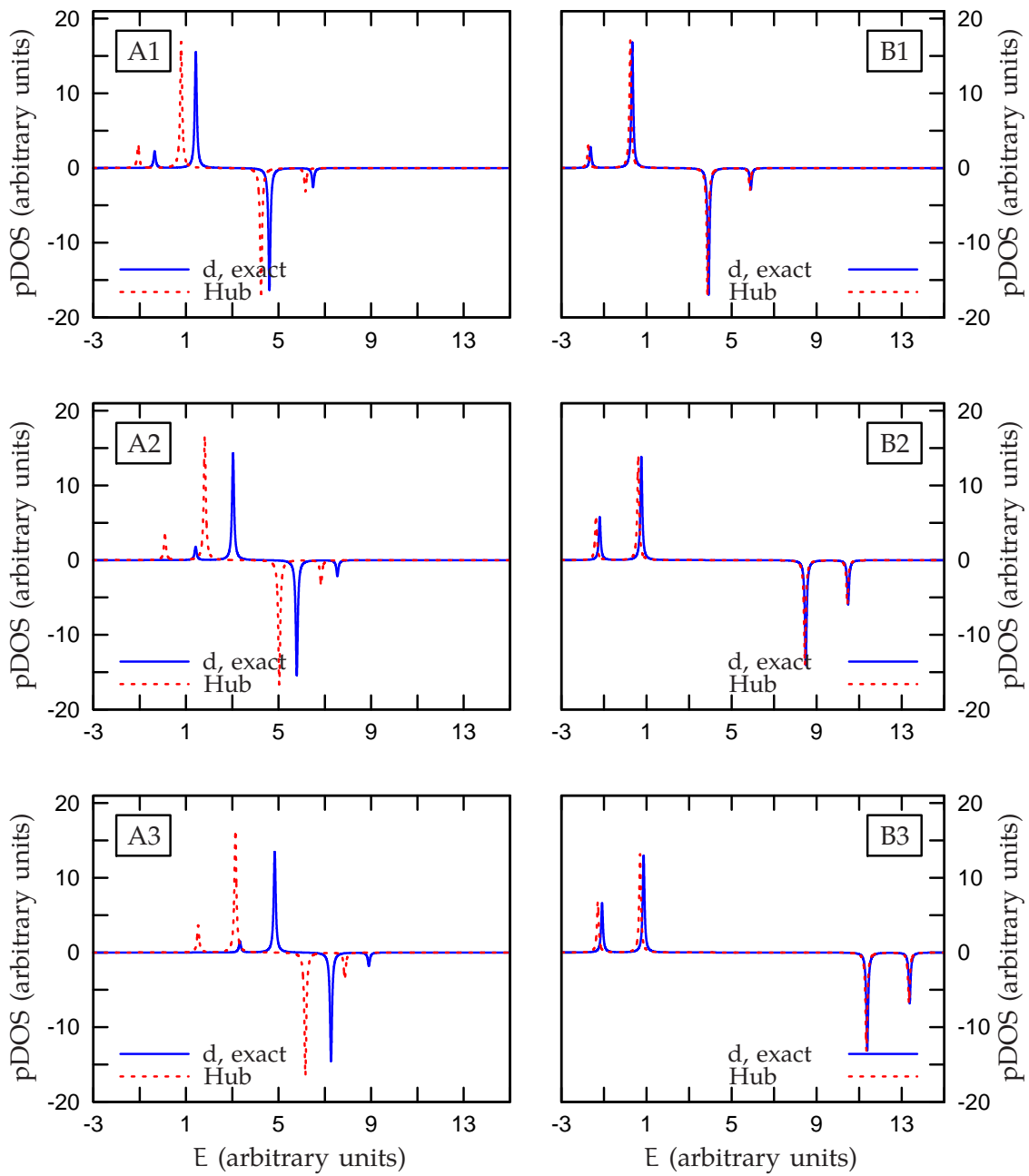


**Figure 7.6.:**

*Left:* Exact spectrum and Hubbard-type model (Hub) description of the d space, where  $t_I = -1.0$  and  $U_I = 4.0$  in all calculations and  $t_{II}$  changes from  $-3.0$  in A1 to  $-5.0$  in A2 and  $-7.0$  in A3.

*Right:* In B1, B2 and B3 the values of  $t_I = -1.0$  and  $t_{II} = -1.0$  were kept constant and  $U_I$  was changed from  $6.0$  in B1 to  $9.0$  in B2 and  $12.0$  in B3.

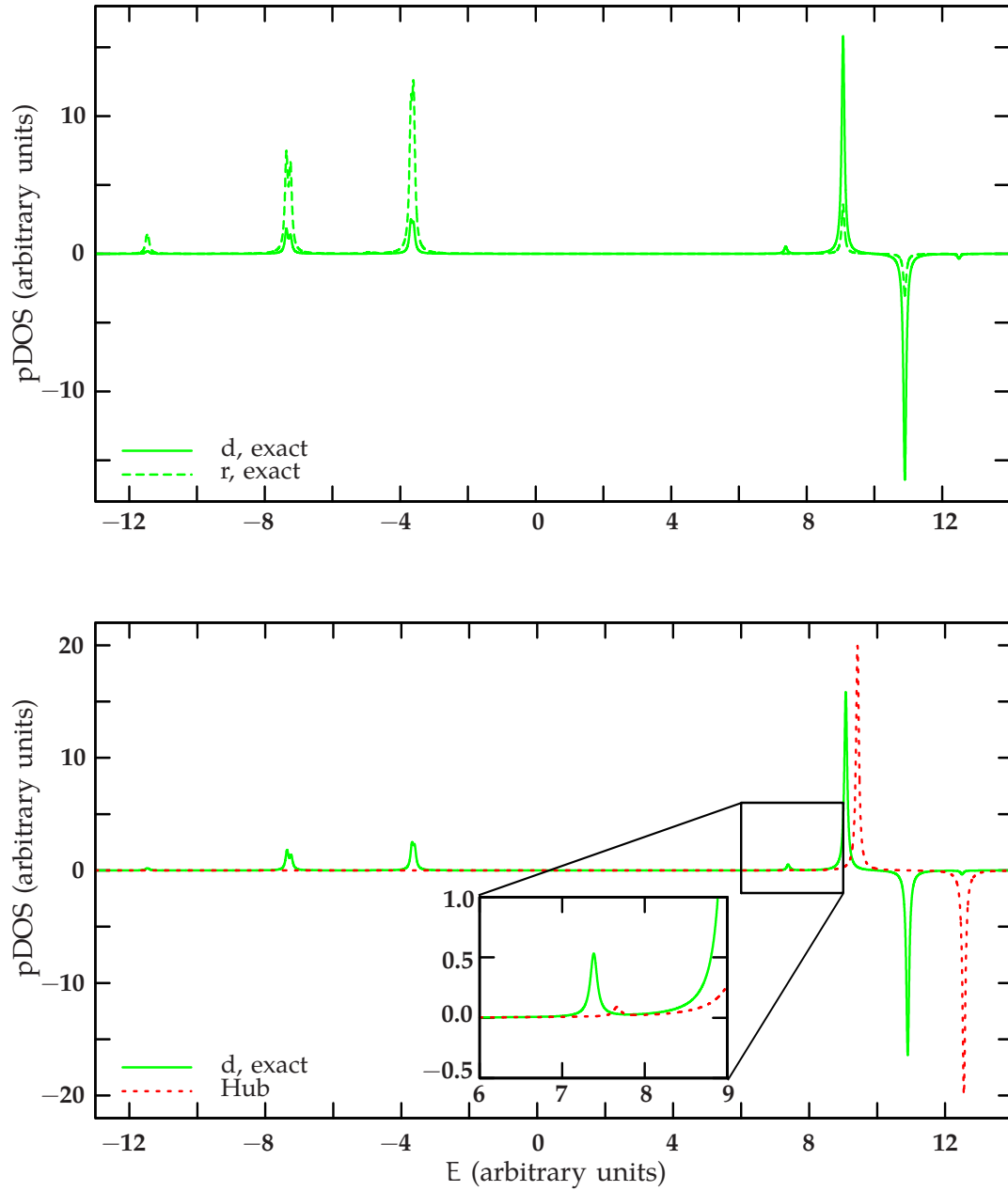


**Figure 7.7.:**

*Top:* The exact pDOS of the  $d$  and  $r$  space, where  $t_I = -1.0$ ,  $t_{II} = -5.0$  and  $U_{II} = 4.0$ . In all calculations,  $U_I$  is set to zero.

*Bottom:* The exact pDOS of the  $d$  space compared to the spectrum of the effective, Hubbard-type model (Hub) for the same choice of parameters.

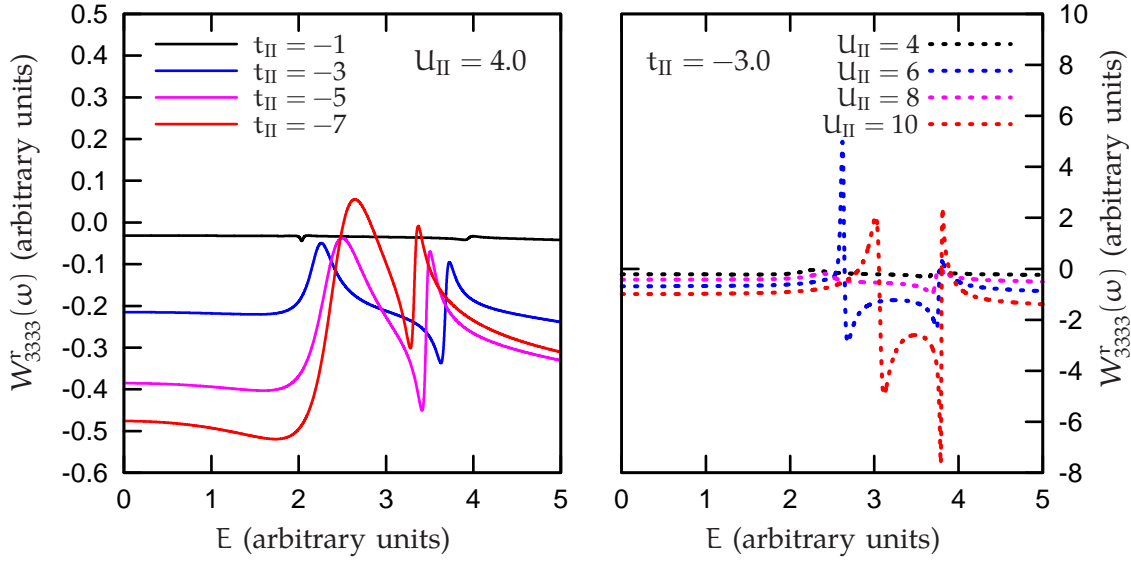


**Figure 7.8.:** Frequency dependence of the induced on-site Coulomb interaction  $W_{3333}^r(\omega)$  obtained from (left) four different choices of  $t_{II}$  with  $U_{II} = 4.0$  and (right) four different choices of  $U_{II}$  with  $t_{II} = -3.0$ .

is a direct consequence of the screening of the Coulomb potential  $U_{II}$ , which is non-zero for the given choice of parameters. The screening induces an on-site Coulomb repulsion in the  $d$  space, i.e.

$$W_{iii}^r(\omega) \neq 0, \quad i \in d, \quad (7.58)$$

which leads to the formation of Hubbard bands.

The effective Hubbard-type model does not reproduce the exact spectrum of the  $d$  space very well for the given choice of parameters as demonstrated in the graph on the bottom of figure 7.7. The satellites at the positions of the peaks in the  $r$  space are not reproduced at all for the reasons discussed previously. Furthermore, the positions of the two main peaks in  $d$  space come out wrong. The same is true for the position of the Hubbard bands, which are also present in the spectrum from the effective model but which are very small as can be seen in the inset of the graph.

The deficiencies of the Hubbard-type model have several reasons. On the one hand, the density  $\rho^d(\mathbf{r})$  entering into the approximation for the double-counting term (7.51) still differs from  $\tilde{\rho}(\mathbf{r})$  in the exact expression for the double-counting correction for the reasons discussed before. On the other hand, an additional approximation has to be made now in the construction of the Hamiltonian (7.26) for the effective model, namely the neglect of the frequency dependence of  $\mathbf{W}^r(\omega)$ . Figure 7.8 shows the frequency dependence of the induced on-site Coulomb

interaction  $W_{3333}^r(\omega)$  for different choices of  $t_{\text{II}}$  in the graph to the left and for variations of  $U_{\text{II}}$  on the right. In both graphs,  $W_{3333}^r(\omega) \approx W_{3333}^r(0)$  only for  $\omega \lesssim 2$ . Furthermore, the frequency dependence becomes larger if either one of the two parameters is increased. The changes of the absolute value of  $W_{3333}^r(\omega)$  largely depend on the choice of the values for  $U_{\text{II}}$ . However, there is no screening at all if  $t_{\text{II}} = 0$ , such that the effect truly originates from the combination of the two parameters  $t_{\text{II}}$  and  $U_{\text{II}}$ . For all choices of  $t_{\text{II}}$  and  $U_{\text{II}}$  investigated here,  $W_{3333}^r(\omega)$  starts to deviate from its  $\omega \rightarrow 0$  limit at frequencies much smaller than the frequency range comprising the exact spectrum of the d space. Hence, any changes in the pDOS of the d space related to the frequency dependence of  $W_{3333}^r(\omega)$  are not accounted for by the effective, Hubbard-type model.

In summary, for any choice of  $t_{\text{II}}$  other than zero the effective, Hubbard-type model cannot reproduce the exact many-body spectrum quantitatively. The main source of error is the inequality  $|\tilde{\Psi}_j^N\rangle \neq |\Psi_j^N, d\rangle$  originating from  $t_{\text{II}} \neq 0$ , since the double-counting correction, eq. (7.43), can no longer be exactly determined and the true number of particles in d space deviates from the number of particles that is kept constant in the construction of the effective model.

### 7.2.2. Valence electrons and empty states

In the second part of this section, results are presented from calculations with one up and one down electron occupying the orbitals of the 4-orbital model, which results in the orbital occupation shown schematically in the left picture of figure 7.9. If the orbital filling discussed in the first part of this section simulates a partially filled valence band in the presence of a fully occupied band, the present setup can be interpreted as a model for a partially filled valence band and a conduction band. Here, the lower two energy levels of the 4-orbital model form the d space and the unoccupied levels 3 and 4 make up the r space.

To carry out calculations, matrix elements of the hopping matrix  $\mathbf{t}$  and the interaction matrix  $\mathbf{U}$  entering the Hamiltonian (7.6) have to be defined. Like in the calculations presented before, most matrix elements are set to zero. The non-zero elements are given by

$$e_{\text{I}} \equiv -t_{11} = -t_{22}, \quad (7.59)$$

$$e_{\text{II}} \equiv -t_{33} = -t_{44}, \quad (7.60)$$

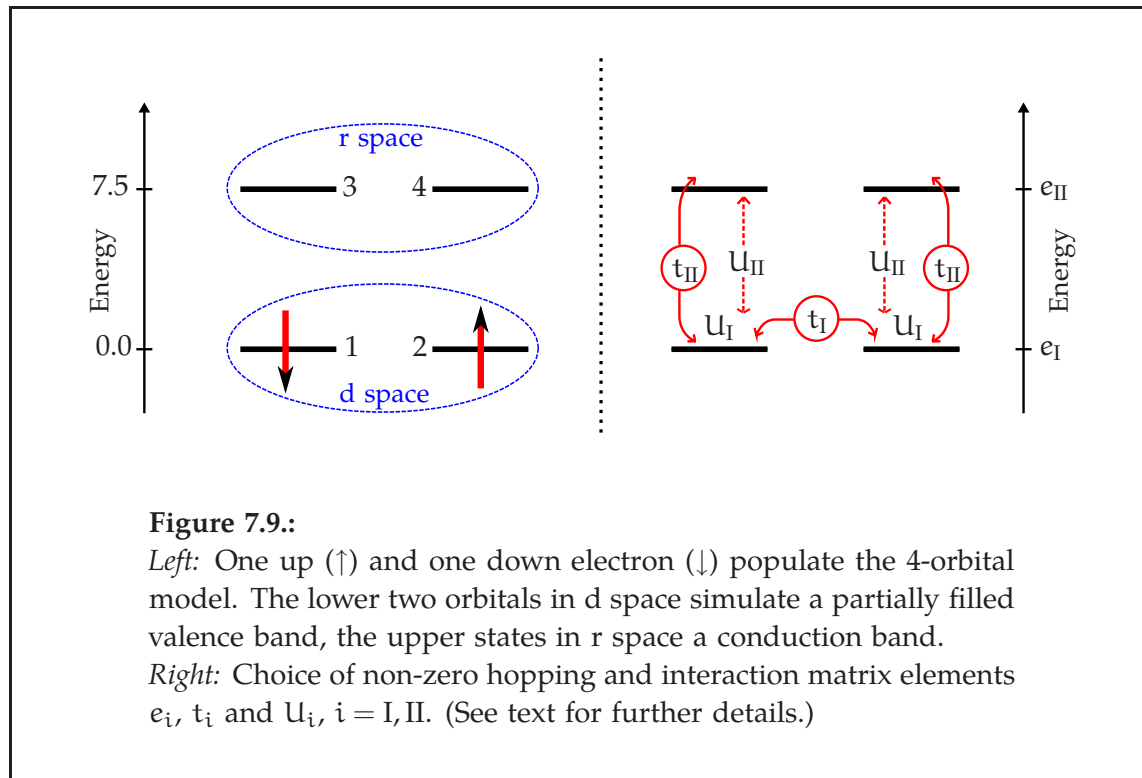
$$t_{\text{I}} \equiv -t_{12}, \quad (7.61)$$

$$t_{\text{II}} \equiv -t_{13} = -t_{24}, \quad (7.62)$$

$$U_{\text{I}} \equiv U_{1111} = U_{2222}, \quad (7.63)$$

$$U_{\text{II}} \equiv U_{1331} = U_{2442}. \quad (7.64)$$

The effect of these parameters on the electrons in the system is illustrated in



the right picture of figure 7.9. In all calculations presented here,  $e_I$  is set to 0.0 and  $e_{II} = 7.5$ . The parameters  $t_I$  and  $U_I$  denote matrix elements different from those in the calculations presented earlier in this section, since now the d space is composed of the lower two orbitals in the present setup. Previously, the influence of the parameters  $t_I$  and  $U_I$  as well as the effect of  $U_{II}$  on the spectrum of the d space was investigated. For the present definition of the d space, these three parameters have almost the same effect. In fact, if  $t_{II} = 0$ , the only difference is observed for  $U_{II} \neq 0$ , which does not lead to an additional contribution to the Hartree potential due to the lack of charges in r space in the present setup.

However, for  $t_{II} \neq 0$  changes in the many-body spectra may occur, which require the presence of empty states and have therefore not been observed previously. The newly observed spectral features can be attributed to the combination of two effects, of which one originates from the parameters  $U_I$  and the other one is caused by  $t_{II}$ . The parameter  $t_I$  was set to  $-1.0$  in all calculations. This parameter is chosen to be negative to make the system insulating as explained earlier. The remaining parameter  $U_{II}$  was set to zero.

The influence of the parameter  $U_I$  on the pDOS of the d and r space for three different values 2.0, 8.0 and 20.0 for  $U_I$  is demonstrated in the graphs A1, A2 and A3 of figure 7.10. Here,  $t_{II}$  was also set to zero. Thus, no electrons can hop between the two subspaces and the choice of  $U_I \neq 0$  has no influence at all

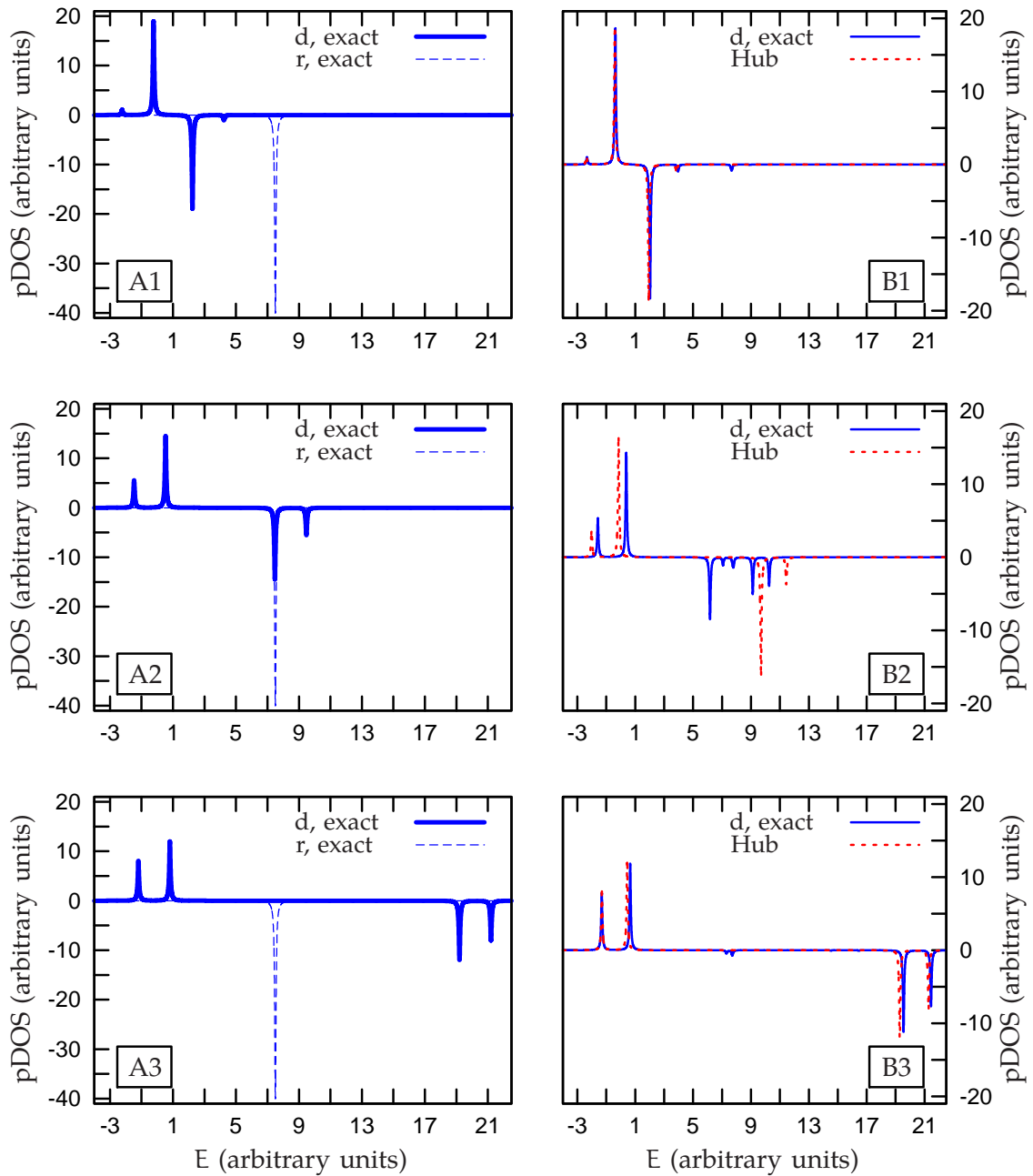


**Figure 7.10.:**

*Left:* Exact spectrum of the d and r space, with  $t_I = -1.0$ ,  $t_{II} = 0.0$  and  $U_{II} = 0.0$  in all calculations and  $U_I$  was increased from 2.0 in A1 to 8.0 in A2 and 20.0 in A3.

*Right:* In B1, B2 and B3, the pDOS of the d space and the spectrum of the Hubbard-type model (Hub) are shown for the same values of  $t_I$ ,  $U_I$  and  $U_{II}$  as in A1, A2 and A3. The parameter  $t_{II}$  is set to  $-1.0$  in all calculations.

on the pDOS of the  $r$  space, which is solely determined by the choice of  $e_{II}$ . In the pDOS of the  $d$  space,  $U_I \neq 0$  leads to the formation of two Hubbard bands. Furthermore, it yields a contribution to the Hartree potential, which leads to the observed shift of the unoccupied part of the pDOS in  $d$  space to higher energies. The spectrum from the effective Hubbard model is not shown in the graphs A1, A2 and A3 in figure 7.10 but it is clear from the previous discussions that the effective model exactly reproduces the pDOS of the  $d$  space for the given choice of parameters, since all non-zero matrix elements in the Hamiltonian (7.26) can be determined exactly.

The situation changes if  $t_{II}$  becomes non-zero, which leads to a hybridization between the states forming the  $d$  and  $r$  space. The graphs B1, B2 and B3 of figure 7.10 show a comparison of the exact pDOS of the  $d$  space with the spectra obtained from the effective model. In all calculations,  $t_{II}$  was set to  $-1.0$  and the parameter  $U_I$  was again changed from  $2.0$  to  $8.0$  and  $20.0$ . All other parameters were the same as in the calculations yielding the spectra shown in figure 7.10 A1 through A3.

The largest difference between the spectrum of the effective model and the exact pDOS of the  $d$  space can be observed in figure 7.10 B2. Here,  $U_I$  is almost identical to  $e_{II}$ . Therefore, the unoccupied part of the pDOS in  $d$  space is located in the same energy range as the pDOS of the  $r$  space, as can be seen in 7.10 A2. Thus, even the small value  $-1.0$  of  $t_{II}$  leads to a strong hybridization between the states in  $r$  space and the unoccupied part of the spectrum of the  $d$  space. Consequently, the unoccupied part of the pDOS in  $d$  space consists of one larger peak and four satellites of different height. The effective, Hubbard-type model is not capable of reproducing these features which originate from the hybridization between the two subspaces. This has been discussed previously in the context of the discrepancies between the spectrum of the effective model and the exact pDOS of the  $d$  space observed in figure 7.6. Here, the effective model completely fails to reproduce the unoccupied part of the exact spectrum, because the hybridization between the unoccupied states in  $d$  space with the orbitals in  $r$  space becomes particularly large for  $U_I \approx e_{II}$ . On the other hand, the hybridization between the occupied states in  $d$  and the empty states in  $r$  space is much smaller. Hence, the corresponding part in the spectrum of the effective model is in good agreement with the occupied part of the pDOS.

If  $U_I$  is small as in B1, the unoccupied part of the pDOS in  $d$  space is only slightly shifted to higher energies. Thus, the hybridization between all parts of the spectrum of the  $d$  and  $r$  spaces is small and the effective model can reproduce the exact pDOS both qualitatively and almost quantitatively. The overall agreement of the spectra is also good if  $U_I$  is as large as in B3, because the unoccupied part of the  $d$ -space spectrum is located at much higher energies than the peak positions of the pDOS in  $r$  space. Consequently, the hybridization

between the subspaces is also small causing only minor discrepancies between the spectrum of the effective model and the exact spectrum.

Finally, it should be emphasized that the effect observed in 7.10 B2 only occurs in the present setup if  $U_I \approx e_{II}$  and  $t_{II} \neq 0$ . In general, the occurrence of such an effect requires the hybridization between the subspaces. Furthermore, one of the two subspaces has to be empty. Otherwise, a contribution to the Hartree potential felt by the electrons in one subspace will always increase the relative distance between the peak positions of the spectra of the subspaces, as demonstrated, e.g., in figure 7.3 B and C.

### 7.3. Discussion and Summary

The interaction between partially filled and fully occupied atomic orbitals as well as the interplay between partially occupied and empty orbitals was investigated using a simple toy model. For both scenarios, an effective, Hubbard-type model was constructed to describe the subspace containing only those orbitals, which were partially occupied. The resulting spectra were compared to the density of states obtained from the exact solution. Provided that the Hubbard model is constructed according to the scheme introduced here, it can reproduce the exact solution both qualitatively and almost quantitatively for the majority of configurations realized with different choices of the model parameters. Moreover, discrepancies between the results from the Hubbard model and the exact solution can be attributed to the design of the Hubbard-type model itself and are not mere artifacts resulting from the choice of parameters used in the model calculations. Hence, the results of the calculations yield some general indications for the construction of Hubbard-type models used to describe correlated subspace, which can help to design more sophisticated model setups or to improve *ab initio* calculations based on Hubbard-type models. In the construction of these models, the following aspects should be considered carefully.

If the atomic orbitals in the correlated subspace do not hybridize strongly with other orbitals not contained in the subspace, the Hubbard model can yield an accurate approximation for the exact many-body spectrum of the subspace. This approximation even becomes exact if the hybridization is zero. It is important to realize that the hybridization can also be influenced indirectly by the strength of the interaction between the particles in the subspace. For example, if the on-site Coulomb interaction in the correlated subspace of the toy model is of the same size as the energy difference between single-particle energies of orbitals inside and outside of the subspace, the linear combinations of the atomic orbitals yielding the exact many-body states contain large contribution from all these orbitals, even if the hopping matrix elements between the orbitals itself are small.

In this case, the many-body states and the corresponding eigenvalue spectrum cannot be reproduced by a Hubbard-model based approach taking into account only the states of the subspace.

Secondly, the excitation energies obtained from the Hubbard model will only resemble the exact many-body excitation energies if all mean-field type contributions contained in the Hamiltonian of the whole  $N$ -electron system are properly taken into account in the construction of the the Hubbard Hamiltonian. For example, charges not contained in the subspace described by the Hubbard model yield a contribution to the Hartree potential felt by the electrons in the subspace. Since the two-particle term of the Hubbard Hamiltonian only captures the interaction between particles in the subspace, this contribution to the Hartree potential has to be included in the one-particle term of the Hamiltonian. The technique introduced here incorporates these contributions to the Hartree potential into the one-particle term of the Hubbard Hamiltonian. In principle, the procedure could be generalized to incorporate the effect of any single-particle potential into the one-particle term. However, this design of the one-particle term comes at a price: by construction, it incorporates all contributions to the Hartree potential including those from interactions between the charges in the subspace. The latter ones are also accounted for by the two-particle term of the Hubbard model and have to be subtracted. Otherwise, they would be taken into account twice in the calculation. From the above considerations, it is, in principle, clear which contributions have to be subtracted. However, even for the simple toy model the expression for the double-counting correction cannot be evaluated exactly as soon as the orbitals in the subspace hybridize with orbitals that are not contained in the subspace. The model calculations presented here clearly demonstrate that the capability of the Hubbard model to reproduce the exact excitation energies of the many-body spectrum of the subspace largely depends on the treatment of the double-counting correction.

Last but not least, the treatment of interactions between particles in the subspace can lead to differences in the calculated spectra. In reference [84], an expression for the effective interaction between two particles in a subspace was derived, which is, in general, frequency dependent. However, the neglect of this frequency dependence is inevitable in the construction of the Hubbard Hamiltonian which therefore will only yield accurate results if the frequency dependence is small. In the model calculations presented here, the exact, frequency-dependent interaction between two particles in a subspace was calculated for different choices of the model parameters. It was shown that the frequency dependence of the screened interaction is influenced by the overlap of the single-particle orbitals and also by the size of the Coulomb integrals. Hence, the specific properties of each electronic system determine if the frequency dependence is negligible or not.

In summary, the Hubbard model can yield an accurate description of the spectrum of a correlated subspace if the hybridization between the orbitals inside and outside the subspace is small. If the hybridization is too strong, the subspace could be augmented such that all orbitals with a large overlap are contained. In addition, a well-thought-out double-counting correction has to be designed if the Hubbard model is to reproduce the exact eigenvalue spectrum of the many-body solution in the subspace quantitatively. Finally, if the frequency dependence of the screened interaction is strong, the spectrum obtained from the Hubbard model will only yield a poor approximation to the exact density of states of the subspace. This problem might as well be circumvented by changing the definition of the subspace. However, if the frequency dependence is crucial for the accurate description of the problem at hand, other theoretical concepts like the Green function or the path integral formalism have to be employed, which naturally incorporate the frequency dependence of the interaction.

The goals of this thesis were a) to explore the structure-composition-properties relation in complex perovskite transition-metal oxides from the electronic structure point of view employing state-of-the-art first-principle methods based on density-functional theory (DFT) and the GW approximation (GWA), and b) to investigate the limitation of model approaches, in particular the Hubbard model, frequently used to analyze the electronic structure of materials where the system size or the strength of the electron-electron correlation hamper the applicability of *ab initio* schemes. The findings of the investigations are discussed and summarized in this chapter.

The established success of DFT-based schemes originates from their wide range of applicability in electronic structure calculations for the ground-state properties of real materials and their capability to predict the electronic structure of new materials thus meeting the demands of modern, intelligent materials design. Moreover, the combination of these approaches with the GWA, a Green-function technique based on many-body perturbation theory, has emerged as the method of choice to investigate the single-particle excitation spectra of solids. Throughout this work, the FLAPW method is used for all first-principles calculations. As an all-electron approach, this method is particularly suitable to describe multicomponent materials comprising transition metals or rare earths such as the perovskite transition-metal oxides. Furthermore, it is considered the most precise computational scheme in solid state physics today to calculate the electronic structure from first principles.

This versatile technique was first applied in GW calculations to a series of prototypical perovskite transition-metal oxides including the ferroelectrics BaTiO<sub>3</sub> and PbTiO<sub>3</sub>, the antiferroelectrics PbZrO<sub>3</sub> and PbHfO<sub>3</sub>, the high- $\kappa$  dielectrics BaZrO<sub>3</sub> and BaHfO<sub>3</sub> as well as SrTiO<sub>3</sub> and CaTiO<sub>3</sub>, which are all predicted to be

insulating in agreement with experimental data. A comparison of the band gaps obtained from GW calculations for the room-temperature crystal phases with optical gaps taken from experiment shows good agreement for all compounds. It was also demonstrated that small distortions from the high-temperature cubic crystal phases yielding the room-temperature crystal structures lead to significant quantitative changes of the band gaps. This emphasizes the necessity to consider the correct room-temperature crystal structure in electronic structure calculations if the results are to be compared with experimental data. On the other hand, the energies of high-lying core states are little affected by the room-temperature distortions of the crystal structure. The energy corrections obtained from the GWA for these states are small and the results resemble those from DFT calculations. Good agreement with experimental data is attained as well.

As the chemical composition of the above perovskite transition-metal oxides is similar, changes in the electronic structure obtained for the high-temperature cubic crystal phases with respect to changes in the composition of the compounds were also investigated in this work. The valence bands of all compounds are composed of oxygen 2p states and the low-lying conduction bands are composed of transition metal d states except for  $\text{PbZrO}_3$  and  $\text{PbHfO}_3$  where they are composed of Pb 6p states. Thus, the fundamental band gaps of  $\text{CaTiO}_3$ ,  $\text{SrTiO}_3$ , and  $\text{BaTiO}_3$  are very close. The band gaps of  $\text{BaZrO}_3$  and  $\text{BaHfO}_3$  are also similar but much larger than the one of  $\text{BaTiO}_3$ , because the d states of Zr and Hf are less tightly bound than those of Ti while the chemical and physical properties of Zr and Hf are virtually identical due to the lanthanide contraction. In contrast, the size of the band gaps of  $\text{PbTiO}_3$ ,  $\text{PbZrO}_3$ , and  $\text{PbHfO}_3$  are again comparable, because the Ti 3d and the Pb 6p states forming the lowest unoccupied states in these materials are located roughly at the same energies.

Secondly, GW calculations were carried out for the three compounds  $\text{LaCrO}_3$ ,  $\text{LaMnO}_3$ , and  $\text{LaFeO}_3$ . In the three band insulators, the electron correlation is considered to be enhanced due to the partial filling of the d bands of the transition metals. The partial filling also leads to the formation of finite spin-magnetic moments at the transition-metal sites that order antiferromagnetically. Results from DFT calculations obtained from the generalized-gradient approximation employing the PBE functional or from calculations using the hybrid functional HSE are investigated as starting points for many-body perturbation theory. The size of the magnetic moments and the fundamental band gaps are underestimated in PBE calculations. If the HSE functional is used instead, the magnetic moments are improved with respect to experimental data but the band gaps are systematically overestimated. Nevertheless, the HSE results yield a good starting point to employ the GWA in the case of  $\text{LaCrO}_3$  allowing to quantitatively reproduce the fundamental band gap as well as photo-emission spectra. For  $\text{LaMnO}_3$  and  $\text{LaFeO}_3$ , the calculated spectra and band gaps are in better agreement with ex-

perimental data if the PBE results are used as starting point for GW calculations. However, the band gap of  $\text{LaFeO}_3$  is still slightly underestimated.

In summary, the single-shot GW approximation based on PBE or HSE results from DFT calculations employing the FLAPW method substantially improves the band gaps and photo-emission spectra obtained from DFT calculations for all perovskite transition-metal oxides investigated in this work. Furthermore, it yields good agreement with experimental data apart from minor discrepancies. Small deviations can result from approximations inherent to the *ab initio* scheme, e.g., the expression used to approximate the exchange-correlation energy in DFT calculations or the neglect of vertex corrections in the GWA. For example, the band gaps of  $\text{LaMnO}_3$  and  $\text{LaFeO}_3$  obtained from calculations employing the HSE functional are strongly overestimated such that the influence of screening in a subsequent GW calculation is underestimated. In contrast, the band gap of  $\text{LaFeO}_3$  predicted by PBE calculations is much too small. This leads to an overestimation of the effect of screening. These examples demonstrate that the single-shot GW approach depends on the DFT starting point, whose accuracy is determined by the level of approximation used in the DFT calculation. A scheme in which the GW self-energy is determined self-consistently could remove this deficiency of the present approach. Furthermore, the necessity to include vertex corrections describing excitonic effects in calculations for the dielectric function has been discussed in the investigation of the absorption spectra of  $\text{SrTiO}_3$  and  $\text{BaTiO}_3$ .

Last but not least, it was demonstrated that spin-orbit coupling (SOC) has a sizeable effect on the conduction band spectrum of  $\text{PbTiO}_3$  and, especially,  $\text{PbZrO}_3$  and  $\text{PbHfO}_3$  due to severe changes in the energies of the Pb 6p states. However, GW calculations for complex oxide materials like the perovskite transition-metal oxides, which fully incorporate the SOC, are not feasible at present. Self-consistent GW calculations as well as the inclusion of vertex corrections and the SOC in the GWA should thus be the subject of future investigations in first-principles calculations for perovskite transition-metal oxides.

Finally, the limitation of the applicability of the Hubbard model in simulations of the electronic structure of real materials is investigated. The Hubbard model allows to gain insight into the electronic structure of strongly correlated materials as it takes the on-site term of the electron-electron interaction explicitly into account. As the explicit treatment of the electron-electron interaction is numerically expensive, only a small part of the whole excitation spectrum of a real material can be simulated. This raises the question how the parameters of the Hubbard model have to be determined in order to yield the best approximation for this particular part of the spectrum.

A test system was constructed to simulate partially filled single-particle states

located close in energy to fully occupied or empty states. The exact many-body excitation spectrum, which is obtained from solutions of the N-electron Schrödinger equations employing the particle-number formalism, is compared to the spectrum simulated by a Hubbard model for a given subspace of the full test system. The Hubbard model is constructed in such a way that the effective single-particle term exactly reproduces all single-particle contributions to the Hamiltonian of the N-electron Schrödinger equation. The electron-electron interaction term of the model comprises the screened interaction obtained from constraint RPA (cRPA). In principle, cRPA allows to calculate the exact interaction strength between particles in any given subspace of the test system as the exact many-body response function of the test system can be determined. However, the frequency dependence of the screened interaction has to be neglected in the construction of the Hubbard model.

It is illustrated that the Hubbard model qualitatively reproduces the exact spectrum of the subspace for large parts of the parameter space. However, the spectrum is only reproduced quantitatively if the states defining the subspace do not hybridize with those states not contained in the subspace. In particular, the simulation of the spectrum becomes increasingly inaccurate if the hybridization gets large even if the electron-electron interaction between charges inside and outside the subspace are manually set to zero. In addition, the neglect of the frequency dependence of the screened interaction may cause further deviations. In summary, a Hubbard model of a subspace that is well separated in energy from states outside the subspace may yield an accurate approximation for the spectrum of the subspace. If the hybridization between states inside and outside the subspace is large, these states should be included in the construction of the Hubbard model to obtain a satisfactory description of the exact spectrum.

## A.1. Hedin Equations

In this section, the Hedin equations [13] to determine the self-energy are derived using the Schwinger functional derivative method [68, 69]. To obtain the self-energy a time-dependent, external potential  $\phi(\mathbf{r}_1, t_1)$  is introduced as a mathematical tool. It is set to zero once the self-energy is obtained. Furthermore, the interaction (or Dirac) representation of the field operators is used. Consequently, the Heisenberg operators in the representation of the N-electron Hamiltonian, eq. (2.64), have to be replaced by the corresponding Dirac operators  $\hat{\psi}_D^\dagger, \hat{\psi}_D$  and the following term has to be added to the Hamiltonian

$$\hat{\phi}(\tau) = \int d^3r \phi(\mathbf{r}, \tau) \hat{\psi}_D^\dagger(\mathbf{r}, \tau) \hat{\psi}_D(\mathbf{r}, \tau). \quad (\text{A.1})$$

The Dirac operators are related to the Heisenberg operators via

$$\hat{\psi}(\mathbf{r}, t) = \hat{U}^\dagger(t, 0) \hat{\psi}_D(\mathbf{r}, t) \hat{U}(t, 0) \quad (\text{A.2})$$

with the time evolution operator  $\hat{U}$  given by

$$\hat{U}(t, t_0) = \hat{T} \exp \left[ -i \int_{t_0}^t d\tau \hat{\phi}(\tau) \right]. \quad (\text{A.3})$$

To simplify the notation, the sets of space-time coordinates  $(\mathbf{r}_1, t_1)$ ,  $(\mathbf{r}_2, t_2)$  and so on are denoted from now on by natural numbers 1, 2 etc. and the following

abbreviations are used:

$$\delta(12) = \delta(\mathbf{r}_1 - \mathbf{r}_2)\delta(t_1 - t_2), \quad (\text{A.4})$$

$$v(12) = v(\mathbf{r}_1 - \mathbf{r}_2)\delta(t_1 - t_2), \quad (\text{A.5})$$

$$\int d1 = \int d^3r_1 \int dt_1, \quad (\text{A.6})$$

$$1^+ = (\mathbf{r}_1, t_1 + \eta). \quad (\text{A.7})$$

In the interaction representation the Green function (2.56) is given by

$$G(12) = -i \frac{\langle N, 0 | \hat{T} [\hat{U}(\infty, -\infty) \hat{\psi}_D^\dagger(1) \hat{\psi}_D(2)] | N, 0 \rangle}{\langle N, 0 | \hat{U}(\infty, -\infty) | N, 0 \rangle}. \quad (\text{A.8})$$

Taking the functional derivative of  $G$  with respect to  $\phi$  leads to

$$\frac{\delta G(12)}{\delta \phi(3)} = G(12)G(33^+) - G_2(1323^+), \quad (\text{A.9})$$

which can be solved for the two-particle Green function. The second term on the right-hand side in the equation of motion of the quasiparticle Green function, eq. (2.66), is thus replaced by

$$\begin{aligned} -i \int v(1^+3)G_2(1323^+) d3 &= -i \underbrace{\left( \int v(13)G(33^+) d3 \right)}_{V^H(1)} G(12) + i \int v(1^+3) \frac{\delta G(1,2)}{\delta \phi(3)} d3 \\ &= V^H(1)G(12) + \int \Sigma(13)G(32) d3. \end{aligned} \quad (\text{A.10})$$

The first term on the right-hand side is identified as the product of the Hartree potential  $V^H$  and  $G$  using the identity  $n(1) \equiv -iG(11^+)$ . In the second term, the self-energy was introduced that can be written as

$$\begin{aligned} \Sigma(12) &= i \iint v(1^+3) \frac{\delta G(14)}{\delta \phi(3)} G^{-1}(42) d3 d4 \\ &= -i \iint v(1^+3)G(14) \frac{\delta G^{-1}(42)}{\delta \phi(3)} d3 d4 \\ &= i \iint W(1^+3)G(14)\Gamma(42;3) d3 d4. \end{aligned} \quad (\text{A.11})$$

From the first to the second line, the following identity was exploited

$$\frac{\delta}{\delta \phi(4)} \int G(13)^{-1}G(32) d3 = \int d4 \left[ G(13) \frac{\delta G^{-1}(32)}{\delta \phi(4)} + \frac{\delta G(13)}{\delta \phi(4)} G^{-1}(32) \right] = 0, \quad (\text{A.12})$$

while in the third line two quantities were introduced: the screened interaction  $W$  and the vertex function  $\Gamma$ . The latter is defined as functional derivative of the inverse Green function with respect to the effective potential

$$\Gamma(12;3) = - \left. \frac{\delta G^{-1}(12)}{\delta \phi^{\text{eff}}(3)} \right|_{\phi=0}, \quad (\text{A.13})$$

and  $\phi^{\text{eff}}$  is the sum of the potential  $\phi$  and the Hartree potential. It can be expressed via the response function  $R$

$$\phi^{\text{eff}}(1) = \phi(1) + V^{\text{H}}(1) = \phi(1) + \iint v(13) \underbrace{\left. \frac{\delta n(3)}{\delta \phi(2)} \right|_{\phi=0}}_{\equiv R(32)} \phi(2) d2 d3, \quad (\text{A.14})$$

which in turn can be written as a geometric series using the polarization function  $P$

$$R(12) = P(12) + \iint P(13)v(34)R(42) d3 d4. \quad (\text{A.15})$$

The polarization function  $P$  describes reactions of the density to changes in the effective potential

$$P(12) = \left. \frac{\delta n(1)}{\delta \phi^{\text{eff}}(2)} \right|_{\phi=0}. \quad (\text{A.16})$$

With the help of  $R$ , the inverse dielectric function can be written as a geometric series as well

$$\varepsilon^{-1}(12) = \left. \frac{\delta \phi^{\text{eff}}(2)}{\delta \phi(2)} \right|_{\phi=0} = \delta(12) + \int v(13)R(32) d3, \quad (\text{A.17})$$

whose inversion yields

$$\varepsilon(12) = \delta(12) - \int v(13)P(32) d3. \quad (\text{A.18})$$

Finally, an expression for the screened interaction is given by

$$W(12) = \int \varepsilon^{-1}(13)v(32) d3 = v(12) + \iint v(13)P(34)W(42) d3 d4. \quad (\text{A.19})$$

The screened potential  $W$  is the potential felt by a test charge at position 2, which is generated by a quasiparticle at position 1.

To complete the derivation of the Hedin equations, the following expression for the inverse Green function is obtained from the Dyson equation (2.74)

$$G^{-1}(12) = G_{\text{H}}^{-1}(12) - \Sigma(12). \quad (\text{A.20})$$

This can be used to rewrite the equation for the vertex function as

$$\Gamma(12;3) = \delta(12)\delta(13) + \frac{\delta\Sigma(12)}{\delta\phi^{\text{eff}}(3)}, \quad (\text{A.21})$$

and with the identity

$$\begin{aligned} \frac{\delta G(12)}{\delta\phi^{\text{eff}}(3)} &= \frac{\delta}{\delta\phi^{\text{eff}}(3)} \iint G(14)G^{-1}(45)G(52) d4 d5 \\ &= 2\frac{\delta G(12)}{\delta\phi^{\text{eff}}(3)} + \iint G(14)\frac{\delta G^{-1}(45)}{\delta\phi^{\text{eff}}(3)}G(52) d4 d5 \end{aligned} \quad (\text{A.22})$$

the vertex function becomes

$$\Gamma(12;3) = \delta(12)\delta(13) - \iiint \frac{\delta\Sigma(12)}{\delta G(45)}G(56)\Gamma(67;3)G(74) d4 d5 d6 d7 \quad (\text{A.23})$$

and analogously

$$P(12) = -i\frac{\delta G(11^+)}{\delta\phi^{\text{eff}}(2)} = -i\iint G(13)\Gamma(34;2)G(41) d3 d4. \quad (\text{A.24})$$

The equations (A.11), (A.19), (A.23), (A.24) together with the Dyson equation (2.74) constitute Hedin's set of integro-differential equations, whose self-consistent solution, in principle, solves the many-electron problem exactly.

## A.2. Vertex Correction from $v^{\text{xc}}$ in the GWA

Using the Kohn-Sham Green function  $G_0$ , eq. (2.82), instead of the Hartree Green function  $G_H$  in the first iteration of the Hedin equations changes the vertex function  $\Gamma$  in eq. (A.23), since the exchange-correlation potential constitutes a static but non-vanishing self-energy

$$\Sigma_0(1,2) = \delta(12)v^{\text{xc}}(1). \quad (\text{A.25})$$

It was shown by Del Sole, Reining, and Godby [205] that the first iteration of the Hedin equations still produces a self-energy of the GW form

$$\Sigma(12) = iG_0(12)\tilde{W}(12) \quad (\text{A.26})$$

if the screened interaction is renormalized yielding an effective screened interaction given, in operator form, by

$$\tilde{W} = v[1 - P_0(v + K^{\text{xc}})]^{-1}, \quad (\text{A.27})$$

where the exchange-correlation kernel  $K^{xc}$  is given by the functional derivative of  $v^{xc}$  with respect to the single-particle density

$$K^{xc}(12) = \frac{\partial v^{xc}(1)}{\partial n(2)} \quad (\text{A.28})$$

and  $P_0$  is the polarization function in the RPA, eq. (2.78).

Del Sole *et al.* employed the self-energy obtained from eq. (A.26) in a band structure calculation for Si and found only little changes in the relative positions of the quasiparticle bands. Morris *et al.* [70] used the same scheme to study a variety of physical properties of some closed-shell atoms and jellium. Their calculations even show that inclusion of the vertex corrections yield results inferior to those obtained from the GW approximation without vertex correction. It was argued that the reason for the failure of the LDA starting point with the inclusion of the theoretically consistent vertex lies within the self-interaction error in the LDA. The self interaction should lead to correcting terms in the diagrammatic expansion of the self-energy. Therefore, inclusion of higher-order terms might remedy the reported unphysical behavior of the approximation for  $\Sigma$  given by eq. (A.26). Earlier works [74, 76] employed vertex corrections by systematically adding higher-order diagrams in the calculation of the RPA polarizability and the GW self-energy and confirm the results of reference [205].



# APPENDIX B

---

## INPUT PARAMETERS

The input parameters used in calculations with FLEUR and SPEX for all compounds investigated in this work are tabulated in this section. The notation used in the tables is explained below.

To improve the representation of semicore levels and unoccupied states LOs for each atom in the unit cell can be added to the LAPW basis and the MPB. The LOs are tabulated according to their band index and angular moment, for example the notation  $s_{\underline{n},m}$  connotes that two LOs describing an  $s$  state were used, where the first one is located in band  $n$  and the second one in band  $m$ , respectively. An underlined number indicates that the corresponding LO is used to describe a semicore level. All other LOs are located in the conduction bands.

For each input parameter used in a SPEX calculation a keyword is defined. The keyword together with the parameter(s) are passed along to the SPEX code, which interprets the data on the basis of the definition of the keyword. All input parameters used in SPEX calculations are tabulated with respect to the corresponding keywords, which are explained in the following. A complete list of all keywords can be found in the documentation of the SPEX code [18]. All energies are measured in Hartree (htr).

Keyword	Argument	Definition
GCUT	$x$	Plane-wave cutoff $G'_{\max}$ for the IPWs of the MPB measured in $\text{bohr}^{-1}$ (cf. section 5.1.1)
LCUT	$n$	Cutoff $L_{\max}$ (one for each atom) for the angular moment of the radial functions of the MPB (cf. section 5.1.1)

Keyword	Argument	Definition
BANDS	n	Bands per atom in the unit cell <i>BANDS is not a regular SPEX keyword but similar to the keyword NBANDS (cf. documentation [18]).</i>
BZ	$N_x N_y N_z$	Defines a $\mathbf{k}$ -point set $N_x \times N_y \times N_z$ according to (3.41).
MB	x	Corresponds to the reformulated cutoff value $(4\pi/v_{\min})^{1/2}$ introduced in section 5.1.1, which is measured in bohr <sup>-1</sup> .
SEL	n, m	Determines the pairs of LAPW radial functions $u_{a l 0}^\sigma(\mathbf{r})$ for each atom whose products form the MT functions of the MPB. The integer number n corresponds to the maximum l quantum number of the radial functions used in the construction of the MPB radial functions to represent products of occupied states, m plays the same role in the representation of the unoccupied states. <i>SEL is not a regular SPEX keyword but is similar to the actual keyword SELECT (cf. documentation [18]).</i>
FSPEC	x y	Defines the exponential frequency mesh for the Hilbert transformation in eq. (3.37). In this work, the argument x denotes the first nonzero mesh point and the second argument is a factor defining the positions of the other mesh points $f_i$ according to $y = (f_{i+1} - f_i)/(f_i - f_{i-1})$ .
MESH	n + m x	Defines an imaginary frequency mesh, which is used e.g. to calculate the polarization function in eq. (3.37). The total number of mesh points is n + m, where the n points are distributed evenly between zero and the last frequency point x. An additional number of m points can be added to obtain a finer sampling of the frequencies close to zero.
CONTOUR	D d	In this work, D is chosen to be a range that defines an equidistant mesh (relative to the KS energy) used for the contour integration in eq. (3.40). The second argument d defines the step size of an equidistant mesh for the screened interaction.



**SrTiO<sub>3</sub>**

cubic phase at T = 296K [108]

lattice const. (bohr)       $a = 7.372$   
atoms per unit cell      5

**FLEUR** $G_{\max}$  5.8 bohr<sup>-1</sup>

atom	$l_{\max}$	MT radius	local orbitals
Sr	12	3.00 bohr	s <u>4</u> ,6,7,8,9,10
			p <u>4</u> ,6,7,8,9,10
			d 5,6,7,8,9,10
			f 5,6,7,8,9,10
Ti	8	2.00 bohr	s <u>3</u> ,5,6,7
			p <u>3</u> ,5,6,7
			d 4,5,6,7,8
			f 5,6,7,8
O	6	1.65 bohr	s 3,4,5
			p 3,4,5,6
			d 4,5,6
			f 5,6

**SPEX**

GCUT            4.0 bohr<sup>-1</sup>  
BANDS           200  
BZ                 $6 \times 6 \times 6$   
MB                5.5 bohr<sup>-1</sup>  
FSPEC           0.01 htr 1.05  
MESH            6+3 10.0 htr  
CONTOUR       {-0.1..0.1,0.01}; 0.01 (htr)

atom	LCUT	SEL	local orbitals
Sr	6	4,4	s <u>4</u> ,6    p <u>4</u> ,6    d 5    f 5
Ti	6	4,4	s <u>3</u> ,5    p <u>3</u> ,5    d 4    f 5
O	6	4,4	s 3      p 3      d 4    f 5

<b>BaTiO<sub>3</sub></b>						
cubic phase at T = 474.15K [206]				tetragonal phase at T = 300K [109]		
<b>lattice const. (bohr)</b>		a = 7.566		a = 7.542; c = 7.625		
<b>atoms per unit cell</b>		5		5		
<b>FLEUR</b>				<b>FLEUR</b>		
<b>G<sub>max</sub></b>		5.9 bohr <sup>-1</sup>		5.6 bohr <sup>-1</sup>		
<b>atom</b>	<b>l<sub>max</sub></b>	<b>MT radius</b>	<b>local orbitals</b>			
Ba	12	3.00 bohr	s <u>5</u> ,7,8,9,10,11 p <u>5</u> ,7,8,9,10,11 d 6,7,8,9,10,11 f 6,7,8,9,10			
Ti	8	2.05 bohr	s <u>3</u> ,5,6,7 p <u>3</u> ,5,6,7 d 4,5,6,7,8 f 5,6,7,8			
O	8	1.85 bohr	s 3,4,5 p 3,4,5,6 d 4,5,6 f 5,6			
<b>SPEX</b>				<b>SPEX</b>		
<b>GCUT</b>		4.2 bohr <sup>-1</sup>		4.2 bohr <sup>-1</sup>		
<b>BANDS</b>		220		200		
<b>BZ</b>		4 × 4 × 4		4 × 4 × 4		
<b>MB</b>		6.5 bohr <sup>-1</sup>		5.5 bohr <sup>-1</sup>		
<b>FSPEC</b>		0.01 htr 1.05		0.01 htr 1.05		
<b>MESH</b>		6+3 10.0 htr		6+3 10.0 htr		
<b>CONTOUR</b>		{-0.1..0.1,0.01}; 0.01 (htr)		{-0.1..0.1,0.01}; 0.01 (htr)		
<b>atom</b>	<b>LCUT</b>	<b>SEL</b>	<b>local orbitals</b>			
Ba	6	4,4	s <u>5</u> ,7	p <u>5</u> ,7	d 6	f 6
Ti	6	4,4	s <u>3</u> ,5	p <u>3</u> ,5	d 4	f 5
O	6	4,4	s 3	p 3	d 4	f 5
Ba	7	4,4	s <u>5</u> ,7	p <u>5</u> ,7	d 6,7	f 6
Ti	7	4,4	s <u>3</u>	p <u>3</u>	d 4	
O	5	4,4	s 3	p 3		

**BaZrO<sub>3</sub>**

cubic phase at T = 298K [110]

lattice const. (bohr)       $a = 7.926$   
atoms per unit cell      5

## FLEUR

 $G_{\max} \quad 5.8 \text{ bohr}^{-1}$ 

atom	$l_{\max}$	MT radius	local orbitals
Ba	14	3.00 bohr	s <u>5</u> ,7,8,9,10,11 p <u>5</u> ,7,8,9,10,11 d 6,7,8,9,10,11 f 5,6,7,8,9,10
Zr	12	2.15 bohr	s <u>4</u> ,6,7,8 p <u>4</u> ,6,7,8 d 5,6,7,8 f 5,6,7,8
O	8	1.80 bohr	s 3,4,5 p 3,4,5,6 d 4,5,6 f 5,6

## SPEX

GCUT             $3.8 \text{ bohr}^{-1}$   
BANDS           240  
BZ                 $6 \times 6 \times 6$   
MB                 $6.0 \text{ bohr}^{-1}$   
FSPEC           0.01 htr    1.05  
MESH            6+3    10.0 htr  
CONTOUR        $\{-0.1..0.1,0.01\}; 0.01 \text{ (htr)}$

atom	LCUT	SEL	local orbitals
Ba	7	4,4	s <u>5</u> p <u>5</u>
Zr	7	4,4	s <u>4</u> p <u>4</u>
O	7	4,4	

**BaHfO<sub>3</sub>**

cubic phase at T = 300K [111]

lattice const. (bohr)      a = 7.882

atoms per unit cell      5

## FLEUR

G<sub>max</sub>    6.05 bohr<sup>-1</sup>

atom	l <sub>max</sub>	MT radius	local orbitals
Ba	14	3.00 bohr	s <u>5</u> ,7,8,9,10,11 p <u>5</u> ,7,8,9,10,11 d 6,7,8,9,10,11 f 5,6,7,8,9,10
Hf	12	2.13 bohr	s <u>5</u> ,7,8,9 p <u>5</u> ,7,8,9 d 6,7,8,9 f <u>4</u> ,6,7,8,9
O	8	1.80 bohr	s 3,4,5 p 3,4,5,6 d 4,5,6 f 5,6

## SPEX

GCUT      3.8 bohr<sup>-1</sup>

BANDS      220

BZ      6 × 6 × 6

MB      6.0 bohr<sup>-1</sup>

FSPEC      0.01 htr    1.05

MESH      6+3    10.0 htr

CONTOUR    {-0.1..0.1,0.01}; 0.01 (htr)

atom	LCUT	SEL	local orbitals
Ba	7	4,4	s <u>5</u> ,7    p <u>5</u> ,7    d 6    f 5
Hf	7	4,4	s <u>5</u> ,7    p <u>5</u> ,7    d 6    f <u>4</u> ,6
O	7	4,4	s 3      p 3      d 4    f 5

<b>PbTiO<sub>3</sub></b>												
cubic phase at T = 823K [163]				tetragonal phase at T = 293K [112]								
<b>lattice const. (bohr)</b>		a = 7.426		a = 7.374; c = 7.831								
<b>atoms per unit cell</b>		5		5								
<b>FLEUR</b>				<b>FLEUR</b>								
<b>G<sub>max</sub></b>		6.0 bohr <sup>-1</sup>		5.6 bohr <sup>-1</sup>								
<b>atom</b>	<b>l<sub>max</sub></b>	<b>MT radius</b>	<b>local orbitals</b>			<b>l<sub>max</sub></b>	<b>MT radius</b>	<b>local orbitals</b>				
Pb	14	2.05 bohr	s 7,8,9,10,11 p 7,8,9,10,11 d 6,7,8,9,10,11 f 6,7,8,9,10			12	3.00 bohr	s 7,8,9,10,11 p 7,8,9,10,11 d 6,7,8,9,10 f 6,7,8,9,10				
Ti	12	2.80 bohr	s <u>3</u> ,5,6,7 p <u>3</u> ,5,6,7 d 4,5,6,7,8 f 5,6,7,8			10	1.75 bohr	s <u>3</u> ,5,6,7 p <u>3</u> ,5,6,7 d 4,5,6,7 f 5,6,7				
O	10	1.65 bohr	s 3,4,5 p 3,4,5,6 d 4,5,6 f 5,6			8	1.55 bohr	s 3,4,5 p 3,4,5,6 d 4,5,6 f 5,6				
<b>SPEX</b>				<b>SPEX</b>								
<b>GCUT</b>		5.0 bohr <sup>-1</sup>		4.4 bohr <sup>-1</sup>								
<b>BANDS</b>		200		200								
<b>BZ</b>		4 × 4 × 4		4 × 4 × 4								
<b>MB</b>		6.5 bohr <sup>-1</sup>		6.5 bohr <sup>-1</sup>								
<b>FSPEC</b>		0.01 htr 1.05		0.01 htr 1.05								
<b>MESH</b>		6+3 10.0 htr		6+3 10.0 htr								
<b>CONTOUR</b>		{-0.1..0.1,0.01}; 0.01 (htr)		{-0.1..0.1,0.01}; 0.01 (htr)								
<b>atom</b>	<b>LCUT</b>	<b>SEL</b>	<b>local orbitals</b>			<b>LCUT</b>	<b>SEL</b>	<b>local orbitals</b>				
Pb	6	4,4	s 7	p 7	d 6	f 6	6	4,4	s 7	p 7	d 6,7	f 6
Ti	6	4,4	s <u>3</u> ,5	p <u>3</u> ,5	d 4	f 5	6	4,4	s <u>3</u>	p <u>3</u>	d 4	
O	6	2,3	s 3	p 3	d 4	f 5	5	2,3	s 3	p 3		





## B.2. Input parameters – part 2

Input parameters for FLEUR and SPEX calculations for the compounds presented in chapter 6 are listed below. Lattice constants and atomic positions were taken from experiment. The latter can be found in the according references and are not listed here.

For calculations employing hybrid functionals, an additional convergence parameter  $n_{\max}$  has been introduced in the implementation in FLEUR. Details can be found in reference [85]. For the HSE calculations presented in chapter 6,  $n_{\max}$  was set to 650 for  $\text{LaCrO}_3$  and  $\text{LaMnO}_3$  and to 700 for  $\text{LaFeO}_3$ .

---



---

### $\text{LaCrO}_3$

---

orthorhombic phase at  $T = 298\text{K}$  [115]

**lattice const. (bohr)**       $a = 10.356$ ;  $b = 14.664$ ;  $c = 10.424$

**atoms per unit cell**      20

---

### FLEUR

$G_{\max}$     4.2 bohr<sup>-1</sup>

atom	$l_{\max}$	MT radius	local orbitals			
La	12	2.80 bohr	s <u>5</u> ,7,8	p <u>5</u> ,7,8	d 6,7,8	f 5,6,7
Cr	8	2.28 bohr	s <u>3</u> ,5,6	p <u>3</u> ,5,6	d 4,5,6	f 5,6
O	6	1.31 bohr	s 3	p 3	d 4	

---

### SPEX

GCUT            3.0 bohr<sup>-1</sup>

BANDS            55

BZ                 $2 \times 2 \times 2$

MB                5.0 bohr<sup>-1</sup>

FSPEC            0.025 htr    1.05

MESH            6    10.0 htr

CONTOUR         $\{-0.1 \dots 0.1, 0.02\}$ ; 0.02 (htr)

atom	LCUT	SEL	local orbitals	
La	6	3,4	s <u>5</u>	p <u>5</u>
Cr	5	3,4	s <u>3</u>	p <u>3</u>
O	4	2,3		

---



---

---



---

**LaMnO<sub>3</sub>**


---

orthorhombic phase at T = 293K [116]

**lattice const. (bohr)**       $\alpha = 10.463$ ;  $b = 14.541$ ;  $c = 10.852$   
**atoms per unit cell**      20

---

**FLEUR**

**G<sub>max</sub>**    4.4 bohr<sup>-1</sup>

atom	$l_{\max}$	MT radius	local orbitals			
La	12	2.90 bohr	s <u>5</u> ,7,8	p <u>5</u> ,7,8	d 6,7,8	f 5,6,7
Mn	8	2.26 bohr	s <u>3</u> ,5,6	p <u>3</u> ,5,6	d 4,5,6	f 5,6
O	6	1.31 bohr	s 3	p 3	d 4	

---

**SPEX**

**GCUT**            2.9 bohr<sup>-1</sup>  
**BANDS**            52  
**BZ**                 $2 \times 2 \times 2$   
**MB**                4.8 bohr<sup>-1</sup>  
**FSPEC**            0.025 htr    1.05  
**MESH**            6    10.0 htr  
**CONTOUR**        {-0.1...0.1,0.02}; 0.02 (htr)

atom	LCUT	SEL	local orbitals	
La	6	3,4	s <u>5</u>	p <u>5</u>
Mn	5	3,4	s <u>3</u>	p <u>3</u>
O	4	2,3		

---



---

**LaFeO<sub>3</sub>**

orthorhombic phase at T = 293K [117]

**lattice const. (bohr)**      a = 10.512; b = 14.866; c = 10.493**atoms per unit cell**      20**FLEUR****G<sub>max</sub>**    4.4 bohr<sup>-1</sup>

<b>atom</b>	<b>l<sub>max</sub></b>	<b>MT radius</b>	<b>local orbitals</b>			
La	12	2.95 bohr	s <u>5</u> ,7,8	p <u>5</u> ,7,8	d 6,7,8	f 5,6,7
Fe	8	2.36 bohr	s <u>3</u> ,5,6	p <u>3</u> ,5,6	d 4,5,6	f 5,6
O	6	1.33 bohr	s 3	p 3		

**SPEX**GCUT            2.9 bohr<sup>-1</sup>

BANDS            50

BZ                2 × 2 × 2

MB                4.8 bohr<sup>-1</sup>

FSPEC            0.025 htr    1.05

MESH            6    10.0 htr

CONTOUR        0.1...0.1,0.02}; 0.02 (htr)

<b>atom</b>	<b>LCUT</b>	<b>SEL</b>	<b>local orbitals</b>	
La	6	3,4	s <u>5</u>	p <u>5</u>
Fe	5	3,4	s <u>3</u>	p <u>3</u>
O	4	2,3		



## APPENDIX C

### A CASE STUDY BEYOND THE GWA

#### C.1. Proof of formula (7.42)

A mathematical proof will be given here as to why the transformation matrix  $\mathbf{T}^d$  yields the effective Hartree Hamiltonian  $\tilde{\mathbf{H}}^H$  with the desired properties according to eq. (7.42) in section 7.1.2, chapter 7. In the following, the eigenvectors of the matrix  $\mathbf{H}^d$  are denoted by  $C_j^d = (c_{1j}, c_{2j})^T$  and the vectors  $(1, 0)^T$  and  $(0, 1)^T$  are labeled  $E_j, j = 1, 2$ . The matrix  $\mathbf{T}^d$  diagonalizing  $\mathbf{H}^d$  was already introduced in eq. (7.41). Then,  $\tilde{\mathbf{H}}^H$  also has the eigenvectors  $C_j^d$  and the desired eigenvalues  $\epsilon_j^d$ .

$$\tilde{\mathbf{H}}^H C_j^d \stackrel{(7.42)}{=} (\mathbf{T}^d)^{-1} \mathbf{D}^d \mathbf{T}^d C_j^d \quad (\text{C.1})$$

$$= (\mathbf{T}^d)^{-1} \mathbf{D}^d E_j \quad (\text{C.2})$$

$$= (\mathbf{T}^d)^{-1} \epsilon_j^d E_j \quad (\text{C.3})$$

$$= \epsilon_j^d (\mathbf{T}^d)^{-1} E_j \quad (\text{C.4})$$

$$= \epsilon_j^d C_j^d \quad (\text{C.5})$$

#### C.2. The lack of screening for $U_{II} = 0$

In subsection 7.2.1, it was claimed that there is no screening of the on-site Coulomb interaction in the subspace  $d$ , if the parameters  $t_I, t_{II}$  and  $U_I$  are non-zero but  $U_{II} = 0$ . If this is true, the only non-zero matrix elements of  $\mathbf{W}^T$  in the two-particle term of the Hubbard Hamiltonian (7.26) are identical to the matrix elements determined by the choice of  $U_I$ .

The elements of the matrix  $\mathbf{W}^r(\omega)$  of the screened interaction can be ordered in such a way, that the lower right  $(4 \times 4)$  block labeled  $(\mathbf{W}^r(\omega))_{22}$  contains all matrix element from projections onto the states in the d space

$$\mathbf{W}^r(\omega) = \begin{pmatrix} (\mathbf{W}^r(\omega))_{11} & (\mathbf{W}^r(\omega))_{12} \\ (\mathbf{W}^r(\omega))_{21} & (\mathbf{W}^r(\omega))_{22} \end{pmatrix}. \quad (\text{C.6})$$

Then, the elements of  $(\mathbf{W}^r(\omega))_{22}$  for  $\omega = 0$  define the matrix  $\mathbf{W}^r$  in the two-particle term of the Hubbard Hamiltonian. To calculate the matrix  $\mathbf{W}^r(\omega)$ , the matrix  $\mathbf{P}^r(\omega)$  of the polarization function defined in (7.31) has first to be determined, which in turn requires to solve the matrix equations yielding  $\mathbf{P}^d(\omega)$  and  $\mathbf{P}(\omega)$

$$\mathbf{P}^{(d)}(\omega) = \mathbf{R}^{(d)}(\omega) \cdot [\mathbf{1} + \mathbf{U} \cdot \mathbf{R}^{(d)}(\omega)]^{-1}. \quad (\text{C.7})$$

For the given choice of parameters, the matrices  $\mathbf{P}(\omega)$  and  $\mathbf{U}$  are of the following form

$$\mathbf{P}(\omega) = \begin{pmatrix} (\mathbf{P}(\omega))_{11} & (\mathbf{P}(\omega))_{12} \\ (\mathbf{P}(\omega))_{21} & (\mathbf{P}(\omega))_{22} \end{pmatrix}, \quad \mathbf{U} = \begin{pmatrix} \mathbf{0} & \mathbf{0} \\ \mathbf{0} & (\mathbf{U})_{22} \end{pmatrix}. \quad (\text{C.8})$$

Furthermore, the block matrix  $(\mathbf{P}(\omega))_{22}$  is identical to  $\mathbf{P}^d(\omega)$  and the only non-zero matrix elements of  $\mathbf{U}$  in  $(\mathbf{U})_{22}$  are determined by  $U_I$ . It follows immediately that  $\mathbf{P}^r(\omega)$  acquires the form

$$\mathbf{P}^r(\omega) = \begin{pmatrix} (\mathbf{P}(\omega))_{11} & (\mathbf{P}(\omega))_{12} \\ (\mathbf{P}(\omega))_{21} & \mathbf{0} \end{pmatrix} \quad (\text{C.9})$$

and

$$\begin{aligned} \mathbf{W}^r(\omega) &= [\mathbf{1} - \mathbf{U} \cdot \mathbf{P}^r(\omega)]^{-1} \cdot \mathbf{U} \\ &= \begin{pmatrix} \mathbf{1} & \mathbf{0} \\ -(\mathbf{U})_{22}(\mathbf{P}(\omega))_{21} & \mathbf{1} \end{pmatrix}^{-1} \cdot \begin{pmatrix} \mathbf{0} & \mathbf{0} \\ \mathbf{0} & (\mathbf{U})_{22} \end{pmatrix} = \mathbf{U}. \end{aligned} \quad (\text{C.10})$$

Consequently,  $\mathbf{W}^r = (\mathbf{U})_{22}$  for the given choice of parameters. Thus, the bare Coulomb interaction in d space is not screened.

## BIBLIOGRAPHY

- [1] *Properties and applications of perovskite-type oxides*, edited by L. G. Tejuca and J. L. G. Fierro (Marcel Dekker Inc., New York, 1992)
- [2] A. S. Bhalla, R. Guo, and R. Roy, *Mat. Res. Innovat.* **4**, 3 (2000)
- [3] E. Wainer and A. N. Salomon, *Elect. Rept. Titanium Alloy Manufacturing Co.* **8** (1942)
- [4] E. Wainer and A. N. Salomon, *Elect. Rept. Titanium Alloy Manufacturing Co.* **9** (1943)
- [5] S. Miyake and R. Ueda, *J. Phys. Soc. Jpn* **1**, 32 (1946)
- [6] B. M. Wul and I. M. Goldman, *Doklady Akademii Nauk S.S.S.R.* **46**, 177 (1945)
- [7] A. von Hippel, R. G. Breckenridge, F. G. Chesley, and L. Tisza, *J. Ind. Eng. Chem.* **38**, 1097 (1946)
- [8] B. M. Wul and I. M. Goldman, *Doklady Akademii Nauk S.S.S.R.* **51**, 21 (1946)
- [9] G. Shirane, K. Suzuki, and A. Takeda, *J. Phys. Soc. Jpn.* **7**, 12 (1952)
- [10] B. Jaffe, R. S. Roth, and S. Marzullo, *J. Appl. Phys.* **25**, 809 (1954)
- [11] J. G. Bednorz and K. A. Müller, *Z. Phys. B* **64**, 189 (1986)
- [12] P. Hohenberg and W. Kohn, *Phys. Rev.* **136**, B864 (1964)
- [13] L. Hedin, *Phys. Rev.* **139**, A796 (1965)
- [14] W. G. Aulbur, L. Jönsson, and J. W. Wilkins, *Solid State Physics* **54**, 1 (1999)
- [15] D. I. Bilc, R. Orlando, R. Shaltaf, G.-M. Rignanese, J. Íñiguez, and P. Ghosez, *Phys. Rev. B* **77**, 165107 (2008)
- [16] M. S. Kim and C.-H. Park, *J. Korean Phys. Soc.* **56**, 490 (2010)

- 
- [17] Y. Nohara, S. Yamamoto, and T. Fujiwara, *Phys. Rev. B* **79**, 195110 (2009)
- [18] "FLEUR: The Jülich FLAPW code family," <http://www.flapw.de>, last accessed on 2011-07-24
- [19] O. K. Andersen, *Phys. Rev. B* **12**, 3060 (1975)
- [20] C. Friedrich, S. Blügel, and A. Schindlmayr, *Phys. Rev. B* **81**, 125102 (2010)
- [21] T. Kotani and M. van Schilfhaarde, *Solid State Commun.* **121**, 461 (2002)
- [22] C. Friedrich, A. Schindlmayr, and S. Blügel, *Comput. Phys. Comm.* **180**, 347 (2009)
- [23] J. Heyd, G. E. Scuseria, and M. Ernzerhof, *J. Chem. Phys.* **118**, 8207 (2003)
- [24] A. V. Krukau, O. A. Vydrov, A. F. Izmaylov, and G. E. Scuseria, *J. Chem. Phys.* **125**, 224106 (2006)
- [25] J. P. Perdew, K. Burke, and M. Ernzerhof, *Phys. Rev. Lett.* **77**, 3865 (1996)
- [26] P. W. Anderson, *Phys. Rev.* **115**, 2 (1959)
- [27] J. Hubbard, *Proc. R. Soc. London* **276**, 238 (1963)
- [28] J. Hubbard, *Proc. R. Soc. London* **277**, 237 (1964)
- [29] J. Hubbard, *Proc. R. Soc. London* **281**, 401 (1964)
- [30] J. Kanamori, *Prog. Theor. Phys.* **30**, 275 (1963)
- [31] A. Georges, G. Kotliar, W. Krauth, and M. J. Rozenberg, *Rev. Mod. Phys.* **68**, 13 (1996)
- [32] V. I. Anisimov, A. I. Poteryaev, M. A. Korotin, A. O. Anokhin, and G. Kotliar, *J. Phys. Cond. Matt.* **9**, 7359 (1997)
- [33] K. Held, I. A. Nekrasov, N. Blümer, V. I. Anisimov, and D. Vollhardt, *Int. J. Mod. Phys. B* **15**, 2611 (2001)
- [34] E. Pavarini, S. Biermann, A. Poteryaev, A. I. Lichtenstein, A. Georges, and O. K. Andersen, *Phys. Rev. Lett.* **92**, 176403 (Apr 2004)
- [35] G. Kotliar, S. Y. Savrasov, K. Haule, V. S. Oudovenko, O. Parcollet, and C. A. Marianetti, *Rev. Mod. Phys.* **78**, 865 (2006)
- [36] M. Born and R. Oppenheimer, *Ann. der Physik* **389**, 457 (1927)
- [37] W. Kohn and L. J. Sham, *Phys. Rev.* **140**, A1133 (1965)
- [38] A. Seidl, A. Görling, P. Vogl, J. A. Majewski, and M. Levy, *Phys. Rev. B* **53**, 3764 (1996)
- [39] U. von Barth and L. Hedin, *J. Phys. C* **5**, 1629 (1972)
- [40] H. J. F. Jansen, *Phys. Rev. B* **38**, 8022 (1988)
- [41] L. L. Foldy and S. A. Wouthuysen, *Phys. Rev.* **78**, 29 (1950)

- [42] C. Elster, <http://www.phys.ohiou.edu/~elster/phys735> (2009), last accessed on 2011-01-22
- [43] D. D. Koelling and B. N. Harmon, *J. Phys. C* **10**, 3107 (1977)
- [44] C. Li, A. J. Freeman, H. J. F. Jansen, and C. L. Fu, *Phys. Rev. B* **42**, 5433 (1990)
- [45] J. C. Slater, *Phys. Rev.* **81**, 385 (1951)
- [46] D. M. Ceperley and B. J. Alder, *Phys. Rev. Lett.* **45**, 566 (1980)
- [47] J. P. Perdew and Y. Wang, *Phys. Rev. B* **33**, 8800 (1986)
- [48] D. C. Patton, D. V. Porezag, and M. R. Pederson, *Phys. Rev. B* **55**, 7454 (1997)
- [49] J. E. Jaffe, Z. Lin, and A. C. Hess, *Phys. Rev. B* **57**, 11834 (1998)
- [50] C.-O. Almbladh and U. von Barth, *Phys. Rev. B* **31**, 3231 (1985)
- [51] J. Paier, M. Marsman, K. Hummer, G. Kresse, I. C. Gerber, and J. G. Angyan, *J. Chem. Phys.* **124**, 154709 (2006)
- [52] B. I. Min, H. J. F. Jansen, T. Oguchi, and A. J. Freeman, *Phys. Rev. B* **34**, 369 (1986)
- [53] P. Larson and W. R. L. Lambrecht, *Phys. Rev. B* **74**, 085108 (2006)
- [54] S. Y. Savrasov and G. Kotliar, *Phys. Rev. Lett.* **90**, 056401 (2003)
- [55] J. P. Perdew and A. Zunger, *Phys. Rev. B* **23**, 5048 (1981)
- [56] P. Mori-Sanchez, A. J. Cohen, and W. Yang, *J. Chem. Phys.* **125**, 201102 (2006)
- [57] A. D. Becke, *J. Chem. Phys.* **104**, 1040 (1996)
- [58] J. Harris and R. O. Jones, *J. Phys. F* **4**, 1170 (1974)
- [59] D. C. Langreth and J. P. Perdew, *Solid State Commun.* **17**, 1425 (1975)
- [60] O. Gunnarsson and B. I. Lundqvist, *Phys. Rev. B* **13**, 4274 (1976)
- [61] J. P. Perdew, M. Ernzerhof, and K. Burke, *J. Chem. Phys.* **105**, 9982 (1996)
- [62] C. Møller and M. S. Plesset, *Phys. Rev.* **46**, 618 (1934)
- [63] C. Adamo and V. Barone, *J. Chem. Phys.* **110**, 6158 (1999)
- [64] A. L. Fetter and J. D. Walecka, *Quantum Theory of Many-Particle Systems* (McGraw-Hill San Francisco, 1971)
- [65] J. C. Inkson, *Many-Body Theory of Solids: an Introduction* (Plenum Press, New York, 1984)
- [66] W. Nolting, *Grundkurs theoretische Physik*, Vol. 7 (Springer-Verlag, Berlin, 2009)

- [67] G. C. Wick, *Phys. Rev.* **80**, 268 (1950)
- [68] J. Schwinger, *Proc. Natl. Acad. Sci. USA* **37**, 452 (1951)
- [69] P. C. Martin and J. Schwinger, *Phys. Rev.* **115**, 1342 (1959)
- [70] A. J. Morris, M. Stankovski, K. T. Delaney, P. Rinke, P. García-González, and R. W. Godby, *Phys. Rev. B* **76**, 155106 (2007)
- [71] W. von der Linden and P. Horsch, *Phys. Rev. B* **37**, 8351 (1988)
- [72] G. E. Engel and B. Farid, *Phys. Rev. B* **47**, 15931 (1993)
- [73] B. Holm and U. von Barth, *Phys. Rev. B* **57**, 2108 (1998)
- [74] E. L. Shirley, *Phys. Rev. B* **54**, 7758 (1996)
- [75] M. van Schilfgaarde, T. Kotani, and S. Faleev, *Phys. Rev. Lett.* **96**, 226402 (2006)
- [76] H. J. de Groot, R. T. M. Ummels, P. A. Bobbert, and W. van Haeringen, *Phys. Rev. B* **54**, 2374 (1996)
- [77] R. T. M. Ummels, P. A. Bobbert, and W. van Haeringen, *Phys. Rev. B* **57**, 11962 (1998)
- [78] D. F. DuBois, *Ann. Phys. (NY)* **8**, 24 (1959)
- [79] V. I. Anisimov, F. Aryasetiawan, and A. I. Lichtenstein, *J. Phys.: Condens. Matter* **9**, 767 (1997)
- [80] P. H. Dederichs, S. Blügel, R. Zeller, and H. Akai, *Phys. Rev. Lett.* **53**, 2512 (1984)
- [81] O. Gunnarsson, O. K. Andersen, O. Jepsen, and J. Zaanen, *Phys. Rev. B* **39**, 1708 (1989)
- [82] O. Gunnarsson, *Phys. Rev. B* **41**, 514 (1990)
- [83] V. I. Anisimov and O. Gunnarsson, *Phys. Rev. B* **43**, 7570 (1991)
- [84] F. Aryasetiawan, M. Imada, A. Georges, G. Kotliar, S. Biermann, and A. I. Lichtenstein, *Phys. Rev. B* **70**, 195104 (2004)
- [85] M. Betzinger, C. Friedrich, and S. Blügel, *Phys. Rev. B* **81**, 195117 (2010)
- [86] P. Kurz, *Non-Collinear Magnetism at Surfaces and in Ultrathin Films*, Ph.D. thesis, Aachen University (2000)
- [87] J. Korringa, *Physica* **13**, 392 (1947)
- [88] W. Kohn and N. Rostoker, *Phys. Rev.* **94**, 1111 (1954)
- [89] J. C. Slater, *Phys. Rev.* **51**, 846 (1937)
- [90] T. L. Loucks, *Augmented Plane Wave Method* (W. A. Benjamin, Inc., New York, 1967)
- [91] P. M. Marcus, *Int. J. Quantum Chem. Suppl.* **1**, 567 (1967)

- [92] D. D. Koelling and G. O. Arbman, *J. Phys. F* **5**, 2041 (1975)
- [93] D. J. Singh, *Plane Waves, Pseudopotentials and the LAPW Method* (Kluwer Academic Publ., 1994)
- [94] M. Betzinger, *Efficient Implementation of the Non-Local Exchange Potential within the FLAPW Method*, Master's thesis, Aachen University (2007)
- [95] D. Singh, *Phys. Rev. B* **43**, 6388 (1991)
- [96] E. E. Krasovskii, A. Yaresko, and V. Antonov, *J. Electron Spectrosc. Relat. Phenom.* **68**, 157 (1994)
- [97] L. Dagens and F. Perrot, *Phys. Rev. B* **5**, 641 (1972)
- [98] E. O. Kane, *J. Phys. Chem. Solids* **1**, 82 (1956)
- [99] H. Ehrenreich and M. H. Cohen, *Phys. Rev.* **115**, 786 (1959)
- [100] S. L. Adler, *Phys. Rev.* **126**, 413 (1962)
- [101] N. Wiser, *Phys. Rev.* **129**, 62 (1963)
- [102] G. Rose, *Journal für praktische Chemie* **19**, 459 (1840)
- [103] J. E. Huheey, *Inorganic Chemistry: Principles of Structure and Reactivity*, 4th ed. (HarperCollins College Publishers, New York, 1993)
- [104] M. Imada, A. Fujimori, and Y. Tokura, *Rev. Mod. Phys.* **70**, 1039 (1998)
- [105] V. M. Goldschmid, *Geochemische Verterlungsgesetze der Elemente* (Norske Videnskap, Oslo, 1927)
- [106] L. Pauling, *The nature of the chemical bond and the structure of molecules and crystals*, 3rd ed. (Cornell University Press, Ithaca NY, 1960)
- [107] M. Yashima and A. Roushown, *Solid State Ion.* **180**, 120 (2009)
- [108] Y. A. Abramov, V. G. Tsirelson, V. E. Zavodnik, S. A. Ivanov, and I. D. Brown, *Acta Crystallogr. Sect. B* **51**, 942 (1995)
- [109] G. H. Kwei, A. C. Lawson, S. J. L. Billinge, and S. W. Cheong, *J. Phys. Chem.* **97**, 2368 (1993)
- [110] I. Levin, T. G. Amos, S. M. Bell, L. Farber, T. A. Vanderah, R. S. Roth, and B. H. Toby, *J. Solid State Chem.* **175**, 170 (2003)
- [111] T. Maekawa, K. Kurosaki, and S. Yamanaka, *J. Allo. Comp.* **407**, 44 (2006)
- [112] R. Ranjan, A. K. Kalyani, R. Garg, and P. S. R. Krishna, *Solid State Commun.* **149**, 2098 (2009)
- [113] Y. Kuroiwa, Y. Terado, S. J. Kim, A. Sawada, Y. Yamamura, S. Aoyagi, E. Nishibori, M. Sakata, and M. Takata, *Jpn. J. Appl. Phys.* **44**, 7151 (2005)
- [114] H. Fujishita, A. Ogawaguchi, and S. Katano, *J. Phys. Soc. Jpn.* **77**, 064601 (2008)

- [115] G. Li, X. Kuang, S. Tian, F. Liao, X. Jing, Y. Uesu, and K. Kohn, *J. Solid State Chem.* **165**, 381 (2002)
- [116] J. B. A. A. Elemans, B. van Laar, K. R. van der Veen, and B. O. Loopstra, *J. Solid State Chem.* **3**, 238 (1971)
- [117] S. E. Dann, D. B. Currie, M. T. Weller, M. F. Thomas, and A. D. Al-Rawwas, *J. Solid State Chem.* **109**, 134 (1994)
- [118] R. D. Shannon, *Acta Crystallogr. Sect. A* **32**, 751 (1976)
- [119] I. B. Bersuker, *Phys. Lett.* **20**, 589 (1966)
- [120] R. E. Cohen, *Nature (London)* **358**, 136 (1992)
- [121] H. Bethe, *Ann. Physik* **3**, 133 (1929)
- [122] J. H. van Vleck, *Phys. Rev.* **41**, 208 (1932)
- [123] J. H. van Vleck, *J. Chem. Phys.* **3**, 807 (1935)
- [124] H. Hartmann and H. L. Schlafer, *Z. Naturforsch.* **6a**, 751 (1951)
- [125] F. Hund, *Z. Phys.* **36**, 657 (1926)
- [126] R. S. Mulliken, *Phys. Rev.* **32**, 186 (1928)
- [127] R. S. Mulliken, *Rev. Mod. Phys.* **4**, 1 (1932)
- [128] J. E. Lennard-Jones, *Trans. Faraday Soc.* **25**, 668 (1929)
- [129] J. E. Lennard-Jones, *Proc. Cambridge Philos. Soc.* **27**, 469 (1931)
- [130] J. E. Lennard-Jones, *Proc. R. Soc. London* **198**, 14 (1949)
- [131] J. E. Lennard-Jones and J. A. Pople, *Proc. R. Soc. London* **202**, 166 (1950)
- [132] I. B. Bersuker, *Electronic Structure and Properties of Transition Metal Compounds: Introduction to the Theory*, 2nd ed. (John Wiley & Sons Inc., 2010)
- [133] Y. Tezuka, S. Shin, T. Ishii, T. Ejima, S. Suzuki, and S. Sato, *J. Phys. Soc. Jpn.* **63**, 347 (1994)
- [134] W. C. Koehler and E. O. Wollan, *J. Phys. Chem. Solids* **2**, 100 (1957)
- [135] F. A. Cotton, *J. Chem. Educ.* **41**, 466 (1964)
- [136] J. H. de Boer and E. J. W. Verwey, *Proc. Phys. Soc., London* **49A**, E59 (1937)
- [137] R. Peierls, *Proc. Phys. Soc., London* **A49**, 72 (1937)
- [138] N. F. Mott, *Proc. Phys. Soc. London* **62**, 416 (1949)
- [139] J. Zaanen, G. A. Sawatzky, and J. W. Allen, *Phys. Rev. Lett.* **55**, 418 (1985)
- [140] P. W. Anderson, *Phys. Rev.* **124**, 41 (1961)
- [141] D. Vanderbilt, *Current Opinion in Solid State and Materials Science* **2**, 701 (1997)

- [142] D. E. Kotecki, J. D. Baniecki, H. Shen, R. B. Laibowitz, K. L. Saenger, J. J. Lian, T. M. Shaw, S. D. Athavale, C. Cabral, P. R. Duncombe, M. Gutsche, G. Kunkel, Y.-J. Park, Y.-Y. Wang, and R. Wise, *IBM Journal of Research and Development* **43**, 367 (1999)
- [143] J. F. Scott, *Ferroelectric Memories*, Advanced Microelectronics (Springer, Berlin, 2000)
- [144] R. Waser, *Nanoelectronics and Information Technology*, 2nd ed. (Wiley-VCH, Berlin, 2005)
- [145] T. Omata, Y. Noguchi, and S. Otsuka-Yao-Matsuo, *Journal of The Electrochemical Society* **152**, E200 (2005)
- [146] G. Łupina, O. Seifarth, G. Kozłowski, P. Dudek, J. Dąbrowski, G. Lippert, and H.-J. Müssig, *Microelectronic Engineering* **86**, 1842 (2009)
- [147] K. Ueda, H. Yanagi, R. Noshiro, H. Hosono, and H. Kawazoe, *J. Phys.: Condens. Matter* **10**, 3669 (1998)
- [148] T. D. Kang, H. Lee, G. Xing, N. Izumskaya, V. Avrutin, B. Xiao, and H. Morkoc, *Appl. Phys. Lett.* **91**, 022918 (2007)
- [149] S. G. Choi, A. M. Dattelbaum, S. T. Picraux, S. K. Srivastava, and C. J. Palmstrom, *J. Vac. Sci. Technol. B* **26**, 1718 (2008)
- [150] L. S. Cavalcante, J. C. Sczancoski, V. M. Longo, F. S. de Vicente, J. R. Sambrano, A. T. de Figueiredo, C. J. Dalmaschio, M. S. Li, J. A. Varela, and E. Longo, *Opt. Commun.* **281**, 3715 (2008)
- [151] V. Trepakov, A. Dejneka, P. Markovin, A. Lynnyk, and L. Jastrabik, *New J. Phys.* **11**, 083024 (2009)
- [152] R. D. King-Smith and D. Vanderbilt, *Phys. Rev. B* **49**, 5828 (1994)
- [153] H. Lee, Y. S. Kang, S.-J. Cho, B. Xiao, H. Morkoc, T. D. Kang, G. S. Lee, J. Li, S.-H. Wei, P. G. Snyder, and J. T. Evans, *J. Appl. Phys.* **98**, 094108 (2005)
- [154] W. Maus-Friedrichs, M. Frerichs, A. Gunhold, S. Krischok, V. Kempter, and G. Bihlmayer, *Surf. Sci.* **515**, 499 (2002)
- [155] E. A. Kotomin, Y. F. Zhukovskii, S. Piskunov, and D. E. Ellis, *Journal of Physics: Conference Series* **117**, 012019 (2008)
- [156] C. Friedrich, A. Schindlmayr, S. Blügel, and T. Kotani, *Phys. Rev. B* **74**, 045104 (2006)
- [157] H. Bross and G. M. Fehrenbach, *Z. Phys. B* **81**, 233 (1990)
- [158] F. R. McFeely, L. Ley, S. P. Kowalczyk, and D. A. Shirley, *Solid State Commun.* **17**, 1415 (1975)
- [159] F. Aryasetiawan and S. Biermann, *Phys. Rev. Lett.* **100**, 116402 (2008)

- [160] M. van Schilfgaarde, T. Kotani, and S. Faleev, *Phys. Rev. Lett.* **96**, 226402 (2006)
- [161] A. Svane, N. E. Christensen, M. Cardona, A. N. Chantis, M. van Schilfgaarde, and T. Kotani, *Phys. Rev. B* **81**, 245120 (2010)
- [162] A. Okazaki and M. Kawaminami, *Mater. Res. Bull.* **8**, 545 (1973)
- [163] A. M. Glazer and S. A. Mabud, *Acta Crystallogr. Sect. B* **34**, 1065 (1978)
- [164] S. Teslic and T. Egami, *Acta Crystallogr. Sect. B* **54**, 750 (1998)
- [165] V. Madigout, J. L. Baudour, F. Bouree, C. Favotto, M. Roubin, and G. Nihoul, *Philos. Mag. A* **79**, 847 (1999)
- [166] R. E. Cohen and H. Krakauer, *Ferroelectrics* **136**, 65 (1992)
- [167] G. Onida, L. Reining, and A. Rubio, *Rev. Mod. Phys.* **74**, 601 (2002)
- [168] M. Rohlfing and S. G. Louie, *Phys. Rev. B* **62**, 4927 (2000)
- [169] J. Tauc, *Optical Properties of Solids* (North-Holland, Amsterdam, 1971)
- [170] E. A. Davis and N. F. Mott, *Philos. Mag.* **22**, 903 (1970)
- [171] *Handbook of Ellipsometry*, edited by H. G. Tompkins and E. A. Irene (William Andrews Publications, Norwich, NY, 2005)
- [172] H. Fujiwara, *Spectroscopic Ellipsometry: Principles and Applications* (John Wiley & Sons Inc., 2007)
- [173] K. van Benthem, C. Elsässer, and R. H. French, *J. Appl. Phys.* **90**, 6156 (2001)
- [174] G. Lupina, J. Dąbrowski, P. Dudek, G. Kozłowski, P. Zaumseil, G. Lippert, O. Fursenko, J. Bauer, C. Baristiran, I. Costina, H.-J. Müssig, L. Oberbeck, and U. Schröder, *Appl. Phys. Lett.* **94**, 3 (2009)
- [175] V. I. Zametin, *Phys. Status Solidi B* **124**, 625 (1984)
- [176] F. Urbach, *Phys. Rev.* **92**, 1324 (1953)
- [177] S. H. Wemple, *Phys. Rev. B* **2**, 2679 (Oct 1970)
- [178] M. Cardona, *Phys. Rev.* **140**, A651 (1965)
- [179] X. G. Tang, H. R. Zeng, A. L. Ding, P. S. Qiu, W. G. Luo, H. Q. Li, and D. Mo, *Solid State Commun.* **116**, 507 (2000)
- [180] M. P. Moret, M. A. C. Devillers, K. Wörhoff, and P. K. Larsen, *J. Appl. Phys.* **92**, 468 (2002)
- [181] Y. Yuan, X. Zhang, L. Liu, X. Jiang, J. Lv, Z. Li, and Z. Zou, *Int. J. Hydrogen Energy* **33**, 5941 (2008)
- [182] G. Xing, N. Izyumskaya, V. Avrutin, T. D. Morkoc, H. Kang, and H. Lee, *Appl. Phys. Lett.* **89**, 122912 (2006)

- [183] F. L. Battye, H. Höchst, and A. Goldmann, *Solid State Commun.* **19**, 269 (1976)
- [184] K. Ueda, H. Yanagi, H. Hosono, and H. Kawazoe, *J. Phys.: Condens. Matter* **11**, 3535 (1999)
- [185] G. Pari, S. Mathi Jaya, G. Subramoniam, and R. Asokamani, *Phys. Rev. B* **51**, 16575 (1995)
- [186] I. Solovyev, N. Hamada, and K. Terakura, *Phys. Rev. B* **53**, 7158 (1996)
- [187] P. Ravindran, R. Vidya, H. Fjellvag, and A. Kjekshus, *J. Cryst. Growth* **268**, 554 (2004)
- [188] T. Arima, Y. Tokura, and J. B. Torrance, *Phys. Rev. B* **48**, 17006 (1993)
- [189] D. D. Sarma, N. Shanthi, and P. Mahadevan, *Phys. Rev. B* **54**, 1622 (1996)
- [190] P. Herve, T. Ngamou, and N. Bahlawane, *J. Solid State Chem.* **182**, 849 (2009)
- [191] W. E. Pickett and D. J. Singh, *Phys. Rev. B* **53**, 7550 (1996)
- [192] V. I. Anisimov, J. Zaanen, and O. K. Andersen, *Phys. Rev. B* **44**, 943 (1991)
- [193] V. I. Anisimov, I. V. Solovyev, M. A. Korotin, M. T. Czyżyk, and G. A. Sawatzky, *Phys. Rev. B* **48**, 16929 (1993)
- [194] Z. Yang, Z. Huang, L. Ye, and X. Xie, *Phys. Rev. B* **60**, 15674 (1999)
- [195] E. O. Wollan and W. C. Koehler, *Phys. Rev.* **100**, 545 (1955)
- [196] D. D. Sarma, N. Shanthi, S. R. Barman, N. Hamada, H. Sawada, and K. Terakura, *Phys. Rev. Lett.* **75**, 1126 (1995)
- [197] S. Satpathy, Z. S. Popović, and F. R. Vukajlović, *Phys. Rev. Lett.* **76**, 960 (1996)
- [198] R. Tyer, W. Temmerman, Z. Szotek, G. Banach, A. Svane, L. Petit, and G. A. Gehring, *Europhys. Lett.* **65**, 519 (2004)
- [199] T. Saitoh, A. E. Bocquet, T. Mizokawa, H. Namatame, A. Fujimori, M. Abate, Y. Takeda, and M. Takano, *Phys. Rev. B* **51**, 13942 (1995)
- [200] H. Wadati, D. Kobayashi, H. Kumigashira, K. Okazaki, T. Mizokawa, A. Fujimori, K. Horiba, M. Oshima, N. Hamada, M. Lippmaa, M. Kawasaki, and H. Koinuma, *Phys. Rev. B* **71**, 035108 (2005)
- [201] R. W. Godby, M. Schlüter, and L. J. Sham, *Phys. Rev. B* **37**, 10159 (1988)
- [202] M. Grüning, A. Marini, and A. Rubio, *J. Chem. Phys.* **124**, 154108 (2006)
- [203] S. Biermann, F. Aryasetiawan, and A. Georges, *Phys. Rev. Lett.* **90**, 086402 (2003)
- [204] F. Aryasetiawan, J. M. Tomczak, T. Miyake, and R. Sakuma, *Phys. Rev. Lett.* **102**, 176402 (2009)

- [205] R. Del Sole, L. Reining, and R. W. Godby, *Phys. Rev. B* **49**, 8024 (1994)
- [206] J. W. Edwards, R. Speiser, and H. L. Johnston, *J. Am. Chem. Soc.* **73**, 2934 (1951)
- [207] H. Fujishita, Y. Ishikawa, S. Tanaka, A. Ogawaguchi, and S. Katano, *J. Phys. Soc. Jpn* **72**, 1426 (2003)